Development and validation of human *in vitro* articular cartilage models

A thesis submitted to the Faculty of Science, Agriculture and Engineering for the Degree of Doctor of Philosophy

by

Annachiara Scalzone

School of Engineering

Newcastle University

May 2022

ABSTRACT

Osteoarthritis (OA) is a multifactorial disease characterised by the whole joint degeneration. The low availability, reproducibility, and reliability of early-stage *in vitro* disease models are currently limiting research into novel treatments. The aim of this PhD project was to develop new *in vitro* models and evaluate their effectiveness.

Firstly, a scaffold-free spheroids-based model of Articular Cartilage (AC) was developed, taking inspiration from the clinically approved Chondrosphere® technique. This approach utilised a bankable cell type (immortalised mesenchymal stem cells differentiated in chondrocytes (Y201-C)) and produced a standardisable and reproducible AC-like construct, showing high expression of chondrogenic markers and AC matrix production. By optimising a cocktail of pro-inflammatory mediators (Interleukin-1β, 6 and TNF-α) the main features of OA pathogenesis at early-medium disease stage could be introduced. The obtained *in vitro* OA model was used as platform for evaluating a novel microRNA-based polyplex treatment, showing potential for further therapeutics testing.

The main limitation of scaffold-free models is to adequately recapitulate the heterogeneous composition and high level of AC zonal organisation, and the influence of subchondral bone (SB) in OA pathogenesis. Therefore, the second part of this PhD was focused on the design, manufacturing, and optimisation of a four-zones osteochondral model by combining multiple manufacturing techniques (electrospinning, bioprinting, soft lithography and fusion deposition modelling); different materials (natural-based hydrogels for the AC side and a thermo-plastic polymer for the SB side) and two cells type (Y201 for SB and Y201-C for AC). The physico-chemical properties and biological performances of each individual layer were studied in healthy and OA conditions, before their assembly as whole zonal model. Each layer reproduced features of the corresponding native zone in terms of matrix and cells organisation, gene expression and matrix production. Also, the main OA features (e.g. degradation of collagen from the surface, chondrocytes hypertrophy within the deep layer) were observed in OA condition.

In conclusion this project has successfully developed and validated human *in vitro* models closely mimicking AC with characteristic pathological features of early-stage OA. These models provide novel insights to inform future production of reliable and scalable human *in vitro* models for testing novel OA treatments.

“Trying and trying again”

Galileo Galilei

To my mum, my dad and Carlotta

ACKNOWLEDGMENTS

For my PhD journey, I would like to express my sincere gratitude to all those who made it possible for me to complete my studies.

First, I would like to acknowledge the Engineering and Physical Sciences Research Council for supporting and funding my project. A special thank goes to my supervisory team: Dr. Piergiorgio Gentile, my mentor and my guide, for trusting in me and giving me the opportunity to work and grow up professionally with him, Dr. Ana Ferreira-Duarte for her great ideas, source of inspiration for my project, Prof. Kenny Dalgarno for his great research advices and strong support in each step of my PhD and Dr. Xiao Wang, who made me passionate about the world of biology and gave me the opportunity to work with EVs.

I would like to thank Prof. Gloria Gallego-Ferrer for allowing me to work in their laboratory at "Universidad Politécnica de València", and to help me during my PhD placement. I also thank Dr Laia Tolosa for the imaging support at the "Instituto de Investigación Sanitaria La Fe" of Valencia. Also, I thank Maria and Sandra, for the amazing researchers they are, the help they gave me during my project in Valencia, and the great friends they became for me.

I would like to acknowledge the support of the Newcastle University Bio-imaging facility and the Electron Microscopy service. I would also like to acknowledge Dinu Iuga of University of Warwick for the support in the h-NMR analysis.

I would like to thank the awesome friends and colleagues I met during these years, for making this experience enjoyable and Newcastle, my second home. Especially my biggest thanks go to Marcin, Barbara, Joe and Priscila, who made a big change in my life.

I would like to thank my family for the endless support and the love they gave me. I would like to thank my grandfather Bruno for being the first one believing in me as a scientist.

I would also like to acknowledge my friends in Italy, especially Chiara, because no matter the distance, it is a blessing to have you in my life.

I finally thank Roberto, my life companion, for being by my side as a friend and as a partner, for celebrating with me all the successes and for being my safe harbour during the failures.

TABLE OF CONTENTS

LIST OF FIGURES

Chapter 2:

forces and other factors (1-2). These molecules could bind specific receptors of synovium cells and chondrocytes, stimulating the production of pro-inflammatory mediators (3-4), responsible for chondrocytes enhanced catabolic activity of and inhibition of its biosynthetic activity, as well as for the activation of osteoclast activity mediated by osteoblast degeneration (5-6). All these events lead to the ECM degradation (7).

Figure 2.9: Proteolytic cleavage sites within the aggrecan core protein in AC by: ADAMTS4/5 (A), calpain (C); HtrA1 (H), MMPs (M). (**A**). Cleavage site for Coll II in AC by MMPs (M) (**B**). Factors regulating expression and activity of collagenases (MMPs) and aggrecanases (ADAMTS) in OA; the expression and activity of MMPs and ADAMTs can be stimulated (green) or inhibited (red) by several inter-related mechanisms: inflammatory cytokines, via Histone deacetylases (HDAC), induce NF-kB dependant expression of Hypoxia-inducible factor-2 (HIF-2α), resulting in increased expression of MMPs and ADAMTS and increased RUNX2 expression via Indian hedgehog (IHH); mechanical damage has the same effect on IHH, while the inhibitors of HDAC can have chondroprotective effect; High temperature requirement A (HtrA), highly expressed during OA, allows collagen binding with discoin domain receptors (DDR) causing downstream of signalling events such as MMP13 expression; Activated protein (APC) and Matriptase 1 increase MMP expression, as well as FGF-2, which act as a transducer of protective mechanical signals suppressing ADAMTS; CITED2, which is a mediator of mechanical responses in AC and suppresses MMPs; syndecan4 acts as an ADAMTS5 stimulator and on the other side miRNA 140 as ADAMTS5 inhibitor (**C**).

Figure 2.10: Scheme of the Chondrosphere® (CO.DON, AG) technique: (1) chondrocytes harvesting, (2) preparation of cells spheroids and suspension in isotonic sodium chloride solution, (3) injection in the cartilaginous defect (10 – 70 spheroids per cm^2) within a syringe - Arthroscopic view after transplantation into an AC defect. [courtesy of Dr. Schreyer,ev. Elisabethenstift Hospital,Darmstadt,GE]

Figure 2.11: MicroRNA biology and function: MicroRNA is transcribed in the nucleus to either pri-miRNA or premiRNA. The pre-miRNA is then transported to the cytoplasm, where it is further cleaved to generate mature miRNA. MiRNA binds to its target mRNAs by forming a complex with the miRNA induced silencing complex (RISC). Translation of mRNA into protein is inhibited when miRNA and mRNA are partially complementary. When miRNA and mRNA complement one other nearly perfectly, the mRNA is destroyed.

Figure 2.12: Scaffold-free approaches for obtaining *in vitro* models: cell sheet engineering (**A**), aggregate engineering (**B**) and self-assembling (**C**).

Figure 2.13: Representation of electrospinning process and Taylor cone (**A**). Schematic illustration of the effect of the concentration, flow rate, and voltage on electrosprayed/ electrospun nano/microstructures (**B**). Electrospinning process for the obtainment of Random (using a plate collector) or aligned (using a rolling collector) fibers. Bars=10 μm.

Figure 2.14: Schematic illustration of the procedures for obtaining a patterned polymer by starting from a positive substrate via PDMS via soft lithography technique: the desired pattern is designed with a computer-aided design (CAD) software program and the topographically patterned substrate (which will have the same pattern of the final desired structure) is manufactured (e.g. via 3D printing) (1); liquid PDMS, mixed with curing agent, is poured onto the micropatterned master substrate and thermally cured (2-4); the PDMS pattern is

transferred back into a replica of the original master by solidifying a liquid prepolymer such as UV-curable or thermally curable hydrogels precursor, against the soft PDMS mould (5-6).

Figure 2.15: Bioprinting fabrication technique. Illustration of bioprinting technique and bioinks formulation, which has cells as mandatory component and materials as optional element (**A**); Modalities of bioprinting processes: extrusion-based bioprinting, laser-assisted bioprinting, ink-jet bioprinting (**B**); Biomaterial properties for an ideal bioink in order to respect the biofabrication window for the rational design of bioinks, based on three parameters: printability; biocompatibility and mechanical stability (**C**).

Chapter 3:

Figure 3.1: Schematic representation of the GGMA synthesis process.

Figure 3.2: Schematic representation of the CSDP synthesis process.

Figure 3.3: Picture of a cylindrical hydrogel sample (GGMA-GEL) during unconfined compression test performed with a mechanical testing machine (EZ SX, Shimadzu), cell load 20 N.

Chapter 4:

Figure 4.1: Scheme of the manufacturing and characterisation process: from: ***(1)*** cell expansion (HC, Y201, Y201-C, TC28a2) and their re-suspension in cell culture media supplied with MC (0.25 % w/v); ***(2)*** formation of spheroids (2 x 20^5 cells per spheroid) in a round bottom 96-well plate, their culture for 7 days and characterisation (Growth kinetics analysis, Live/Dead, CellTiter-Glo® 3D, CellTox™ Green, TEM, RealTim-Glo Assay and SEM); ***(3)*** assembly of spheroids on a GEL coated PLGA electrospun membrane (10 spheroid per cm^2 of membrane) and their characterisation over 21 days of culture (Imaging, SEM, GAGs quantification and RT-qPCR).

Figure 4.2: Scheme explaining how the RealTime apoptosis and necrosis assay works. Healthy cells give a negative signal, cells in early apoptosis stage give a Luminescence (RLU) positive signal, while cells in secondary necrosis dive a RLU and Fluorescence (RFU) positive signal [re-adapted from www.promega.uk].

Figure 4.3: Manufacturing process of the OA in vitro model: HC and Y201-C cells expansion (1), Spheroids culture and characterisation in a round bottom 96-well plate for 10 days (2) with the addition of IL-6, IL-1ß, TNF-α proinflammatory mediators at day 3 of spheroids culture (3), Chondrospheres culture and characterisation for further 11 days on a GEL-coated electrospun PLGA membrane (4).

Figure 4.4: Pictures taken from the bottom of the round bottomed 96-well plate. Each well contains $2x10^5$ Y201-C cells per spheroids, cultured in DMEM/F12 media supplemented with 0.25 % MC. Picture taken after 24 h of spheroids culture (**A**). The arrow is pointing the spheroids on a microscope slide (**B**).

Figure 4.5: Manufacturing of spheroids with four different cell types: TC28a2, Y201, HC, Y201-C. Scheme of the spheroid's formation analysis from the seeding to the spheroid formation (**A**). Phase contrast brightfield images of spheroids after 72 hours with TC28a2 (**B**), Y201 (**C**), HC (**D**) and Y201-C (**E**). Scheme of the cell type used for the experiments: code, name of the cells and result of the trial of spheroids formation in 72 hours (**F**).

Figure 4.6: HC and Y201-C spheroids pictures taken at day 1, day 3 and day 7. Bars: 100 µm (**A**). Graphs reporting the change in spheroids diameter and area at the respective time points for HC and Y201-C (**B**). Analysis of the circularity and roundness for HC and Y201-C (**C**). Statistics: **** p<0.0001.

Figure 4.7: HC and Y201-C spheroids Live/Dead assay at day 1, day 3 and day 7, for HC (**A**) and Y201-C (**B**). Bars:100µm. Calcein stains live cells (green) and Ethidium Bromide (EthBr) stains dead cells (red).

Figure 4.8: HC and Y201-C spheroids metabolic activity via CellTiter-Glo® 3D assay at day 1, day 3 and day 7 for both cells type (**A**). Cells viability percentage obtained by CellTox™ Green Assay (**B**). Statistics: **** p<0.0001, *** p<0.005.

Figure 4.9: TEM images of changes to cellular ultrastructure during spheroids maturation in vitro at day 2 and day 7 for HC (**A-F**) and Y201-C (**G-L**) in the core (**A,B,D,E,G,H,J,K**) and in the peripheral zone (**C,F,I,L**); specific organelles are reported: nuclei (N), mitochondria (M) and endoplasmic reticula (ER) and cellular degeneration in form of chromatin clumping and nuclear fragmentation (red arrow) and vacuolisation (purple arrow).

Figure 4.10: Apoptosis-Necrosis assessment via Real-time assay at early stage (day 1 - day 3) and late stage (day 5 – day 7) for HC and Y201-C. Graphs for HC and Y201-C at early and late stages reporting the apoptosis percentage (**A**) and the necrosis percentage (**B**).

Figure 4.11: SEM analysis of HC and Y201-C spheroids at day 2 (**A,C**) and day 7 (**B,D**). Inserts report a higher magnification on the surface morphology of spheroids.

Figure 4.12: Chondrosphere fusion trial after 21 days of culture in 48-well plate with (**A**) or without (**B**) the addition of MC.

Figure 4.13: Chondrosphere formation and maturation after 21 days of culture. Brightfield images taken of spheroids seeded on the membrane and some higher magnifications in inserts for HC (**A**) and Y201-C (**B**). SEM images of chondrosphere after 21 days of culture on PLGA-GEL membrane of HC (**C**) and Y201-C (**D**). Higher magnification in the areas of interest (1, 2).

Figure 4.14: GAGs quantification analysis on HC (**A**) and Y201-C (**B**) for the chondrospheres at day 0,14 and 21 of culture. Results are normalised to spheroids at day 1. Statistics: **** p<0.0001.

Figure 4.15: RT-qPCR analysis graphs showing the fold-change ($2^{-\Delta\Delta Ct}$) at day 1 and day 21 of chondrospheres culture relative to spheroid at day 1: SOX9 for HC (**A**) and Y201-C (**D**), ACAN for HC (**B**) and Y201-C (**E**) and COL2A1 for HC (**C**) and Y201-C (**F**). Statistics: ****p<0.0001.

Figure 4.16: Spheroids growth. Images of HC spheroids at day 1 (**A**), day 4 (**B-D**) and day 10 (**E-G**) in Healthy (**A,B,E**) LC-OA (**C,F**) and HC-OA (**D-G**) conditions. Bars: 300 µm. Diameter length analysis (**H**). Statistics: ****p<0.0001.

Figure 4.17: Spheroids growth. Images of Y201-C spheroids at day 1 (**A**), day 4 (**B-D**) and day 10 (**E-G**) in Healthy (**A,B,E**) LC-OA (**C,F**) and HC-OA (**D-G**) conditions. Bars: 300 µm. Diameter length analysis (**H**). Statistics: ****p<0.0001.

Figure 4.18: HC (**A**) and Y201-C (**B**) cells metabolic activity evaluated with MTS assay at day 1, day 4 and day 10 of spheroids culture in Healthy, LC-OA and HC-OA. Statistics: **p<0.05 and *p<0.01.

Chapter 5:

Images of the spheroids (**A**), analysis of the average diameter in each condition (**B**), morphometric analysis of spheroids roundness and circularity (**D**). Arrows pointing at the inhomogeneous surface of the MS-P spheroids in (**A**).

Figure 5.7: Analysis of cells viability via staining of all cells nuclei with HOECHST (blue) and dead cells with propidium iodide (PI) (red). Arrows pointing at the MS. Bars = 100 µm (**A**). Metabolic activity evaluation for Y201-C (**B**). The conditions exploited were CTRL-H, MS-H, CTRL-P, MS-P. Statistics: ****p<0.0001.

Figure 5.8: TEM analysis performed for CTRL-H and MS-H at day 7. Images taken at the peripheral region of the spheroids (**A,B,E,F**) and in the middle of the spheroid (**C,D,G,H**).

Figure 5.9: RT-qPCR results showing the fold change of *sox9* (**A**), *col2a1* (**B**), *acan* (**C**), *mmp13* (**D**) and *adamts-5* (**E**) at day 21, with respect of day 1. Conditions analysed: CTRL-H and CTRL-P, Y201-C without the MS and without the bioreactor stimulation; MS-H and MS-P, Y201-C with the MS and without the bioreactor stimulation; EXP-H and EXP-P, Y201-C with the MS and with the bioreactor stimulation. Statistics: ****p<0.0001.

Figure 5.10: Graphs representing the ζ- potential and size distribution of the different polyplexes at 0, 5, 10, 15, 20, 199, 250, 500, 2000 µg/mL of CH.

Figure 5.11: Cell viability performed at 24 and 48 hours using CH at 3 different concentrations (0 µg/mL, 5 µg/mL, and 250 µg/mL). In blue are stained cells nuclei (HOECHST) and in red dead cells (EthBrom) (**A**). Cells metabolic activity assessment at day 1 and day 2 in the same three conditions (**B**). Statistics: ***p<0.001.

Figure 5.12: Immunostaining images of CH/miR-140 polyplexes at 24 and 48 hours. The images shown are a merge of DAPI, Phalloidin Rhodamine (PhallRhod) and labelled mirna (mirFI). Images are taken at 20 x at 24 and 48 h for the three conditions (**A**)and at 20 x and 40 x at 48 h for the CH 250 µg/mL condition.

Figure 5.13: Gene RT-qPCR analysis to evaluate the expression of *sox9* (**A**)*, acan* (**B**)*, col2a1* (**C**)*, mmp13* (**D**) and *adamts-5* (**E**)*,* for assessing the therapeutic treatment of CH/miRNA based polyplexes in an OA *in vitro* model, compared to OA conditions and healthy conditions. The fold change at day 10 with respect to day 1 is reported in the graphs. A graph reporting the *col2a1/col1a2* ratio is reported as well (**G**). Statistics: *p<0.05, ***p<0.001, ****p<0.0001.

Figure 6.14: Histological analysis of cryosections of HC spheroids at day 1 and at day 10 in healthy, OA and OA+polyplexes conditions. H&E staining of cells nuclei and cytoplasm (**A-D**), Picrosirius red staining of collagen (**E-H**), Alcian blue staining of GAGs (**I-L**).

Chapter 6:

Figure 6.1: Scheme of the manufacturing process for the zonal model: (1) manufacturing of SB via FDM of PLA with Rokit INVIVO bioprinter (6 x 6 x 1 mm); (2) DL manufacturing, based on GG3, via soft-lithography, with PDMS moulding (6 x 6 x 3 mm); (3) combination of SB and DL constructs, during UV exposure; (4) bioprinting of Y201-C-loaded GG2-MH bioink for the obtainment of the ML (6 x 6 x 2 mm); (5) electrospinning of PCL/GEL membranes and seeding with Y201-C for the manufacturing of the SL (6 x 6 mm); (6) combination of SL and ML; (7) formation of the zonal construct by merging the SL-ML construct with the SB-DL construct, via CSDP hydrogel loaded with Y201-C and seeding of the SB with Y201.

Figure 6.2: Chemical characterisation of GG and GGMA. FTIR-ATR spectra of low-acyl GG and GGMA freeze-dried samples **(A);** NMR graph of GG before and after the methacrylation, relative to the ^{13}C CP, ^{1}H MAS and 2D ^{1}H-^{13}C heteronuclear correlation spectra with related ^{1}H and ^{13}C projections (**B**); XPS data relevant to C1s curve fittings of GG and GGMA samples, whose attributions and atomic percentages were reported in **Table 6.5** (**C**).

Figure 6.3: Analysis of Gelation time for GG2, GG3 and GG2-MH hydrogels with Photo-crosslinking or a combination of Ionical and Photo-crosslinking: Tube inverted vial test at 0 minutes (**A,B**), 3 (**C,D**) and 10 minutes (**E,F**).

Figure 6.4: Water Uptake study of GG2, GG3 and GG2-MH at different time points up to 48 hours (insert: zoom on the first 8h of uptake).

Figure 6.5: Morphological analysis of GG2, GG3 and GG2-MH hydrogels. SEM images representing cross-section microstructure of: GG2 at 35x (**A**) and 100 x (**B**); GG2-MH at 35x (**A**) and 100 x (**B**) and (C,D) GGMA-MH hydrogels at magnifications 35x (A,C) and 100 x (B,D). Bars=500 μm; (E) Distribution analysis of the pores within the ranges <100 μm, 100–1500 μm, 150–200 μm, >200 μm for GGMA (black) and GGMA-MH (grey).

Figure 6.6: Unconfined compression test of GGMA-based hydrogels. Example of stress(σ) vs. strain (ε) curves for GG2 (black arrow pointing at the breakage point) (**A**), GG3 (**B**) and GG2-MH (**C**). Report of the Young's Modulus for GG2, GG3 and GG2-MH. Statistics: *p<0.05.

Figure 6.7: Rheological analysis of GG2, GG2-MH and GG3 hydrogels. Strain sweep test at 37 °C showing Storage (G') and Loss (G") moduli as a function of the strain in the range 0.1 -20 % (**A**); Complex modulus (G*) as a function of the strain (0.1-20%) (**B**); Temperature sweep test in the temperature range 15-50 °C and record of G' an G" in LVER at each temperature (**C**); Report of G* at 2% strain, apparent viscosity (η) and strain value at yield point (Yield γ %) (**D**).

Figure 6.8: Chemical characterisation of CS and CSDP. FTIR-ATR spectra of CS powder and freeze-dried CSDP samples **(A);** NMR graph of CS and CSDP (**B**); XPS data relevant to C1s and N1s curve fittings of CS, DP and CSDP samples (**C**).

Figure 6.9: Physico-chemical characterisation of CSDP10 and CSDP20 hydrogels: SEM images of the freeze-dried hydrogels. Bars= 500 μm. (**A**) Water Uptake study of at different time points up to 48 hours (**B**); Unconfined compression test of CSDP hydrogels: example of stress(σ) vs. strain (ε) curves (**C**).

Figure 6.10: Images of the 3D-printed PLA grid for the SB manufacturing, at different magnifications.

Figure 6.11: Assessment of the functionalisation effect on the PLA structure. SEM analysis on PLA to assess the morphology before (**A,B**) and after the functionalisation with DOPA (**C,D**), with DOPA and GEL (1%w/v) via poly-dopamine coating (**E,F**) and with GEL (1% w/v) and nHA (5% w/w) via poly-dopamine coating (arrows pointing at the nHA deposits) (**G,H**). Bar= 100 μm (**A,C,E,G**) and 500 μm (**B,D,F,H**). Magnification: 35x (**A,C,E,G**) and 100 x (**B,D,F,H**). Representative microCT images of all the 3D printed scaffolds pre-functionalisation (**I**) and post-functionalisation with DOPA (**J**), DOPA/GEL (**K**) and DOPA/GEL/nHA (**L**). All the scaffolds are 13 x 13 x 1 mm. Table reporting the total porosity (%) in the four conditions (**M**).

Figure 6.12: Y201s viability on PLA 3D printed scaffolds. Live/Dead viability assessment (calcein staining live cells in green and Ethidium Bromide staining dead cells in red) at day 3 on PLA/DOPA (**A**) and PLA/GEL (**B**); and at day 3 (**C**) and day 7 (**D**) on PLA/GEL/nHA. Number of metabolically active cells at day 1, day 7 and day 21 on PLA/GEL and PLA/GEL/nHA, evaluated with MTT assay (**E**). Statistics: ****p<0.0001.

Figure 6.13: Cells distribution and morphology on PLA/GEL/nHA scaffold. Immunostaining of cells cytoskeleton (PhalloidinRhodamine) and Nuclei (DAPI) on PLA/GEL/nHA at day 3 (**A**) and day 7 (**B**): arrows indicate mitosis. Bars= 100 µm. SEM images after 1 day of cells seeding at 250 x (**C**) and 1500 x (**D**).

Figure 6.14: Gene RT-qPCR and Western Blot analyses to evaluated respectively genes and proteins expression for assessing the ability of nHA functionalization to promote Y201s osteogenic differentiation onto PLA/GEL/nHA scaffolds, compared to bare PLA/GEL. Relative expression of *runx2* (**A**), *alpl* (**B**) and *sparc* (**C**) by Y201s via RT-qPCR at day 1 and day 21 of culture. Proteins densitometric quantification expressed as intensity normalised to GAPDH at day 1, 7, 14 and 21, for RUNX2 (**D**), ALP active peptide 200KDa (**E**) and ON (**F**). Western blotting membrane of Y201s at days 1, 7, 14 and 21 incubated with ALP, RUNX2, ON and GAPDH antibodies (**G**). Statistics: *p<0.05, **p<0.01, ***p<0.001, ***p<0.0001.

Figure 6.15: Immunofluorescence images of Osteonectin staining (red) and cells nuclei (blue) on PLA/GEL (**A-C**) and PLA/GEL/nHA (**D-F**) scaffolds at day 21 of culture. Bars= 100 µm.

Figure 6.16: Analysis of mineralisation on PLA scaffolds with (PLA/GEL/nHA) and without (PLA/GEL) the presence of nHA: Images at day 1 (**A,B**), day 7 (**C,D**) and day 21 (**E,F**). Higher magnification in the inserts. Bars= 2 mm. Quantification of Alizarin Red at days 1, 7 and 21 (**G**).

Figure 6.17: Gene RT-qPCR and Western Blot analyses to evaluated respectively genes and proteins expression for assessing the pathological features of PLA/GEL/nHA scaffold with (SB-P) and without (SB-H) the presence of cytokines. Relative gene expression of *runx2* (**A**), *collIa2* (**B**), *spp1* (**C**) and *vegf* (**D**) at day 1, day 14 and 21 in SB-H and SB-P conditions. Proteins densitometric quantification expressed as fold-change at days 7, 14 and 21 with respect of day 1 for RANKL (**E**) and OPG (**F**). Western blotting membrane incubated for RANKL, OPG and GAPDH at days 1, 7, 14 and 21 in SB-H and SB-P samples (**G**). Statistics: *p<0.05, **p<0.01, *** p<0.001 and **** p<0.0001.

Figure 6.18: Alizarin red analysis at days 1, 7, 14 and 21 in SB-H and SB-P samples, both qualitative (**A-F**) and qualitative (**G**). Higher magnification in the inserts. Bars= 2 mm.

Figure 6.19: Manufacturing process of DL: PLA master fabrication via FDM (1), PDMS molding (2) and the obtained finale GG3 construct, to be filled with CSDP and Y201-C in the holes (3).

Figure 6.20: Viability of Y201s-C embedded within DL-emulating hydrogel. Live/Dead viability assessment at day 1 and day 7: live cells are stained in green (**A,C**) and dead cells are stained in red (**B,D**). Histogram of cell viability obtained by MTS assay at days 1, 3 and 7 (**E**). Statistics: *** p<0.001.

Figure 6.21: DAPI/Phalloidin staining at day 1 (**A**) and day 7 (**B**), with a focus on the x,z axys, to observe the cells organisation through the channels of GG3 (**C**). SEM images at day 1: 50 x (**D**), 250 x (**E**) and 2500 x (**F**).

Figure 6.22: Assessment of DL in OA (DL-P) and healthy (DL-H) conditions. Immunofluorescence staining for ACAN (green) and COLLX (red) at days 1 and 21 for DL-H and DL-P: cell nuclei were counterstained with DAPI (**A**). Scale bar: 100 µm. Graph showing the percentage of ACAN and COLLX positive cells with respect to the nuclei (**B**). GAGs quantification at day 1, 14 and 21 in DL-H and DL-P samples: acellular GG-CSDP15 background was subtracted and data were extrapolated from a standard curve.

Figure 6.23: Stress relaxation curves obtained for DL construct at day 1 (**A**) and at day 14 in healthy (**B**) and pathological (arrow pointing at the breakage point) (**C**) conditions. Table reporting for each sample the Peak Young's modulus, the viscoelastic relaxation time (τ_1) and the poroelastic relaxation time (τ_3).

Figure 6.24: Morphological analysis of cells within the DL-H and DL-P constructs, after 21 days of culture.

Figure 6.25: Bioprinting procedure for GG2 and GG2-MH for manufacturing AC ML: scheme of the bioprinting process with encapsulated Y201-C and the optimised printing parameters for the Rokit INVIVO bioprinter (**A**). Images of the obtained GG2 and GG2-MH constructs: a four layers grid (left) and a 10-layers construct obtained with GG2-MH selected bioink at different magnifications (right).

Figure 6.26: Zoom in on the filament extruded before being deposited on the printing bed for GG2 (**A**) and GG2-MH (**B**): the red lines are indicating the change in the diameter alongside the length of the filament; (F,J) Phase contrast pictures of GGMA and GGMA-MH extruded filaments; (G,K) GFP images of GGMA and GGMA-MH extruded filaments.

Figure 6.27: Assessment of cells viability within the bioprinted GG2 (**A,B**) and GG2-MH (**C,D**) at day 1 and day 3, via confocal microscopy: 3D view. All cells nuclei are stained in blue (Hoechst) and dead cells are stained in red (Ethidium Bromide). The amount of dead cells are quantified with Image J software, from the obtained images (**E**). Evaluation of the number of metabolically active cells, via MTS assay (**F**). Statistics: ****p<0.0001, ***p<0.001.

Figure 6.28: Immunostaining of cells nuclei (blue, DAPI) and cytoskeleton (red, PhRhod): 2D images at days 1, 3 and 7 for GG2 (A,C,E) and GG2-MH (B,D,F); 3D view at day 7 for GG2 (G) and GG2-MH (H). Bars= 100 µm.

Figure 6.29: SEM analysis of GG2 (**A,B**) and GG2-MH (**C,D**) hydrogels after 21 days of culture at 2000 x (**A,C**) and 4000 x (**B,D**).

Figure 6.30: Histological analysis of cryosections of GG2 and GG2-MH at day 1 and at day 21 in healthy (GG2-H and GG2-P) and OA conditions (GG2-MH-H and GG2-MH-P). H&E staining of cells nuclei and cytoplasm (**A-F**), Picrosirius red staining of collagen (**G-L**), Alcian blue staining of GAGs (**M-R**). Bars= 150 µm.

Figure 6.31: GAGs quantification for GG2 (**A**) and GG2-MH (B) at days 1, 7 and 21 in healthy and OA conditions.

Figure 6.32: Gene RT-qPCR analysis to evaluated the expression of *sox9* (**A,B**)*, acan* (**C,D**)*, col2a1* (**E,F**)*, mmp13* (**G,H**) and *adamts-5* (**I,J**)*,* for assessing the pathological features of GG2 and GG2-MH construct in presence (GG2-P and GG2-MH-P) and absence of cytokines (GG2-H and GG2-MH-H). The fold change at day 21 with respect to day 1 is reported in the graphs. Fold change of SOX9, ACAN, COL2A1, MMP13 and ADAMTS-5 for GG2-MH-H and GG2-MH-P after 21 days of culture with respect to GG2-H (**J**) and GG2-P (**K**). In the dotted rectangles are

Figure 6.46: Cells distribution and morphology within the zonal model at day 1 (**A-F**) and day 7 (**G-L**). Staining of cells nuclei with DAPI and cytoskeleton with Phalloidin Rhodamine. Bars= 150 µm.

Figure 6.47: Histological analysis of zonal construct cryosections at day 21 in healthy (**A**) and pathological (**B**) conditions. H&E staining of cells nuclei and cytoplasm, Picrosirius red staining of collagen and Alcian blue staining of GAGs. Bars= 150 µm.

Figure 6.48: Morphological analysis of the obtained construct at day 1: total construct (**A**); zoom on different part of the construct: SL-ML interface (**B**), ML-DL interface (**C**), SL (**D**), morphology of the membrane and Y201-C on it (insert) (**E**).

Figure 6.49: Morphological analysis of the obtained construct at day 21 in healthy conditions: total construct (**A**); zoom on different part of the construct: SL (**B**), ML-DL interface (**C**), SB (**D**), SL-ML interface (**E**).

Figure 6.50: Morphological analysis of the obtained construct at day 21 in OA conditions: total construct (**A**); zoom on different part of the construct: SL-ML interface (**B**), SL – red arrows pointing at the apoptotic bodies (**C**), DL (**D**) and SB(**E**).

LIST OF TABLES

Chapter 2:

LIST OF ABBREVIATIONS

3D - Three-dimensional
ΔΔCt - Delta delta threshold cycle
AC - Articular cartilage
ACI - Autologous chondrocyte implantation
ACAN – Aggrecan
ADAMTS – A disintegrin and metalloproteinase with thrombospondin motifs
ANOVA - Analysis of variance
ASCs - Adipose stromal cells
BMAC – Bone Marrow Aspirate Concentrate
BMP - Bone morphogenetic protein
BMSCs - Bone marrow mesenchymal stem cells
BSA - Bovine serum albumin
CAD – Computer-Aided design
cDNA - Complementary deoxyribonucleic acid
CD-RAP - Cartilage-derived retinoic acid-sensitive protein
CILP - Cartilage intermediate layer protein
CO_2 - Carbon dioxide
Coll - Collagen
COMP - Cartilage oligomeric matrix protein
COL1A2 - Collagen1 typeA2
COL2A1 - Collagen2 typeA1
COX2 - Cyclooxygenase-2
CS - Chondroitin sulfate
CSDP – Chondroitin sulfate dopamine
Ct - Cycle threshold
DAPI - 4',6-Diamidino-2-Phenylindole
DD - Deacetylation degree
DGCR8 – DiGeorge syndrome critical region gene
DMEM - Dulbecco's modified Eagle's medium
DMOADs - Disease-modifying OA drugs
DMSO – Dimethyl sulphoxide
DNA - Deoxyribonucleic acid
DS – Dermatan sulfate
DW – Dry Weight
dH_2O - Distilled water
ECM - Extracellular matrix
EDC - 1-Ethyl-3-(3-dimethylaminopropyl)-carbodiimide hydrochloride
EDTA - Ethylenediaminetetraacetic acid
FBS – Fetal Bovine Serum
FDA – Food and Drugs Administration
FDM – Fusion Deposition Modelling
FTIR-ATR - Fourier transform infrared spectroscopy with attenuated total reflection
FWHM - Full width at half maximum
GAGs - Glycosaminoglycans
GAPDH - glyceraldehyde-3- phosphate dehydrogenase
GEL - Gelatin

GelMA - Methacrylate gelatin
GF – Growth Factors
GG – Gellan Gum
GGMA – Methacrylate Gellan Gum
GFP - Green Fluorescence protein
HA - Hyaluronic acid
HC – Primary foetal human chondrocytes
H&E - Haematoxylin & Eosin
HEPES - (4-(2-hydroxyethyl)-1-piperazineethanesulfonic acid)
HIF-2 - Hypoxia-inducible factor-2
ICRS - International Cartilage Repair Society
IGF-1 - Insulin-like growth factor-1
IHC – Immunohistochemistry
IHH - Indian hedgehog
IL- Interleukin
iPSCs - Induced pluripotent stem cells
ITS - Insulin-Transferrin-Selenium
LVER - Linear viscoelastic region
MA – Methacrylic anhydride
MAPK - Mitogen-activated protein kinases
MACI - Matrix-associated autologous chondrocyte implantation
MES - 2-(N-Morpholino) ethane sulfonic acid
MH – Manuka Honey
MMPs - Metalloproteinases
MRI - Magnetic resonance imaging
miRNA – Micro Ribonucleic Acids
mRNA - Messenger ribonucleic acid
MS - Microspheres
MSCs - Mesenchymal stem cells
MTT - Thiazolyl Blue Tetrazolium Bromide
MW - Molecular weight
MWCO – Molecular Weight cut-off
NF-κβ - Nuclear factor kappa B
nHA – nanohydroxyapatite
NHS - N -hydroxy succinimide
NICE - National Institute for Care and Excellence
NMR - Nuclear Magnetic Resonance Spectroscopy
NSAIDs - Nonsteroidal anti-inflammatory drugs
OA – Osteoarthritis
OCT – Optimal Cutting Temperature
PBS - Dulbecco's phosphate buffer saline
PCL - Polycaprolactone
PCR - Polymerase chain reaction
PDA – Polydopamine
PDMS - Polydimethylsiloxane
PEG - Polyethylene glycol
PEMF – Pulsed Electromagnetic Field
PFA - Paraformaldehyde
PG - Proteoglycan

PGA - Polyglycolic acid
PGE2 - Prostaglandine2
PLGA - Poly-L-lactic-co-glycolic acid
PLLA - Poly L-lactic acid
PTHrP - Parathyroid hormone-related protein
PRP – Platelet-rich plasma
PRR – Pattern Recognition Receptors
PVA – Polyvinyl alcohol
qPCR - Quantitative PCR
REM – Replica moulding
RFP - Red Fluorescence protein
RNA - Ribonucleic acid
rpm - Revolutions per minute
RT - Reverse transcriptase
SB – Subchondral Bone
Shh - Sonic hedgehog protein
SOX9 - Sex determining region Y-box 9
STL - Standard Tessellation Language
SZP - Superficial zone protein
TE – Tissue Engineering
TEM - Transmitted electron microscopy
TGFβ - Transforming growth factor-beta
TIMPs - Tissue inhibitors of metalloproteinases
TLR - Toll-like receptors
TNF-α - Tumour necrosis factor alpha
VEGF - Vascular endothelial growth factor
Wnt - wingless-type MMTV integration site family
WW – Wet Weight
XPS - X-ray photoelectron spectroscopy

Chapter 1. Introduction

Articular Cartilage (AC) is an avascular tissue with a heterogeneous composition with a high level of organisation, which makes it difficult for it to be repaired when damaged (Mescher, 2016). Among different forms of joint diseases, the progressive degeneration of AC due to osteoarthritis (OA) is the most common, with a global prevalence in the hip of 0.8 % and knee of 3.8 % (Versus Arthritis, 2021). In the UK over 8.75 million people, aged 45 and over, have sought OA treatment (Arthritis Research UK, 2011).

The main methodologies involved in OA treatment are: (*i*) non-pharmacological (e.g., physical therapy) and pharmacological (e.g., non-steroidal anti-inflammatory drugs) for mild to moderate degenerative joint diseases with the aim of reducing pain, and (*ii*) surgical operations (e.g., joint replacement, bone marrow stimulation techniques and osteochondral plugs), which are very successful in reducing pain and increasing mobility (Alford & Cole, 2005; Glyn-Jones et al., 2015). In the last decade, regenerative medicine techniques have increased in popularity (Kloppenburg & Berenbaum, 2020). One of these strategies is autologous chondrocyte implantation (ACI), firstly used in humans in 1987, with the pilot study published in 1994 and over 35,000 patients had been treated worldwide by 2010 for cartilage defects (Armoiry et al., 2019; Ogura et al., 2017; Harris et al., 2010).

ACI has gone through several evolutions, and the most recent is called Chondrosphere™ (or Spherox), considered the 4th generation ACI, that has been approved and recommended by the National Institute for Health and Care and Excellence (NICE), to treat symptomatic AC defects for up to 10 cm^2 (Armoiry et al., 2019; Cummins et al., 2017). This approach is based on the use of different doses of spheroids of human autologous chondrocytes and their transplantation into the AC defect (Davies & Kuiper, 2019; Cummins et al., 2017). Although Chondrosphere® has been clinically approved, it is expensive with a cost of £10,000 per patient per therapy and this technique is not promoted as an OA treatment (Armoiry et al., 2019).

OA disease pathogenesis is due to a joint action of physico-chemical and mechanical factors, where the progressive breakdown of AC and underlying subchondral bone (SB) are the main pathological features of OA (Glyn-Jones et al., 2015). However, there are still uncertainties about a long-term surgical treatment for OA joints, mainly because of the lack of knowledge about the OA evolution process and its internal mechanisms (March et al., 2016).

In this context, engineered AC *in vitro* models are ideal candidates for in-depth research into the physiology, biology, and progression of OA disorders. This is driving research into early-stage disease causes, as a key element for exploring, designing, and testing new therapeutic treatments in reliable and predictive models (Craig I. Johnson et al., 2016; Grenier et al., 2014). The benefits of using *in vitro* models are their easy manipulation, the importance of the ethical philosophy of refining, reducing, and replacing the use of animals in research (3R's principle) (European Parliament, 2010), the low reliability of animal studies when translated to human, and the high costs of *in vivo* studies (Peric et al., 2015).

Traditional 2D monolayer culture systems lack the ability to replicate the spatial organisation and cell-cell interaction found in the native AC. To obtain a functional AC-like tissue *in vitro*, capable of reliably recreating the mechanical, compositional, and structural properties of AC, it is necessary to design a 3D environment, able to support and stimulate the growth, organization and activity of the cells (Piluso et al., 2019). Several works involving the manufacture of *in vitro* AC construct can be found in literature, and these can mainly be categorised as scaffold-free and scaffold-based approaches.

Scaffold-free approaches aim to produce tissues by mimicking developmental processes, where 3D cell aggregate cultures are techniques which enables cell communications, by recapitulating the conditions of AC development (DuRaine et al., 2015; Sun et al., 2022). Numerous efforts have been made to identify novel cell sources. Since chondrocytes are already committed to cartilage development, most research groups focused on their use. However, obtaining autologous chondrocytes might result in donor-site morbidity and cell de-differentiation during 2D growth. Therefore, mesenchymal stromal cells (MSCs), such as those obtained from bone marrow, provide an alternative cell source, reducing donor-site morbidity. MSCs can be grown in monolayer culture and conditioned with certain growth factors (GFs) (e.g., transforming growth factor-beta (TGFβ)) *in vitro* to differentiate into chondrocyte-like cells (Brodkin & Garc, 2004).

Scaffold-based approaches combine chondrogenic cells with biomaterials, and several biomaterials able to influence cell fate towards ECM production have been explored, mainly natural-based hydrogels due to their similarity to AC ECM (Armiento et al., 2018; Hutmacher, 2006; Ngadimin et al., 2021). Scaffold based approaches can also incorporate GFs to further influence cell fate towards an anabolic metabolism (Kwon et al., 2019).

Despite the numerous efforts made in AC tissue engineering to identify novel cell sources, biomaterials and signalling factors, most research has focused on the manufacturing of a homogeneous *in vitro* construct, able to mimic the overall bulk properties of the native tissue by combining cells and biomaterials. AC, on the other hand, is a highly structured anisotropic tissue with spatially variable structure, composition, and mechanical characteristics. The tissue's biomechanical and biochemical function depends on its depth-dependent structure and composition (Klein et al., 2009; Kalamegam et al., 2018).

In the last years, an emergent approach, based on the manufacture of AC zonal-engineered *in vitro* models, is attracting the attention of the scientific community. Its primary goal is to recapitulate heterogenous functional, compositional and structural features of the AC, to obtain an *in vitro* construct representative of mature cartilage with respect to: zonal organisation (superficial, middle, deep layer and SB), biochemical composition (decreasing collagen II and increasing proteoglycans content from the surface to the deep zone), cellular morphology (flatten in the superficial layer, rounded and randomly distributed in the middle layer and piled up in the deep layer) and mechanical properties (Young's modulus increasing with the depth from 0.1 MPa to 8.0 MPa). Researchers have reported the manufacture of a partial and total zonal-engineered construct, investigating the cells source, their number, or the ECM composition. However, to date relatively few studies have attempted to successfully engineer reliable and reproducible zonal *in vitro* constructs with a structure and composition mimicking that of the native tissue (Ren et al., 2016a; Brown et al., 2020a; Gegg & Yang, 2020; Owida et al., 2018).

Furthermore, to study the OA pathophysiology, three mechanisms to induce the pathology and monitor its progression within *in vitro* AC models have been explored: (1) chemical induction, using a variety of pro-inflammatory mediators to simulate the ECM degradation seen in human OA; (2) mechanical induction, via injurious (i.e. biopsy punch and scalpel) or excessive and hyperphysiological mechanical loads to AC constructs; and (3) biological induction, using osteoarthritic cells (Grenier et al., 2014; Yeung et al., 2019; Bartolotti et al., 2021; Salgado et al., 2021). To date, no studies performed on healthy and pathological 3D zonal *in vitro* AC models are reported in literature.

1.1 Aim, rationale, and objectives

This thesis aimed to develop and evaluate scalable process to produce *in vitro* healthy and pathological models representative of AC tissue, to be used as platforms for testing novel therapeutics treatments. To this goal, two strategies were explored: a scaffold-free approach using multicellular spheroids and a biomaterial-based zonal approach, by mimicking the depth-dependent AC features.

Rationale: Although significant progresses were recently made in OA research, very little is yet known about the molecular mechanisms of OA initiation and progression. In addition, current OA treatments present several drawbacks, e.g., high costs, formation of transient fibro-cartilaginous tissue and only symptomatic pain relief. Therefore, a better understanding of the OA pathophysiological mechanisms within reliable *in vitro* models will accelerate the development of novel efficient and affordable therapeutic strategies for OA. These developed strategies are expected to significantly advance the biomedical field, contributing to the definition of new platforms *in vitro*, which could answer to the specific need of researchers, patients, surgeons, and medical doctors.

Hypothesis: The hypothesis behind this research is that engineered *in vitro* constructs, with a biomimetic internal and external spatial arrangement, may mature into functional tissue equivalents and in this way would be possible to analyse damaged or diseased AC. The closer *in vitro* model allows the reproduction of the native AC tissue complexity, more value the model will acquire. To test this hypothesis, the following objectives were considered:

- Objective 1: To develop a scaffold-free *in vitro* spheroids-based AC model, taking inspiration from the clinically approved Chondrosphere® technique, by using a bankable cell type. Cells viability, gene expression of chondrogenic markers and AC ECM production were assessed within this model.
- Objective 2: To use the scaffold-free model to study the OA on-set and development *in vitro,* by optimising a pro-inflammatory mediator – based chemical strategy and evaluating their effect on cells anabolic and catabolic activity.
- Objective 3: To use the obtained OA scaffold-free model as platform for evaluating novel advanced therapeutic treatments: microRNA-based polyplex treatment and a magnetic field-based bioreactor stimulation. This element of the research was performed in collaboration with the Universitat Politècnica de València.

- Objective 4: Design, manufacture, and optimisation of a four-zone *in vitro* osteochondral zonal model reproducing the hierarchical structure of the native tissue, by combining multiple manufacturing techniques, different materials and two cell types.
- Objective 5: Analysis of the obtained construct in terms of cell behaviour, matrix composition and organisation in healthy and pathological conditions.

1.2 Thesis structure

The structure of this PhD thesis consists of seven chapters, as follows:

Chapter 1 provides an overview of the research field, the rationale of this research together with the aim and objectives of this work. Herein it will be explained the structure of the thesis with a brief overview of each chapter's content.

Chapter 2 focuses on the literature review of the fundamental concepts of the thesis, including an introduction on the AC tissue, its degeneration in OA and the relative disease therapeutic treatment strategies exploited. Then, there are reported the rationale of AC *in vitro* tissue modelling and the requirements in terms of cells, biomaterials and stimuli for its design and manufacturing; also, it will be paid attention on the traditional approaches involved in this field, highlighting the importance of proposing a zonal-engineered AC model.

Chapter 3 contains all the materials and general methodologies involved in the work performed in this PhD project. The manufacturing techniques exploited for the different objectives of my work are reported in the single chapters, together with specific optimisation protocols and results and discussion.

Chapter 4 focuses on the manufacturing of a spheroid-based scaffold-free *in vitro* model of AC, in line with a clinical approved technique (Chondrosphere® (CO.DON AG)). This obtained model will be used to study the OA progression by optimising a novel strategy based on a cytokines-based chemical induction.

Chapter 5 is centred on the assessment of microRNA-based and magnetic-field bioreactor-based strategies within the scaffold-free *in vitro* model, as potential novel strategies for OA therapeutic treatment.

Chapter 6 focuses on the design, manufacturing, and characterisation of the zonal model of AC in healthy and pathological condition. At first instance, it was studied each layer singularly in terms of cells and materials choice, manufacturing technique optimisation, physico-chemical properties, and cells behaviour. Then, the single zones were assembled as whole zonal model, and cells viability and quality of the tissue produced were assessed.

Chapter 7 provides an overall discussion and the impact of the obtained results on the fields of AC *in vitro* model studies and OA research, as well as some limitation of the current project and recommendations for future studies.

Chapter 2. Scientific Background

2.1 Overview of the Human Cartilage

Cartilage is a strong and flexible connective tissue distributed in different parts of the human body (**Figure 2.1A**) (Mescher, 2016). Its main purpose is to provide a framework on which bone deposition may begin. Another important purpose of cartilage is to act as shock-absorbing and sliding surface for joints and to facilitate bones movements due to its smooth-surfaced and resilient properties, thus reducing friction and preventing damage (Ng et al., 2017).

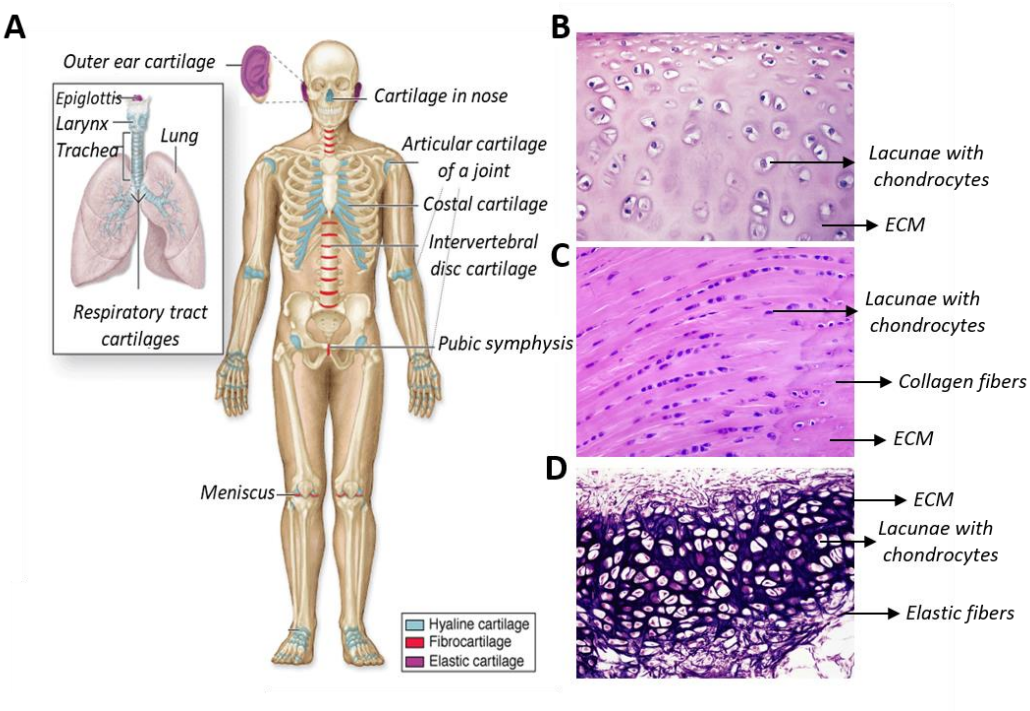

Figure 2.1: Overview of the cartilage distribution within the human body (**A**). There are three types of cartilage distributed in many areas of the skeleton: hyaline cartilage (**B**), fibrocartilage (**C**), and elastic cartilage(**D**). Readapted from Mescher et al. (Mescher, 2016).

The only cells found in cartilage are chondrocytes (from the greek *chondros*, cartilage and *kytos*, cell) and their precursors, chondroblasts (blast, germ), which are embedded in an extensive extracellular matrix (ECM) composed of fibres and ground substance. Chondrocytes make up "cell nests," groups of chondrocytes within lacunae, while chondroblasts are responsible for the secretion and maintenance of the ECM, whose main components are collagen (Coll), mainly type II, proteoglycans (PGs), mainly aggrecan, and small amounts of several glycoproteins. As a consequence of different functional requirements in the body, three forms of cartilage have evolved, exhibiting variations in ECM composition, adapted to

local biomechanical needs: hyaline (**Figure 2.1B**), fibro- (**Figure 2.1C**) and elastic (**Figure 2.1D**) cartilage (Bhosale & Richardson, 2008).

The hyaline cartilage, (i.e. found in the nasal septum, at the ends of the ribs, and in the tracheal rings.) is the most common and the weakest of the three types of cartilage. It has a glassy appearance (from the greek *hyalos*, glass), when fresh, and it is composed of type II collagen fibers (Coll II) and chondromucoprotein. Chondrocytes are located within lacunae and surrounded by the cartilage they have produced. Hyaline cartilage has a perichondrium, a sheath of dense connective tissue that surrounds cartilage in most places, forming an interface between the cartilage and the tissues it supports. It is populated by spindle-shaped cells which can differentiate into chondroblasts, that will eventually develop into chondrocytes The hyaline cartilage found lining bones in joints is called articular cartilage (AC) (**Figure 2.1B**).

The fibrocartilage, (i.e. found in the invertebral discs and joint capsules, in attachments of certain ligaments) is the strongest kind of cartilage, because it has a dense arrangement of cartilage fibers, that are organised in an orderly manner, oriented in the direction of functional stresses. This type of cartilage does not have a perichondrium, as it usually represents a transitional layer between hyaline cartilage and tendons or ligaments. It is primarily composed of type I collagen (Coll I) and the chondrocytes are surrounded by an ECM which helps differentiate fibrocartilage from dense connective tissue (**Figure 2.1C**).

Finally, the elastic cartilage (i.e. found in the walls of the external auditory canals and larynx) is composed of a thread-like network of elastic fibers, where chondrocytes are dispersed. It provides strength and elasticity, and it maintains the shape of certain structure. Elastic cartilage is similar to hyaline cartilage, but contains elastic bundles (elastin), in addition to Coll II fibers, scattered throughout the matrix and possesses a perichondrium (**Figure 2.1D**) (Bhosale & Richardson, 2008).

2.1.1 Articular Cartilage formation

Chondrogenesis is a well-orchestrated process mediated by interactions between cellular receptors, growth factors (GFs), and surrounding matrix proteins. ECM enzymes, lead to the activation of cell signalling pathways and gene expression in a temporal-spatial-specific manner (**Figure 2.2**) (Zhu, Gong, Lui, et al., 2017). Cartilage derives from a common precursor tissue, the embryonic mesenchyme.

The first step of the chondrogenesis is the condensation and mitotic proliferation of MSCs, mediated by paracrine factors such as fibroblast growth factor (FGF) and TGFβ. This is followed by MSCs differentiation, characterised by the cells rounding up, by retracting their extensions, their rapid multiplying, and the cellular condensations. Then, the aggregated cells start to produce ECM, mainly Coll I, Coll IIa and fibronectin. In this phase, it is possible to refer to MSCs as chondroprogenitor cells, that is a population of stem/progenitor cells, capable of chondrogenic differentiation and can be derived from multiple tissue sources including AC, synovium, and adipose tissue. These cells can be recognised by the expression of the transcription factor *sox9*, which is critical for chondrocyte differentiation and function (**Figure 2.2A**) (Williams et al., 2003; Goldring, 2012).

Following the strong interaction with the ECM, chondroprogenitors differentiate in chondroblasts. These cells possess a ribosome-rich basophilic cytoplasm and thereby condensations of these cells give rise to a tissue, mainly composed of Coll IIb, Coll IX, aggrecan and Cartilage Oligomeric Protein (COMP). Together with *sox9*, cells express *sox5* and *sox6*, whose cooperate with *sox9* to implement the chondrocyte differentiation program (Liu & Lefebvre, 2015). Synthesis and deposition of their own matrix then begin to separate the chondroblasts from one another. As the chondroblasts secrete matrix and fibres, they become trapped inside it. The matrix enclosed compartments where they sit in are called lacunae and they mature into cells called chondrocytes. In growing cartilage, the chondrocytes can divide, and the daughter cells remain close together in groups, forming a cluster of 2-4 cells (**Figure 2.2B**).

During late maturation, chondrocytes size increases, becoming hypertrophic and they secrete Coll X. Following the onset of hypertrophy, chondrocytes direct mineralization and vascular invasion, mediated by Vascular endothelial growth factor (VEGF). On vascularization, osteoblasts are transported by blood vessels into the cartilage, producing bone matrix using the residual cartilage template as a scaffold (**Figure 2.2C**). Concomitantly, hypertrophic chondrocytes undergo programmed cell death and are replaced by the bone matrix (Gao et al., 2017). Other chondrogenesis markers, mediating the process from early stage to the terminal differentiation, are shown in **Figure 2.2** and will be mentioned and widely explained in the following sections.

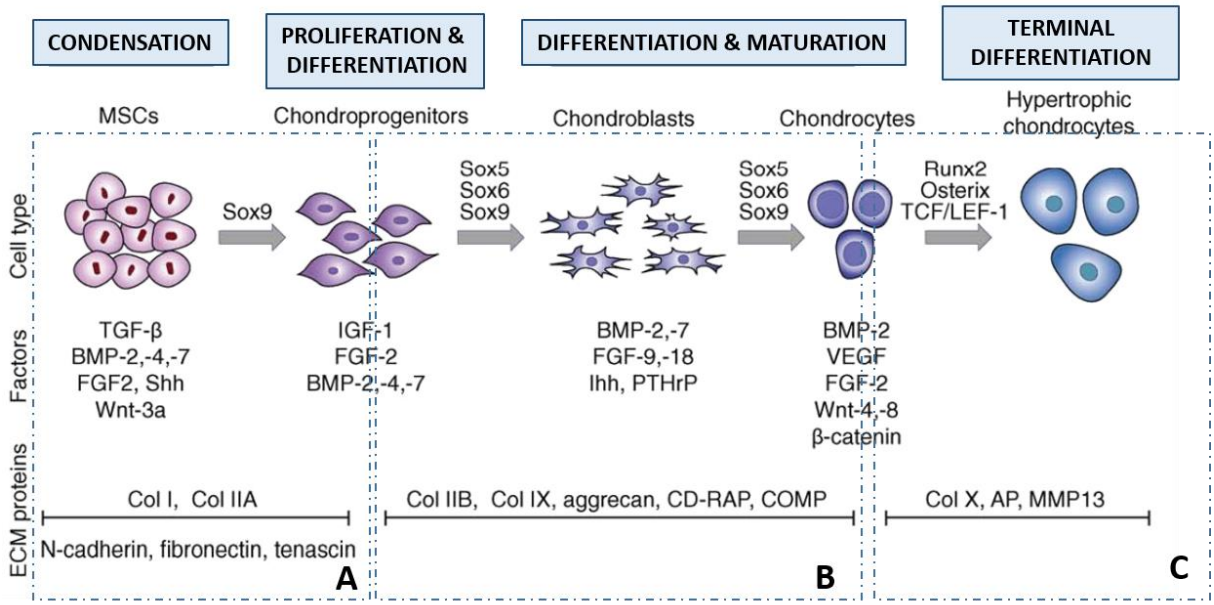

Figure 2.2: Schematic MSCs chondrogenic differentiation process and relative factors and ECM protein involved in each phase of this process: condensation and proliferation of MSCs (**A**); differentiation and maturation (**B**); terminal differentiation of chondrocytes towards hypertrophic phenotype (**C**). Abbreviations: bone morphogenetic protein (BMP); sonic hedgehog (Shh); wingless-type MMTV integration site family (Wnt); insuline growth factor (IGF); Indian hedgehog (Ihh); parathyroid hormone-related protein (PTHrP); cartilage-derived retinoic acid-sensitive protein (CD-RAP); matrix metalloprotease (MMP). Readapted from Gao et al. (Gao et al., 2017).

2.1.2 Composition, structure, and ultrastructure

AC is an avascular, aneural and alymphatic tissue with a very poor regenerative potential once reaching maturity (Buckwalter, 1998). Its oxygen and nutrients supply are provided by synovial fluid, which by itself lacks of oxygen. Therefore, AC environment is low in oxygen, ranging from 7 % to 1 % starting from the surface towards the interface with the bone. Indeed, chondrocytes cells have a specific and adapted response to low oxygen environment (Lafont, 2010). Recent studies have reported that hypoxia enhances chondrogenic differentiation of MSCs (in comparison to control cultures at ambient oxygen tension) and promote tissue function, by upregulating expression of main AC genes expression in chondrocytes (Murphy et al., 2009). Chondrocytes (1 – 5 % of the total AC volume) vary in size, shape, number and gene expression profile, based on the anatomical zones of the AC and their average density is about 1 x 10^4 cells/mm^3 (Alford & Cole, 2005). Chondrocytes are surrounded by an hydrated ECM of collagen fibers and proteoglycans (PGs) (**Figure 2.3**), as well as glycoprotein and other

molecules which all together are responsible for the maintainance of the AC tissue homeostasis (**Table 2.1**) (Guilak et al., 2006; Zhang et al., 2009; Sophia Fox et al., 2009a).

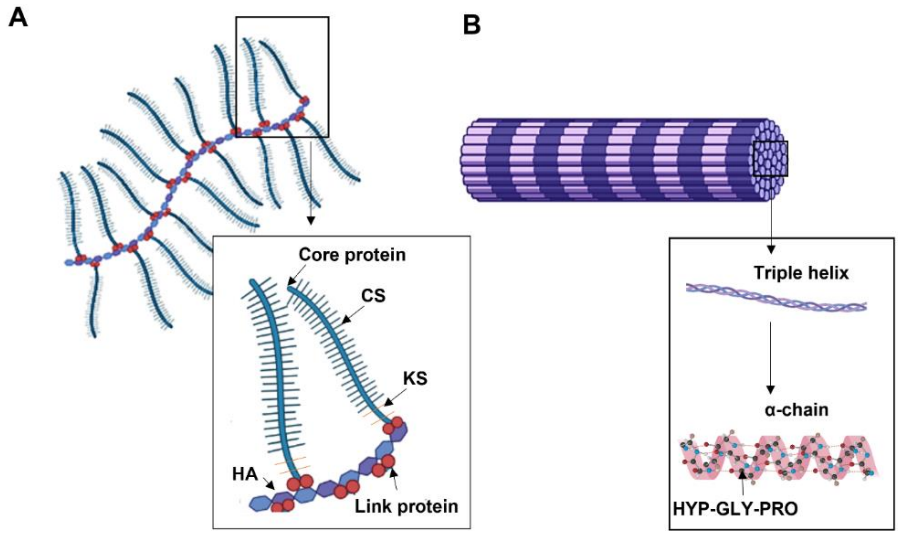

Figure 2.3: Representation of the two main elements of AC. Example of a PG, the aggrecan, made of a HA core with side PG chains made of KS and CS attached to a protein core, which is non covalently binded to HA via a link protein (**A**). Example of Coll II composed of triple helixes of α-chains, each made of HYP-GLY-PRO aminoacid sequences (**B**).

- Proteglycans

PGs (10-40 % Dry Weight (DW)) consist of a protein core (10 % of Molecular Weight (MW)) to which one or more polysaccharide linear chains, called glycosaminoglycans (GAGs) (90 % of MW), are covalently attached (Roughley, 2006). There are several type of proteoglycans in ECM and their diversity is caused by the protein core, polysaccharide chains and length. GAGs, composed of repeating disaccharide units, are categorised in five groups based on their sugars: hyaluronan (HA), chondroitin sulfate (CS), dermatan sulfate, heparan sulfate and keratan sulfate (KS). GAGs are linear negatively charged chains, because of the presence of sulfate or carboxylic groups and this promotes the retention of water which gives compressive strenght to the relative tissue. Aggrecan is the main PG which populates the AC (3-6 % of Wet Weight (WW)). It is composed of a core protein upon which are anchorated highly charges GAG chains (CS and KS) and it forms a PG big aggregate by binding to a HA backbone through the link protein (**Figure 2.3A**). Other PGs within AC are biglycan, decorin and fibromodulin, which have as well a role in the AC ECM assembly, together with collagen, during development and repair.

- Collagen

Collagens (60 % DW) are the major type of insoluble fibrous proteins of most tissues' ECM. Collagen structure consist of three polypeptidic α-chains, which are wound together in a triple helix by hydrogen bonds: each α-chain is made of aminoacid sequences which consist in glycine repeated in every third unit $(Gly\text{-}X\text{-}Y)^n$. The aminoacid composition of polypeptide chains is primarily glycine and proline, with hydroxyproline providing stability via hydrogen bonds along the molecule length. Approximately 20 % of collagen amino acids are iminoacids, prolyne and glycine (HYP-GLY-PRO) (**Figure 2.3B**) (Shoulders & Raines, 2009). Although the predominant AC collagen is Coll II (>70 %) and forms the primary component of the macro-fibrillary framework, there are also present other types of collagen fibres (Col VI, IX, X, and XI) (Buckwalter & Mankin, 1998). With maturation, the content of Coll II increases from 75 % in fetal cartilage to 95 % in adult cartilage (Zhang et al., 2009).

- Other molecules

The remaining AC component is water and small amounts of molecules (inorganic salts as NaCl, CaCl, KCl, non-collagenous proteins, glycoproteins and lipids) (Ng et al., 2017; Roughley, 2001). Glycoprotein are another class of molecules present in AC tissue ECM. Even if these are made of protein and polysaccharides as PGs, they possess a greater percentage of protein. Examples of glycoprotein are Laminin and Fibronectin. Especially the latter plays a main role for cell attachment to the ECM via the $\alpha_5\beta_1$, due to the presence of Arg-Gly-Asp (RGD) units. Other non collagenous proteins are, for instance, COMP, matrilin-1 and matrilin-3 which are structural protein (Murray et al., 2016; Guilak et al., 2006; Zhang et al., 2009).

The average thickness of AC, from the superficial layer to the calcified zone is about 2.5 mm, but based on the different areas of the body (high or low load-bearing), there are differences in thickness (Hunziker et al., 2002). AC is divided into three different main zones, differing for their ECM composition, its organisation, cells morphology, shape and size, mechanical properties, and metabolic properties (**Figure 2.4**). All these characteristics determine the complex zonal structure. And each zone plays a different role in contributing to the functional properties of AC (Bautista et al., 2016). In **Table 2.1** are reported the main characteristic of each layer.

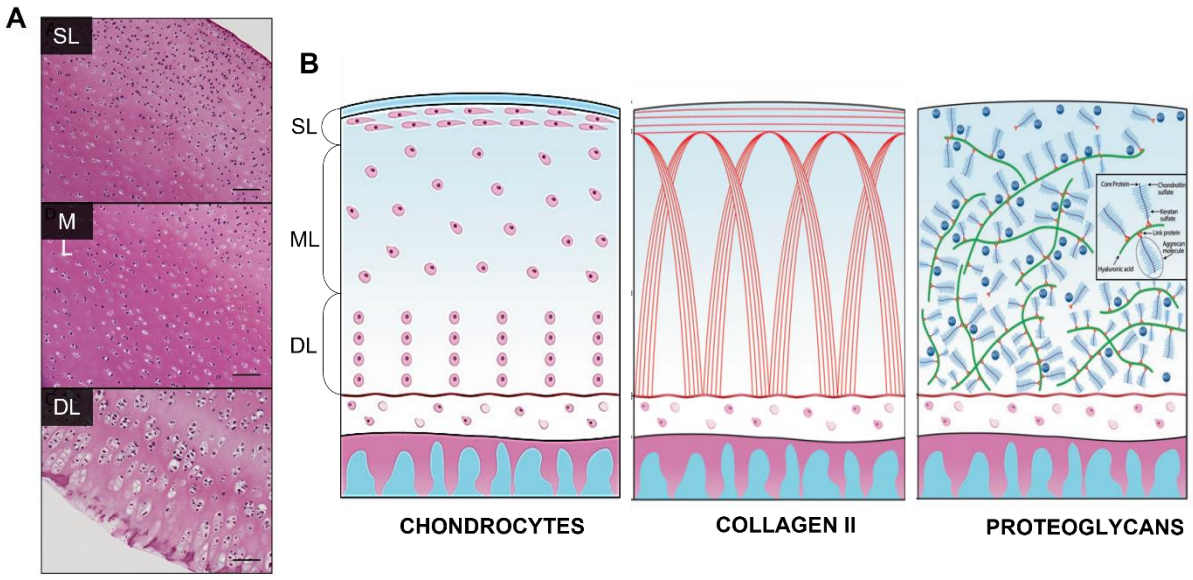

Figure 2.4: Zonal representation of AC. H&E staining of longitudinal cross sections of decellularized cartilage. Bar=100µm (**A**). Schematic representation of AC chondrocyte morphology and orientation, Coll II organisation and proteoglycans distribution within the superficial layer (SL), Middle layer (ML) and deep layer (DL) of AC tissue (**B**). Readapted from Bautista et al. (Bautista et al., 2016).

ZONE	ECM	CELLS	BIOMECHANICS	REF.
<u>SUPERFICIAL</u> Thickness: 10-20 %	• Highest Coll II amount (86 % DW) • Lowest PGs amount (15 % DW) • High H_2O (84 % WW) • Parallel Coll II fibers	Flat and parallel Nb: 14-24 x 10^3 cells/mm^3	Highest tensile strenght (TM: 8.3±3.7MPa) CM: 1.2±0.2MPa Low frictional coefficient	(Li et al., 2017; Saarakkala et al., 2004)
<u>MIDDLE</u> Thickness: 40-60 %	• Medium amount of Coll II and PGs • Moderate H_2O • Oblique Coll II fibers	Rounded and randomly dispersed Nb: 9-18 x 10^3 cells/mm^3	Superficial shear and compressive properties	(Dimaraki et al., 2021a; Brown et al., 2020b)
<u>DEEP</u> Thickness: 20-30 %	• Lowest amount of Coll II (67 % DW) • Highest PGs (20 % DW) • Low H_2O (40-60 % WW)	Rounded/ ellipsoid in columns	Compressive stiffness (CM: 7.8±1.4MPa) TM: 4.1± 1.9MPa	(Zelinka & Kandel, 2019; Brittberg et al., 1994)

	• Perpendicular Coll II fibers	Nb:7-9 x 10^3 cells/mm^3		

Table 2.1: The zonal function and zonal properties and composition of AC in superficial zone, middle zone and deep zone. Info on Compressive modulus (CM) and Tensile Modulus (TM) of each zone.

The superficial zone (10 % - 20 % of the total AC thickness) contains the highest density of collagen within the tissue with a low PGs and high-water content. Here, the collagen fibres (mostly type II and type IX collagen) are the thinnest and most densely packed to form an oriented lamina that covers the joint. This zone is in direct contact with the synovial fluid. Here, there is the highest amount of chondrocytes, which appear elongated (fibroblasts-like) and oriented parallel to the surface and the direction of shear stress (Quinn et al., 2005). They secrete the lubricin, which is the vital superficial zone protein, which helps the lubrication and low friction coefficient of this zone. It is believed that the composition and organization of this zone contribute to tensile strength, resist shear during articulation, and adjust fluid permeability (fundamental for nutrients transport to the underlying zones) (Zhang et al., 2009; Khrishnan et al., 2003; Buckley et al., 2008). Moreover the integrity of this layer is imperative in the protection and maintenance of deeper layers: in fact, the disruption of this zone alters the mechanical properties of the AC and, thus, contributes to the development of Osteoarthritis (OA) (Ng et al., 2017) .

The middle zone (40 % - 60 % of the total AC thickness) has 50 % more PGs content and 20 % less collagen content compared to the upper layer. It contains thicker collagen fibrils with an oblique orientation and randomly distributed (Chen et al., 2006; Roughley, 2001). Chondrocytes content is lower in this zone and they appear spherical, embedded in abundant ECM of collagen and PGs (Quinn et al., 2005). Functionally, the middle zone is the first line of resistance to compressive forces (Sophia Fox et al., 2009).

The deep zone (20 – 30 % of the AC) is composed by large chondrocytes surrounded by a Coll VI containing pericellular matrix, which together with the chondrocyte is known as a *chondron*. In this zone, the vertically oriented thick collagen fibres run parallel to stacks of chondrons, and are inserted across the tidemark (a visible basophilic line that separates deep and calcified zones), the PGs content is the highest, while the water content is at its lowest amount (Armiento et al., 2018). This layer has been thought to provide the greatest resistance to

compressive forces imposed by articulation, due to the high amount of PGs (Ng et al., 2017). The collagen fibers in this layer have the function of strenghten the bond between cartilage and bone. The number of chondrocytes in this zone is the lowest and cells are arranged in a perpendicular manner in the same direction as the collagen fibres and they appear to have a rounded-elongated morphology (Quinn et al., 2005). Cells within the deep zone of AC are 10-fold more synthetically active compared to the other layers.

Also, below these three layers, there is the calcified zone, which is a mineralized layer (20-250 µm) and transitional zone that forms an interface between cartilage and the stiffer bone (Murray et al., 2016). It contains small volume of cells embedded in a calcified matrix and thus, showing a very low metabolic activity. The chondrocytes in this zone express hypertrophic phenotype and they synthesize Col X, responsible for providing important structural integrity and provide a shock absorber along with the SB (Armiento et al., 2018; Sophia Fox et al., 2009a; Kalamegam et al., 2018).

2.1.3 Interaction between articular cartilage and subchondral bone

Located below the calcified cartilage there is the SB, which, together with the AC forms the osteochondral unit (Gobbi et al., 2021). The SB possesses an organic and an inorganic phase and it has multiple functions (**Table 2.2**). This tissue is organised in two zones:

- Subchondral bone plate, which is similar to the cortical bone. It is composed of osteons consisting of concentric lamellae surrounding the central Haversian canal. It has small holes through which blood vessels penetrate the calcified cartilage. Its thickness and mineralisation density depends upon age, location, stress applied and weight.
- Subchondral spongiosa is a trabecular bone, more porous and metabolically active than the subchondral plate. Trabeculae are oriented in different direction within the different locations providing a unique network, which is adapted to the local mechanical influences through the remodelling activity of osteoblasts and osteoclasts, the two-cell type populating the bone.

SB has the role of supporting the AC by absorbing 30 % of the joint load (compared to the 1-3 % absorbed by AC). Indeed, it has a great shock-absorbing ability and consequently any damage to the SB, such as micro fractures, can change the bone elasticity by abnormal remodelling and can lead to AC degeneration (Murray et al., 2016). In addition to being fed by the synovium, AC receives nutrition from the SB through the arteriovenous complex and nerves, which penetrate the SB through canals and can diffuse from the SB to the calcified AC

and deep zone. These penetrating blood vessels enable signalling molecules and nutrients to reach the deep layers of cartilage accounting for about the 50 % of the glucose, oxygen and water required from AC (Gobbi et al., 2021). SB is populated by MSCs with multipotent potential, that can migrate towards the AC in the setting of osteochondral injuries, to contribute to the formation of fibrous repair (Madry et al., 2017). The overall structure of the osteochondral unit with its multiple layers enables the transmission and distribution of the forces necessary for the mechanical adaptation to the joint (Lepage et al., 2019).

PHASE	COMPONENTS	FUNCTION	REF.
Organic	Collagen (mainly Type I)	Tensile strength	(Luo & Amromanoh, 2021)
	PGs	Compressive strenght	
	Non-collagenous matrix protein (Osteocalcin and Osteonectin)	Promote mineralisation and bone formation	
	GFs and cytokines (TGFβ, IGF, IL-1, IL-6,BMPs)	Support bone cell differentiation, growth and turnover	
Inorganic	• Calcium hydroxyapatite • Osteocalcium phosphate	Compressive strenght	(Luo & Wu, 2020)

Table 2.2: Subchondral bone: components and their function.

2.2 Biomechanics of Articular Cartilage

As anticipated, the main role of AC is to provide a low-friction, wear-resistance surface able to withstand large loads over decades, by facilitating load support and transfer while allowing translation and rotation between bones. Each articulating joint, based on the body location experiences a different force exerted (e.g., the force exerted on the knee, hip, ankle, and shoulder are respectively 3.5, 3.3, 2.5 and 1.5 times a person's bodyweight). The mechanical characteristics, together with the biochemical properties, play an important role in the joint performances and any change in these could dramatically alter the loading profile, beginning a degradation process which could end-up in a total loss of the tissue (D'Lima et al., 2012; Mente & Lewis, 1989).

Being a fluid-saturated, fiber-reinforced, porous, permeable, composite matrix, AC possesses unique static and dynamic mechanical properties (Buckwalter, 1998). The perception of mechanical stress within cartilaginous tissues at cellular level is an important modulator of chondrocyte function and their sensing of mechanical forces leads to deep changes in the health and normal function of the joint (Guilak, 2000). These are generally mechano-electrochemical events that, coordinate with other environmental, hormonal, and genetic factors, regulate chondrocyte's metabolic activity and contribute to the ECM maintenance (Mow et al., 1980).

PGs are mainly responsible for the AC static stiffness and is even important for the dynamic functional properties of cartilage, while the tensile resilience and strength of cartilage is imparted primarily by the network of Coll II fibres (Darling et al., 2009; Lee et al., 2017). A link between the fluid, PGs and collagen is established through the permeability of the cartilage matrix. The total fluid content in cartilage is controlled by the swelling pressures, due to the high density of fixed charges of the sulphated GAGs of PGs that draw water into cartilage, resulting in high osmotic pressure, which is restrained by the collagen fibres network, thus giving rise to the compressive behaviour of cartilage. The packing and orientation of collagen fibrils modulate the fluid flow in the tissue, and PGs resist the fluid flow throughout the tissue, both being factors which influence the permeability (Federico & Herzog, 2008). A compression test is a suitable method for determining the behaviour of cartilage under a compressive load and it is used to evaluate the compressive elastic Young's modulus, representative of AC stiffness. It was reported that the compressive modulus increased nearly 27-fold from the superficial zone (79 ± 39 kPa) to the deepest zone (2.10 ± 2.69 MPa). The compressive properties of AC vary along the depth of the tissue and is primarily related to the differences in the fluid flow in each zone (Muzzarelli et al., 2012).

When tissue is loaded in compression, about 70 % of the water is expelled, resulting in potential fluid shear-stress at or near the cellular membrane. This shear stress, as mechanical stimulation, can impact chondrocytes through changes in membrane potential, solute transport, and cellular deformation. It is believed that articular chondrocyte metabolism is modulated by direct effects of shear forces that act on the cell through mechano-transduction (Buckley et al., 2008; Middendorf et al., 2020).

Also, an important property of AC is its viscoelasticity, which is given by its biphasic nature, made of a solid and a fluid phase and their interactions (Mow et al., 1980). Volumetric changes occur when a fluid is squeezed out from AC under compressive load. Upon removal of the load, AC recovers its initial dimensions, and this happens thanks to a combination between the elasticity of the solid matrix and the absorption of the surrounding fluid. This behaviour of AC can be determined by stress-relaxation test, where a known strain is applied on the unloaded sample (**Figure 2.5**). During the application of the strain slope there is a large rise of stress; in fact, the largest lateral deformation occurs, stressing the collagen fibrils in their tensile direction, exhibiting strain-dependent stiffening until the point of peak stress where the peak Young's modulus (E_P) is calculated; from this point, the relaxation behaviour at the fixed strain value reached, starts (Li et al., 2003). This phase mainly results from the AC ECM permeability, believed to be dependent on the PG and fluid content (Mow et al., 1980). As the fluid leaves the cartilage, load is shifted to the solid matrix and stress is reduced, starting a slow relaxation process of fluid redistribution within the matrix till the equilibrium, where the equilibrium Young's modulus (E_Y), defined as the stiffness of the cartilage as all the fluid flows out, is recorded (Alexopoulos et al., 2005).

Physiological level of stress is fundamental for chondrogenesis and stimulation of the matrix synthesis: repetitive loads lead to an increase in cartilage thickness and PGs production. However, when the load is excessive it becomes hyper-physiological and could have adverse effect on chondrocytes behaviour (Klein et al., 2007).

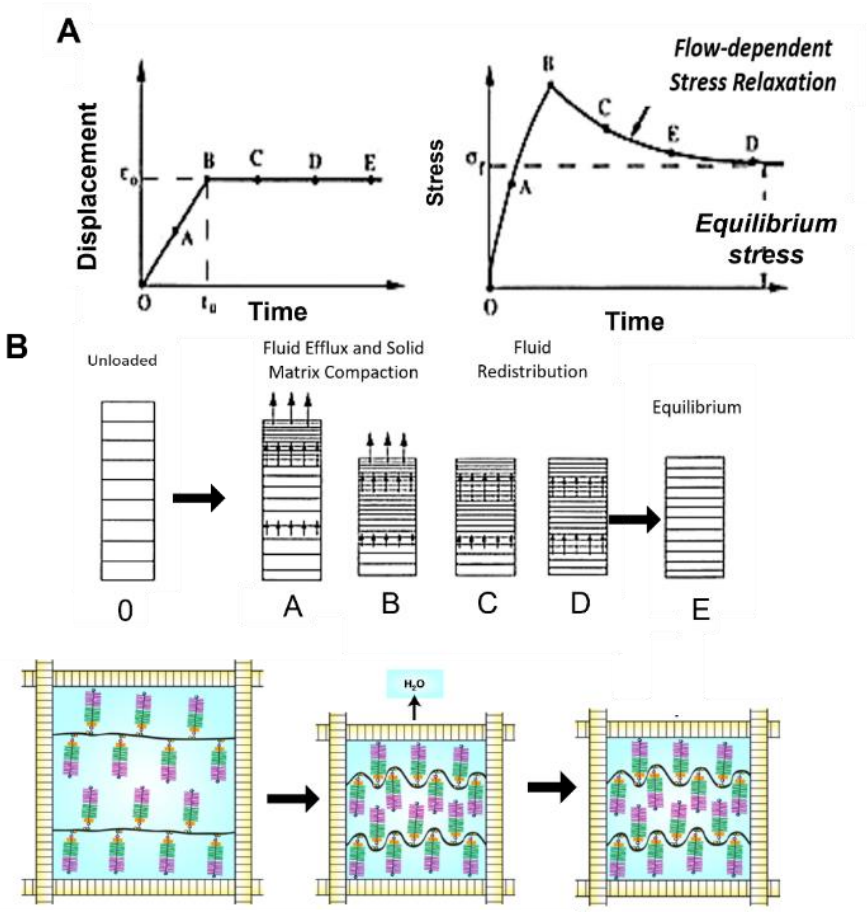

Figure 2.5: Stress-relaxation test. Curves showing the displacement vs. time and the resulting stress vs. time **(A).** Relative explanation of the dynamic process highlighting the function of aggrecan in AC: proteoglycan aggregates are entrapped by collagen fibrils. In the relaxed state the aggregates swell until swelling is balance by tensile forces in the collagen fibrils. Under compression, water is displaced and the GAGs chains are brought into closer proximity, so increasing their swelling potential and balancing the applied load **(B).** Readapted from Mente et al. (Mente & Lewis, 1989).

2.3 Articular Cartilage degeneration in Osteoarthritis

AC damages are caused by several conditions and diseases, such as traumatic injuries, infections, and arthritis. Among 200 different forms of existing arthritis (inflammation (*itis*) of the joints (*arthr*)), the progressive degeneration of AC due to OA is the most common and chronic form of joint disease in the Western World nowadays (Neogi, 2013). This is a degenerative disease of the whole joint (AC, SB and synovium), characterised by the progressive AC degradation, thickening of the SB and its growth within the joint, loss and

pathological changes of the synovial tissue, which lead to significant joint pain, swelling and stiffness for people affected (Glyn-Jones et al., 2015). Also, OA is one of the top five causes of disability amongst non-hospitalised adults (Arthritis Research UK, *www.arthritisresearchuk.org*) and the economic burden of this disease for the society is great (Lutz et al., 2008). It is reported that one third of people over 45 years in UK are affected by OA in 2021, for a total of over 8.5 million people, with a prevalence of knee and hip (Versus Arthritis, 2021). The total annual National Health Service expenses related to arthritis and musculoskeletal conditions in England is roughly £5 billion, and the situation is only likely to worsen in the future, with an ageing population and rising rates of obesity. Indeed, although advancing age is a major risk factor for the development of OA, there are other significant contributing factors including: gender, affecting more female than male for hormonal reasons; obesity, with an increase in risk of development doubled compared to healthy/normal body weight people; a history of joint trauma; joint malalignment and consequent wear and tear phenomenon; genetic predisposition, lifestyle, because people doing physical activity regularly reduces risk of hip and knee OA pain by 6 % (Zhang Y and Jordan M, 2010).

Several methods of assessing the severity of OA, in terms of both radiographic and clinical symptoms, have been proposed in the literature, but the oldest and most widely used radiographic assessment scale was proposed by Kellgren and Lawrence in 1957, which classifies radiographs on a grading scale of 0–4 with a score of 2 or greater corresponding to significant OA (**Figure 2.6**). This classification was accepted in 1961 by World Health Organisation as the radiological definition of OA for the purpose of epidemiological studies (Kellgren & Lawrence, 1956):

- **Grade 0 (none)**: absence of X-ray changes of OA.
- **Grade 1 (doubtful)**: minimum disruption, doubtful joint space narrowing and possible osteophytic lipping (prominent osteochondral nodules); there is already 10 % of cartilage loss.
- **Grade 2 (minimal)**: definite osteophytes and possible joint space narrowing; cartilage starts to break down.
- **Grade 3 (moderate)**: moderate multiple osteophytes, definite narrowing of joint space and some sclerosis and possible deformity of bone ends; gaps in cartilage can expand until they reach the bone.

- **Grade 4 (severe)**: large osteophytes, great narrowing of joint space, severe sclerosis, and definite deformity of bone ends; loss of 60 % of cartilage.

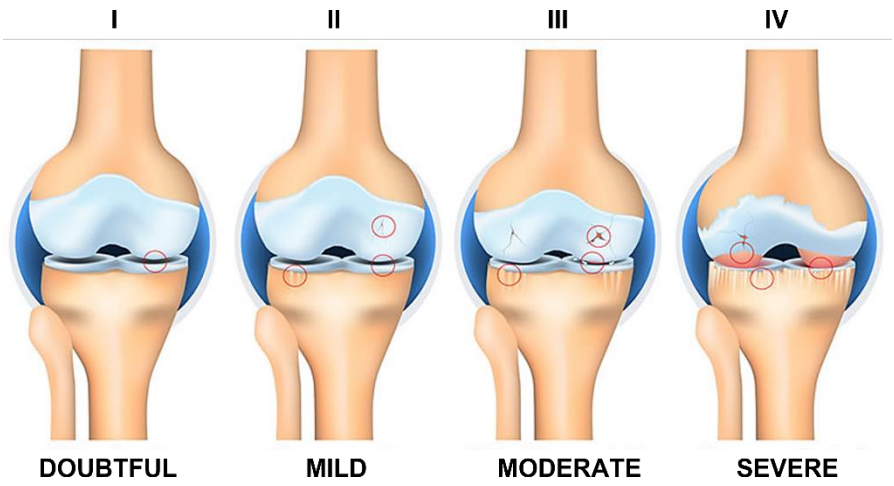

Figure 2.6: Classification of OA severity according to K-L grading score: Grade I (doubtful), Grade II (Mild), Grade III (Moderate) and Grade IV (Severe). Readapted from Kellgren et al. (Kellgren & Lawrence, 1956).

2.3.1 Osteoarthritis features

Age related 'wear and tear', chondrocytes' poor response to GFs, altered bio-mechanical properties of AC, mitochondrial dysfunction, oxidative stress and inflammation are all implicated in the pathogenesis of OA, highlighting the multifactorial and complex nature of this degenerative joint disease (Zhang Y and Jordan M, 2010; Mobasheri et al., 2014). Under normal conditions, the chondrocytes maintain the ECM with a low turnover, with synthesis and degradation of the ECM in equilibrium. However, in OA tissue, there is perturbed ECM homeostasis (Goldring & Marcu, 2009).

It is generally believed that degeneration of cartilage during OA is characterized by two phases: (1) a biosynthetic phase (anabolic – pathway which requires energy to build up large molecules from smaller one) during which the chondrocytes, attempt to repair the damaged ECM to maintain the AC structure and function, hyper proliferating, increasing their metabolic activity and clustering in the region of the damage; (2) degradative phase (catabolic – pathway which releases energy and is used to breakdown large molecules in smaller one), in which chondrocytes produce enzymes which digests the ECM, matrix synthesis is inhibited, and the consequent erosion of the cartilage is accelerated (Akkiraju & Nohe, 2015) (**Figure 2.7**). At early OA stages, the surface of the affected cartilage shows fibrillation with initially small defects,

gradually extending down to the underlying bone. This process is associated with duplication of the tidemark separating calcified AC from SB. At sites of microcracks and fissures in the osteochondral junction, vascular elements from the marrow space penetrate the SB and calcified cartilage (Martel-Pelletier et al., 2016). With the progression of OA, chondrocytes phenotype also changes from maturation state to hypertrophy (as anticipated in **Figure 2.2**). Eventually, they can be seen to undergo apoptotic loss. However, the exact mechanism of change from healthy to OA is still poorly understood (Tío et al., 2022).

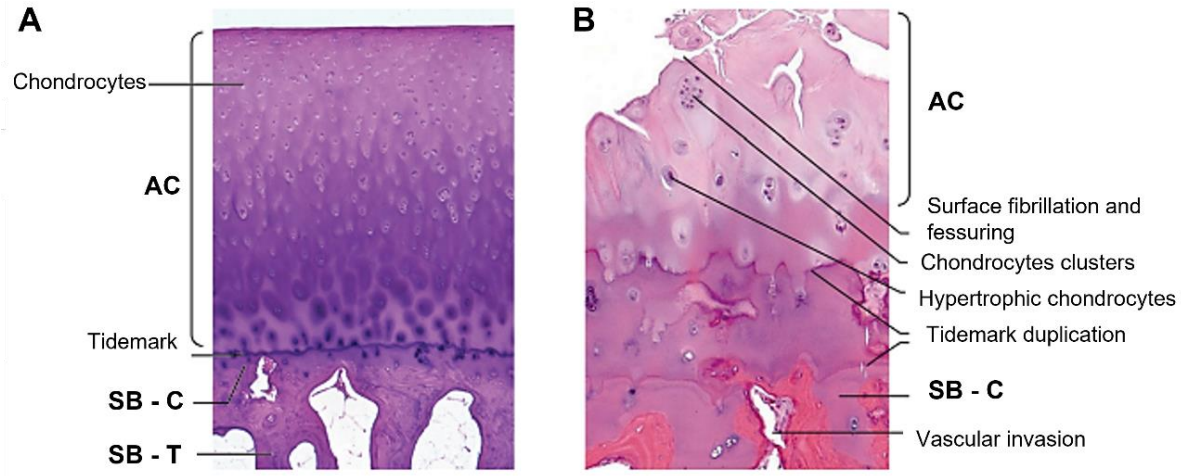

Figure 2.7: Cross-section of the articular surface of a diarthrodial joint illustrating histologically the main structural elements, including the AC, tidemark, calcified cartilage, and subchondral cortical and trabecular bone in healthy state (**A**) and pathological state, characterized by fissuring and fragmentation of the AC, chondrocyte proliferation and hypertrophy, duplication and advancement of the tidemark, expansion of the zone of calcified cartilage, thickening of the subchondral cortical plate and vascular invasion of the bone and calcified cartilage(**B**). Readapted from Martel-Pelletier et al. (Martel-Pelletier et al., 2016).

2.3.2. Osteoarthritis: its pathophysiology

For a long time, OA was considered a non-inflammatory disease that was the result of 'wear-and-tear' and abnormal mechanics. However, in the last decade, it became prominent the belief that inflammation not only exists in most OA patients, but also actively contributes to the disease's progression. Although there are a lot of uncertainties upon whether synovial inflammation is the cause or the effect of OA, it is well recognised that OA is a multi-factorial disease (Lattermann, 2022; Glyn-Jones et al., 2015).

In the **Figure 2.8** is reported a schematic overview of the processes that contribute to inflammation in OA, according to the most broadly supported view upon OA pathogenesis. The main trigger events could be an injurious or excessive mechanical stress on the joint, the

joint malalignment and related friction and “wear” phenomenon, or some infection and then inflammation in tissues surrounding the joint or in the joint itself (van den Bosch, 2019). These events lead to a release of AC ECM fragments which comprise alarmins (or Damage Associated Molecular Patterns, DAMPS), which are endogenous molecules released upon cell stress or non-programmed cell death. Here, it starts the synovial inflammation: alarmins binds pattern recognition receptors (PRR) in chondrocytes (cartilage) and synovial fibroblasts and stimulates both neovascularization and the influx of inflammatory cells in the synovium (in fact high levels of many alarmins have been described in the synovial fluid of OA patients). Of central importance in PRR family there are Toll-like receptors (TLRs) and especially TLR-2 and TLR-4, which have been shown to bind a multitude of ECM degradative enzymes such as low molecular weight hyaluronan, tenascin C, fibronectin, biglycan and aggrecan (Nefla et al., 2016). The activated synovial cells start to produce pro-inflammatory cytokines (mainly interleukin (IL)-6, IL-1β, tumour necrosis factor (TNF)-α), which have different effect on chondrocytes and osteoblasts. Within chondrocytes the increase of inflammatory mediators results in: shifting the otherwise tightly controlled anabolic/catabolic cartilage homeostasis toward a more catabolic state, by stimulating the production of degradative enzymes such as metalloproteases (MMP) and a disintegrin and metalloproteinase with thrombospondin motifs (ADAMTS) and inhibiting the expression of Coll II and PGs, via multiple signaling pathways such as HIF, Nuclear factor kappa B (NF-κβ), Mitogen-Activation Protein Kinase (MAPK) (Akkiraju & Nohe, 2015; Bennett et al., 2018). On the other side, it is reported that inflammatory cytokines such as these pro-inflammatory cytokines may play critical roles in osteoclast formation, which are multinucleated giant cells involved in bone absorption, by promoting receptor activator of NF-κB ligand (RANKL) production, by osteoblast precursors (bone marrow stromal cells (BMSCs)) and/or mature osteoblasts, which is the key osteoclastic cytokine; and/or by upregulating the receptor RANK on osteoclast precursors, thus increasing their sensitivity to prevailing RANKL concentration; and/or by reducing OPG production, which is a decoy receptor, preventing association of RANKL with RANK receptor, thus moderating osteoclastogenesis and bone resorption (Maruotti et al., 2017; Papadaki et al., 2019; Weitzmann, 2013). Osteoclast’s activation results in an imbalance of osteoblast/osteoclasts

activity resulting in elevated bone loss resorption within the SB, as well as production of catabolic factors including cathepsin K and MMP13 (Tat et al., 2009).

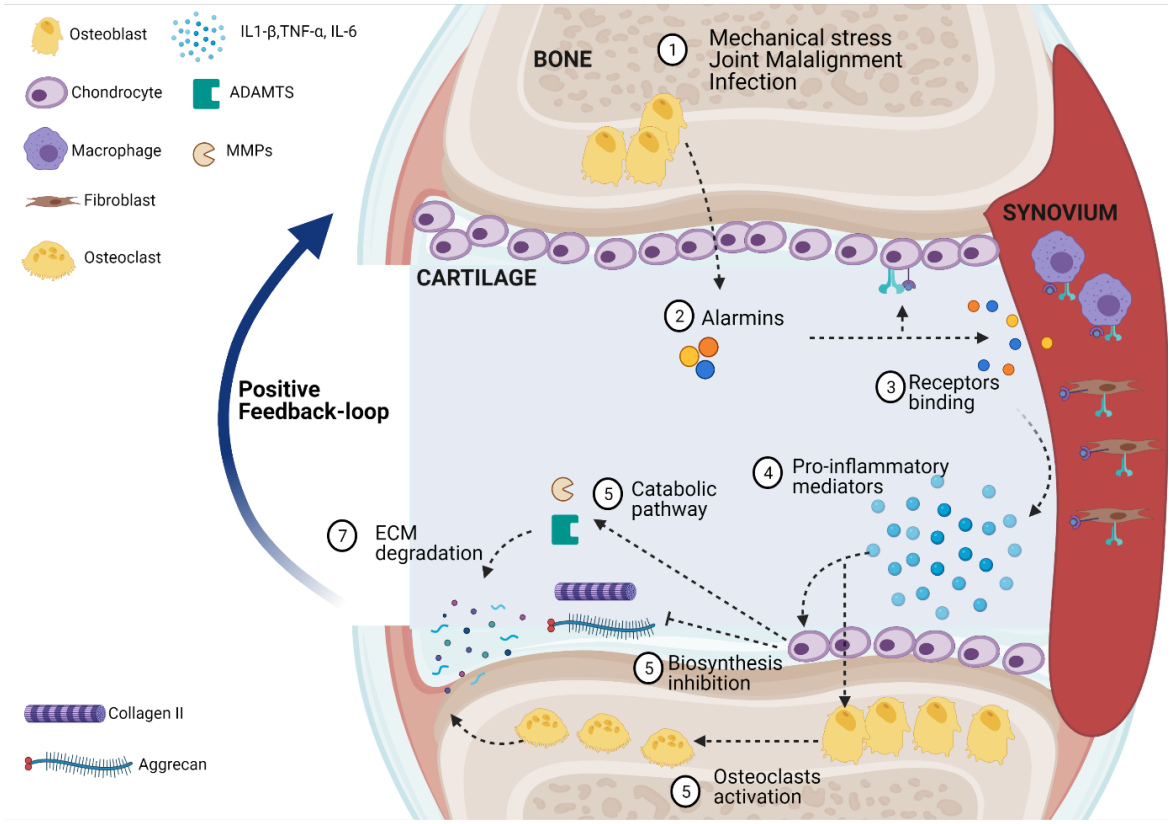

Figure 2.8: Crosstalk between AC, SB and the synovium in the pathogenesis of OA. Alarmins are released from the AC matrix and/or the chondrocytes in response to adverse mechanical forces and other factors (1-2). These molecules could bind specific receptors of synovium cells and chondrocytes, stimulating the production of pro-inflammatory mediators (3-4), responsible for chondrocytes enhanced catabolic activity of and inhibition of its biosynthetic activity, as well as for the activation of osteoclast activity mediated by osteoblast degeneration (5-6). All these events lead to the ECM degradation (7).

Therefore, the synthesis of catabolic degradative enzyme is closely involved in the breakdown of the AC. GAGs loss, collagen breakdown and formation of new fragments and alarmins, which could restart the cycle by activating new receptors on cells, may lead to a positive feedback loop where progressive generation of fragments leads to increased degradation of the ECM, by restarting the cycle (Okamura et al., 2015; Martel-Pelletier et al., 2016).

2.3.3 Role of cytokines in OA

Cytokines are a large group of proteins, peptides or glycoproteins secreted by specific cells of immune system, which role is to mediate and regulate immunity, inflammation, and haematopoiesis. A growing attention was directed towards the special role of the cytokine network in the OA disease pathogenesis: their role is to influence the catabolic and anabolic processes, which are vital in tissues often subject to high mechanical load, such as human

joints. As aforementioned, because of disrupting the said balance, in presence of cytokines there is a progressive degeneration of AC and consequent development of a positive feedback loop process which lead to a gradual loss of joint functions and pain (Goldring, 2000a).

During the progression of OA, the production and behaviour of various cytokines can vary according to the stage of the disease. Also, these molecules are classified into pro-inflammatory and anti-inflammatory cytokines. The pathophysiological degeneration of OA joint is largely mediated by pro-inflammatory cytokines which are critical mediators of the altered metabolism and enhanced catabolism of OA tissue. Their primary effects within the joint, is a critical impact on AC, consisting of the induction of aging and apoptosis of chondrocytes, a decreased synthesis of the key components of AC ECM, as well as an increased synthesis and release of many proteolytic enzymes responsible for AC destruction, which include MMPs and ADAMTS. They impact via intracellular pathways of signal transduction on the production of cytokines as well as other inflammatory compounds, free radicals, and enzymes, thus demonstrating an autocrine, paracrine, and self-propelling effect on the inflammation process (Goldring, 2000a).

IL-1β, IL-6 and TNF-α are the main pro-inflammatory cytokines involved in OA pathophysiology. Besides, IL-15, IL-17, IL-18, IL-21, Leukaemia Inhibitory Factor (LiF) and chemokines are also implicated (**Table 2.3**) (Blom et al., 2007; Kapoor et al., 2011). On the other side anti-inflammatory cytokines are responsible for the modulation of an inflammatory response and act protectively on joint tissue by inhibition of inflammatory cytokines synthesis. In fact, this inhibition results in an increased PGs synthesis, inhibited apoptosis of chondrocytes, decreased synthesis and secretion of metalloproteinases, and decreased level of prostaglandine2 (PGE2). Also, the action of anti-inflammatory cytokines is mainly performed relating to cells stimulated by inflammatory cytokines, whereas no significant differences are noted in the metabolism of cells not subject to such stimulation. However, the effect of anti-inflammatory cytokines is not sufficient to stop the disease progression, by blocking the promotion of the catabolic pathway. An example of anti-inflammatory cytokines is IL-10 (Wojdasiewicz et al., 2014).

CYTOKINE	**CHARACTERISTICS**
IL-1ß	High in OA synovium, AC and SB Decrease of PGs synthesis in chondrocytes Induces the production of IL-6, NO and PGE2 and MMPs release

	Induces chondrocytes apoptosis
TNFα	High in OA synovium, AC and SB Suppress synthesis of glycoproteins and Coll II in chondrocytes Induces production of IL-6, PGE2 and MMPs release Induces chondrocytes apoptosis
IL-6	High in OA patients' synovial fluid and sera Reduces Coll II expression Inhibits PGs synthesis Reduces chondrocytes proliferation Upregulates MMP1, MMP13
IL-15	Present in OA synovial fluid at early stage of OA Collaborates with MMP1 and MMP3
IL-17	Mild decrease of proteoglycans synthesis Upregulates the MMPs and NO Induces the production of IL-1ß, TNF-α, IL-6
IL-18	Present in OA chondrocytes Mild increase of PGs synthesis. Induces the production of IL-1ß, TNF-α
IL-21	Present in OA synovial fluid at early stage of OA
LIF	Present in OA synovium Induces PGs degradation, MMPs synthesis and NO production

Table 2.3: Pro-inflammatory cytokines involved in OA physiopathology and their characteristics.

IL-1ß, IL-6 and TNFα are the key inflammatory cytokines involved in the OA pathogenesis, which are synthetised by chondrocytes, osteoblasts, synovial membrane's cells, and mononuclear cells that were previously present in the joint or infiltrated its structure during the inflammatory response. In most of the phenomena occurring during OA, there is a marked synergism between these cytokines and the level of both cytokines is elevated in SB, AC and synovium of OA patients. Chondrocytes produce low levels of IL-6 under normal conditions, but several cytokines and GFs active in OA, such as IL-1β, TNFα and TGFβ, directly stimulate its production in human chondrocytes, osteoblasts, and macrophages. The main action of IL-6, IL-1β and TNF-α is to affect the anabolic activity of chondrocytes, interfering with their synthesis of AC ECM key structural proteins such as Coll II and aggrecan. Also, these cytokines stimulate chondrocytes to release proteolytic enzymes from the group of MMPs, mainly interstitial collagenase (MMP1), stromelysin-1 (MMP3), and collagenase 3 (MMP13), which have a destructive effect on cartilage components, as well as they have effect on ADAMTS production, which is responsible for the proteolysis of aggrecan molecules. Amongst them, ADAMTS-4 (aggrecanase-1) and ADAMTS-5 (aggrecanase-2) are involved in OA pathogenesis. Chondrocytes subjected to the effect of IL-1ß, IL-6 and TNFα also tend to age more rapidly and

to induce apoptosis (Wojdasiewicz et al., 2014). Also, IL-6 is the key cytokine, which causes changes in the SB and the degeneration of the osteochondral portion. (Wojdasiewicz et al., 2014; Bennett et al., 2018; Goldring, 2000b). The proinflammatory and catabolic effects of cytokines are mediated through the activation of several signalling pathways, including the c-Jun N-terminal kinase and p38 mitogen-activated protein kinase (also known as extracellular signal-regulated kinase) pathways and, most importantly, NF-κB signalling, which mediates the expression of several inflammatory genes such as those that encode IL-6, Nitric Oxide (NO), cyclooxygenase-2 (COX2) and PGE2 (Kapoor et al., 2011).

2.3.4 Degradative enzymes: MMPs and ADAMTs

Aggrecan loss is a crucial initial event in the development of OA, which is followed by essentially irreversible collagen degradation and ultimately leads to a loss of cartilage function (Hollander et al., 1995). Aggrecan consists of a protein backbone of 210–250 kDa and its core protein folds into three globular domains (G1, G2, and G3): at the N-terminal G1 and G2 are connected by a short 128–amino acid polypeptide referred to as the aggrecan interglobular domain (IGD), while the second G2 and the third G3 domain at C-terminal are separated by a 1491–amino acid sequence carrying a great number of GAGs chains (Porter et al., 2005). In cartilage, aggrecan forms aggregates with link protein and the non-sulfated HA, to form aggregate of very high MW, via the G1 domain. The depletion of aggrecan during OA can be attributed to the increased proteolytic cleavage of the core protein and, the IGD domain is the one undergoing the depletion. The aggrecan lacking G1 domain is then free to leave the matrix and not contributing to AC functions. There are two main IGD domains representing proteolytic cleavage: Asn341/Phe342, at which all MMPs present in cartilage mainly act, and Glu373/Ala374 at which several members of ADAMTS act (Tortorella et al., 2001; Verma & Dalal, 2011; Sandy et al., 1992; Collins-Racie et al., 2004). Other cleavage sites belong to the GAG-attachment region between the G2 and G3 globular domains. The pathologic cleavage of aggrecan at Glu373/Ala374 (the ‘aggrecanase’ site) was identified as the major site of aggrecan degradation in human joint disease by analysis of synovial fluid samples from a range of human joint pathologies including OA. This is also the primary site of aggrecan cleavage in response to inflammatory stimuli. The main responsible for this process are the aggrecanases, a class of proteinases (ADAMTS-1, ADAMTS-4, ADAMTS-5, ADAMTS-8, and ADAMTS-9), which have shown to degrade the cartilage proteoglycan–aggrecan during OA. ADAMTS-4 and ADAMTS-5 have received most attention in the OA pathology, because seems to be the most active aggrecanases (Gendron et al., 2007; Verma & Dalal, 2011).

The regulation of these aggrecanases activity is crucial for maintaining a balance between aggrecan anabolism and catabolism. In normal human body, a control mechanism for aggrecan catabolism may involve endogenous inhibitors like tissue inhibitor of matrix metalloproteinase (TIMP-3) of the aggrecanases, but in diseases such as OA, the balance between TIMP-3 and ADAMTS-4 synthesis is disturbed in favour of catabolism. Which aggrecanase is mainly responsible for aggrecan degradation during human AC destruction *in vivo*, however, remains debatable up to date. It has been studied that ADAMTS-4 mRNA was induced by inflammatory cytokines such as IL-1β and TNFα in human AC, but ADAMTS-5 mRNA was not regulated by cytokines and it expressed constitutively. Also, the ADAMTS-4 was up-regulated upon the influence of TGFβ in AC at the mRNA level. Furthermore, an exposure to TNF-α or IL-1β blocking agents reduces only the activity of ADAMTS-4. This finding from *in vitro* studies deviates from the animal studies, which show that ADAMTS-5 mRNA expression is up-regulated by catabolic cytokines. Therefore, it is still not clear which aggrecanase plays the main role in pathological cartilage degradation in humans (Verma & Dalal, 2011; Tortorella et al., 2001).

MMPs start participating in this process during development of the disease and continue with the degradation of collagen (Nagase & Kashiwagi, 2003). Along with aggrecan breakdown, degradation of collagen is a central feature of OA. Several *in vitro* studies on cartilage explants suggest that collagen degradation occurs only after aggrecan is lost from the tissue, and that the presence of aggrecan protects the collagen from degradation (Karsdal et al., 2008). Furthermore, while aggrecan loss can be reversed, collagen degradation is irreversible, and AC cannot be repaired once collagen is lost. Collagen can be degraded by only a few mammalian enzymes, namely cathepsin K and the collagenolytic MMPs: MMP1, 8, 13 and 14. Amongst them, MMP13 is thought to be the primary collagenase in OA. The degradation of Coll II occurs through a triple helical cleavage, which results in denaturation of the triple helix at physiological temperatures and pH. The cleavage site is Gly775–Leu/Ile776, within each chain of the triple helical collagen molecule, at approximately three quarters of the distance from the amino terminal end of each chain. The cleaved collagen fragments denature into non-helical gelatin derivatives, thus becoming vulnerable to further degradation by these collagenases and by other proteinases (Billinghurst et al., 1997). The MMPs are strongly inhibited by all four of the mammalian TIMPs (TIMP-1, -2, -3 and -4). **Figure 2.9** summarises

the main factors involved in MMPs and ADAMTS expressions (Fath et al., 2006; Vogel et al., 1997; Vincent et al., 2007; Amiable et al., 2011; Yokota et al., 2003; Echtermeyer et al., 2009).

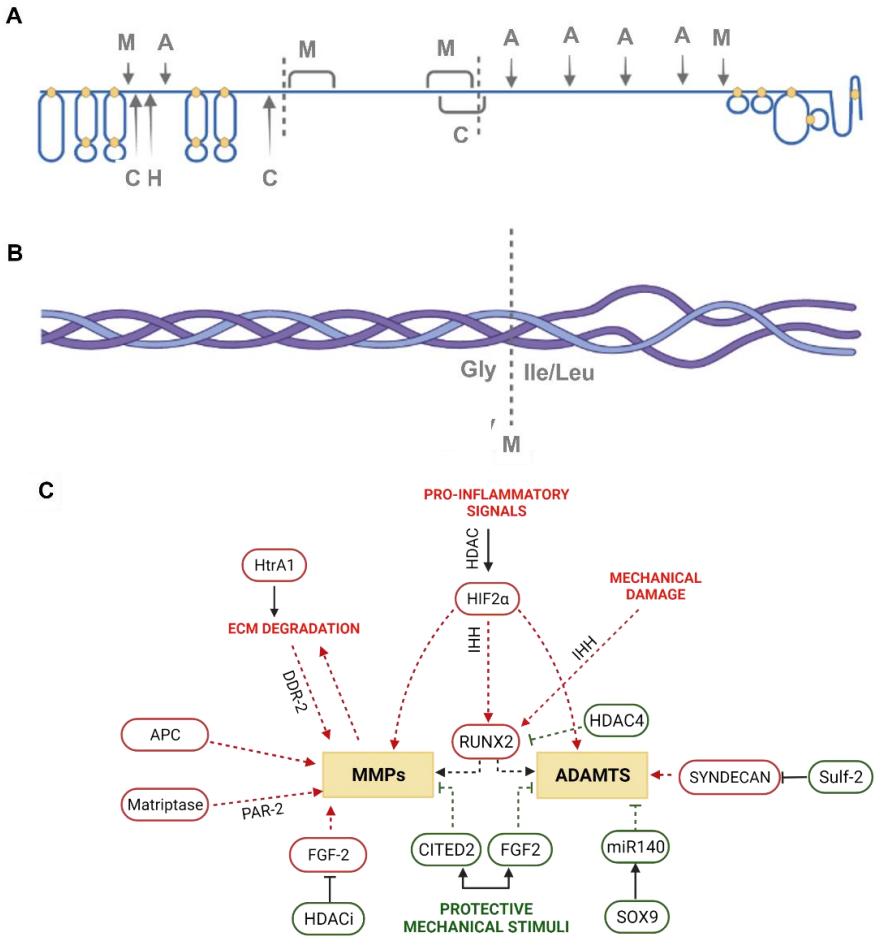

Figure 2.9: Proteolytic cleavage sites within the aggrecan core protein in AC by: ADAMTS4/5 (A), calpain (C); HtrA1 (H), MMPs (M). (**A**). Cleavage site for Coll II in AC by MMPs (M) (**B**). Factors regulating expression and activity of collagenases (MMPs) and aggrecanases (ADAMTS) in OA; the expression and activity of MMPs and ADAMTs can be stimulated (green) or inhibited (red) by several inter-related mechanisms: inflammatory cytokines, via Histone deacetylases (HDAC), induce NF-kB dependant expression of Hypoxia-inducible factor-2 (HIF-2α), resulting in increased expression of MMPs and ADAMTS and increased RUNX2 expression via Indian hedgehog (IHH); mechanical damage has the same effect on IHH, while the inhibitors of HDAC can have chondroprotective effect; High temperature requirement A (HtrA), highly expressed during OA, allows collagen binding with discoin domain receptors (DDR) causing downstream of signalling events such as MMP13 expression; Activated protein (APC) and Matriptase 1 increase MMP expression, as well as FGF-2, which act as a transducer of protective mechanical signals suppressing ADAMTS; CITED2, which is a mediator of mechanical responses in AC and suppresses MMPs; syndecan4 acts as an ADAMTS5 stimulator and on the other side miRNA 140 as ADAMTS5 inhibitor (**C**).

2.4 Osteoarthritis treatment strategies

2.4.1 Non-surgical and surgical treatments

OA treatment options depends upon the injury site, the extent of the damage, as well as the patient profile. Current clinical treatments for OA include non-surgical (pharmacological and non- pharmacological) measures for mild to moderate degenerative joint disease, and surgical approaches for moderate to severe degenerative joint diseases, for improving tolerance for functional activity based on the severity and stage of the disease (Bhosale & Richardson, 2008).

Physical therapy, exercises and weight loss are regularly utilised non-pharmacological treatments especially for the elderly, who have a higher risk of co-morbidities and pharmaceutical toxicity. However, in OA patients, these techniques have only proved to have a moderately good effect on pain, physical function, and quality of life (Glyn-Jones et al., 2015).

Analgesics, nonsteroidal anti-inflammatory drugs (NSAIDs), oral corticosteroids, hormones, chondroprotective agents, calcium and vitamins, and intra-articular steroid injections are common pharmacological therapies for reducing OA inflammation and pain, but they are not completely curative and have side effects. Hyaluronic acid visco-supplementation for knee OA pain reduction was investigated, which showed minor clinical advantages without affecting disease progression. There has been a growing interest in the last years in searching for potential new medications and some new therapeutic targets include chondrogenesis inducers, anti-inflammatory cytokines, matrix degradation inhibitors and apoptosis inhibitors (Ng et al., 2017).

Non-invasive therapeutic modalities, such as magnetic resonance treatment and pulsed electromagnetic field (PEMF) therapy, have shown positive effects on OA patients. Electromagnetic waves consisting of coupled electric and magnetic fields. PEMF uses frequencies at the lower end of the electromagnetic spectrum, up to 500 Hz, since at higher frequencies it could have peculiar biological effects, stimulating biological currents in the tissues. Compared to electrical stimulation, by use of electrodes, whose electrical field can be attenuated through some tissue and then, needs to be applied at high density having detrimental effect on humans, magnetic field penetrates unaffected through electrically insulating regions (skin or bones) and, therefore, it is possible to avoid the application of high density of stimulating current. Few groups reported that PEMFs increased chondrocytes

anabolic activity and phenotypic maturation without side effect or may cause a significant reduction in some of the most relevant proinflammatory cytokines in human chondrocytes, but the underlying mechanism of action of PEMFs in OA are not entirely understood (Murray et al., 2016; Hu et al., 2020). Several surgical options exist for OA treatment, that started since 1959 with Pridie's resurfacing technique inspired by observing that full thickness defects showed an ability to repair thanks to the involvement of the SB; this allows the resident progenitor cells to infiltrate the site of the defect and promote the repair process (Pridie & Kh., 1959; Insall, 1974). From this discovery, a series of bone marrow stimulation techniques were developed such as joint debridement, subchondral drilling, and micro fracture ((Alford & Cole, 2005). These repair strategies led to tissue with inferior mechanical properties and deteriorated clinical results. Osteochondral plugs as autograft and allograft for the treatment of cartilage defects were first introduced during the 1970s. Major drawbacks still exist, such as the lack of available tissue, the donor site morbidity, and the mechanical inferiority of an osteochondral plug taken from a non-load bearing area for autologous grafting and the mismatch between the graft and the implant and the host immune reactions for the allograft (Zhang et al., 2009). As an alternative approach, mosaicplasty, firstly described in 1993, has been adopted in the treatment of small to medium size defects (up to 4 cm^2), to improve integration of the plug and the tissue (Matsusue et al., 1993). When these methods fail, in severe cases (Grade IV of W-L scale), the diseased osteochondral tissue is partially or completely removed and resurfaced in joint replacement therapy (TJR). To replace the injured joint, an artificial implant with a metal shell (such as titanium, stainless steel, or alloys), a polymer piece (such as polyethylene), and a metal stem, is inserted. There is a potentially substantial market for complete knee and hip replacements as the population's average age rises. However, often revision surgeries are needed due to complications, such as wear and tear or loosening of the implant or infections, as well as because of the short life span of current implants (in fact, it should be decided very cautiously for young people especially) (Katz, 2006).

2.4.2. Regenerative medicine techniques

Regenerative medicine techniques were introduced in the 90's. Amongst these, autologous chondrocyte implantation (ACI) was first used in rabbits in 1987 with the first pilot study published in 1994 by Brittberg et al (Brittberg et al., 1994). By 2010, over 35,000 patients had been treated worldwide. This technique implies the harvest of 200-300 mg of cartilage from a non-load-bearing area in the knee. Then, the cartilage is sent to a lab for processing: it is

digested, the isolated chondrocytes are expanded *in vitro* for 2 to 3 weeks, and the expanded final number of cells is re-sent to the surgeon as a cell suspension. The cells are then be injected into the defect covered with a periosteal flap (1st generation ACI). All post-operative failures occurred within the first two years.

Geistlich (Switzerland) produced Chondro-Gide™, a porcine Col I and III membrane, to replace the periosteum (2nd generation ACI). Preliminary studies gave satisfactory outcomes, although re-operation was still required to deal with some cases of delamination, graft failure, or the inability of the regenerated tissue to integrate with the surrounding native cartilage. Long-term follow-up provided evidence that Chondro-Gide™ alleviated pain and swelling to increase the level of knee functionality, resulting in a better quality of repaired tissue (McCarthy & Roberts, 2013).

Third generation ACI, matrix-autologous chondrocyte implantation (MACI™), consisting of suspending expanded chondrocytes in a hydrated scaffold (the first Tissue Engineering technique involved in AC), was commercially developed by Verigen (Germany and USA). This technique showed several advantages, such as better control of cell distribution throughout the defect, cells sustainment and the potential to manage more extensive osteochondral defects. MACI failure rate was stated at 10.7 % at seven years compared to 33 % of the 1st generation; in fact, it showed significant improvement respect to clinical outcomes (Basad et al., 2015). MACI is the first FDA-approved cellularised scaffold product that applies tissue engineering processes to grow cells on scaffolds using healthy cartilage tissue; it has been already authorised, as well, in certain EU countries, but EU licence was suspended due to commercial reasons (Autologous et al., 2017). Some MACI implants commercially available are Hyalograft® and Bioseed® scaffolds (Kreuz et al., 2009).

Recently, the use of stem cell-based therapy is emerging as viable alternative for OA treatments, thanks to MSCs ability to proliferate and differentiate in different cell lines. The harvest of multinucleated cells from within the bone-marrow and direct injection to the cartilage defect area using the bone-marrow aspirate concentrate (BMAC) system, which is gaining prominence amongst the clinicians as it helps to circumvent the labour-intensive protocols with cell culture and the associated high costs. This treatment was approved by FDA and it appears to be a safe procedure that is growing exponentially. However, the interaction of the transplanted cells with the host tissue, their differentiation into AC, fulfilment of the

biomechanical properties and long-term benefits remains to be understood (Cotter et al., 2018) .

2.4.3. Chondrosphere® technique

There is a recent prospective randomized, called Chondrosphere® (or Spherox™) that is considered the 4th generation ACI based on the use of different doses of spheroids of human autologous matrix-associated chondrocytes and their implantation. Briefly, primary chondrocytes are harvested from patient's cartilage biopsy and the cells are expanded in a monolayer culture. After the expansion step, chondrocytes are transferred to coated culture plates, where they cannot adhere to the surface, but start to form cell aggregates, spheroids. The optimal culture period for the spheroids to achieve optimal size is claimed to be less than 2 weeks. When spheroids are formed, these are washed and suspended in isotonic sodium chloride solution (0.9 % sodium chloride (NaCl) in phosphate buffer solution (PBS)) and injected within the defect site, after debriding and removing the synovial fluid (EMA, 2017) The NICE from 2017 approved the Chondrosphere® as clinically effective approach for patients with a large defect size (up to 10 cm^2) defining it as follows: "Autologous chondrocyte implantation using Chondrosphere® is recommended as an option for treating symptomatic AC defects of the femoral condyle and patella of the knee (International Cartilage Repair Society grades III or IV) in adults, only if (1) the person has not had previous surgery to repair AC defects, (2) there is minimal osteoarthritic damage to the knee as assessed by clinicians and experienced in investigating knee cartilage damage using a validated measure for knee OA, and (3) the defect is over 2 cm^2"(National Institute For Health and Care Excellence, 2017b). It was demonstrated that, when spheroids are in contact with each other's and with their native ECM environment, after injection, they arrange themselves in 3D cell aggregates, adhere to full-thickness cartilage defects and appear to produce a cartilaginous ECM which fuses with native cartilage, thus generating an autologous cartilage-like repair tissue (**Figure 2.10**) (Schubert et al., 2009). The results were ideal in terms of synthesize cartilage-specific proteins and matrix components, mainly GAGs and Coll II, that were deposited in the intercellular space. This technique allows to overcome problems such as chondrocyte de-differentiation, during *in vitro* monolayer expansion, and the resulting decreased capacity of re-implanted chondrocytes to regenerate hyaline AC because of the phenotype loss. However,

this technique has some disadvantages including the high cost (£10,000 per patient per each therapy) (Cummins et al., 2017; National Institute For Health and Care Excellence, 2017b).

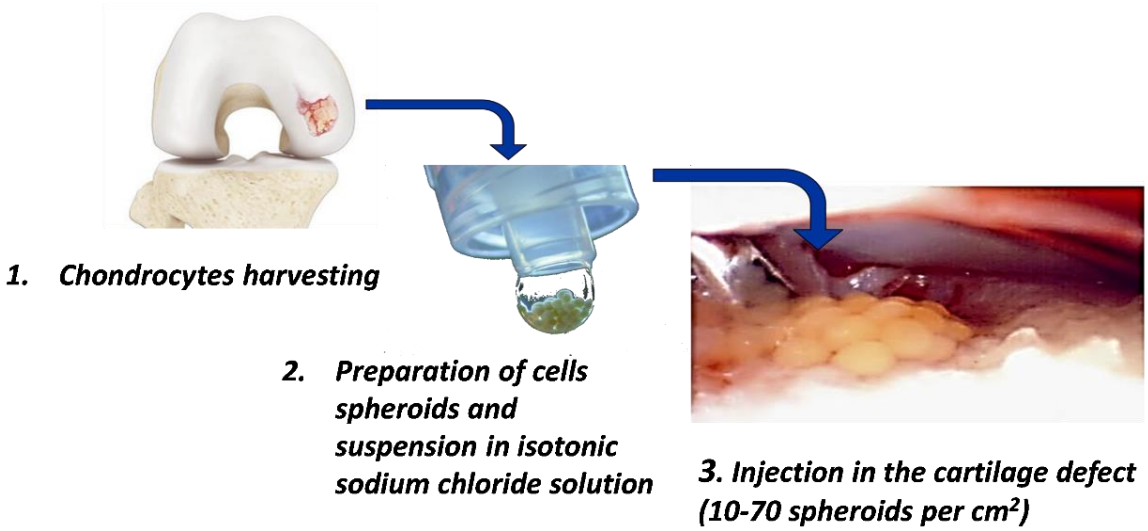

Figure 2.10: Scheme of the Chondrosphere® (CO.DON, AG) technique: (1) chondrocytes harvesting, (2) preparation of cells spheroids and suspension in isotonic sodium chloride solution, (3) injection in the cartilaginous defect (10 – 70 spheroids per cm^2) within a syringe - Arthroscopic view after transplantation into an AC defect. [courtesy of Dr. Schreyer,ev. Elisabethenstift Hospital,Darmstadt,GE]

2.5 New trends in Osteoarthritis treatment

There are currently no disease-modifying OA drugs (DMOADs) available, therefore their development is vital. Most of the research in this field focuses on identifying methods for either preventing cartilage breakdown or boosting its repair. Since the role of MMPs and ADAMTS during OA pathogenesis is well established, these proteases are an attractive target for DMOADs development (McClurg et al., 2021).

Because reversible aggrecan breakdown is considered to occur before irreversible collagen loss, and ADAMTS-5 is assumed to be the essential "aggrecanase" in both murine and human OA, it got a lot of attention. For example, Novartis out-licensed anti- ADAMTS-5 nanobody (M6495) which proved to protect mice against surgically induced OA *in vivo* (Siebuhr et al., 2020).

The adverse effect of targeting MMPs and ADAMTS is that these inhibitors could target aggrecanases and collagenases outside of the joint. For example, it was found a potential involvement of ADAMTS-5 in wound healing, glucose metabolism, inflammation, and brain plasticity (Santamaria et al., 2021). On the other side MMP13 was found to play physiological functions in wound healing, muscle regeneration, and fracture repair, all of which should be considered when developing MMP13 inhibitors for OA treatment (Smith et al., 2020).

Alternatives to direct suppression of metalloproteinase activity are being investigated. An option is to increase the amounts of endogenous MMP and ADAMTS inhibitors in cartilage. TIMP-3 is the only one of the four mammalian tissue inhibitors of MMPs, that efficiently inhibits both MMPs and ADAMTSs. Alternatively, GFs that block metalloproteinase-mediated cartilage breakdown, while encouraging anabolic repair pathways, can be used to induce AC repair (Meliconi et al., 2013).

Local injectable treatment using biologic agents such as platelet-rich plasma (PRP) or stem cell–based preparations has been linked to considerable improvements in joint pain and function in OA patients and has grown in popularity over the last decade. PRP treatment for OA includes injecting a preparation of autologous plasma with high platelet levels directly into the joint. Platelets are activated by abundant cartilage ECM proteins in the joint, resulting in the release of cytoplasmic components such as TGFβ-1, platelet-derived growth factor (PDGF), IGF, and FGF2, which promote aggrecan and Coll II synthesis while reducing expression and activity of catabolic MMPs. BMAC, as anticipated, is an autologous cell-based therapy that attempts to harness the regenerative power of MSCs, cytokines, and GFs present in bone marrow. The primary contents of BMAC are MSCs, which make up 0.001 % and 0.01 % of the total content and GFs, mainly TGFβ, BMP-2 and BMP-7, and IL-1Ra. BMAC enables for larger anti-inflammatory and anabolic factor concentrations to be delivered locally without increasing proinflammatory or catabolic factor concentrations (Weber et al., 2021).

An alternative is the direct injection of cells. MSCs are the most promising cell type, with multiple clinical trials demonstrating their ability to improve joint function and reduce pain in knee OA patients. Both *in vitro* and *in vivo* investigations demonstrated MSCs therapeutic potential in preventing AC degeneration with over 100 clinical trials (http://www.clinicaltrials.gov) for evaluating the safety and effectiveness of MSC intra-articular injection in OA patients (Giannasi et al., 2020). However, there are some concerns about the injection of MSCs, such as their low availability and difficulty of high number of cells to reach the target site, regulatory difficulties limiting their use, genetic instability, and chromosomal alteration during long-term *ex-vivo* culture, and their immunogenicity (Vizoso et al., 2017).

To address these restrictions, researchers have concentrated on the secretome of MSCs over the past 15 years. In fact, MSCs favourable effects on tissue repair and regeneration was

mainly found to be related to their paracrine activity, which is defined by their ability to produce GFs, cytokines, and chemokines that coordinate interactions within the microenvironment and impact tissue regeneration, rather than cell–cell interaction. These substances can prevent apoptosis, boost cells proliferation, enhance ECM production, and alter the immune system (Wu, 1995). Extracellular vesicles (EVs) (exosomes, microvesicles) containing peptides, small proteins, and bioactive compounds such as microRNA (miRNA) make up most of the stem cell secretome. To mediate their physiologic action, these vesicles are released by cells in the surrounding microenvironment and most MSCs therapeutic actions are mediated by soluble mediators that are transported through EVs. EVs were studied on OA-like murine chondrocytes by Cosenza et al., revealing their protective role on chondrocytes from apoptosis and encouraged macrophage polarisation toward an anti-inflammatory phenotype. Also, exosomes from MSCs were found to prevent the onset of OA (Cosenza et al., 2017; D'arrigo et al., 2019). Similarly, Vonk et al. and Tofiño Vian et al. studied the effect of exosomes on OA chondrocytes, showing good results in terms of decreased interleukins and MMPs production, and increased Coll II expression (Tofiño-Vian et al., 2018; Vonk et al., 2014).

2.5.1 miRNA treatment for OA

MiRNAs have a role in the homeostasis of AC during the progression of OA. These are a class of endogenous non-protein-coding short RNA that have been discovered as important post-transcriptional regulators. These molecules primarily affect biological response, by regulating post-transcriptional gene expression (Li et al., 2015).

The generation of miRNA is a multistep process that starts in the nucleus and finishes in the cytoplasm (**Figure 2.11**). RNA polymerase II or III transcribes miRNA genes to produce long RNA precursors with a single or many stem loops, which is called Primary (pri)-miRNA and it has a hairpin look and partly complementary sequences in the stem region, which houses the future miRNA. The primiRNA is cleaved by Drosha (a highly conserved RNase-III-type enzyme), which is a miRNA processor associated with DiGeorge syndrome critical region gene (DGCR8), into a shorter precursor miRNA called pre-miRNA, which has a stem loop or hairpin structure composed of 70 – 100 nucleotides in the nucleus. Pre-miRNAs are transported to the cytoplasm by the exportin-5 pathway and are sliced by the RNAse III called Dicer. This produces a 22-nucleotide double-stranded miRNA duplex, including the mature miRNA and the passenger miRNA strand. The passenger miRNA strand is destroyed, while the mature miRNA (the one with the thermodynamically less stable 5'-end) is transported to the RNA-

induced silencing complex (RISC), which contains Argonaute proteins. Depending on the degree of base-pairing similarity between the miRNA and the target mRNA's 3'-untranslated regions (3'-UTRs), miRNA causes gene silence via translation repression or targeted mRNA cleavage. When perfect base-pairing between miRNAs and their targets occurs, miRNA causes cleavage or degradation of target mRNA (O'Brien et al., 2018).

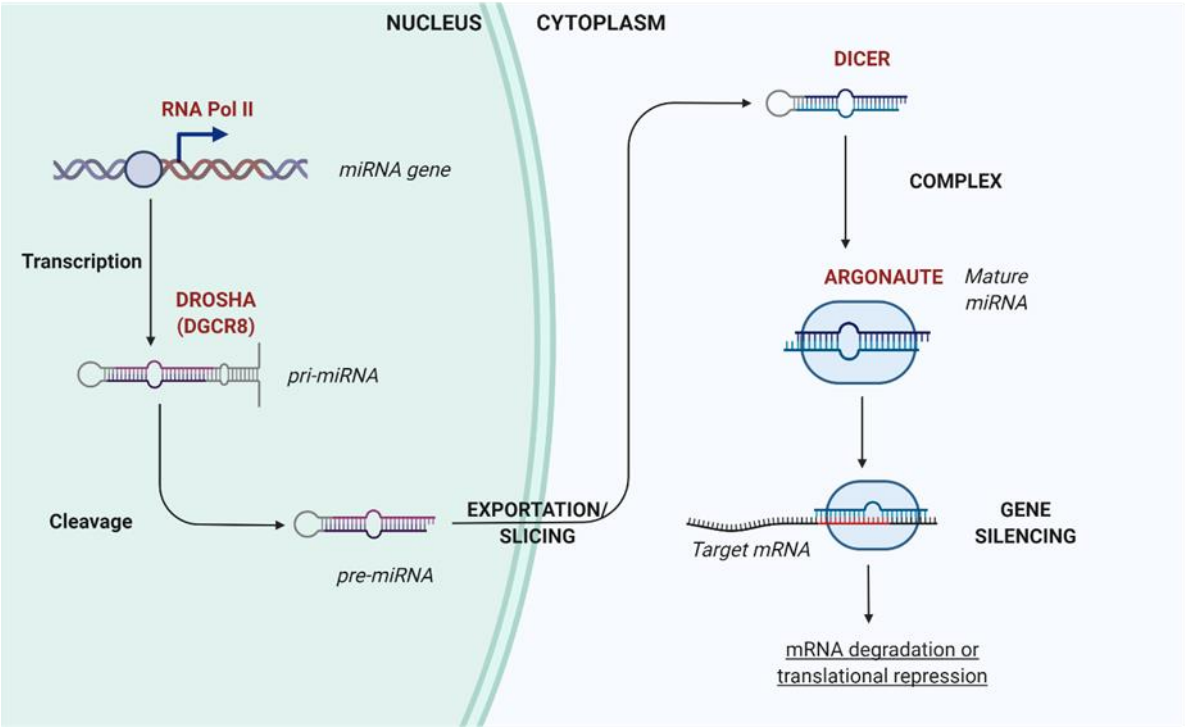

Figure 2.11: MicroRNA biology and function: MicroRNA is transcribed in the nucleus to either pri-miRNA or premiRNA. The pre-miRNA is then transported to the cytoplasm, where it is further cleaved to generate mature miRNA. MiRNA binds to its target mRNAs by forming a complex with the miRNA induced silencing complex (RISC). Translation of mRNA into protein is inhibited when miRNA and mRNA are partially complementary. When miRNA and mRNA complement one other nearly perfectly, the mRNA is destroyed.

MiRNAs can play crucial roles in cell proliferation, migration, invasion, and differentiation by binding to the 3' untranslated region (3'UTR) of target genes. Dysregulation of numerous miRNAs has been implicated with OA-related ECM degradation. ADAMTS-4 and ADAMTS-5, for example, are downstream of miR-140, which is linked to chondrocyte death (Miyaki et al., 2010). On the other side MMP13 is found to be up-regulated when miR-27b is down-regulated (Park et al., 2013). Although many studies have indicated the close relationship between miRNAs and ECM degradation in OA, the corresponding upstream or downstream have not been illuminated clearly yet. In **Table 2.4** are reported the miRNA involved in OA pathogenesis with a chondroprotective role, together with their specific function. Particularly miRNA-140

was widely studied and literature results indicate that miR-140 plays dual roles in both AC development and homeostasis, in part via regulating ADAMTS5, a major AC matrix-degrading protease in OA (Miyaki et al., 2010).

miRNAs	TARGET	FUNCTION	REF.
miRNA-140	SMAD3 MMP13 ADAMTS4/5 IL-1β RALA	Suppression of SMAD2/3 pathway; Inhibition of MMP13 and ADAMTS4/5 and IL-1β; upregulation of SOX9,ACAN,COL2A1	(Miyaki et al.)
miRNA-25	IL-1β	Chondrocytes proliferation and reduced apoptosis	(He & Deng, 2021)
miRNA-29	COL3A1 Osteonectin	Promotes osteogenesis, inhibits osteoblast differentiation	(Le et al.)
miRNA-19b	IL-1β	Chondrocytes proliferation and reduced apoptosis	(Y. Li et al.)
miRNA-27b	NF-κB MMP13	Responsible of AC homeostasis Inhibition of MMP13	(Akhtar et al.)
miRNA-127	MMP13	Inhibition of MMP1/13	(Dong et al.)
miRNA-148	MMP13 COL10A1 ADAMTS5	Show pro-anabolic and anti-catabolic activities	(Vonk et al.)
miRNA-543	IL-1β	Responsible of AC homeostasis	(Xiao et al.)

Table 2.4: miRNA involved in AC chondroprotection during OA progression.

2.6 *In vitro* models of AC

Although the progressive breakdown of AC and underlying SB, mediated by synovium, are the well-known main pathological features of OA, the disease pathogenesis is due to a joint action of physico-chemical and mechanical factors, leading to a damage in the AC matrix (Lories & Luyten, 2018). In this scenario, engineered AC *in vitro* models are suitable candidates in the endeavours of deeply investigation on physiology, biology, and progression of OA diseases. This is pushing the research forward the early-stage causes of the disease as a crucial keystone to explore, design and testing new therapeutic treatments in reliable and predictive models (Chen et al., 2006). Particularly, the advantages of moving forward *in vitro* models' choice are:

(i) ease of manipulating *in vitro* systems, (ii) shift towards the newly adopted EU Directive about the ethical philosophy of Refining, Reducing and Replacing use of animals in the research (3Rs' principle), (iii) low reliability of studies on animals when translated to human and (iv) high costs involved within *in vivo* studies (Armiento et al., 2018; Sophia Fox et al., 2009b).

2.6.1 Tissue engineering approach: cells, biomaterials and biophysical stimuli

Tissue engineering (TE) is a promising strategy for manufacturing *in vitro* model of AC tissue. One of the goals of AC TE is to create constructs that resembles the native tissue's structure, metabolic characteristics, and biomechanical capabilities. This approach exploits the bottom-up principle, based on growing TE constructs based on biomaterials which are loaded with cell lines and cultured *in vitro* under physiological conditions (37 °C, 5 % CO_2) to generate artificial tissues. Only a few literature studies have generated tissue-engineered structures with cartilage characteristics that are almost identical to natural cartilage. The three main elements of TE are cells, biomaterials and physiological stimuli to mimic the natural environment.

- Cells

Cells choice is critical for cartilage TE, as they determine the degree of damaged tissue regeneration that may be achieved. Seeded cells in AC tissue engineering come from autologous cartilage cells (chondrocytes) or MSCs with multiple differentiation potential (Chen et al., 2006).

Chondrocytes are the cells naturally found in AC; these can be isolated from several sources (e.g. AC or cartilage of nose, rib or ears) and each zone gives cells with different properties (elastic, hyaline or fibrous). Chondrocytes cells can be obtained from a biopsy: for example, from an explant of 5 mm x 10 mm. it is possible to obtain around 250,000 cells. Therefore, chondrocytes are culture-expanded to obtain enough cells needed for obtain *in vitro* AC models (up to 100 million cells/mL) (Puelacher et al., 1994). The expansion process can lead to a loss of their chondrocytic phenotype and their de-differentiation in fibroblasts before becoming senescent: this results in a decrease in aggrecan and Coll II synthesis. Consequently, stromal stem cells have been widely exploited to obtain *in vitro* model of AC. Adult stem cells, known as MSCs, can be obtained from both human and animal sources. Human MSCs are non-haematopoietic multipotent stem cells that can develop into three distinct lineages: mesodermal (chondrocytes), ectodermal (neurocytes), and endodermal (hepatocytes). These cells can be extracted from a variety of human tissues, including bone marrow, adipose tissue, amniotic fluid, dental tissue, endometrium, and the umbilical cord. MSCs are known to have

high proliferation rate, and these can differentiate into chondrocytes using some signals such as GFs or mechanical stimuli. This process of differentiation can be reproduced *in vitro* by adding some GFs which are responsible for MSCs differentiation, within the MSCs culture medium. Also, BM-MSCs showed promises as therapeutic agent in OA treatments, as widely explained in *section 2.5* (Shah et al., 2021). Other cells source used for AC are: AC-derived progenitor cells (ACPCs), which were found to have a similar behaviour to MSCs and expansion does not alter differentiation, but their disadvantage is their limited abundance due to the use of autologous sources; and induced pluripotent stem cells (iPSCs), based on the idea that a large number of autologous cells can be derived from a small starting population of cells and this holds great promise for cartilage TE (Rikkers et al., 2022; Urlic & Ivkovic, 2021).

- Biomaterials

Biomaterials are a fundamental element in AC TE, by providing cells with a suitable environment that allows them to adhere, proliferate, and differentiate to obtain a functional AC-like tissue. A biomaterial is a three-dimensional (3D) matrix or scaffold that can facilitate cellular signalling and tissue remodelling on both a physical and biological level. Both natural and synthetic biomaterials have been employed for AC TE. Synthetic biomaterials are frequently employed in bone and cartilage tissue engineering due to their favourable mechanical properties. For AC, poly(glycolic acid) (PGA), poly(L-lactic acid) (PLA), or a copolymer of PGA and PLA (PLGA) have been employed as scaffolds, however they lack signalling molecules such as the RGD sequence for cell attachment, which prevents them from being widely used alone. The physical and chemical features of synthetic scaffolds, on the other hand, can be altered to influence cellular function. To induce cell-specific bioactivities, cell adhesion molecules, enzymatic degradation sites, or GF-binding regions can be inserted into the synthetic scaffold. On the other side, natural biomaterials (e.g. collagen, alginate, gellan gum (GG), hyaluronic acid (HA), gelatin (GEL), chitosan) can mimic the ECM of AC tissue and are more biocompatible for cell culture. However, they possess lower mechanical properties (Kwon et al., 2019; Silva et al., 2009).

Hydrogels, which are both water-based and water insoluble, were discovered as an excellent scaffold for engineering a tissue with a high-water content, such as AC, because of their capacity to recapitulate the AC solid/liquid ratio and efficiently repair injured tissue (Armiento et al., 2018). Hydrogels are water-swollen networks that support the transfer of cells, bioactive substances, nutrients, and waste. They can also homogeneously suspend cells in a

3D environment, retaining a rounded morphology that may produce a chondrocytic phenotype. Importantly, hydrogels can be physically or chemically crosslinked, allowing the material to be held together by molecular entanglements and secondary forces including ionic, hydrogen bonding, and hydrophobic interactions, as well as covalently attached. They are intelligent materials that react to environmental factors such as temperature, pH, ionic strength, and electric field. However, hydrogels have low mechanical property, which is considered the major drawback for their use in TE, as found in the load-bearing bone and cartilage tissues. To solve this problem, one approach is increasing polymer concentration and crosslinking density (Scalzone et al., 2021a). The biomechanical and biological features of various biomaterials for cartilage tissue regeneration were reported in **Table 2.5.**

- Biophysical stimuli

There is currently no appropriate *in vitro* culture technique for AC tissue regeneration. Simulating the natural cellular environment is one way to identify the best culture environment *in vitro*. To this aim it is possible to apply biophysical stimuli, which can be divided in biochemical and biomechanical stimuli (Kwon et al., 2019)

GFs have long been known as essential contributors in neocartilage formation. Many studies have demonstrated the beneficial effects of GFs such as TGFβ-1, TGFβ-2, TGFβ-3, bone morphogenetic proteins (BMPs), FGF-2 and insulin-like GF-1 (IGF-1) on chondrogenic development. For example, TGFβ-1–3, IGF-I, PDGF, and BMP7 stimulate PRG4 expression in the superficial zone, while TGFβ-1–3, IGF-I, PDGF, and BMP7 stimulate Cartilage Intermediate Layer Protein (CILP) expression in the middle zone of human AC (Schmidt et al., 2008; Mori et al., 2006). Also, Matrilin 3 has been demonstrated to stimulate chondrogenesis in a BMSCs cultures and Kartogenin to stimulate chondrogenic differentiation in MSCs and alleviated Coll II breakdown by 1.8-fold in an OA model (Cai et al., 2019). Hypoxia is another critical element commonly found in AC, since it is avascular. *In vitro*, hypoxia (5 % O_2) has been shown to increase MSC proliferation and chondrogenesis, as well as GAGs production, compared to normoxia condition (20 % O_2) (Bae et al., 2018). Hypoxia has also been demonstrated to enhance PRG4 gene expression in chondrocyte subpopulations (Ruan et al., 2013).

TYPE	NAME	ADVANTAGES	DISADVANTAGES	REF.
Natural polymer	Alginate	High functionality, rapid gelation, low cost, structurally similar to GAG	Poor cell adhesion, poor mechanical strength	(Jeuken et al., 2016; Arno et al., 2020)
	Agarose	High functionality, thermo-reversible gelation, low cost, structurally like GAGs	Poor cell adhesion, poor bioactivity, limited mechanical properties	(Mauck et al., 2006; Zarrintaj et al., 2018)
	Chitosan	Antibacterial, pH and temperature responsiveness, cationic features (electrostatic interaction with anionic GAGs), low cost, structurally like GAGs	Poor water solubility, low mechanical properties	(Scalzone et al., 2019a; Liu et al., 2020)
	CS	Component of AC ECM, easy to functionalise	Rapid degradation, low mechanical properties	(Scalzone et al., 2020; X. Li et al., 2021; Lee et al., 2021; Shin et al., 2021a; Yang et al., 2020)
	Collagen	Component of AC ECM, good cell-matrix interaction	High cost, potential immunogenicity, low mechanical properties	(Ren et al., 2016a; Wei et al., 2021; Kilmer et al., 2020)
	GEL	Biologically active for cellular interaction, low immunogenicity, easy to process and functionalise	Rapid degradation, low thermal stability, low mechanical properties	(Tsai et al., 2020; Q. Li et al., 2021)
	GG	pH and temperature responsiveness, structurally similar to GAGs	Poor cell adhesion, small temperature window, weak mechanical strength	(Lee et al., 2021; Bonifacio et al., 2020; Baek et al., 2019; Oliveira et al., 2009)

	HA	Component of AC ECM, easy to functionalise	Rapid degradation, weak cell adhesion, low mechanical properties	(Mohan et al., 2017; Park et al., 2019)
	Silk fibroin	High mechanical properties, low immunogenicity, structurally similar to collagen, morphologic flexibility	Low biodegradability, Source variability	(Lee et al., 2021; Liu et al., 2020)
Synthetic polymer	PEG	Good biocompatibility, low immunogenicity, easy to process and functionalise, mechanically tuneable	Biologically inert for cellular interaction, non biodegradable	(Wang et al., 2017; Yu et al., 2014)
	Poly lactic acid (PCL)	Easy to manufacture, low melting temperature, long term mechanical stability	Poor bioactivity, hydrophobic	(Wang et al., 2017; Yu et al., 2014; Scaffaro et al., 2016)
	PLA PGA PLGA	Good biocompatibility and biodegradability, easy functionalisation, low immunogenicity	Low bioactivity, could produce inflammatory response	(Marycz et al., 2020; Iulian et al., 2018)
	Poly vinyl alcohol (PVA)	Good water absorption and retention, chemical resistance, good mechanical properties	Biologically inert, non degradable	(Chen et al., 2021)

Table 2.5: Biomechanical and biological features of various biomaterials for cartilage tissue regeneration.

A particular focus can be put on mechanical stimuli, such as shear stress, compression and hydrostatic pressure which showed to affect AC synthesis and chondrocytes behaviour a lot. For example, cyclic compression boosts GAG production, which is beneficial in the medium and deep zones of AC (Gilbert et al., 2021), while shear stimulation enhances PRG4 production, which is beneficial for the superficial zone (Grad et al., 2005; Davisson et al., 2002). Furthermore, mechanical stimuli have been found to have a frequency and amplitude-dependent effect on AC ECM production. Static and low-frequency strain (0.3 Hz) suppressed GAGs synthesis by chondrocytes in agarose scaffolds, whereas a frequency of 1 Hz at 15 % strain amplitude enhanced it. When the frequency was increased to 3 Hz, however, the amount of GAG synthesised reduced (Lee & Bader, 1997). In agarose scaffolds, cyclic compression at 10 % strain frequency of 1 Hz for 4 hours per day triggered chondrogenic development of rabbit BMSCs (Huang et al., 2004). In addition, Chen et al. optimised the parameters of cyclic dynamic compressive loading for both a monoculture of chondrocytes or a co-culture of chondrocytes and adipose stem cells within a cryogel made of GEL/CS/HA/CH. In both cultures with a stimulation at a frequency of 1 Hz, 20 % strain and 3 h/day stimulation, chondrocytes showed the highest level of AC matrix production and gene expression, while stem cells in co-culture showed a great chondrogenic potential (Chen et al., 2018). Mechanical stimuli can be applied by using bioreactors, which are devices able to provide physiological requirements of the cell such as nutrition, GFs and mechanical environment. Various bioreactors have been used in cartilage and bone TE such as dynamic compression bioreactors, tensile bioreactors, hip simulator-based bioreactor, and spinner flask (Zhao et al., 2016). Among all of these, dynamic compression bioreactors are the most used to improve matrix production in tissue-engineered cartilage (Klein et al., 2009). Also, the combination of shear stress and compression was analysed by resulting in increased Coll II production.

2.6.2 Gellan Gum methacrylate

GG is a linear anionic polysaccharide containing one carboxyl side group and is made up of four repeating carbohydrates: 1,3-b-D-glucose, 1,4-b-Dglucuronic acid, 1,4-b-D-glucose, 1,4-a-L-rhamnose. It was first described by Moorhouse et al., and this material has a wide range of applications in the food industry (FDA approved) and biomedical science, owing to its ability to be processed into clear gels that are heat and acid stress resistant (Moorhouse et al., 1981). GG is commercially prepared by microbial fermentation from the bacterium *Sphingomonas elodea* or *Pseudomonas elode* (Warren & In Het Panhuis, 2015). There are two types of GG:

acetylated (Gelrite™) and deacetylated (Kelcogel™), with the latter being the most common and commercially available. Both form thermo-reversible gels with mechanical characteristics ranging from soft and elastic in the acetylated form, to rigid and brittle in the totally deacetylated form. Gellan molecules are present in the form of random coils at high temperature and in the form of double helices at low temperature, resulting in the construction of a three-dimensional network (Zand-Rajabi & Madadlou, 2016a). The chemical nature and quantity of cations present in GG solutions have a significant influence on the gelation of the solution. The helix creation and partial aggregation at low temperature (near the body temperature) due to the sol/gel transition may generate an ordered structure at low GG concentrations, but this does not lead to gel formation since there is the electrostatic contact between carboxyl side groups, which prevents the tight binding of helices and their cohesive aggregation (Quinn et al., 1993; Miyoshi et al., 1996). The insertion of cations reduces electrostatic repulsion, allowing for tight helical binding and aggregation in form of gels. Also, cations composition influences its gelation capabilities, with divalent cations (Ca^{+2}, Zn^{+2}, Pb^{+2}, Al^{+3} etc) promoting gelation far more strongly than monovalent ones. The electrostatic repulsion between the ionised carboxylate groups on the GG chains is screened in monovalent cations, resulting in gelation. On the other side, there is a chemical bonding between divalent cations and two carboxylate groups belonging to glucuronic acid molecules in the Gellan chains. In addition to that, it was discovered that K^+ ions instead of Na^+ and Ca^{2+} divalent ions instead of Mg^{2+}, have a more remarkable effect on the GG viscoelasticity (Zia et al., 2018).

GG's advantages in biomedical applications include its lack of toxicity, biodegradability, ability to be used as an injectable system in a minimally invasive manner. It also showed good processability, a wide spectrum of mechanical and suitable rheological properties. The presence of this carbohydrate residue, which contains carboxylic groups, could give this substance additional capabilities. Indeed, being negatively charged polysaccharide, it can produce polyelectrolytes with the oppositely charged polymers like chitosan (Oliveira et al., 2009). GG applications in biomedical field include: (i) gene therapy and cell-based therapy (Vieira et al., 2019); (ii) protein carrier and drug delivery system, in form of hydrogel, macrocapsules and microcapsules, for asthma or cancer therapy (Palumbo et al., 2020); (iii) TE of multiple tissues and disease modelling (Stevens et al., 2016). GG structure is similar to native AC GAGs, due to the glucuronic acid residues in their repeating unit. Oliveira et al. used GG for the first in AC TE, by encapsulating human nasal chondrocytes obtaining a hydrogel

with viscoelastic properties within the range of other hydrogels used for cells encapsulation and being cytocompatible, showing a potential role in AC regeneration approaches (Oliveira et al., 2009). However, GG has some drawbacks such as: poor stability in physiological condition due to the exchange of divalent ions with monovalent ones, leading to a loss of mechanical properties; thermally reversible “weak gel" property, because at high temperatures, GG has a disordered coiled shape, while at lower temperatures, it undergoes a thermally reversible coil-double helix transition; low cell attachment and anomalous differentiation behaviours, because it does not participate in the specific cell binding interactions (Kang et al., 2015).

Several chemical modifications of GG (methacrylation, esterification or peptidic functionalisation via click chemistry) and combination with other polymers (e.g., HA, GEL), or biologically active molecules (e.g., bioactive glasses, hydroxyapatite, calcium phosphate) were exploited to overcome these limitations. Among them, the addition of methacrylate groups in the GG chain was proposed for the first time by Coutinho et al. for the obtainment of Methacrylated Gellan Gum (GGMA) (Coutinho et al., 2010). GGMA can be physically (with cations) and chemically crosslinked (through photo crosslinking due to MA groups). The photo-crosslinking reaction involves the presence of a photo-initiator compound and irradiation by light, typically ultraviolet (UV), to initiate a free radical polymerization reaction that propagates through carbon–carbon double bonds to form high-molecular-weight kinetic chains and form covalent crosslinks between the polymer chain. This approach can be used to tune the mechanical and physical properties of GG, to make it suitable for the desired application. GGMA showed low cytotoxicity and higher mechanical properties (Young’s modulus up to 148 kPa), compared to bare GG (Daniela F. Coutinho et al., 2010). In addition, the functionalisation with methacrylate groups leads to an improved water solubility and processability at physiological temperature of GG and, therefore, the obtained GG-MA hydrogels are compatible with cell encapsulation, and their mechanical properties, as well as their stability, are improved as compared to unmodified GG hydrogels (Silva-Correia et al., 2013). GGMA alone, or in combination with some fillers or other polymers, was studied for different TE applications (**Table 2.6**). Also, it was exploited for AC TE for the first time by Vilela et al, by encapsulating adipose-derived stem cells, obtaining a construct with highly favourable characteristics and biological performance both *in vitro* and in vivo (Vilela et al., 2018).

AIM	FORMULATION	APPLICATIONS	ADVANTAGES	REF.
BIOFUNCTIONALITY	GG/HA	Osteochondral tissue Intervertebral disk Vasculature Scar tissue	Improved cell binding	(Bellini et al., 2015; Cerqueira et al., 2014; Cencetti et al., 2011)
	GG/Fibronectin	TE applications	Improved cell binding, differentiation of endothelial cells	(Da Silva et al., 2014)
	GG/GEL	Cardiac tissue Bone tissue	Increased cell binding, mechanical strength, promoted cells physiological activity	(Wen et al., 2014; Kirchmajer & Panhuis, 2014; Koivisto et al., 2019)
	GG/nanohydroxyapatite	Bone tissue	Increased cells adhesion, proliferation and mineralisation	(Jamshidi et al., 2016; Bastos et al., 2021)
STRENGTH	GG/ALP	Bone tissue	Improved strength and stiffness, promoted cells attachment and differentiation	(Jamshidi et al., 2016; Bastos et al., 2021; Douglas et al., 2014, 2017)
	GG/PLGA microspheres	Intervertebral disk	Improved strength and stiffness	(Zong et al., 2020)
	GG/PCL fibers	Nucleus pulposus	Improved mechanical properties and biomimicry	(Thorvaldsson et al., 2013)
	GG/ AuNr	Bone tissue	Increased strength and microstructure	(Vieira et al., 2019)

BIOFUNCTIONALITY &STRENGTH	GGMA	Intervertebral tissue AC Soft tissues	Photocrosslinking, reinforcement, cells adhesion	(Vieira et al., 2019; Silva-Correia et al., 2013; Pacelli et al., 2016; Daniela F. Coutinho et al., 2010)
	GGMA/GelMA	Load bearing tissue	Photocrosslinking Reinforcement	(Shin et al., 2014)
	GGMA/laponite	Wound dressing	Increased mechanical properties, Good drug releasing system	(Pacelli et al., 2016)
	GGMA/Silk fibroin/Chondroitin sulfate	AC	Good mechanical properties, cell growth and expression of AC-specific ECM and genes	(Lee et al., 2021)
	GG/Manuka Honey	AC tissue	Antibacterial, increased mechanical stiffness, Promoted cells activity	(Bonifacio et al., 2018)
	GG/glycerol/HNT nanotubes	Soft TE	Increased biocompatibility, viscosity, mechanical properties and cells activity	(Bonifacio et al., 2017)

Table 2.6: TE applications of Gellan gum polymer combined with several polymers or molecules to improve the biofunctionality, strength or both properties.

2.6.3 Chondroitin sulfate dopamine

CS is a polysaccharide molecule which constitutes 80 % of AC GAGs, and it is the major component of AC ECM. It is a sulphated linear GAG with D-glucuronic acid and DN-acetyl-galactosamine units that repeat. CS is present in multiple tissues of the human body and plays an important role in regulating cell functions, such as cell migration and receptor binding. CS has a high-water content because of its high charge density, resulting in mechanical weakness. However, it is involved in a variety of mechanical and biological functions, including resistance to compressive load, nutrient and water absorption, anti-inflammatory activity, and chondrocyte metabolism on a cellular scale (Shin et al., 2021a). Due to degradation, the content of CS in cartilage declines with age (Ngadimin et al., 2021). Indeed, CS scaffolds have not been successful in inducing AC regeneration, despite its advantages in AC TE, due to their weak mechanical qualities and the rapid degradation. Furthermore, due to its negative charge and absence of adhesive motifs, CS has a low cell affinity (Han et al., 2018). Therefore, researchers have unavoidably attempted to circumvent these restrictions by combining CS with supporting materials including various natural or synthetic polymers (e.g., HA, chitosan, alginate, polyacrylamide, polyethylene glycol, etc.).

For example, CS was combined with GEL obtaining a multi-compositional, macroporous, extracellular matrix-based microribbon scaffolds to regenerate cartilage with biochemical, mechanical, and morphological zonal organization encapsulating MSC. The construct showed good collagen deposition and AC tissue formation (Gegg & Yang, 2020). Jiang et al, instead combined collagen, CS and HA in a three-phase hydrogel for the encapsulation of allogeneic chondrocytes with a diffusion chamber system that was implanted *in vivo* into a rabbit cartilage defect. The three phases system promoted cell growth and matrix synthesis, facilitating cartilage repair, compared to the mono-phase (Jiang et al., 2018). Similarly, Yu et al studied a high-performance biological interpenetrating hydrogel, composed of GEL, HA and CS via click chemistry reaction, showing high mechanical properties systems (Yu et al., 2013).

Polydopamine (PDA), which shares structural similarities with secreted adhesion proteins from marine mussels, has recently been shown to have significant adherence to a variety of substrates, with the potential to improve cells attachment and their proliferation. PDA's strong adhesiveness is due to the active catechol groups on the surface, which aid cell adhesion by interacting with reactive groups on cell membranes (amino groups, carboxyl groups, and catechol groups). In particular, the Mytilus edulis foot protein (3,4-dihydroxy-L-

phenylalanine and lysine) contains a catechol amine motif that can affect adhesiveness and cohesiveness depending on the pH: Catechol has an adhesive effect in acidic pH, resulting in a surface coating, whereas basic pH allows it to increase its cohesive capabilities, resulting in the production of hydrogels. In terms of adhesiveness, catechol moieties form strong connections through a variety of methods, including covalent bonds, hydrogen bonds, p–p stacks, and coordination bonds. Crosslinking reactions (e.g., dismutation and Cat–Cat bonds, hydrogen bonds, and van der Waals and other cohesive forces established with the polymeric chains) result from the production of transitory quinone groups in an alkaline environment and the formation of hydrogels (Scalzone et al., 2020). Han et al introduced a CS-PDA in a Polyacrylamide system for AC application, demonstrating good cell affinity, and a growth-factor-free and biomimetic microenvironment for chondrocyte growth and cartilage regeneration (Han et al., 2018).

2.7 3D *in vitro* models: strategies

It's becoming clear that typical tissue culture models (monolayer cultures) aren't realistic of the original cellular environment, and that they can lead to untruthful conclusions. As a result, to obtain a functional AC-like tissue *in vitro*, capable of reliably recreating the properties, e.g., mechanical, compositional, and structural of the AC, it is necessary to design a 3D environment, that better reflects the original environment able to support and stimulate the growth, organization and activity of the cells (Kalamegam et al., 2018). Several works, involving the manufacture of *in vitro* AC construct, can be found in literature, and are mainly categorised in scaffold-free and biomaterials-based approaches.

2.7.1 Scaffold-free approaches

Scaffold-based approaches have been successfully exploited in musculoskeletal TE because they are analogous to the condensation and differentiation that occurs during the developmental process of cartilage tissue (DuRaine et al., 2015). Scaffold-free approaches are characterised by the presence of high number of cells. Although autologous cells are ideal for improving clinical translation, obstacles such as a lack of primary cells and donor site morbidity have led to the adoption of allogeneic and xenogeneic sources (DuRaine et al., 2015). Also, exogenous stimuli, such as GFs, enzymes, and mechanical stimulation, are used to increase ECM formation and maturation to reproduce a functional tissue. Scaffold-free approaches could be subdivided in self-organisation process, which are cell sheet engineering and

aggregate engineering, and self-assembly process, which is the self-assembling technique (**Figure 2.12**) (De Moor et al., 2020).

- Cells sheet approach involves external manipulation to generate the desired structure. Cells are expanded in monolayer over long periods to achieve high confluence to generate a cell sheet. The sheet is pulled from the substrate once enough ECM has been created for the culture to form a cohesive layer. This technique was employed for the RevaFlex (formerly DeNovo ET) (ISTO Technologies, Missouri, USA) which is an AC repair technology using a sheet of expanded juvenile allogeneic chondrocytes obtaining good results. Cells-sheet approach was used as well in miniature pigs, achieving successful defect filling and integration. However, this technique has the drawback of cells de-differentiation during the sheet formation process (McCormick et al., 2013).
- The aggregate approach involves external force (i.e., rotational speed and duration) to obtain the aggregates formation that can decrease cell viability or lead to loss of cell type homogeneity. Rotational culture may have better diffusion and nutrient/gas exchange than static cultures due to this motion, making it an appealing TE technique. Aggregate culture is a common TE culture method because it can be utilised to generate cartilaginous microtissues as well as (re)differentiate cells to a chondrocytic phenotype. It was firstly exploited with the micromass culture by Johnston et al. in 1998, has been used for example in the Chondrosphere® technique. Aggregate engineering, while capable of overcoming diffusion restrictions in the production of cartilaginous tissues, has drawbacks due to a lack of substrate interaction during the early stages of suspension culture before cell interaction and coalescence. This leads to low proliferation. The most promising strategies for employing aggregates to design musculoskeletal cartilages include fusing small aggregates to produce bigger tissues or injecting aggregates into defects (Sun et al., 2022).
- The self-assembling does not employ external forces to form tissues. Indeed, self-assembling cellular spheroids of predictable and repeatable size can be obtained, as a pre-set number of cells are seeded into a mould with a known shape. Even though this technique requires high number of cells per construct (10–100 million cells/mL) and displays diffusion problems, it has been successfully tested with primary bovine articular chondrocytes, dermis-isolated adult stem cells, and co-culture of bovine articular and meniscus cells. To address the issue of the number of cells, MSCs are good candidates and

to overcome the further issue of poor nutrients diffusion, several dynamic cultures have recently been introduced (Dissanayaka & Zhang, 2020; De Pieri et al., 2021).

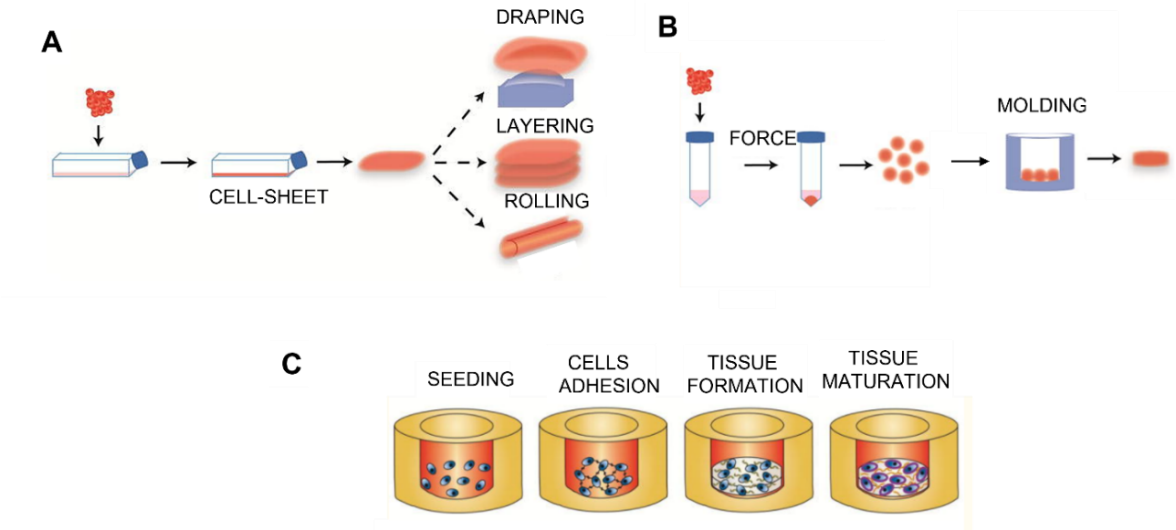

Figure 2.12: Scaffold-free approaches for obtaining *in vitro* models: cell sheet engineering (**A**), aggregate engineering (**B**) and self-assembling (**C**).

Although many promising scaffold-free approaches have been developed, there are still some drawbacks such as: they rely on specific cell populations and matrix synthesis to produce a specific structure; it is often needed long culture period and big number of cells.

On the other side, scaffold-based biomaterial approaches have the potential to directly provide structure, mechanical strength, and organisation through scaffold design (Klein et al., 2009).

2.7.2 Scaffold-based approaches

The primary goal of scaffold-based techniques was to obtain a homogeneous tissue *in vitro* able to mimic the overall bulk properties of native tissue by combining cells and biomaterial in chondrogenic conditions, without considering the importance of the zonal hierarchical native AC organisation (Sun et al., 2016). For this purpose, multiple fabrication techniques were employed, as widely explained in the following *section 2.8*. Being AC a soft tissue, most of the literature work focused on building up a monophasic hydrogel-based network, as these are matrices offering several opportunities for producing organized tissues providing a physiological-like environment with properties similar to natural ECMs, such as high content of water, porosity, and cytocompatibility. Despite the great progress achieved in manufacturing tissue engineered scaffolds with biomaterials simulating the native AC tissue, these constructs can hardly mimic the tissue's microenvironment. Indeed, only few

information were obtained on the construct organisation at sub-millimetric scale. AC is anisotropic and highly organised with a spatial-varying structure, composition and mechanical properties and its depth-dependent organisation is fundamental for the overall biochemical and biomechanical properties of the construct (Klein et al., 2007). Thus, to obtain a biomimetic *in vitro* construct it is highly required to consider this heterogenous nature of the native tissue.

2.7.3 Zonal-engineered articular cartilage

In the last years, an emergent approach, based on the manufacturing of AC zonal-engineered *in vitro* models, is attracting the attention of the scientific community. Its primary goal is to recapitulate heterogenous functional, compositional, and structural features of the AC (**Figure 2.4**), to obtain an *in vitro* construct indistinguishable from mature cartilage with respect to: zonal organisation, biochemical composition, cellular morphology and mechanical properties (Sharma et al., 2007).

Different literature works have reported the creation of a partial and total zonal-engineered construct, investigating the cells source (i.e. chondrocytes harvested from different zones of native AC) or number (according to each native layer) (Brown et al., 2019; Kim et al., 2003; Klein et al., 2003; Ren et al., 2016b) and ECM composition (i.e. proteoglycans-based biomaterial to replicate the deep layer and aligned fibers to recapitulate the tangential zone) (Owida et al., 2018; Gegg & Yang, 2020; Brown et al., 2020b). Scaffold-free models have been manufactured for studying the zonal nature of AC, for example by Klein et al. which used chondrocytes subpopulation from superficial and middle layers of AC in monophasic or biphasic culture. Although they got insight into the importance of considering the zonal property of cartilage, the lack of scaffold and support lead to a construct with 20 x lower mechanical properties compared to fetal bovine AC (Klein et al., 2003). Walzer et al., instead, created a 3D architecture of collagen alignment in chondroprogenitors pellet cultures, resulting in the formation of zonally organized engineered hyaline cartilage, comparable to the 3 zones of native cartilage (Walzer et al., 2021). However, the size of the pellets is often too small to obtain a relevant size construct, and the zonal variations are spherical rather than depth-dependent. An alternative investigated by Shen et al, was the use of cell-sheet engineering approach, by stacking layers of superficial, middle, and deep zones chondrocytes to obtain a stratified construct with greater viability, proliferation and increased expression of chondrogenic markers compared to mixed cells construct (Shen et al., 2021).

Cell-free models were analysed as well, to evaluate some properties of AC zonal tissue. Liu et al., designed and 3D printed a tri-layered scaffold made of GelMA (15 % w/v) for the AC top layer, a combination of GelMA/nanohydroxyapatite (nHA) (20/3 % w/v) for interfacial layer, and a 30/3 % GelMA/nHA hydrogel for subchondral bone. The physico-chemical properties of the obtained construct showed to be appropriate for reproducing AC and SB tissues simultaneously (Liu et al., 2019). Also, Jia et al, developed a biomimetic multilayered scaffold including an oriented AC ECM-derived cartilage layer, a porous 3D printed PLGA/βtricalcium phosphate (PLGA/TCP) bone layer, and an intermediate PLGA/TCP compact interfacial layer. The obtained scaffold showed to be not only good as a template for osteochondral tissue regeneration, but it could also generate a smooth osteochondral interface with an integrated tidemark (Jia et al., 2018). Similarly, Girao et al. suggested a method for fabricating 3D biomimetic, anisotropic, multilayered fibrous scaffolds through electrospinning, PCL into three types of bulk materials with fibres aligned horizontally, randomly, and vertically, and then joined with graphene oxide collagen gel to make a multilayered scaffold. The measured parameters of each layer of the scaffold demonstrated that this is a reasonable strategy for designing and achieving fibre orientations and mechanical properties that are similar to native AC (Girão et al., 2018).

Lots of challenges are present within the existent models, for example the difficulty in distinguishing different zones in the native tissue for isolating chondrocytes and the relatively low availability of zonal chondrocytes or the poor integration and mechanical discontinuity between different layers made of different materials. **Table 2.7** reports chronologically the main studies regarding the manufacturing of cell and biomaterials-based zonal AC tissue with the related findings obtained.

MODEL	MATERIALS/CELLS/FABRICATION	OUTCOMES & LIMITATIONS
<u>Zonal model with respect to cell properties and phenotype</u>		
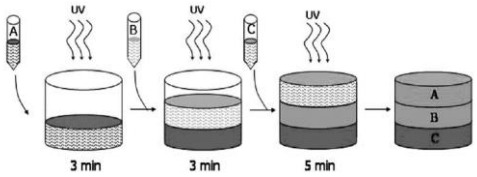 (Klein et al., 2003)	<u>Cells:</u> Chondrocytes from superficial (A), middle (B), deep (C) AC <u>Material/Fabrication:</u> UV-curable PEGDA (10 % w/v) gel **Biomimetic content:** Cell phenotype	⇧ Feasibility of isolation protocol ⇧ Cell viability and maintenance in the each layer of hydrogel ⇩ Single zones thickness and cell density. ⇩ Low availability of zonal cells ⇩ Biomechanical and structural AC engineering.
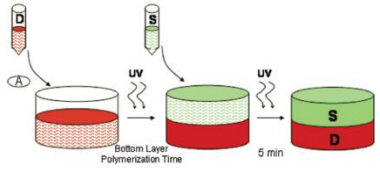 (Sharma et al., 2007)	<u>Cells</u>: Chondrocytes from superficial (S) and deep zone (D) or full thickness of AC (20 x10^6 cells/mL) <u>Material/Fabrication:</u> UV-curable PEOD (10 % w/v) gel **Biomimetic content:** Cell phenotype	⇩ Bilayered constructs demonstrated greater shear and compressive strength ⇩ Lack of demonstration of the interaction between layers.
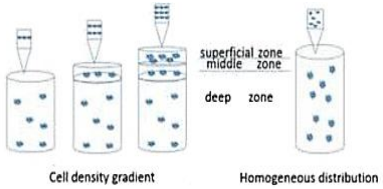 (Ren et al., 2016b)	<u>Cells</u>: Chondrocytes at 3:2:1 ratio from top to bottom of zonal model and one density in mono-phase gel <u>Material/Fabrication</u>: Bioprinting a biomimetic cells density gradient hydrogels (Coll II). **Biomimetic content:** Cell density/layers thickness	⇧ Optimised cells density and thickness of the layers ⇩ Lack of easily available and cheap materials ⇩ Difficult phenotype control ⇩ No compositional gradient
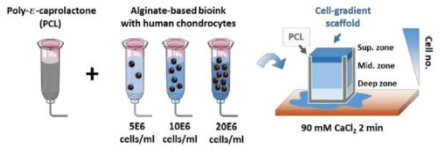 (Dimaraki et al., 2021b)	<u>Cells</u>: Chondrocytes 20, (superficial), 10 (middle), and 5 (deep) million cells/mL <u>Material/Fabrication</u>: Three phases 3D printing of: PCL as a supporting structure and Alg with different cells density for three zones of AC. **Biomimetic content:** Cell density/layers thickness	⇧ Smooth transition between the zones in terms of cell distribution ⇧ Higher sGAG deposition in the highest cell density zone ⇩ Single biomaterial ⇩ Other gradients should be considered

Zonal model with respect to matrix composition and orientation		
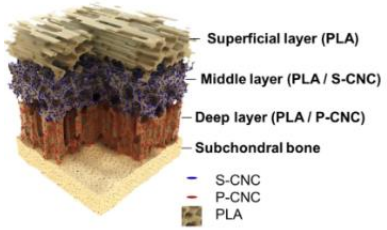 (Camarero-Espinosa et al., 2016)	Cells: Chondrocytes (3 million cells/cm^3) Material/Fabrication: DEEP: PLA and phosphate CNC - orthogonal pores; MIDDLE: PLA and sulphated CNCs; SUPERFICIAL: PLA - parallel tubular pores **Biomimetic content:** ECM composition and orientation	⇧ Good biomaterials gradient ⇧ After 2 weeks of culture, the constructs displayed mechanical properties comparable to the native. ⇩ Lack of cells density organisation ⇩ Post-fabrication cells seeding
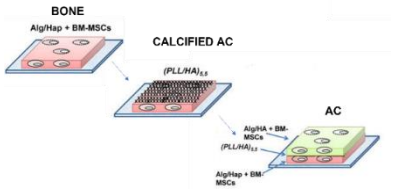 (Schiavi et al., 2018)	Cells: BM-MSC (3 × 10^6 cells/ml) Material/Fabrication: BONE: Alg/Hap gel (1.5 % w/v); CARTILAGE: Alg/HA gel (1.5 % w/v). CALCIFIED: 5.5 PEMs bilayers of PLL/HA. Construct exposed to daily intermittent compressions. **Biomimetic content:** Mechanical loading	⇧ Synthesis of specific matrix ⇧ Welded layers after 8 weeks ⇩ Not faithful choice of zonal adequate biomaterials and cells ⇧ Monophasic cartilage side
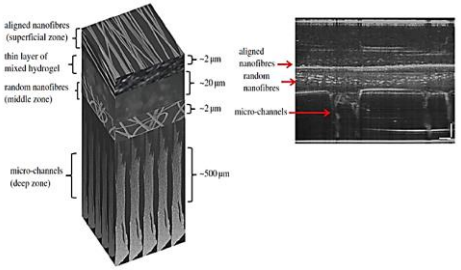 (Owida et al., 2018)	Cells: Chondrocytes Material/Fabrication: HA 10 % w/v in NaOH and PLA nanofibers: aligned in superficial layer, random in the middle, channels in the deep zone **Biomimetic content:** Fibril orientation	⇧ Optimised collagen organisation reproduction. ⇩ Cells density rationale. ⇩ Scalability of the fabrication technique ⇩ Difficulty to obtain high amount of primary cells.

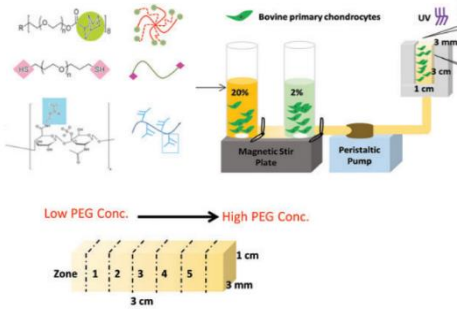 (Zhu et al., 2018)	<u>Cells</u>: Chondrocytes <u>Material/Fabrication</u>: Gradient hydrogel of PEG (20 – 2 % w/v) and 25 % CS-MA **Biomimetic content:** Mechanical stiffness gradient	⇧ Gradient hydrogel with stiffness ranging from 2 to 60 kPa ⇧ Stiffness-dependent upregulation of cartilage markers ⇩ No compositional gradient and cells organisation
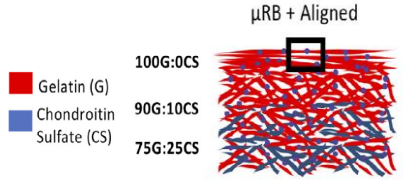 (Gegg & Yang, 2020)	<u>Cells</u>: MSCs <u>Material/Fabrication</u>: Photopolymerisation of Gel/CS gel. DEEP: 75Gel:25CS + unaligned µRB; MIDDLE: 90Gel:10CS +unaligned µRB; SUPERFICIAL: 100Gel:0CS + aligned µRB **Biomimetic content:** ECM composition, fibril orientation; pore properties	⇧ Optimised composition with aligned fibers on top layer helped the production of proper AC ⇩ Needs to be exploited with chondrocytes ⇧ Lack of zonal structural design and cells density
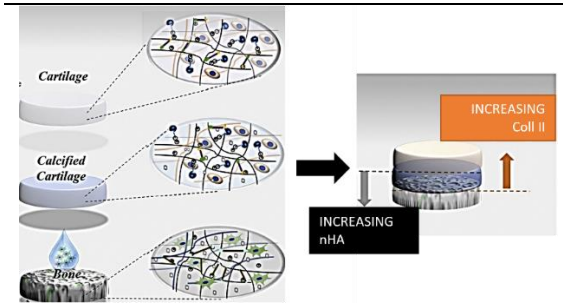 (Korpayev et al., 2020)	<u>Cells</u>: MC3T3-E1 preosteoblasts and ATDC5 chondrocytes <u>Material/Fabrication</u>: BONE: freeze drying of: CH(2 % w/v), Coll I (20:80 with respect to CH), nHA (1 % w/v); CALCIFIED: CH, Coll II, nHA by using thermal gelation; CARTILAGE: Thermal gelation of CH/Coll II (50:50) **Biomimetic content:** ECM composition, mechanical properties	⇧ Stratified scaffold displayed a compact structure and no separation between the layers ⇧ Cells maintained the phenotype in each zone. ⇩ Lack of cartilage zonal structure

Table 2.7: Report of the most relevant zonal-engineered AC *in vitro* model exploited from 2003 to 2021, with schematic of the model, methodology and findings.

2.8 Fabrication techniques

The design of an ideal *in vitro* cartilage is still a hard challenge in TE field and the selection of the raw materials, and their processing technique is a crucial issue to be addressed. The shape, porosity, and mechanical properties of ideal construct are not only related to the qualities of the materials employed (highlighted in *section 2.5*) but are also directly tied to the manufacturing procedures used for mimicking the complicated multi-layered microstructure of real AC tissue. Novel technologies, or a combination of techniques, are required for the fabrication of multilayered scaffolds for AC TE (Fu et al., 2020).

2.8.1. Electrospinning

Electrospinning is a technique for producing micro and nanofibers from a polymeric solution. In TE, fibrous scaffolds have become quite popular: the fibres provide a wide surface area for cell adhesion, as well as interconnected pores for the exchange of nutrition within the scaffold (Ma & Zhang, 1999). Electrospun nanofibrous structures have been intensively investigated because they can imitate the hierarchical architecture of ECM. Furthermore, the nanofiber configuration can be tweaked.

Electrospinning technique uses high electrostatic forces to create polymer fibres: the formation of fibres starts when a critical potential is achieved, and the jet solution is ejected from the Taylor cone and deposited on the collector. There are four main components necessary for this technique: direct current power supply, a metallic needle with a blunt tip, a syringe for containing the electrospun solution, and a grounded conductive collector (**Figure 2.13A**). Aside from the basic setup, many elements can influence the fibre preparation (**Figure 2.13B**):

(i) Process parameters. The applied voltage has a fundamental role for starting the electrospinning process and it has effect on the resulting fibers dimension and morphology. Some authors reported a decrease of resulting fibers length and diameter and a better morphology with the obtainment of uniform fibers, with the increase in voltage. However, others reported opposite results when the voltage overpass a critical value (depending on the polymer-solvent system). Typically, it is used a voltage of 20 - 25 kV between the nozzle and the collector. The solution flow-rate affects the drying of fibres and, hence, their morphology and size of pores: an increase beyond a certain point can result in the beads formation due to lack of drying. The work distance (between tip and collector) has a substantial impact on the fibre diameter by affecting

the drying process and it usually is 10-20 cm (Sill & von Recum, 2008). The collector serves as a conductive substrate for collecting the charged fibres and its conductivity affects the arrangement of the fibres; a collector with a low conductivity allows the deposited fibres to detain some of their charges, causing a repulsive effect on the incoming fibres. Flat aluminium collectors are commonly utilised, or porous metals with varying porosity and pore shape, wire mesh, pin, grids, liquid bath, rotating disc (Yilmaz & Zeugolis, 2020). The collector shape is another element which plays an important role: it is usually a stationary plate, although advances in engineering have allowed the use of a rotating cylinder. Fibres orientation, which is important for seeded cell growth direction, depends mainly upon the collector: a static plate collector can be used for random orientation fibres and a rotating collector for aligned nanofiber (**Figure 2.13C**).

(ii) Solution parameters. If the polymer solution concentration is too low, the fibres will break up and form rings, discs, and beads before reaching the collector, while if the solution concentration overpass a critical level, the capillary tip becomes blocked, resulting in undesirable beaded polymer fibres. The viscosity of the polymer solution is also important to provide smooth fibres, as well as the conductivity of the polymer solution, since the electrospinning process is dependent on the charges accumulating in the polymer solution. The diameter of the fibres decreases as the conductivity of the polymer solution increases (Haider et al., 2018). It has also been demonstrated that chain entanglements in the polymer solution, related to the length of the polymer chains and their conformation, and electrospinnability are related. Finally, the solvent plays an important role: good solvents are those in which polymer–solvent interactions are favoured, in contrast to polymer–polymer self-interactions (Shenoy et al., 2005).

(iii) Environmental parameters. Temperature, humidity, pressure, and type of atmosphere. Affect the diameter and shape of the fibres (Narkhede & Rao, 2017).

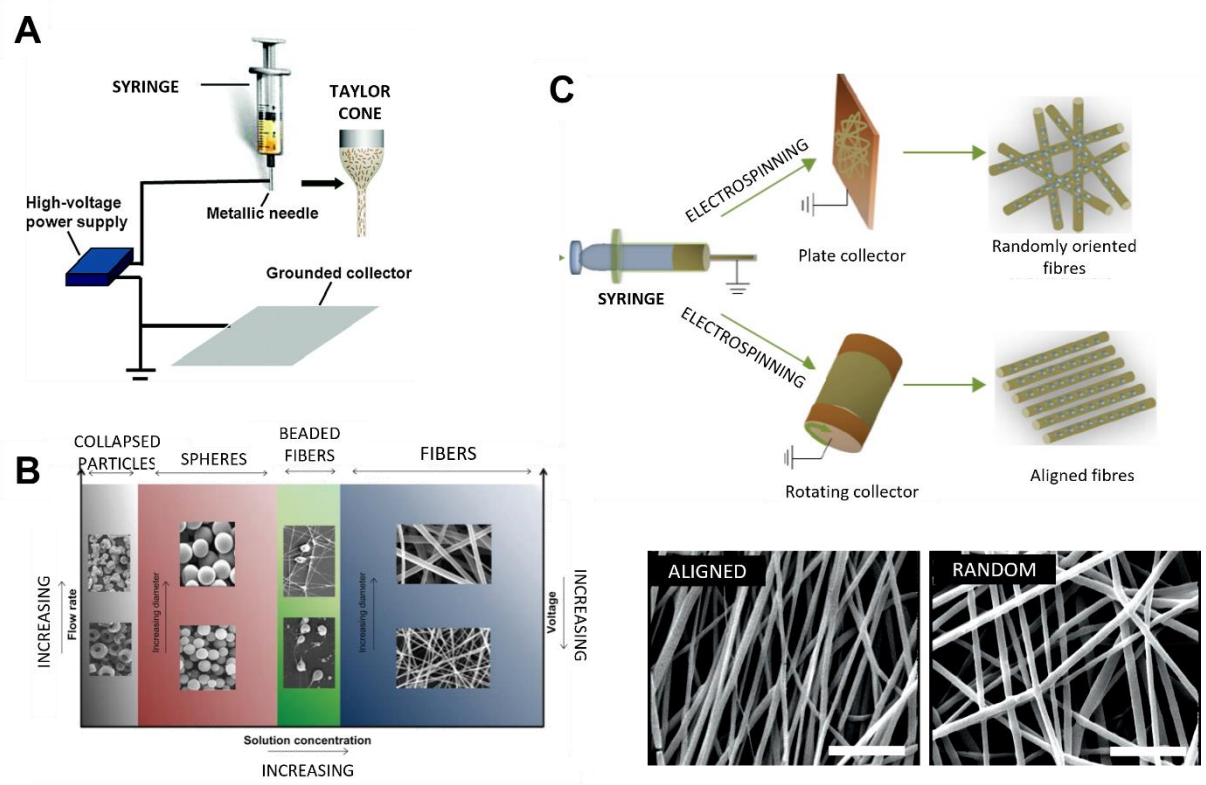

Figure 2.13: Representation of electrospinning process and Taylor cone (**A**). Schematic illustration of the effect of the concentration, flow rate, and voltage on electrosprayed/ electrospun nano/microstructures (**B**). Electrospinning process for the obtainment of Random (using a plate collector) or aligned (using a rolling collector) fibers. Bars=10 µm.

A variety of materials were used for electrospinning including natural and synthetic. Regarding AC TE, the main natural polymers used were Coll II, CH, GEL and keratin (Yilmaz & Zeugolis, 2020). However, to prevent them from degrading in the harsh solvents used in the electrospinning process (Hexafluoroisopropanol, Methylene chloride, Trifluoroethano, Sodium dodecyl sulfate), they must be heavily cross-linked, which can result in cytotoxicity *in vitro*. On the other side synthetic polymers (PCL, PLA, PGA, PLGA, PLLA) are often stronger than natural polymers and can withstand electrospinning without notable losses and have a predictable biodegradability. However, there are some drawbacks for synthetic polymers as abovementioned. Therefore, synthetic polymers electrospinning can be followed by a functionalisation phase or synthetic polymers can be electrospun together with natural polymers to obtain a composites scaffold. For example, Ren et al. electrospun an aligned porous fibrous scaffold made of PLLA which was functionalised with CS via polydopamine coating for promoting the chondrocytes growth and chondrogenic activity (Ren et al., 2019). He et al., instead proposed a composite electrospun membrane made of PCL and GEL as a co-culture platform for MSCs and chondrocytes towards AC regeneration (He et al., 2015). Another interesting method was applied by Levorson et al., who electrospun a scaffold

containing micro and nanofibers of fibrin and PCL, obtaining good cellular response in terms of cells viability and cartilage regeneration (Levorson et al., 2014).

Since electrospinning technique is very promising due to its high versatility (e.g., ability to produce functionalised nanofibrous scaffolds with a variety of orientations, sizes, and mechanical properties), it could be used for producing biomimetic multilayered scaffolds.
Munir et al. developed a three-layer AC scaffold: an aligned electrospun superficial zone, a random electrospun intermediate zone, and a cryo-printed deep zone. Indeed, aligned nanofibres reproduce AC superficial zone with parallel fibres, whereas a random nanofibre configuration, for example, mimics collagen distribution in the middle zone. The multilayered scaffold was discovered to induce the expression of AC key genes and allowed the identification of sulphated GAG when compared to controls. In comparison to the electrospun and control scaffolds, the multilayered scaffold possessed compressive properties that were more akin to those of native cartilage. Furthermore, the cryo-printed deep zone of the multilayered scaffold provided an appropriate starting platform for cartilage defect healing, affecting cell adhesion and stress (Munir et al., 2020). Similarly, as already reported in **Table 2.7**, Girao et al. suggested a method for fabricating 3D biomimetic, anisotropic, multilayered fibrous scaffolds. PCL was electrospun into three different bulk materials with fibres arranged horizontally, randomly, and vertically, and then bonded with graphene oxide collagen gel to create a multilayered scaffold. The features of each layer of the scaffold were measured, demonstrating that this is a viable technique for creating and achieving cartilage-like fibre orientations and mechanical properties (Girão et al., 2018).

2.8.2 Soft lithography

In the scientific world microfabrication and nanofabrication are becoming essential manufacturing technique. In microfabrication, lithography, or the transfer of a pattern to the substrate/surface of a layer, is a critical production step that is often accomplished by photolithography. Despite being a well-established technology, photolithography has difficulties such as limited feature size due to optical diffraction, the need for high-energy radiation for microscopic features, and the expensive cost of complex apparatus needed. It also can't be used on non-planar surfaces. Soft lithography is a simple and low-cost technology which works with a wide range of materials and has a huge surface area. It is a supplement to photolithography by addressing its disadvantages (Lakshminarayanan, 2018). An elastomeric stamp with patterns as negative structures on its surface is a vital component of soft

lithography. The stamp is normally made by casting a liquid precursor against a master having complementary structures patterned on its surface. The capacity of an elastomeric stamp to transmit a pattern with high fidelity is determined by its mechanical qualities: most literature research exploited silicone-based rubber or cross-linked Polydimethylsiloxane (PDMS) Sylgard 184 for stamp production with feature sizes greater than 500 nm. PDMS, firstly developed by Whitesides in 1998 at Harvard, is a Si-based organic polymer widely explored due to its biocompatibility, high flexibility (viscoelasticity), high chemical inertness, optical transparency, and adhesion to metals (Qin et al., 2010; Jana et al., 2016).

Thus, soft lithography with PDMS is widely used to produce patterned scaffolds and there are different types of this technique, with the replica moulding (REM) being the most exploited for biomedical application. REM is a suitable technique for producing several replicas from the same substrate with a good resolution; it allows to pattern large areas, rapidly and onto non-planar surfaces. In **Figure 2.14** are reported the major steps of the procedure generally followed:

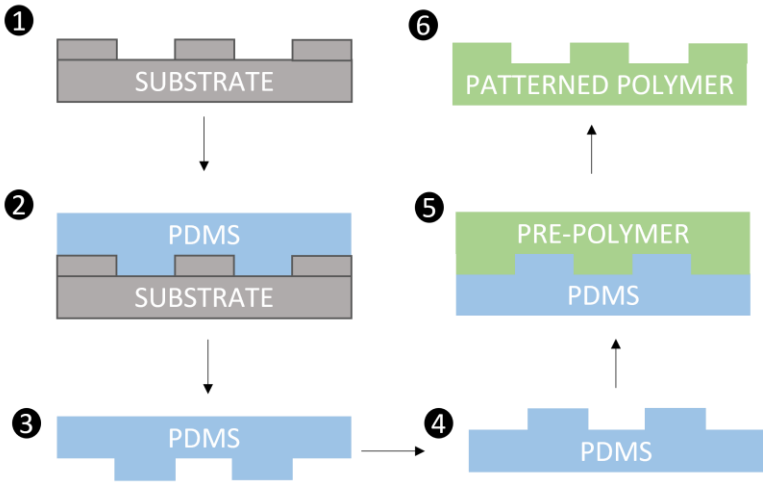

Figure 2.14: Schematic illustration of the procedures for obtaining a patterned polymer by starting from a positive substrate via PDMS via soft lithography technique: the desired pattern is designed with a computer-aided design (CAD) software program and the topographically patterned substrate (which will have the same pattern of the final desired structure) is manufactured (e.g. via 3D printing) (1); liquid PDMS, mixed with curing agent, is poured onto the micropatterned master substrate and thermally cured (2-4); the PDMS pattern is transferred back into a replica of the original master by solidifying a liquid prepolymer such as UV-curable or thermally curable hydrogels precursor, against the soft PDMS mould (5-6).

2.8.3 Fusion deposition modelling

Additive manufacturing (AM) is a method of building up a structure by joining material together by deposition layer-by-layer. The basic principle that underpins nearly all AM

techniques (vat polymerization, material jetting, binder jetting, material extrusion, sheet lamination, powder bed fusion and directed energy deposition) is the creation of a virtual solid model, which is then broken down into a series of two-dimensional (2D) cross-sections and transferred to an AM machine, where it can be combined layer by layer to create the physical 3D hierarchical structures (Vyavahare et al., 2020; Fu et al., 2020). The steps of additive manufacturing are:

1) Creating a 3D CAD object;
2) Converting it into the standard format of Standard Tessellation Language (STL);
3) STL file is imported in slicing software to slice the object in different layers. Here, the printing parameters can be modified (material deposition plane, envelopes number of the parts and their thickness and filling patterns, printing speed and pressure);
4) The file obtained from the slicing software is then used in a printer to print the final object.

Fused deposition modelling (FDM) is the most popular among all techniques because of its low printer cost and the fact that it requires minimal technical skills to operate. This is a fast, versatile, low-cost, and widely used 3D printing approach that fabricates a complex-shaped item quickly and easily. Material extrusion via FDM was patented by Crump in 1988. This technique is based on the extrusion of a feedstock melt filament provided by the device which is controlled by an electric motor. The melted filament is pushed through the fusion printhead towards the nozzle and the nozzle deposits this melt along the X,Y plane on the printing platform. The platform moves down or print head moves up along the Z direction by exactly one layer thickness after the completion of deposition at the successive cross-section. Thus, 3D structures are created in a layer-by-layer routine.

All the polymers having a stiffness of 1 GPa and a processing temperature higher than the transition temperature, but lower than the degradation temperature, can be used for FDM (e.g., PLA, PCL, Ethylene vinyl acetate (EVA) and acrylonitrile butadiene styrene (ABS)) (Chaunier et al., 2018). Amongst them, PLA, being highly processable, biodegradable and user-friendly, is the most widely used bioplastic, generated from the starch of agricultural plants such as corn. PLA is a thermoplastic aliphatic polyester generated by ring-opening polymerization of lactide or polycondensation of lactic acid monomer and is one of the most studied thermoplastic aliphatic polyesters. PLA is available in semicrystalline and amorphous forms. Pure L-lactic or D-lactic acid (PLLA or PDLA) is semicrystalline, whereas PLA made up of

50–93 % L-lactic acid is amorphous. When compared to crystalline PLA, amorphous PLA has higher processability but poor mechanical characteristics. PLA is a potential thermoplastic for FDM, because of its low glass transition temperature (Tg = 60°C - 65°C) and melting temperature (Tm = 173°C - 178°C), reduced coefficient of thermal expansion, and non-adherence to the printing surface. Several literature works have been focused on FDM with PLA for multiple application in TE field. Regarding bone TE, PLA was 3D printed alone or in combination with some molecules (for example with the addition of nHA to increase its bioactivity) by obtaining optimal porous scaffold with suitable compressive strength was significantly higher than those of pure HA ceramic scaffold and cancellous bone (Zhang et al., 2021).

Even though 3D printing has been used for fabrication of *in vitro* tissues such as bone, bladder and trachea, the obtained constructs are mainly 3D structures covered by cells, rather than an organised 3D environment populated by cells in an organised manner (Scalzone et al., 2021a).

2.8.4 Bioprinting technology

Recent advantages in 3D printing and its combination with cell biology and material science allowed the development of bioprinting technology. This approach, by printing cells-loaded inks, have enabled the generation of complex *in vitro* 3D tissue models, that can further recapitulate native tissues physiology with the potential of focusing on their organisation at cellular level, provided via both construct design and controlled deposition of cells at predefined locations (Scalzone et al., 2021a). 3D Bioprinting together with Bioassembly is a biofabrication methodology.

Bioassembly is defined as the fabrication of hierarchical constructs with a prescribed 2D or 3D organization through automated assembly of pre-formed cell-containing fabrication units, generated via cell-driven self-organization or through preparation of hybrid cell-material building blocks, typically by applying enabling technologies, including microfabricated molds or microfluidics (Woodfield et al., 2017).

Bioprinting is defined as the use of computer-aided transfer processes for patterning and assembling living and non-living materials with a prescribed 2D or 3D organization to produce bio-engineered structures serving in regenerative medicine, pharmacokinetic and basic cell biology studies. This layer-by-layer technology makes it possible to spatially pattern cells, bioactive factors, and biomaterials in 3D. Bioprinting, intended as the use of ‘bioink’, a formulation of cells that is suitable to be processed by an automated biofabrication technique,

to print living cells within a material construct, is an evolving aspect of 3D printing technology (**Figure 2.15A**). This technique combines the features of 3D printing such as the complete control over the design, fabrication and modelling of the construct being manufactured with the possibility of incorporating and precisely depositing living cells and biological cues in the 3D space to obtain well- defined geometries with gradient composition of biomaterials and cells. Additionally, by printing with multiple bio-inks, a zonally organized constructs can be generated.

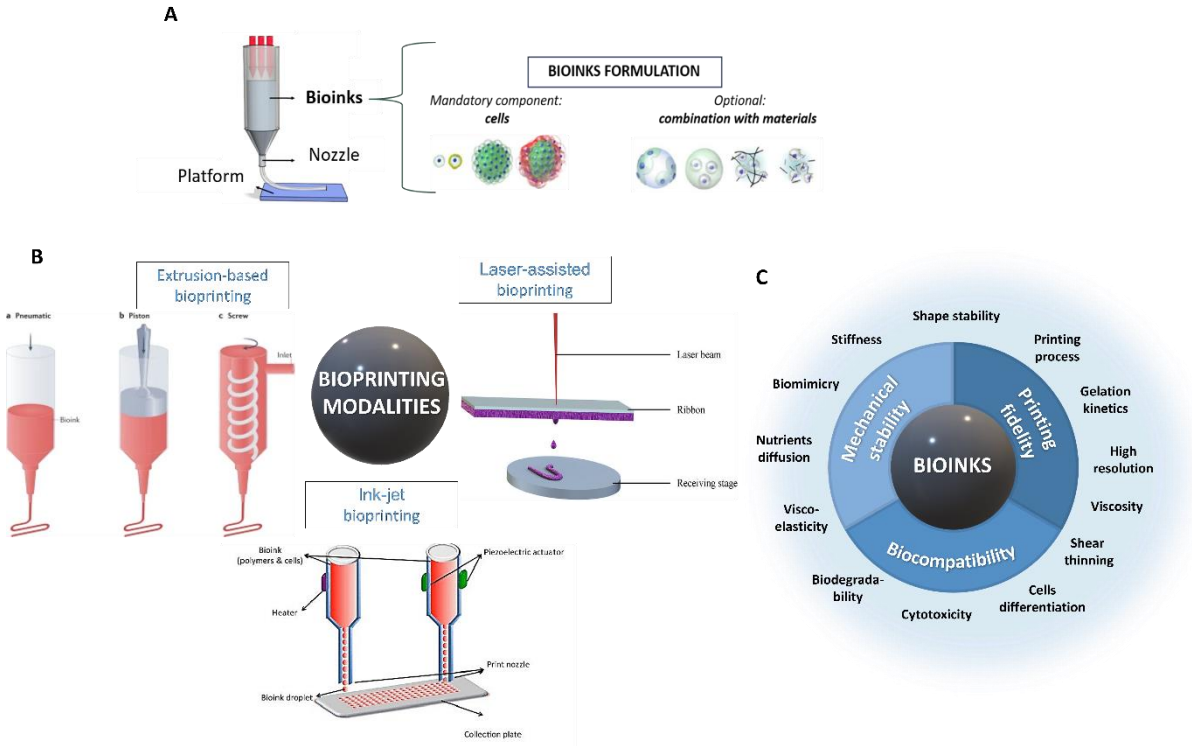

Figure 2.15: Bioprinting fabrication technique. Illustration of bioprinting technique and bioinks formulation, which has cells as mandatory component and materials as optional element (**A**); Modalities of bioprinting processes: extrusion-based bioprinting, laser-assisted bioprinting, ink-jet bioprinting (**B**); Biomaterial properties for an ideal bioink in order to respect the biofabrication window for the rational design of bioinks, based on three parameters: printability; biocompatibility and mechanical stability (**C**).

Few additive manufacturing techniques can be used to 3D bioprinting biological constructions by distributing cell-laden bioinks, which necessitates a cytocompatible deposition procedure. Laser-assisted, inkjet, and extrusion bioprinting are the three most researched approaches for direct bioprinting, according to the literature (**Figure 2.15B**). The main feature of each technique is explained in the **Table 2.8**.

PARAMETERS	INK-JET	EXTRUSION-BASED	LASER-INDUCED
Bioink viscosity	up to 12 mPa/s	up to $6x10^7$ mPa/s	up to 300 mPa/s
Cell density	< 10^6 cells/mL	up to 10^7 cells ml^{-1}	Up to 10^8 cells/mL
Cell viability	> 85 %	40-90 %	> 95 %
Resolution	10-50 µm	200-1000 µm	10-100 µm
Printing speed	$1x10^5$droplet/s	10 µm/s-700 mm/s	200-1600 mm/s
Gelation mechanism	Chemical, photocrosslinking	Chemical, photocrosslinking, thermal	Chemical, photocrosslinking
Costs	Low	Medium	High

Table 2.8: Overview and comparison of the mainstream techniques and specifications for the biofabrication of 3D constructs.

- Inkjet printing ejects bioinks droplets via a nozzle by either thermal energy application (electrically heating to produce vapour bubbles that force droplets to come out through the nozzle) or a piezoelectric actuator (actuation of piezoelectric crystals by applying high-frequency electrical energy). This is an inexpensive, high-throughput and reproducible technique which allows to create picolitre-sized drops and has a printing resolution of 20–100 µm. However, this can be a disadvantage because the printed constructs may not give appropriate structural support. Fabrication of huge 3D structures is a difficult barrier to overcome in transferring inkjet printing to organ printing (X. Li et al., 2020).
- Extrusion systems are used in robotic dispensing procedures, which leads in more stable 3D cell-laden structures. This technique uses air pressure (pneumatic) or mechanical mechanisms to push cell-encapsulated hydrogel filaments through the nozzle (piston or screw). However, because of lack of structural support, integrity, mechanical stability and printability, large free-form tissue structures are difficult to create. Extrusion bioprinting causes shear stresses in the viscous fluids that hold the cells. As a result, dispensing pressure has a greater impact on cell survivability than nozzle diameter, with resulting poorer cell vitality than ink-jet bio-printing (Murphy & Atala, 2014).
- Laser-induced approach directs high-pressure laser pulses onto the donor slide, causing droplets of cell-encapsulated hydrogels to fall onto the collector. This nozzle-free

technique allows to print cells with extreme precision in small constructions without compromising viability or cellular function; also, it can use a wide range of materials (viscosity from 1 to 300 mPa s^{-1}), but it necessitates rapid gelation hydrogels to generate high-resolution printed patterns. There are still limitations in terms of homogeneous cell distribution because the technology necessitates a quick gelation phase to get the correct form and size. Overall, fabricating big 3D constructions is a time-consuming process, which limits its usage in several clinical settings (Ventura, 2021).

For the printing of AC tissue, extrusion-based printing techniques are most often considered since its high economic efficiency, ease of operation and flexibility to a wide range of materials (Wu et al., 2021).

As mentioned before, the most promising carrier materials, for cell-based 3D bioprinting are hydrogels, as they facilitate homogeneous cell encapsulation in a highly hydrated and mechanically supportive 3D environment (Zhu, Gong, Liu, et al., 2017). Hydrogel prepared for extrusion printing must be viscous enough to keep its shape fidelity during printing, to avoid tension driven droplet formation at the nozzle tip for extrusion of continues filaments and must have cross-linking abilities allowing for it to retain the 3D structure after printing. Cross-linking can be induced chemically (e.g. Ca ion to cross-link alginate), thermally, or using UV or visible light with the addition of appropriate initiators. Also, several studies have been conducted on bioinks formulations based on natural polymers, such as collagen, GEL, HA, CS and alginate (Murphy & Atala, 2014), by evaluating the following three primary characteristics (**Figure 2.15C**): biocompatibility, printability, and mechanical stability. Indeed, the chosen bioink should be: (i) printable: flowable or deformable, and able to be deposited precisely with good spatial, temporal, and volumetric control; (ii) able to preserve cell viability during the printing process and support cell viability and functions post-printing until tissue regeneration is complete; (iii) an ideal ink to be printed for the fabrication of high-resolution complex structures; (iv) possess mechanical properties to allow both post-printing and pre-printing mechanical manipulation and cells sustainment. The interplay between the diverse features of bioinks is crucial in achieving a balance among these criteria (Scalzone et al., 2021a). A summary of the properties found in literature studies on different materials in terms of printability, printing technique exploited, and crosslinking mechanisms is reported in **Table 2.9** (Ashammakhi et al., 2019; Murphy & Atala, 2014; Hospodiuk et al., 2017).

POLYMER	TECHNIQUE	PRINTABILITY	CROSSLINKING	REF.
Agarose	IJ, EB, LAB	+	T	(Duarte-Campos et al., 2013)
Alginate	IJ, EB, LAB	+	I	(Datta et al., 2020)
CH	EB	-	I,P	(Tonda-turo et al., 2020)
Collagen	IJ, EB, LAB	+/-	T	(Osidak et al., 2020)
dECM	EB		T	(Hospodiuk et al., 2017)
Fibrin	IJ, EB, LAB	-	E	(Cubo et al., 2017)
GEL	IJ, EB, LAB	-	C, E, T, P	(Schwartz et al., 2020)
GG	EB	+	P, I	(Mouser et al., 2020)
HA	EB	-	E, P, C	(Ashammakhi et al., 2019)
PEG	IJ, EB, LAB	+	P, C	(Xin et al., 2019)
Pluronic	IJ, EB	++	T, C	(Gioffredi et al., 2016)

Table 2.9: Overview of polymers suitable for cell-encapsulation, their crosslinking mechanism, bioprinting technique and relative advantages and disadvantages. Abbreviations: Photocuring (P), Enzymatic (E), Covalent (C), Ionic (I), Thermal (T).

Considering AC applications, Daly et al. evaluated the effects of various bioinks on MSCs behaviour, finding that alginate and agarose bioinks supported more hyaline-like cartilage tissues formation compared to GEL-metacrylate (GelMA)– and poly(ethylene glycol) methyl ether methacrylate (PEGMA)– based bioinks that supported more fibrocartilaginous tissue production (Andrew et al., 2016). Often bioinks are multi-materials formulations. Constantini et al. assessed 3 different formulations of hydrogel for scaffold-based bioprinting of cartilage tissue, which were (1) GelMA, (2) GelMA and CS amino ethyl methacrylate (CS-AEMA), and (3) GelMA, CS-AEMA, and HAMA. Each bioink also contained alginate to aid in stable fiber formation during bioprinting and was loaded with MSCs. GelMA and CS-AEMA have been observed to be the best in chondrogenic formation with the highest Coll II vs. Coll I and Coll X ratios (Costantini et al., 2016). Also, Mouser et al. analysed the effect of GG on GelMA bioink at various concentrations discovering that a concentration of 10/0.5 % GelMA/GG balanced the bioprintability and construct stiffness that impacted cell incorporation (Mouser et al., 2016).

A limitation of using hydrogels is their poor mechanical properties. Co-depositing hydrogel bioinks within fused deposition modelling of thermoplastic polymer, in order to reinforce mechanically cell-laden hydrogels, have been successfully explored. For example, Dimaraki et al. fabricated fabricate scaffolds with three-zone cell density using bioprinting with an alginate-based bioink containing human articular chondrocytes and a PCL support structure, which was fundamental for helping in the maintenance of the structural integrity of the scaffolds during bioprinting and subsequent *in vitro* culture (Dimaraki et al., 2021a).

2.9 *In vitro* model of Osteoarthritis

The goal of generating reproducible and reliable *in vitro* OA models, able to mimic disease complexity, is double: to gain a better knowledge of the illness and to test potential treatment modalities for proof-of-concept studies. There are three different approaches studied in literature for inducing OA:

-Chemical: variety of enzyme types have been used to simulate the ECM degradation seen in human OA, such as collagenase, trypsin or chondroitinase. Also, because the inflammatory environment is a typical hallmark of OA, which activates several catabolic processes, most of the OA *in vitro* model of are based on reproducing this inflammation. To date, numerous biological sources of inflammatory stimuli have been identified, including the use of cytokines, synovial fluid from OA patients, activated macrophages and macrophage-conditioned mediums or EVs from OA cells. At this regard, one of the most frequent strategies, for inducing inflammation, is to use exogenous cytokines in *in vitro* systems (Johnson et al., 2016). From literature, it appears that the cytokines which most influence OA pathogenesis, as explained in *section 3.3.3* are: (i) IL-1β, which was found to inhibit Coll II and PGs and stimulate the production of MMP1,3,13, (ii) IL-6 to activate NF-kB pathway and down-regulate the enzymatic antioxidant defences in chondrocytes with mitochondria disfunction (Fan et al., 2007; Löfgren et al., 2018; Mathy-Hartert et al., 2008); (ii) TNF-α, which can activate the NF-kB pathway, increase the expression of MMPs and inhibits anabolic molecules, and stimulates chondrocytes apoptosis (Meliconi et al., 2013).

- Mechanical induction, via injurious (i.e. biopsy punch and scalpel) or excessive mechanical loads to AC explants in order to initiate damage or hyper physiological (30 % confined compression) compression triggers a shift in cartilage homeostasis towards catabolism and inflammation (Bartolotti et al., 2021). Since OA is often localised to weight-bearing AC, mechanical injuries were proposed as one of the primary initiators of the disease. De Vries-

van Melle et al. developed an *in vitro* osteochondral model to study mechanisms involved in cartilage repair by creating defects of different depths using a dermal biopsy punch and scalpel (de Vries-van Melle et al., 2011), while Lin et al. applied a cyclical loading on cartilage explants with 1 and 5 MPa, and observed progressive changes in cell viability, collagen cleavage and proteoglycan loss after 24 hours (Lin et al., 2004). The cyclic compressive load was exploited as well by Ravalli et al. in a 3D culture of bovine chondrocytes in alginate beads, resulting in the induction of hypertrophic phenotype in cells by the release of RUNX2 and Coll X (Ravalli et al., 2020). Similarly, Thibault et al. subjected cartilage explants to high, but physiological cyclic load levels and characterized the resulting damage using a sequence of unconfined compression stress relaxation tests (Thibault et al., 2002). This mechanically induced *in vitro* degradation model resulted in collagen cleavage with a concomitant increase in matrix permeability. Finally, the physical removal of the superficial zone of AC in order to increase ECM permeability and deformation (phenomena that occurs at the early stages of the disease), is an alternative way to induce OA (Torzilli et al., 1983).

-Biological induction, by using directly osteoarthritic chondrocytes to obtain a more *in vivo*-like environment where these cells undergo a different behaviour compared to healthy ones (Sanchez et al., 2005; Li et al., 2012; Yeung et al., 2018).

Each approach contains some limitation, for example the concentration of cytokines used for *in vitro* studies are lower than the once detected in synovial fluid of OA patient, therefore it is hard to obtain a faithful representation of the native OA environment. On the other side, the use of synovial fluid would allow just a reduced number of experimental studies, because of its biological variability. Conversely the exploitation of co-cultures with macrophages was discovered to closely mimic the early stage of OA. Mechanical-induced OA *in vitro* model have the drawback of the difficult repeatability and standardisation of the process when imposing an injurious load. The use of OA chondrocytes, as well, has some drawback such as the low availability of OA cells from patients, which excludes the possibility of obtaining a standard production of reproducible models (Bartolotti et al., 2021).

To date most of the OA *in vitro* models exploited are 2D monocultures or co-culture and explants. Although monocultures are suitable for screening the effect of some chondroprotective compounds and co-cultures have been fundamental to investigate cell-cell communication as well as the chondroprotective role of MSCs on chondrocytes during OA

progression, 2D models do not reliably reproduce the physiological condition due to the lack of ECM environment and altered cells morphology. On the other side, while explants models clearly provide advantages over monolayer culture, particularly in terms of tissue interactions, yet there are still flaws that must be addressed when employing these models, such as cells death at the edges of the surgical cut, as well as the low availability of explants from the same biological sample. Indeed, changes in the sources could provoke adverse reactions. Therefore, 3D models of OA, while showing the benefits of 2D culture, additionally these provide a customisable environment which is more comparable to physiological conditions, allowing the study of cell-cell interaction, cell-matrix interaction, and cell response to OA-inducing stimuli (Samvelyan et al., 2020).

Given all these limitations, to date, no *in vitro* model has proved to be the gold standard for OA research and therapeutic testing (Craig I. Johnson et al., 2016).

Chapter 3. General methodology

In this chapter, the main methodologies involved in this PhD work are reported, while specific experimental technique used only in one chapter have been reported there.

3.1 Biomaterials synthesis

3.1.1 Gellan gum Methacrylate (GGMA)

The synthesis of Gellan Gum Methacrylate (GGMA) was obtained by reacting Gellan Gum (GG) (Gelrite® CM, Molecular Weight (MW) = 1.000.000 g/mol, Sigma Aldrich, UK) with Methacrylic Anhydride (MA) (Sigma Aldrich, UK), with an optimised protocol, in line with the methodology proposed by Coutinho *et al* (Daniela F. Coutinho et al., 2010) (**Figure 3.1**). First, a TRIS buffer solution (1 M) was prepared by adding 12.11 g of Tris base (Trizma® base, Sigma Aldrich, UK) to 80 mL of distilled water (dH_2O) under stirring. Hydrochloric acid (HCl) (1 M) was slowly added to adjust the buffer pH to 8.5; to reach a final volume of 100 mL, the solution was filled with dH_2O. The pH stability was monitored by utilizing a digital pH-meter (FiveEasy® Plus pH/mV bench meter, Mettler Toledo). Then, the solution was warmed up to 90 °C and then, GG powder was added (1 % w/v) and let dissolve for approximately 30 min, under stirring. Following, MA (8 % w/v) was added to the GG solution, when the solution reached 50 °C, and the reaction was continued for 5 hours, while the pH was monitored and continuously adjusted to 8 - 8.5 with the dropwise addition of sodium hydroxide (NaOH) (1 M). The obtained GGMA solution was purified by dialysis against distilled water for at least 3 days, using dialysis cellulose membranes with MW cut-off (MWCO) of 11 - 14 kDa, to remove un-reacted MA. Then, GGMA solution was stored at -20 °C overnight and subsequently lyophilised for 72 h in a freeze-dryer (Alpha 1–2 LDplus, CHRIST, Germany) at -50 °C and 0.04 mbar, and stored in a vacuum chamber.

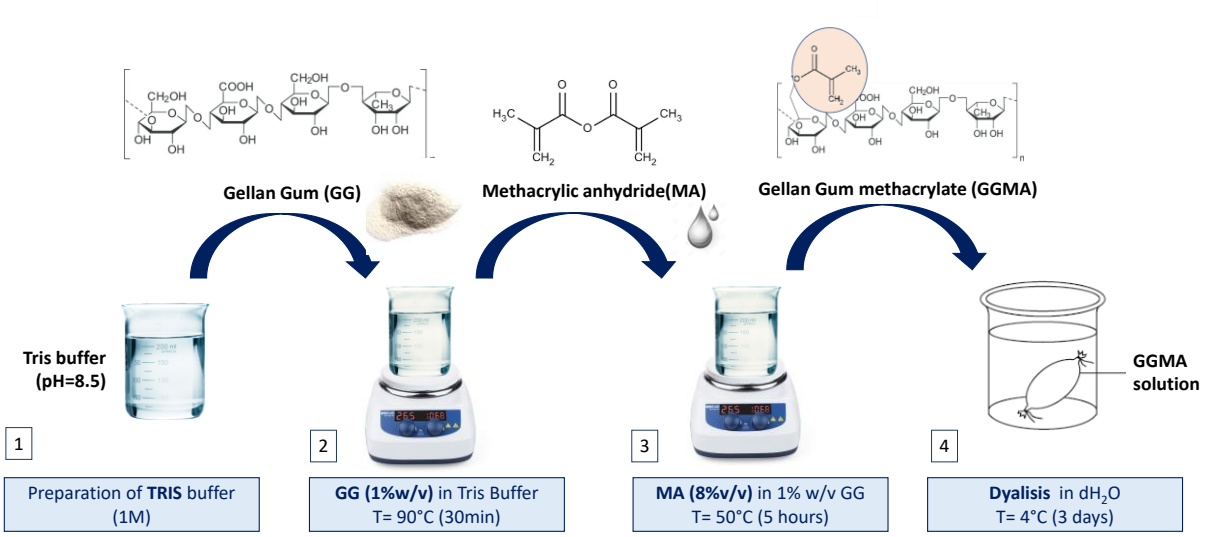

Figure 3.1: Schematic representation of the GGMA synthesis process.

3.1.2 Chondroitin sulfate Dopamine (CSDP)

The synthesis of CSDP was obtained dissolving 5 g of Chondroitin 4-sulfate sodium salt from bovine trachea (CS) (MW = 515.376 g/mol, Sigma Aldrich, UK) in 50 mL of activation buffer solution composed by 0.1 M of 2-(N-Morpholino) ethane sulfonic acid (MES) (MW = 195.24 g/mol, Sigma Aldrich, UK) and 0.5 M of sodium chloride (NaCl) (MW = 58.44 g/mol, Sigma Aldrich, UK) at pH 6. Following, 1.82 g of 1-Ethyl-3-(3-dimethylaminopropyl)-carbodiimide hydrochloride (EDC) (MW = 191.70 g/mol, Sigma Aldrich, UK) and 1.10 g of N -hydroxy succinimide (NHS) (MW = 115.09 g/mol, Sigma Aldrich, UK) were slowly added to the buffer solution until a final molar ration of 1:1:1 CS/EDC/NHS. After 30 min stirring, 1.8 g of dopamine hydrochloride (DP) (MW = 189.64 g/mol) was added to the mixture and let react overnight. After the reaction, the solution was purified by dialysis against dH_2O using cellulose membrane (MWCO = 11 - 14 kDa) for 2 days in 0.1 M MES aqueous solution and 1 day in acidified dH_2O (pH = 1 - 2) and subsequently lyophilized as explained in *section 3.1.1* (**Figure 3.2**). All the process was performed protected by light to avoid the oxidation of the catechol groups.

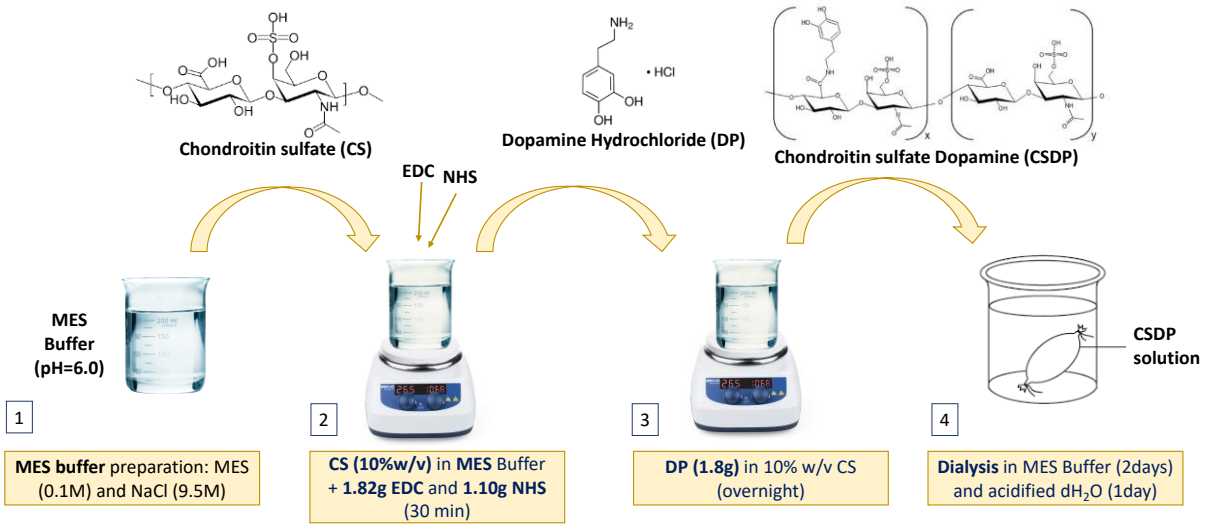

Figure 3.2: Schematic representation of the CSDP synthesis process.

3.2 Hydrogels preparation

3.2.1 GGMA-based hydrogels

Multiple GGMA- based formulations, as reported in **Table 3.1,** were taken into consideration in this PhD work, but only four of them were selected for further experiments, because were the only one showing good printability (according to the tests performed with the ROKIT INVIVO Bioprinter).

Two hydrogel compositions were based on bare GGMA at different polymeric concentration: GGMA 2 % w/v (GGMA 2 %) and GGMA 3 % w/v (GGMA 3 %). The other two hydrogel composition were prepared by combining GGMA with Manuka Honey (MH) (Manuka Guard®, US, Medical grade12+, MGO 400) (GGMA 2 % - MH 5 %).

For the GGMA 2 % and GGMA 3 % hydrogels preparation, GGMA freeze dried powders were dissolved in dH_2O at the proper concentration under constant stirring overnight at 60 °C with the addition the photo-initiator LAP (Lithium phenyl-2,4,6-trimethylbenzoylphosphinate) at 0.1 % w/v concentration. The glass vial was covered by light to not affect the photocrosslinking.

For the GGMA 2 % - MH 5 % sample, 5 g of MH were added to 100 mL of the prepared GGMA 2 % and let under stirring for 1 h at 60 °C.

To obtain hydrogels cylindrical samples for further characterisation, GGMA 2 %, GGMA 2 % - MH 5 % and GGMA 3 % solutions were poured in a 48-well plate, and let photocrosslink at Room Temperature (RT) under UV light (365 nm wavelength, 8 W/m^2, ROKIT INVIVO Bioprinter) for about 10 min, and physically crosslinked with the addition of an equal amount

of cellular media Dulbecco's Modified Eagle Medium/Nutrient Mixture F-12 (DMEM/F12) (Thermo Fisher Scientific, UK) with divalent ions. The gelation time was monitored for all the composition. The hydrogels obtained were stored in the incubator a 37 °C and 5 % CO_2. Some of the obtained hydrogels were stored at -20 °C overnight and then lyophilised for 48 h in a freeze-dryer as reported in *section 3.1.1.* for water uptake and morphological analyses, whilst other hydrogels were covered by DMEM/F12 and stored in incubator at 37 °C for mechanical tests. Prior to use, DMEM/F12 was discarded, samples were washed in Phosphate Buffer Saline (PBS) and left overnight in the fridge to solidify, and subsequently cut with a hollow puncher to obtain cylinder-shaped specimens.

For further tests, GGMA freeze-dried powders were sterilized under UV irradiation (254 nm wavelength) for 30 min before preparing the solutions.

HYDROGEL NAME	GGMA CONTENT (w/v)	MH CONTENT (w/v)
GGMA	**2.0 %**	**-**
	3.0 %	**-**
GGMA - MH	1.0 %	5.0 %
	1.5 %	5.0 %
	2.0 %	**5.0 %**

Table 3.1: Name and composition (% w/v) of the GGMA-based hydrogel manufactured and analysed. Highlighted the formulation selected for further tests.

3.2.2 CSDP hydrogel

Two different CSDP hydrogel concentrations were evaluated: 10 % w/v and 20 % w/v. The hydrogels were formed by the crosslinking of catechol groups. First, CSDP was dissolved in PBS at 10 % w/v (CSDP10) and 20 % w/v (CSDP20) concentration, and the pH of the solution was adjusted to 8-9 by adding NaOH (2 M). After the addition of Sodium Periodate ($NaIO_4$) (Sigma Aldrich, UK), CS-DP hydrogel was spontaneously formed without any further treatment. The gelation time of the hydrogel was measured while varying the amount of $NaIO_4$ (from 1.0 to 2.0 equivalents to the molar amount of Catechol). For CSDP 10 % w/v, 0.6 g of CSDP powder were dissolved in 6 mL solution composed by PBS, NaOH (2 M) and 843 µl of $NaIO_4$ to obtain a molar ratio $NaIO_4$/Catechol 1.5:1.0, which was the one selected in this work. The same procedure, adapting the concentrations was used for CSDP 20 % w/v.

3.3 Chemical characterisation

3.3.1 Fourier transform infrared spectroscopy with attenuated total reflection (FTIR-ATR)

Infrared spectroscopy was carried out to characterize the sample surface and to confirm the composition and to assess the successfulness of the synthesis process. Measurements were obtained with a Spectrum Two PE instrument equipped with a horizontal attenuated total reflectance (ATR) crystal (ZnSe) (PerkinElmer Inc., USA). Samples were placed directly onto the ATR crystal and spectra were collected in absorbance mode. Each spectrum was the result of the average of 16 scans with 4 cm^{-1} resolutions. Measurements were recorded in the wavelength range of 4000 – 550 cm^{-1}.

3.3.2 X-ray photoelectron spectroscopy (XPS)

X-ray photoelectron spectroscopy (XPS) was carried out to study the elemental composition of the samples. A PHI 5000 VersaProbe II (Physical Electronics, United States) was exploited, equipped with a monochromatised AlKa X-ray radiation source. Freeze-dried samples or raw polymer powders were examined recording survey scans (binding energy range 0 – 1200 eV) and high-resolution signals in Fixed Analyzer Transmission mode (pass energy 29.35 eV), scanning areas of ~ 1400 x 200 mm. Spectra were acquired for C_{1s}, N_{1s}, O_{1s}, P_{2p}. The MultiPak software (v. 9.9.0) was exploited for data mining. The surface elemental composition was assessed after normalizing each peak area, referring to the software library for elemental sensitivity factors. High-resolution spectra were fitted with Gaussian–Lorentzian peaks having the same Full width at half maxima (FWHM).

3.3.3 Nuclear Magnetic Resonance Spectroscopy (NMR)

NMR analysis was performed in two ways to analyse the structure of organic compounds: Solid-State NMR Facility (Department of Physics, University of Warwick) for GG and GGMA or Bruker AVANCE (School of Natural and Environmental Science, Newcastle University) for CS and CSDP.

For GG and GGMA, the spectra were measured on a 4 mm HX probe in an 850 MHz spectrometer and the samples were spun at 12 kHz. Regarding the 13C CPMAS experiments, 1024 scans were averaged for GG sample and 4096 scans for GGMA. For the 13C{1H} CP hector experiments 8 scans were averaged for 96 increments for GG and 128 scans with 128 increments for GGMA. All 13C CP spectra were measured using: 2 ms contact time, 3 s relaxation delay and 92.5 kHz 1H decoupling.

For CS and CSDP, ^{1}H and ^{13}C spectra were recorded with either Bruker AVANCE 300 MHz or JEOL 400 MHz spectrometers at RT. NMR tubes of 5mm were used for the sample's preparation by dissolving CS raw powder of CSDP lyophilised in appropriate deuterated solvents. Chemical shifts are reported in ppm relatively to TMS as internal standard.

3.4 Physical characterisation

3.4.1 Measurement of the gelation time

Hydrogel's sol/gel transition time was qualitatively measured at RT in by using the "tube inverting" test, within a 7 mL bijou (Scalzone et al., 2019a). For each hydrogel composition, 1 mL of solution was poured in a bijou and exposed to the proper physical or chemical crosslinking method. Every 30 s, up to 10 min, the bijou was inverted at 45 ° for approximately 10 s to visually assess samples deformation caused by their flow. The gelation time was defined as the time when no flow of the sample was detected.

3.4.2 Water uptake kinetics

Water uptake analysis was performed on gels, which were frozen at -20 °C overnight and lyophilized, as reported in *section 3.1.1*, to eliminate all the water content. Lyophilized hydrogel samples were weighted and placed separately in a 7 mL bijou vial containing 5 mL of PBS and stored at 37 °C in an incubator. The weight of all the samples was measured before immersion in PBS and after 30 min, 1, 2, 4, 6, 24 and 48 h of incubation in PBS. At each time point, the samples were gently dried on a filter tissue paper and weighted. The water uptake percentage was calculated using the following equation (Eq. 1):

$$WU\ (\%) = \frac{W_t - W_i}{W_i} \times 100 \quad (Eq\ 1)$$

where WU is the water uptake ratio, W_i is the initial weight of the hydrogel, W_t is the weight of the hydrogel after the considered time point.

3.5 Mechanical tests

3.5.1 Unconfined compression test

Mechanical properties under compression were evaluated using a mechanical testing machine (EZ-SX, Shimadzu, Japan). Three specimens for each hydrogel composition were tested at RT with 20 N load cell, whereas 1 kN load cell was used for thermoplastics samples. The crosshead speed was set to 1 mm·min^{-1} and the load was applied while the specimen was compressed until break (~ 60 % of original height) (Scalzone et al., 2019a; Bonifacio et al., 2020). Stress vs. Strain (σ/ε) curves were obtained: the stress was calculated by dividing the applied force with

the initial specimen surface area whereas strain was calculated from the displacement of the scaffolds in relation to the original thickness. The compressive Young's compressive moduli (E) were calculated as the slope of the initial elastic/linear region of the curve (0 – 10 % strain).

3.5.2 Stress relaxation

To evaluate the hydrogels viscoelastic stress-relaxation properties, it was followed the protocol used by Bian et al. (Bian, Zhai, Mauck, et al., 2011)(Bian, Zhai, Tous, et al., 2011). Stress relaxation tests were performed with a single compression ramp at a speed of 5 % per minute until reaching 5 % strain. Subsequently, the strain was held constant for 1000 s, while the load was recorded as a function of time. The stresses vs. strain relations of the gels were almost linear in the range 0 – 5 %. The peak stress (E_p) was obtained when reaching 5 % strain. The equilibrium Young's modulus (E_Y) was determined by the equilibrium load obtained after 1000 s of relaxation under unconfined compression. The data obtained were analysed using MATLAB R2019 software, fitting a third order exponential decay (Eq. 2) to the relaxation curves, according to the generalized Maxwell model and three relaxation times were acquired (τ_1, τ_2, τ_3) (Scalzone et al., 2019a). The linear region of the curve, corresponding to the stress increasing with the strain was not reported when fitting the relaxation curves.

$$\sigma(t) = A(e)^{-t/\tau_1} + B(e)^{-t/\tau_2} + C(e)^{-t/\tau_3} + D \quad (Eq\ 2)$$

where σ_t is the total stress, while A1, A2 and A3 are the amplitudes related to the three different relaxation times τ_1, τ_2 and τ_3.

3.5.3 Rheological analyses

Rheological measurements were carried out with Kinexus Pro rheometer (Malvern Instruments Ltd, UK). Measured data were registered with rSpace for Kinexus Pro 1.3 software. Preparations were measured using a cone and plate geometry. The gap between the cone and plate of sample placement was 2 mm. The temperature of the samples was controlled with an accuracy of ± 0.1 °C, by Peltier system of the rheometer. In all measurements a cylindrical cover made of stainless steel was placed over the samples, to create a closed, saturated volume around the sample.

The Strain Sweep Test was performed to verify the values of the strain amplitude to identify the linear viscoelastic region (LVER) and to assess the materials stretchability. LVER is the region where the storage modulus (G') and the Loss modulus (G") were independent of the strain amplitude, being linear and parallel between each other's. This test was performed at

physiological temperature of 37 °C, with a rotational oscillation frequency of 1 Hz. The complex modulus G*, that is the direct measure of the rigidity of a material's soft solid structure when exposed to stresses below the yield stress, was recorded with Eq. 3:

$$G^* = \sqrt{(G')^2 + (G")^2} \quad (Eq\ 3)$$

Also, the apparent viscosity (η) and the strain value at yield point were recorded.

The Temperature Sweep Test was carried out to assess the hydrogels behaviour at different temperature. The oscillatory measurement was set at a frequency of 1 Hz and 1 % strain amplitude. The temperature was increased at the rate of 5 °C in the range of 15 – 45 °C and the values of G' and G" were recorded in the LVER for each temperature.

3.6 Morphological analysis

Morphological analysis was performed using a Hitachi TM3030 SEM at 15 kV and working distance of 2 mm. All samples were cut into small squares (3 mm length), fixed on the aluminium stub using carbon tape and gold-coated using a BIO-RAD Sputter Coater machine. SEM micrographs were post-processing analysed with image software (ImageJ).

3.7 Cell Culture

Four cell types were used within this Thesis, which are: Primary Foetal Human Chondrocytes (HC) (Cell Application, US), Human TERT immortalised bone marrow stromal cells (Y201) kindly provided by Prof P. Genever (York University) at passage 80 (James et al., 2015), TC28a2 human chondrocyte cells (Merck, USA) and Y201 differentiated in chondrocytes (Y201-C).

HC were cultured in ready-to use Chondrocyte Growth Medium (PromoCell, UK) at 37 °C in a humidified atmosphere incubator containing 5 % CO_2. Cells were detached with trypsin-EDTA (PAA-Laboratories GmbH, Germany) at 80 % confluence and sub-cultured to passage 5-7 for experiments.

Y201 were cultured at 37 °C and 5 % CO_2 in Dulbecco's Modified Eagle Medium (DMEM) with low glucose content, supplemented with 10 % Foetal bovine serum (FBS), 2mM L-glutamine and a 1 % Penicillin/Streptomycin (P/S). After the expansion, cells were used for further experiments or were differentiated in chondrocytes at passage 85.

Y201 differentiation was performed by culturing cells for 21 days in serum free DMEM with P/S supplemented with 1 % Insulin-Transferrin-Selenium (ITS)+1, 10 ng/mL TGFβ-3, 40 µg/mL L-Proline, 100 nM Dexamethasone, 50 µg/mL L-Ascorbic acid-2-phosphate. Differentiated

cells (Y201-C) were cultured in DMEM/F12 s with high glucose (4.5 g/L) supplemented with 10 % FBS, 2mM L-glutamine and a 1 % P/S.

TC28a2 human chondrocyte cells (Merck, USA) were obtained at passage 22, and were cultured in DMEM/F12 with high glucose (4.5 g/L) supplemented with 10 % FBS, 2 mM L-glutamine and a 1 % P/S.

3.7.1 Cell Cryopreservation

Cells were trypsinised at ~ 80 % confluency using the procedure described in *section 3.7.* and resuspended in freezing medium, consisting of FBS supplied with 10 % v/v dimethyl sulfoxide (DMSO) (Sigma Aldrich, UK), at a concentration of 10^6 cells per mL. Cell suspension was then transferred in cryopreservation tubes (1 mL per tube) (Corning, USA) and placed in a -80 °C freezer for 3 days to have a controlled rate of cell freezing. Cryopreservation tubes were moved into liquid nitrogen for long-term storage at -196 °C. For defrosting cells, cryogenic tubes were thawed in a water bath at 37 °C for 2 - 3 min, then the cell suspension was resuspended into cold fresh cell culture media and centrifuged at 1200 rpm for 5 min. After the supernatant removal, the pellet was resuspended in cell culture media at the desired density for seeding into a cell culture flask (10^6 cells per 75 cm^2).

3.8 Set-up of pathological model

One of the main goals of this PhD research was the study of *in vitro* model of AC in Healthy and Pathological condition. To set-up the AC pathological model, it was used a cocktail of pro-inflammatory cytokines to emulate the OA environment. Three different conditions were analysed, as reported in **Table 3.2**: Healthy (DMEM/F12); Pathological at low concentration of cytokines (LC-OA) (DMEM/F12 loaded with IL-1ß (1 ng/mL), IL-6 (10 ng/mL) and TNF-α (1 ng/mL)); and Pathological at high concentration of cytokines (HC-OA) (DMEM/F12 loaded with IL-1ß (5 ng/mL), IL-6 (50 ng/mL) and TNF-α (5 ng/mL)).

CYTOKINES	High Concentration (HC-OA)	Low Concentration (LC-OA)	HEALTHY
IL-1β	5 ng/mL	1 ng/mL	-
TNF-α	5 ng/mL	1 ng/mL	-
IL-6	50 ng/mL	10 ng/mL	-

Table 3.2: Culture condition set-up: Healthy, High concentration OA (HC-OA) and Low concentration OA (LC-OA).

3.9 Cell viability assays

3.9.1 Live and Dead

Live/Dead assay (LIVE/DEAD® Cell Imaging Kit, Life Technologies, Thermo Fisher Scientific, UK) was used according to the manufacturer's instructions. This fluorescence-based kit combines calcein AM and ethidium bromide to yield two-color discrimination of the population of live cells (green) from the dead cells (red) population. Each cell culture condition was washed twice with PBS before incubation with the staining solution. For the preparation of Live/Dead solution, 4 µM ethidium homodimer-1 and 10 µM calcein were diluted in PBS, incubated in the dark with for 30 min at 37 °C. Alternatively, a ReadyProbes® Cell Viability Imaging Kit (Thermo Fisher, UK) was used. NucBlue® Live reagent (Hoechst 33342), staining the nuclei of all the cells was combined with ethidium bromide, according to manufacturer's instructions: 4 µL ethidium homodimer-1 and 4 drops of Hoechst in 2 mL of PBS.

Samples were imaged after the incubation with the Live/Dead or ReadyProbes® solutions using a EVOS M5000 microscope or LEICA DM LB2 Microscope or a Nikon A1R confocal laser, inverted microscope (Nikon, Japan) using constant illumination and capture parameters. A Galvano scanner was used to acquire 2 - 5 µm thick z-stacks through the entire thickness of the sample using either 10 x (Nikon Plan Apo λ 10 x NA 0.45; working distance 4 mm, FOV 1.27 x 1.27 mm) or 20 x (Nikon Plan Apo λ 20 x NA 0.75; working distance 1 mm, FOV 0.64 x 0.64 mm) objectives. Some of the images were acquired as z-stacks, and a maximal projection algorithm was used for 3D reconstruction. Micrographs were then analysed using the NIS-Elements and ImageJ v1.46 software packages.

3.9.2 CellTox™ Green

Cell death was quantified using the CellTox™ Green Cytotoxicity assay (Promega, UK), in which cell death is measured with a fluorescent dye that binds the DNA of cells with impaired membrane integrity. At specific time point, cells were treated with CellTox™ Green Dye (1:500 in the Assay buffer), incubated at RT for 15 min and fluorescence was measured at 485/535 nm excitation/emission. Then, the labelled cells were lysed by addition of 4 µL of lysis solution for determination of 0 % viability signal, measuring the fluorescence as before. The results are presented as the percentage of live cells.

3.10 Metabolic Activity Assays

Multiple metabolic activity assays are presented in this section. According to the suitability with the culture system set-up in each chapter, different metabolic assays have been performed. This information is reported in the proper chapter.

3.10.1 MTT Assay

Cells metabolic activity was analysed with the Thiazolyl Blue Tetrazolium Bromide (MTT) assay using a standard kit provided by Sigma Aldrich, UK. MTT solution was obtained dissolving the MTT powder in PBS (5 mg/mL) and this stock solution was mixed with serum-free DMEM without phenol red (1:10). Samples were incubated for 4 h at 37 °C protected from light. Then, MTT solution was removed and replaced by 400 µL of dimethyl sulfoxide (DMSO, Sigma Aldrich, UK) for each well and the plates agitated for 30 min on a Stuart Mini Microtitre Plate Shaker, to dissolve the formazan crystals, a product of digestion of the MTT by the cell. Then, 200 µL of each well solution (in duplicate) was transferred to a clear bottom 96- well plate and a Filter-based FLUOstar® Omega multi-mode reader (FLUOstar® Omega, Germany) was used to measure the absorbance at 570 nm. The estimation of the cell number was performed based on a standard curve, generated by seeding Y201 cells at different densities (0, 5 000, 10 000, 30 000, 50 000, 100 000 and from there on up to 500 000 with a 50 000 increase).

3.10.2 MTS assay

To evaluate cells metabolic activity MTS (3-(4,5-dimethylthiazol-2-yl)-5-(3-carboxymethoxyphenyl)-2-(4-sulfophenyl-2H-tetrazolium) assay (CellTiter 96® AQueous One Solution Cell Proliferation Assay, Promega, UK) was used. MTS solution was prepared diluting at 1:6 the CellTiter 96® AQueous One Solution Reagent in phenol red-free DMEM/F12 supplemented with 10 % FBS and 1 % P/S. MTS solution was added to each well containing samples in different volumes based on the system (spheroids or hydrogels) and left to incubate at 37 °C in a humidified 5 % CO_2 atmosphere for 2.5 h. Then, 90 µL of solution was transferred into a 96-well plate in duplicate or triplicate for each sample. Absorbance was recorded at 490 nm using a FLUOstar® Omega multi-mode reader. The results were analysed using GraphPad Prism 9 software (section 3.20). The incubation time differed depending on the experiment and on the cell type and is reported in the specific section.

3.10.4 Cell Titer assay

CellTiter-Glo® 3D (Promega, UK) was used to quantify the ATP content. At specific time point samples were transferred to a 96-white bottom plate suspended in phenol red-free

DMEM/F12 and CellTiter-Glo solution (1:1). The plate was protected from light at RT while shaking for 10 min using a Stuart Mini Microtitre Plate Shaker, to induce spheroids lysis and then, without shaking for 20 min to stabilise the bio-luminescence signal. The recording was performed in luminescence with a FLUOstar® Omega multi-mode reader.

3.11 Ultrastructural microscopy: Transmitted electron microscopy (TEM)

Cellular ultrastructure (organelles and internal structure) assessment was conducted by TEM using a Phillips CM 100 Compustage (FEI) transmission electron microscope (TEM) (Philips) at HV = 100.0 kV, and digital images were collected using an AMT CCD camera (Deben) with a range of magnification up to 130,000 x. Cells were fixed overnight using a pre-warmed solution of 2 % glutaraldehyde (TAAB Laboratory Equipment) in sodium cacodylate buffer at 4 °C, followed by a post-fixation with 1 % osmium tetroxide (OsO_4) (Agar Scientific, UK). After various dehydration steps, samples were embedded in resin, and cut in ultrathin sections using a diamond knife on a Leica EM UC7 ultra microtome (Leica Microsystems). The sections were stretched with chloroform to eliminate compression, mounted on Pioloform-filmed copper grids (Agar Scientific) and ready to be visualized using an AMT CCD camera (Deben).

3.12 Immunostaining: DAPI and Phalloidin

Cell's morphology was observed by staining their cytoskeleton using rhodamine-phalloidin and the nucleus observed using 4', 6- diamidino-2-phenylindole (DAPI). For the Immunostaining, samples were fixed in pre-warmed 4 % w/v paraformaldehyde (PFA) for minimum 30 min at 4 °C and washed three times with PBS. Cells were permeabilised using 0.1 % v/v Tween20® (Sigma Aldrich, UK) in PBS for three washes. Rhodamine-phalloidin was prepared using 1:1000 dilutions of phalloidin-tetramethylrhodamine B isothiocyanate (Sigma Aldrich, UK) in 0.1 % PBS/Tween20®. Samples were incubated with rhodamine-phalloidin solution for 20 min at RT protected from light. Residue of phalloidin-rhodamine was removed by washing samples with 0.1 % PBS/Tween20® solution three times. Following this, samples were immersed in DAPI solution, prepared diluting DAPI (Vector Laboratories) in 0.1 % PBS/Tween20® (1:2500) for 10 min at RT protected from light. Then, samples were washed other three times with 0.1 % PBS/Tween20® and were imaged using a Nikon A1R inverted confocal microscope at 20 x magnification as explained in *section.3.9.1.*

3.13 Quantitative Real Time PCR analysis (RT-qPCR)

3.13.1 RNA extraction from cells

At specific time points, samples were washed with PBS and frozen in 1.5 mL Eppendorf tubes at -80 °C. RNA isolation was performed using miRNeasy Micro RNA Isolation Kit (Qiagen, USA), based on the use of spin columns. This method allows the extraction of high-quality total RNA from cells while maintaining its integrity due to highly effective inhibition of RNase activity while disrupting cells and dissolving cell components. Cells were incubated with Qiazol (Qiagen, USA) for 10 min at 4 °C and the supernatant was recovered after homogenisation with KIMBLE Dounce tissue grinder set (Sigma Aldrich, UK). Chloroform was added (1:5 ratio), mixed for 5 min and centrifuged for 15 min at 4 °C at 12,000 x g, thus the homogenate separated into a clear upper aqueous layer containing RNA, an interphase, and a lower organic layer containing DNA and proteins. RNA was then precipitated from the aqueous layer and washed using the miRNeasy Micro RNA Isolation Kit following the manufacturer`s instructions. RNA samples were then stored at - 80 °C.

3.13.2 RNA quantification

The total concentration and purity of the isolated RNA was measured using a spectrophotometer (NanoDrop™ 1000, Thermo Fisher Scientific, USA) by loading 1.2 µl of RNA solution. The instrument readout comprises the RNA concentration, the A260/A280 (RNA/DNA) and the A260/A230 (RNA/phenolic compounds) ratios. The last readouts were necessary to ensure the 260/280 ratio was within the range of 1.7 to 2.0 while 260/230 around 2.

3.13.3 Reverse Transcription Polymerase Chain Reaction

Synthesis of cDNA from isolated total RNA was done using High-Capacity cDNA Reverse Transcription Kit (Thermo Fisher, UK), according to manufacturer's instructions, using 500 ng of RNA for each sample. After that, a thermocycler (2720 Thermal Cycler, Applied Biosystems, US) based on cycles of 10 min at 25 °C, 120 min at 37 °C, 5 min at 85 °C was used for the reverse transcription and cDNA-transcripted samples were stored at 4 °C until further use.

3.13.4 Quantitative Polymerase Chain Reaction (qPCR)

The polymerase chain reaction (PCR) was carried out using TaqMan™ Fast Advanced Master Mix (Thermo Fisher Scientific, UK) and commercially available TaqMan RT-qPCR probes (Thermo Fisher Scientific, UK) reported in **Table 3.3**. All samples were analysed with QuantStudio 3 Real-Time PCR System (Thermo Fisher Scientific, US) with the following 40 x

three-step cycle: 10 sec denaturation, 95 °C; 30 s annealing, 60 °C; 15 s elongation, 72 °C). Gene expression was normalized to GAPDH housekeeping gene and expressed relatively using the $2^{-(\Delta\Delta Ct)}$ method (Livak & Schmittgen, 2001a), with expression levels at day 1 controls as calibrator. 1.5 µL of cDNA was used for each well.

RT-qPCR PROBES	ASSAY ID
GAPDH	Hs99999905_m1
SOX9	Hs00165814_m1
COL2A1	Hs00264051_m1
ACAN	Hs00153936_m1
COL1A2	Hs01028956_m1
MMP13	Hs00942584_m1
ADAMTS5	Hs01095518_m1
SPARC	Hs00234160_m1
RUNX2	Hs01047973_m1
ALPL	Hs01029144_m1
COL1A2	Hs01028956_m1
SPP1	Hs00959010_m1
VEGFA	Hs00900055_m1

Table 3.3: List of RT-qPCR probes used in these experiments and relative Assay ID**.**

3.14 Glycosaminoglycans quantification

Quantitative analysis assessment of GAGs production was performed with Alcian Blue 8GX (Merck, BDH) at pH 2.5, obtaining dissolving Alcian Blue powder in 3 % v/v of Acetic Acid at a concentration of 1% w/v. Samples were fixed with 4 % PFA at 4 °C for 30 min at each time point, followed with a double wash with PBS. Then, 200 µL of Alcian Blue solution was added to each sample for 15 min and samples were washed with dH_2O until the blue came out. For evaluating the quantitative GAGs production, 28.66 g of guanidine hydrochloride was dissolved in 50 mL of dH_2O. 500 µL of Guanidine solution was added to each Alcian Blue stained sample's well and let for 3 h acting while shaking every 10 min on a Stuart Mini Microtiter Plate Shaker. Then, 200 µL were taken in duplicate from each well and reading was

performed in absorbance at 630 nm with a Filter-based FLUOstar® Omega multi-mode reader in a 96-clear bottom well plate.

3.15 Morphological analysis on cellular samples

Tescan Vega 3LMU scanning electron microscope was used for analysing the morphology of cellular samples. At the chosen time point, samples were fixed in 2 % glutaraldehyde for 1 h at 4 °C, rinsed in PBS twice and dehydrated in ethanol grades (30 min in 25 % EtOH, 30 min in 50 % EtOH, 30 min in 75 % EtOH, 30 min in 95 % EtOH and twice 1 h in 100 % EtOH). Samples were dried to critical pointing (BALTEC 030, Leica Geosystems Ltd, UK), mounted on carbon discs and gold-coated using a Polaron E5000 SEM Coating unit (Quorum Technologies Ltd, UK). Samples were imaged at different magnifications.

3.16 Histology and Immunohistochemistry

The preparation of samples for Histology and Immunohistochemistry (IHC) and the relative staining process were optimised within this PhD work to obtain proper tissue slices in all the configurations exploited in each chapter.

3.16.1 Cryosections preparation

For the preparation of cryosections from fresh tissue, at specific time points samples were washed with PBS, transferred to a 0.5 mL Eppendorf embedded in Optimal Cutting temperature (OCT) Compound (Agar Scientific, UK). OCT-included samples were snap frozen at -80 °C until further use.

For the preparation of cryosections from fixed tissues, at specific time points samples were washed with PBS, fixed in formalin 10 % overnight at 4 °C. Fixed samples were washed in PBS and transferred in a sucrose solution (30 % w/v in PBS) overnight. Then, the sucrose solution was replaced by a solution made of 30 % sucrose and OCT Compound (1:1) for 1 h. Finally, samples were transferred in cryomolds (Agar Scientific, UK) included in OCT and frozen at -80 °C until further use.

All samples were cryosectioned using a CM1900 cryostat (Leica Biosystems, Germany) at -20 °C. Each section was cut with a thickness of 5 µm in the case of fresh tissue samples and 12 µm for fixed samples, let dry at RT for 2 h and kept frozen until analysis.

To perform Histology and IHC, fresh tissue frozen slides were transferred to cold Acetone (Fisher, UK) at -20 °C for 10 min. Following this, the fixative was let evaporate 15-20 min under

a chemical fume hood and the slides were washed twice with PBS to remove any trace of OCT compound, whereas fixed samples didn't need a further post-fixation and were washed in PBS and ready to be used.

3.16.2 Haematoxylin and Eosin staining

Fixed and washed slides were incubated in Mayer's haematoxylin (Sigma Aldrich, UK) for 30 s and rinsed in running tap water for 1 min to blue haematoxylin-stained nuclei. Slides were dehydrated in 70 % EtOH and 95 % EtOH 30 s respectively prior to immersion in eosin solution (Sigma Aldrich, UK) for 1 min. Samples were further dehydrated in 95 % EtOH and 100 % EtOH for 3 min each and incubated in Histo-Clear® II (National Diagnostics, USA) for 5 min before being mounted in DPX (Sigma Aldrich, UK).

3.16.3 Picrosirius red staining

Fixed and washed slides were incubated in Picrosirius red solution, which stains collagen fibres in red and cell's cytoplasm in yellow, was prepared dissolving 0.5 g of Sirius red in 500 mL of saturated Picric acid, for 1 h. Following, slides were washed twice in Acidified water (0.5 mL of Acetic Acid in 99.5 mL of dH_2O), dehydrated in three changes of absolute EtOH and incubated in Histo-Clear® II for 5 min before being mounted in DPX. Collagen fibers are stained in red and cytoplasm in yellow.

3.16.4 Alcian Blue staining

Fixed and washed slides were incubated in Alcian Blue solution at pH 1.0 in order to stain weakly and strongly sulphated proteoglycans, was prepared dissolving Alcian Blue powder 8GX (Sigma Aldrich, UK) in 0.1 M HCl at a concentration of 1% w/v. Samples were incubated for 20 min, washed fast in 0.1 M HCl and dehydrated in 95 % EtOH and 100 % EtOH for 3 min respectively. Then, slides were incubated in Histo-Clear® II for 5 min before being mounted in DPX. Alcian Blue at pH 1.0 stains weakly and strongly sulphated glycosaminoglycans.

3.16.5 Histology slides Imaging

All the histology slides were let dry overnight under the fume hood and imaged the following dry with Leica M5000 Microscope in RGD Brightfield at 20 x and 40 x magnification.

3.16.6 Immunohistochemistry

For IHC, fixed and washed tissue slices were treated with Sudan Black solution (0.1 % w/v in 100 % EtOH) to reduce the background interference during the immunofluorescence imaging. After the Sudan Black solution removal and slides washing, these were permeabilised with

Triton 100 x solution (0.1 % w/v in PBS) 30 min, immersed in Bovine Serum Albumin (BSA) (2 % w/v in PBS) for 15 min and incubated for 2 h at RT with primary antibodies Anti-Collagen II (ab34712 Abcam) or Anti-Ki67 (NB500-170SS Bio-techne Ltd) or Anti-Aggrecan (ab3778 Abcam) or Anti- Collagen X (14-9771-82 Thermofisher Scientific) respectively at dilution 1:200, 1:100, 1:50 and 1:100 in BSA solution. After washes in PBS, secondary antibodies solutions were added for 1 h: AlexaFluor goat anti-rabbit igG (H + L) (ab150080 Abcam) 1:500 in BSA solution to Anti-Collagen II slides, Fluorescein-labelled goat anti-rabbit IgG (H + L) (F2765, Thermo Fisher Scientific) 1:1000 in BSA solution for Anti-Ki67 and Anti-Aggrecan slides, AlexaFluor Goat Anti-Mouse IgG H&L (ab150115 Abcam) 1:500 in BSA solution. Following, nuclei were stained with Hoechst solution (R37609, Thermo Fisher Scientific, UK), according to manufacturer's instructions. Finally, a drop of Invitrogen ProLong Glass Antifade Mountant (Thermo Fisher Scientific, UK) was added to each slide and covered with a rectangular coverslip. Slides were let dry under the hood for 15 min and imaged using EVOS M5000 Microscope in fluorescence at 40 x magnification.

3.16.7 Immunohistochemistry slides Imaging

All the immunofluorescence slides were let dry overnight under the fume hood and imaged the following dry with Leica M5000 Microscope with Green Fluorescence protein (GFP), Red Fluorescence protein (RFP) and DAPI filters at 20 x and 40 x magnification.

3.17 Immunofluorescence

Immunofluorescence (IF) was performed as immunohistochemistry for Coll II, Coll X, ACAN and Ki-67. In addition, anti-SPARC (ON) was used as primary antibody (ab225716, Abcam), at a concentration of 1:15. For IF samples preparations, at the specific time point, samples were fixed with 4 % PFA at 4 °C for 30 min at each time point, followed with a double wash with PBS. Then cells were permeabilised using 0.1 % v/v Tween20® in PBS for three washes, immersed in Bovine Serum Albumin (BSA) (2 % w/v in PBS) for 15 min and incubated with primary antibody and secondary antibody, as reported in *section 3.16.6*.

3.18 Alizarin Red

To detect the calcium deposits, at specific time points samples were fixed in 4 % PFA for 30 min at 4 °C and then washed in PBS twice and stained with 1 mL of Alizarin Red solution for 30 min at RT. Following, samples were washed with dH_2O multiple times and dried overnight at 50 °C in a 5 % CO_2 atmosphere. Imaging of the samples was performed with stereomicroscope (Leica Microsystems). To quantify the Alizarin Red, 10 % acetic acid was

added to each stained sample and let under shaking on a Stuart Mini Microtiter Plate Shaker for 30 min. The acetic acid solution was then transferred to 1.5 mL Eppendorf, heated to 85 ˚C for 10 min and then place on ice for 5 min. Then the solutions were treated with 10 % ammonium hydroxide to neutralize the acetic pH to 4.1-4.5 and the reading was performed in duplicated at 405 nm absorbance with a Filter-based FLUOstar® Omega multi-mode reader in a 96-clear bottom well plate. The standard curve was obtained in the range 0 – 2 mM Alizarin Red.

3.19 Western Blot analysis

Protein expression analysis was carried out as previously reported (Licini et al., 2020). RIPA Lysis Buffer System (sc-24948, Santa Cruz Biotechnology inc.) combined with protease inhibitors (S8820, Sigma-Aldrich) was used to extract total proteins from samples. The concentration of protein was determined using a DC protein assay (LIT448D, Bio-Rad). Total protein extracts were incubated with Tris-Glycine SDS Sample Buffer (2X) (Novex) and then were fractionated on a 4-15 % SDS-PAGE gels. Electrophoretically, gels (HC1000 Surecast, Thermo Fisher Scientific) were transferred to 0.2 µm Nitrocellulose membranes (Bio-rad), which were incubated with 5% milk in Tris-buffered saline with 0.1 % Tween 20, prior to incubation with primary antibodies at 4 °C. The endogenous control used was mouse anti-GAPDH. After an overnight incubation, the membrane was washed with Tris-buffered saline with 0.1 % Tween 20 and incubated for 1.5 h at RT with anti-rabbit and anti-mouse secondary antibodies coupled to horseradish peroxidase (**Table 3.4**). Thermo Scientific's Pierce ECL Western Blotting Substrate was used to detect antibody binding, and pictures were captured with an Alliance Mini HD9 (Uvitec, Cambridge, UK), and analysed with ImageJ software. Western Blot analysis was performed by Dr. Cerqueni at Department of Clinical and Molecular Sciences, Università Politecnica delle Marche (Ancona, Italy).

REAGENT	ANTIBODY	DILUTION	SOURCE
Primary antibody	Anti-RUNX2	1:200	HPA022040 Sigma Aldrich
Primary antibody	Anti-ALP	1:1000	ab126820 Abcam
Primary Antibody	Anti-ON	1:250	sc-73472 Santa Cruz Biotechnology
Primary antibody	Anti-RANKL	1:750	PA5-110268 Invitrogen
Primary antibody	Anti- TNFRSF11B (OPG)	1:1000	Ma5-15960 Invitrogen

Primary antibody	Anti-GAPDH	1:10000	60004-1-Ig Proteintech
Secondary antibody	Anti-rabbit HRP	1:500	sc-2004 Santa Cruz Biotechnology
Secondary antibody	Anti-mouse HRP	1:15000	A90-116P Bethyl Laboratories

Table 3.4: List of Western Blot probes used in these experiments and relative information**.**

3.20 Statistical analysis

All tests were performed at least in triplicate for each sample in each condition. The results were represented as mean ± standard deviation. Differences between groups were determined using One-way analysis of variance (ANOVA) with Tukey's multiple comparison test using levels of statistical significance of $p<0.0001$ (****), $p<0.001$ (***), $p<0.05$(**) and $p<0.01$(*).

CHAPTER 4. A spheroid-based scaffold free approach to manufacture an *in vitro* articular cartilage validation model

STATEMENT OF SIGNIFICANCE

A fundamental step in this PhD research work was the design and manufacturing of a scaffold-free in vitro model of AC based on an optimised protocol in line with the recent clinically approved Chondrosphere® (CO.DON AG) technique (National Institute For Health and Care Excellence, 2017a)*, which was used as a validation model for the zonal engineered AC. In fact, validating new models would be crucial for the ongoing phase of their development, during which physiological baseline data and responses to compounds are assessed and compared with clinical outcomes, in order to make them suitable as platform for studying pathologies progression and subsequent therapeutic treatments* (Denayer et al., 2014)*. Thus, finding a reliable validation model is highly required.*

4.1. Introduction

This chapter reports the results of a spheroid-based scaffold-free AC model manufactured via a self-assembly technique without the addition of external forces, following a protocol in line with the clinically approved Chondrosphere® (CO.DON AG) technique (**Figure 2.10**) (Eschen et al., 2020). This approach would lead to the obtainment of a few mm thick *in vitro* model of AC, which could be reliable and predictive for validation. The obtained *in vitro* AC model will be loaded with an optimised cocktail of proinflammatory cytokines to study the OA progression. Three main objectives (OBJ) were taken into account:

OBJ 1: To manufacture the formation of spheroids and their characterisation, specifically their growth kinetics, viability, microstructure, and morphology, to obtain a reproducible and standardizable process.

OBJ2: To study how the spheroids fuse when put together to mature into a tissue, to assess whether optimized maturity of the scaffold-free sizable, engineered cartilage could be a suitable in vitro model of cartilage repair via cells gene expression and analyses on the ECM production.

<u>OBJ3:</u> To demonstrate that a bankable cell type (Y201-C) could produce an engineered cartilage-like construct, giving a repeatable and predictive model.

<u>OBJ4:</u> To obtain AC in vitro scaffold free model to optimise an approach for obtaining a reliable OA model, by using a cocktail of different concentration of pro-inflammatory cytokines and assessing their effect in terms of spheroids growth kinetics, cells metabolic activity, apoptosis, proliferation, expression of anabolic and catabolic markers and quality of tissues obtained.

Most of the results presented in this chapter have been published (Scalzone, Wang, et al., 2022). The PLGA-GEL membranes have been fully characterised in a work I am a co-author of (Carmagnola et al., 2020).

4.2 Materials and Methodology

4.2.1 Manufacturing of spheroids and chondrospheres

The manufacturing process of spheroids and chondrospheres is reported in **Figure 4.1**. Briefly, HC, Y201, TC28a2 and Y201-C were expanded as reported in *section 3.7,* in Chondrocyte growth medium, DMEM or DMEM/F12. Spheroids were formed using a round bottom 96-well plate (non-tissue culture treated) (Thermo Fisher Scientific, UK). For the formation of the spheroids, cells were seeded in the 96-well plate at a density of 2 x 10^5 cells/well, suspended in 150 µL of DMEM/F12 with high glucose (4.5 g/L), 10 % FBS, 2 mM L-glutamine, 1 % P/S and supplemented with 0.25 % w/v methylcellulose (MC) at p. 4 for HC cells, p. 15 for Y201-C and p. 81 TC28a2; Y201 (p. 89) were suspended in DMEM with low glucose content, supplemented with 10 % FBS, 2 mM L-glutamine, 1 % P/S and 0.25 % w/v MC (James et al., 2015) . Once cells were seeded, the multi-well plates containing all different types of spheroids were incubated at 37 °C in a humified atmosphere with 5 % CO_2 for 7 days, with medium change every other day.

After 7 days, three different tests were exploited for the obtainment of the chondrospheres. Specifically, ten single spheroids were cultured together in a 48-well plate (i) with MC-supplemented DMEM/F12 medium, (ii) with a MC- free DMEM/F12 medium or (iii) on the top of an electrospun PLGA - dopamine functionalised and GEL - coated membranes (Carmagnola et al., 2020) (kindly supplied by Politecnico di Torino, Italy), mounted in 24-multiwell cell crowns. This last technique was selected for the further culture of the chondrospheres, which were cultured at 37 °C in a humified atmosphere with 5 % CO_2 in DMEM/F12 medium supplemented with 10 % FBS, 2 mM L-glutamine and 1 % P/S for 21 days.

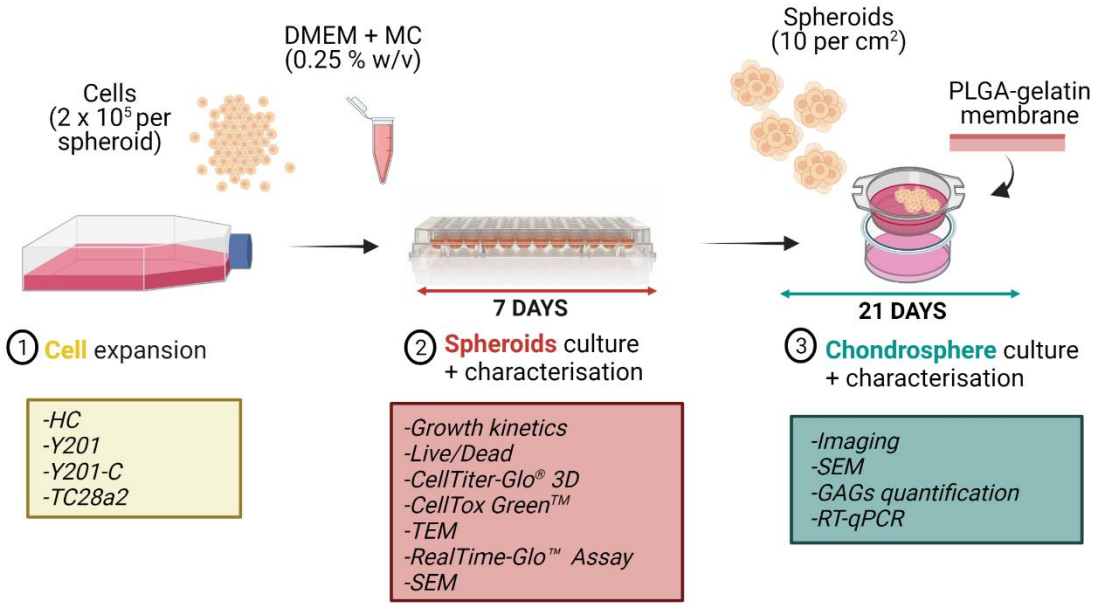

Figure 4.1: Scheme of the manufacturing and characterisation process: from: ***(1)*** cell expansion (HC, Y201, Y201-C, TC28a2) and their re-suspension in cell culture media supplied with MC (0.25 % w/v); ***(2)*** formation of spheroids (2 x 20^5 cells per spheroid) in a round bottom 96-well plate, their culture for 7 days and characterisation (Growth kinetics analysis, Live/Dead, CellTiter-Glo® 3D, CellTox™ Green, TEM, RealTim-Glo Assay and SEM); ***(3)*** assembly of spheroids on a GEL coated PLGA electrospun membrane (10 spheroid per cm^2 of membrane) and their characterisation over 21 days of culture (Imaging, SEM, GAGs quantification and RT-qPCR).

4.2.2 Evaluation of spheroids growth kinetics

First, it was qualitatively analysed the ability of cells to form spheroids with HC, Y201, Y201-C and TC28a2 cells, by using a fluorescence microscope in phase-contrast brightfield (LEICA DM LB2 Microscope). Only the cell types able to form spheroids in three days were selected for further experiments (HC and Y201-C). The changes of HC and Y201-C spheroids shape and dimension were monitored during their culture incubation (after 1, 3 and 7 days) and estimated using a fluorescence microscope in phase-contrast brightfield (LEICA DM LB2 Microscope). The morphometric analysis of the spheroids was performed by measuring diameters and areas of at least 5 spheroids for each time point with ImageJ software. The results were analysed using GraphPad Prism software to calculate the circularity (*Eq. 1*) and roundness (*Eq. 2*) of each spheroid, following the formula reported in literature (Moreira Teixeira et al., 2012):

$$Circularity = \frac{4 \cdot A}{\pi \cdot P} \quad (Eq\ 1)$$

$$Roundness = \frac{4 \cdot A}{\pi \cdot M^2} \quad (Eq\ 2)$$

where A is the area, P the perimeter and M is the major axis dimension. The more circularity and roundness are proximal to 1, the more the spheroids show morphological stability and homogeneity over time.

4.2.3 Viability and metabolic activity assessment

Multiple assays were used to estimate HC and Y201-C spheroids viability and metabolic activity over 7 days of culture.

Live/Dead assay was used according to the manufacturer's instructions, as reported in *section 3.9.1*. At days 1, 3 and 7 of culture, two spheroids of HC or Y201-C were washed twice with PBS and incubated with the staining solution for 30 min at 37 °C. Images were collected using a fluorescence microscope (LEICA DM LB2 Microscope) in GFP and RFP with 5 x objective lens.

CellTiter-Glo® 3D was used to quantify the intra-spheroids ATP content. Three spheroids of HC and Y201-C were harvested at days 1, 3 and 7 from the 96 round-bottom well plate and transferred in a 96-white bottom plate were suspended in 50 µL of phenol red-free DMEM/F12 and 50 µL of CellTiter-Glo® solution, and then incubated and analysed as reported in *section 3.10.4*.

CellTox™ Green Dye assay was used to assess quantitatively cells viability. At days 1, 3 and 7 three HC and Y201-C spheroids were treated with CellTox™ solution prepared as reported in *section 3.9.2* and analysed accordingly.

4.2.4 Spheroids microstructure

For evaluating HC and Y201-C spheroids microstructure at days 2 and 7, TEM analysis was performed, as reported in *section 3.11.* Digital images of spheroids core or spheroids peripheral region were collected using an AMT CCD camera (Deben).

4.2.5 Apoptosis and Necrosis assessment

RealTime-Glo™ Annexin V Apoptosis and Necrosis Assay (Promega, UK) was used to discriminate apoptosis from necrosis in cells within HC and Y201-C spheroids. This is a live-cell (non-lytic) real-time (kinetic) assay in which the exposure of phosphatidylserine on the outer leaflet of cell membranes and binding with Annexin V luciferase fusion proteins during the

apoptotic process is detected with a simple luminescence signal while necrosis upon loss of membrane integrity is detected with a fluorescence signal (DNA-binding dye) (**Figure 4.2**). This assay was performed at early stage of spheroids culture (0 - 48 h) and late stage (6 - 7 days). Luminescent and fluorescent (485/530nm excitation/emission) data were continuously collected every 6 h during 48 h exposure using FLUOstar® Omega multi-mode reader and samples were incubated within each reading at 37 °C in a humified atmosphere with 5 % CO_2.

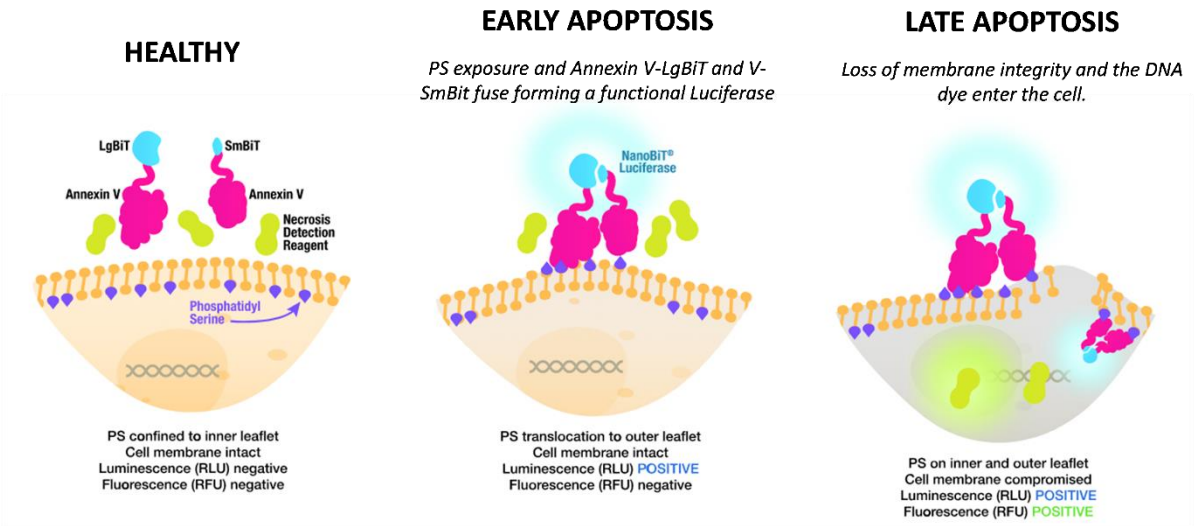

Figure 4.2: Scheme explaining how the RealTime apoptosis and necrosis assay works. Healthy cells give a negative signal, cells in early apoptosis stage give a Luminescence (RLU) positive signal, while cells in secondary necrosis dive a RLU and Fluorescence (RFU) positive signal [re-adapted from www.promega.uk].

4.2.6 Spheroids and chondrospheres morphology

For evaluating the morphology of spheroids and chondrospheres, samples were fixed, dehydrated, critical point dried, gold coated and visualised with a SEM, as reported in *section 3.15*. SEM analysis was performed for HC and Y201-C at day 2s and 7 of spheroids culture and at day 21 of chondrospheres culture. Samples were imaged at different magnifications (350 x, 900 x and 1300 x). Also, images of the spheroid's assembly within PLGA-coated membrane inserts were acquired with a Leica Stereomicroscope at day 21 of culture.

4.2.7 GAGs production and gene expression of chondrospheres

Quantitative assessment of GAGs production by chondrospheres of HC and Y201-C was performed with Alcian Blue, according to *section 3.14.* Chondrospheres were fixed at days 0, 7 and 21 of culture, while spheroids were fixed at day 1 as normalisation control for the chondrospheres. Results are reported for the chondrospheres respect to the sample of

spheroids at day 1. The values were obtained using the calibration curve from the Chondroitin 4-sulfate sodium salt from bovine trachea in a range of 0 – 1 µg.

RT-qPCR was performed at days 1 and 21 for chondrosphere and their fold-regulation was evaluated using the day 1 of spheroids as reference. The protocol used is reported in *section 3.13.* TaqMan qRT-PCR *sox9, acan, col2a1* and *gapdh* probes were quantified and gene expression of *sox9, col2a1* and *acan* was normalized to *gapdh* and expressed relatively using the $2^{-(\Delta\Delta Ct)}$ method of Livak (Livak & Schmittgen, 2001b). Results are presented as the fold change of HC and Y201-C chondrosphere's gene expression of *sox9, acan* and *col2a1* at days 1 and 21.

4.2.8 Manufacturing of in vitro OA model

To set-up the AC pathological model, pro-inflammatory cytokines were introduced to the culture media to emulate the OA environment, as reported in *section 3.8*. Spheroids were formed as reported in *section 4.2.1* and then, incubated at 37 °C and 5 % CO_2 for 10 days. After one day of culture, three different conditions were set for the spheroids (HC-OA, LC-OA and Healthy), as reported in **Table 3.2**, and the media was changed every two days. Following the procedure optimised for the formation of chondrospheres (*section 4.2.1*), after 10 days of spheroids culture five single spheroids were transferred onto the electrospun PLGA-GEL membranes mounted in 48-well plate inserts (10 spheroids per cm^2 of membrane) and cultured in DMEM/F12 medium loaded with the proper concentration of cytokines for further 11 days at 37 °C in a humified atmosphere with 5 % CO_2 (**Figure 4.3**).

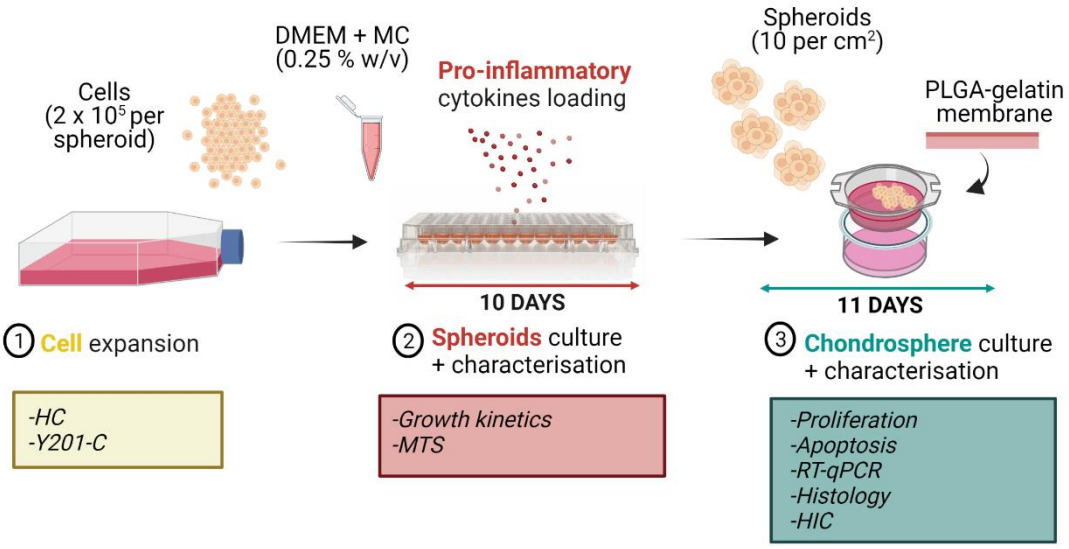

Figure 4.3: Manufacturing process of the OA in vitro model: HC and Y201-C cells expansion (1), Spheroids culture and characterisation in a round bottom 96-well plate for 10 days (2)

with the addition of IL-6, IL-1ß, TNF-α proinflammatory mediators at day 3 of spheroids culture (3), Chondrospheres culture and characterisation for further 11 days on a GEL-coated electrospun PLGA membrane (4).

CYTOKINES	HC-OA	LC-OA	Healthy
IL-1β	5 ng/mL	1 ng/mL	-
TNF-α	5 ng/mL	1 ng/mL	-
IL-6	50 ng/mL	10 ng/mL	-

Table 4.1: Culture conditions for HC and Y201-C: High concentration of cytokines (HC-OA), Low concentration of cytokines (LC-OA) and Healthy.

4.2.9 Spheroids growth kinetics in OA conditions

Spheroid's growth kinetics was monitored and analysed over the 10 days of culture for all conditions as reported in *section 4.2.2.* Images were taken at days 1, 4 and 10 with a EVOS M5000 microscope with 10 x objective lens in phase-contrast brightfield and analysed.

4.2.10 Spheroids metabolic activity in OA conditions

To evaluate HC and Y201-C cells metabolic activity in the three conditions (Healthy, LC-OA and HC-OA) MTS assay was used, as reported in *section 3.10.2.* Three spheroids per each condition were analysed at days 1, 4 and 10. 200 µL of MTS solution was added to each well containing spheroids and left to incubate at 37 °C in a humidified 5 % CO_2 atmosphere for 2.5 h. Then, 90 µL of solution was transferred into a 96-well plate in duplicate for each sample for the readings.

4.2.11 Gene expression analysis in OA model

Gene expression was performed at days 0 and 10 for spheroids and day 21 for chondrospheres, following the same protocol as reported in section 4.2.7, with the addition of the analysis of *col1a2, mmp13* and *adamts5* genes *(**Table 3.3**)*.

4.2.12 Histology and Immunohistochemistry assessment

Samples of both Y201-C and HC in Healthy, HC-OA and LC-OA at day 1, 10 and 21 were analysed. For the preparation of cryosection, as well as for the histology staining (Alcian Blue, Picrosirius Red and H&E), it was followed the protocol reported in *section 3.16*.

For IHC staining, it was followed the protocol in *section 3.15.6*, using as primary antibodies Anti-Collagen II, Anti-Ki-67 and Anti-Aggrecan, and AlexaFluor goat anti-rabbit igG (H + L) for

Anti-Collagen II slides and Fluorescein-labelled goat anti-rabbit IgG (H + L) for Anti-Ki-67 and Anti-Aggrecan samples, as secondary antibodies. Finally, nuclei were counterstained with Hoechst solution. Cells nuclei, stained with Hoechst, were also imaged at 63 x with a Nikon A1R confocal microscope, to assess the apoptotic features.

4.2.13 Statistical analysis

Error bars represent the standard deviation of the mean. Differences between groups were determined using one- or two-way analysis of variance (ANOVA) with Tukey's multiple comparison post-hoc test. Significance between groups was established for *p < 0.05, **p < 0.01, ***p < 0.001 and ****p < 0.0001.

4.3 Results

4.3.1 Spheroid manufacturing optimisation

The round-bottomed 96 well plate led to the production of one spheroid per well, allowing the delivery of the precise cell amount to each well (**Figure 4.4**). The time needed from the cell seeding to the formation of spheroids was ranged between 24 - 72 hours, as reported in **Figure 4.5A. Figure 4.5B-E** shows the phase-contrast brightfield images of the manufactured spheroids after 72 hours of incubation for the four different cell types: TC28a2, Y201, HC and Y201.C (**Figure 4.5F**). Both TC28a2 and Y201 didn't form a compact spheroid, showing fragmented aggregates (**Figure 4.5B,C**), while HC and Y201-C evidenced a compact and rounded-like shaped spheroids (**Figure 4.5D,E**). Therefore, these cells were selected for the following tests.

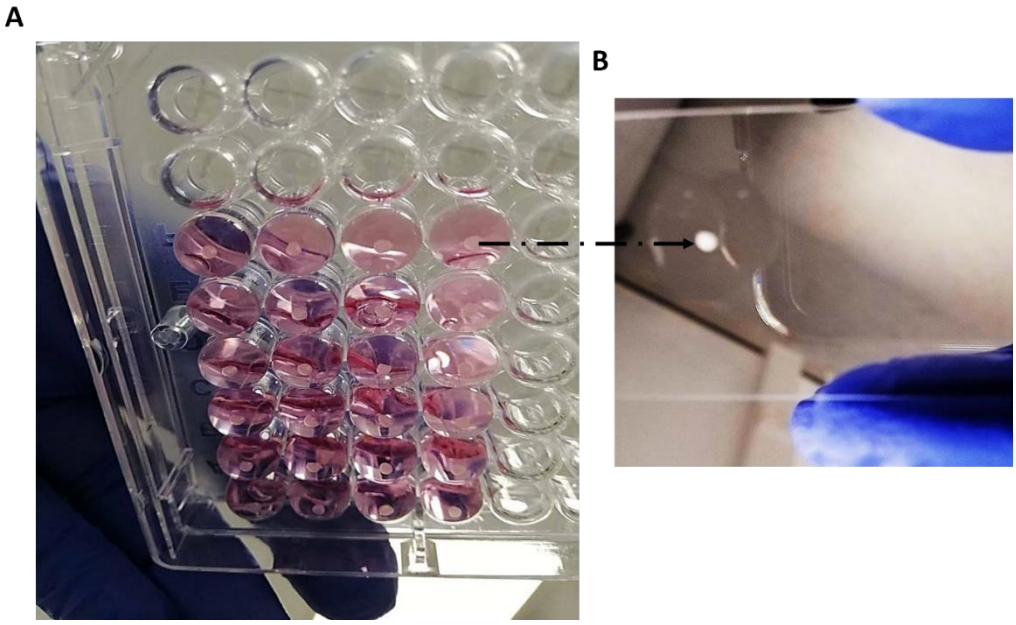

Figure 4.4: Pictures taken from the bottom of the round bottomed 96-well plate. Each well contains $2x10^5$ Y201-C cells per spheroids, cultured in DMEM/F12 media supplemented with 0.25 % MC. Picture taken after 24 h of spheroids culture (**A**). The arrow is pointing the spheroids on a microscope slide (**B**).

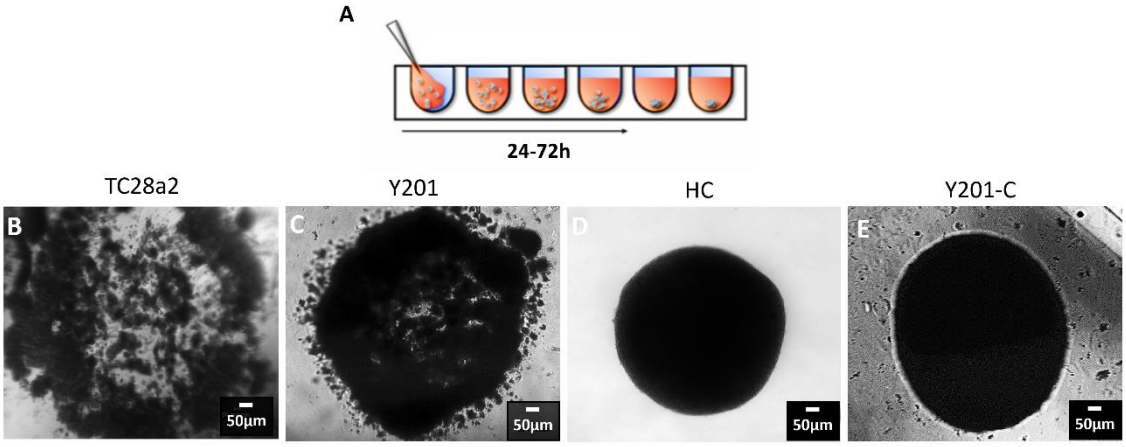

F	Code	Cell type	Formation of spheroids (72h)
	TC28a2	Human tumoral chondrocytes	**Unsuccessful**
	Y201	Human TERT bone marrow immortalised stem cells	**Unsuccessful**
	HC	Human primary foetal chondrocytes	**Successful**
	Y201-C	Y201 differentiated in chondrocytes	**Successful**

Figure 4.5: Manufacturing of spheroids with four different cell types: TC28a2, Y201, HC, Y201-C. Scheme of the spheroid's formation analysis from the seeding to the spheroid formation (**A**). Phase contrast brightfield images of spheroids after 72 hours with TC28a2 (**B**), Y201 (**C**), HC (**D**) and Y201-C (**E**). Scheme of the cell type used for the experiments: code, name of the cells and result of the trial of spheroids formation in 72 hours (**F**).

4.3.2 Spheroid's growth kinetics

To determine the HC and Y201-C spheroids growth dynamics, images were collected at days 1, 3 and 7 (**Figure 4.6A**), and the change in spheroids diameter, area, circularity and roundness were monitored and plotted over 7 days culture (**Figure 4.6B,C**). The diameters and area of spheroids with both HC and Y201-C decreased gradually over culture time (**Figure 4.6B**). In fact, HC spheroids diameter of 1300 ± 150 µm at day 1 was statistically different ($p<0.001$) from both day 3 (790 ± 100 µm) and day 7 (600 ± 90 µm). Furthermore, the HC spheroids area decreased from 0.46 ± 0.05mm^2 at day 1 to 0.38 ± 0.02 mm^2 at day 3 and 0.22 ± 0.01 mm^2 at day 7. Y201-C spheroids followed a similar trend, indeed the diameter at day 1 (1250 ± 60 µm) was statistical different ($p<0.0001$) from day 3 (990 ± 50 µm) and day 7 (800 ± 20 µm). Also, Y201-C spheroids areas decreased over culture, from 0.51 ± 0.02 mm^2 at day 1 to 0.45 ± 0.01 mm^2 at day 3 and 0.35 ± 0.01 mm^2 after 7 days.

Regarding the circularity and roundness, as reported in the graph in **Figure 4.6C**, both HC and Y201-C showed a great circularity with a value between 0.8 and 1 over 7 days of culture. On the other side, the spheroids roundness was higher than 0.75, except for the HC at day 1, where the samples showed a big standard deviation with a value of 0.65 ± 0.18.

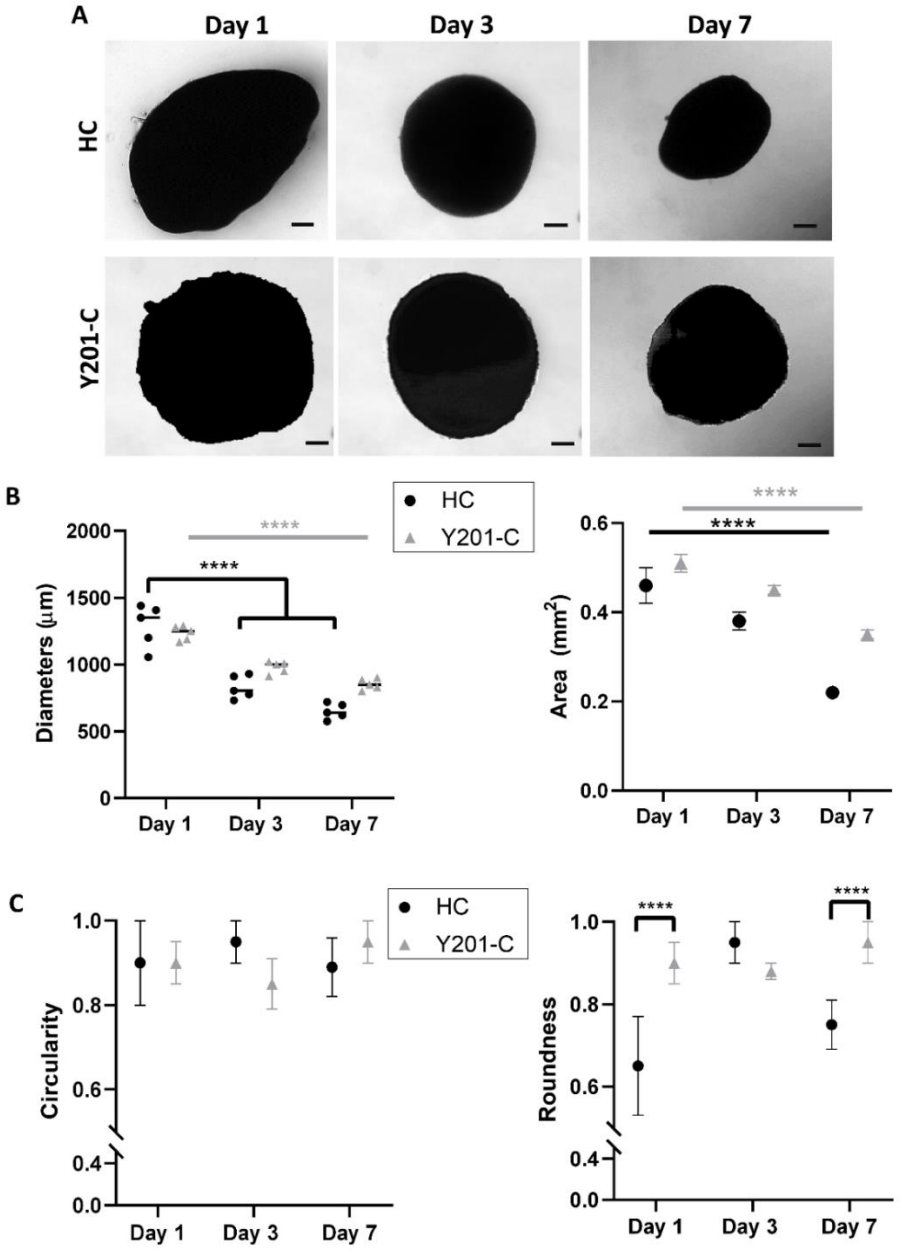

Figure 4.6: HC and Y201-C spheroids pictures taken at day 1, day 3 and day 7. Bars: 100 µm (**A**). Graphs reporting the change in spheroids diameter and area at the respective time points for HC and Y201-C (**B**). Analysis of the circularity and roundness for HC and Y201-C (**C**). Statistics: **** p<0.0001.

4.3.3 Spheroids viability assessment

Spheroids viability was qualitatively evaluated with the Live/Dead assay for HC (**Figure 4.7A**) and Y201-C (**Figure 4.7B**) at days 1, 3 and 7, showing high number of living cells (stained in green by Calcein) at days 1 and 3, with the presence of few dead cells (stained in red by Ethidium Bromide). Both samples showed an increase of dead cells at day 7. The localisation of these dead cells was not specific. The images were captured with a fluorescence

microscope. Attempt to use a confocal microscope to have a 3D image failed due to the high fluorescence of the whole spheroid, making hard to discriminate the single cells. Indeed, multiple viability assays were performed to understand and confirm the behaviour of cells within spheroids in 7 days of culture.

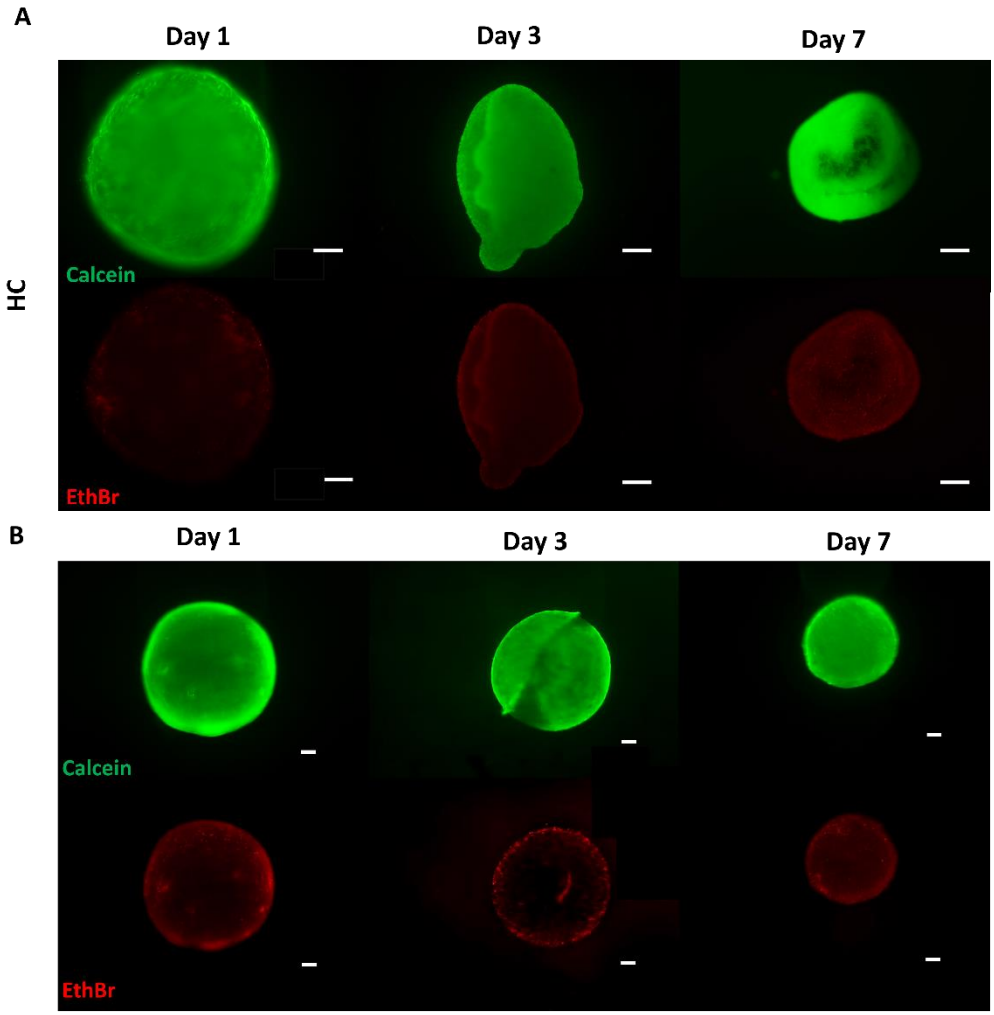

Figure 4.7: HC and Y201-C spheroids Live/Dead assay at days 1, 3 and 7 for HC (**A**) and Y201-C (**B**). Bars: 100 µm. Calcein stains live cells (green) and Ethidium Bromide (EthBr) stains dead cells (red).

Cells metabolic activity within spheroids was estimated analysing ATP production with CellTiter-Glo® 3D assay (**Figure 4.8A**). Both cells showed a similar trend with a statistically significant ($p<0.0001$) decrease of cells metabolic activity at day 7 of culture, compared to day 1. Particularly, HC spheroids presented a value of $3.1 \times 10^5 \pm 0.2 \times 10^5$ RLU at day 1, which was statistically different to $1.9 \times 10^5 \pm 0.1 \times 10^5$ RLU at day 7. On the other side, Y201-C presented a value of $3.5 \times 10^5 \pm 0.5 \times 10^5$ RLU at day 1, statistically different to $1.5 \times 10^5 \pm 0.3 \times 10^5$ RLU for Y201-C spheroids.

Furthermore, time-dependent viability of spheroids quantitatively measured with the CellTox™ Green Kit. This assay uses asymmetric cyanine dye that is excluded from viable cells but stains the DNA from dead cells. Results are reported as the percentage of viable cells. **Figure 4.8B** showed that the viability of cells in Y201-C spheroids decreased from the 95 ± 2 % at day 1 to 68 ± 3 % at day 7 ($p<0.001$), while HC spheroids were less viable, reporting a percentage of living cells about 80 ± 3 % at day 1, which dramatically decreased to 50 ± 2 % at day 7 ($p<0.001$).

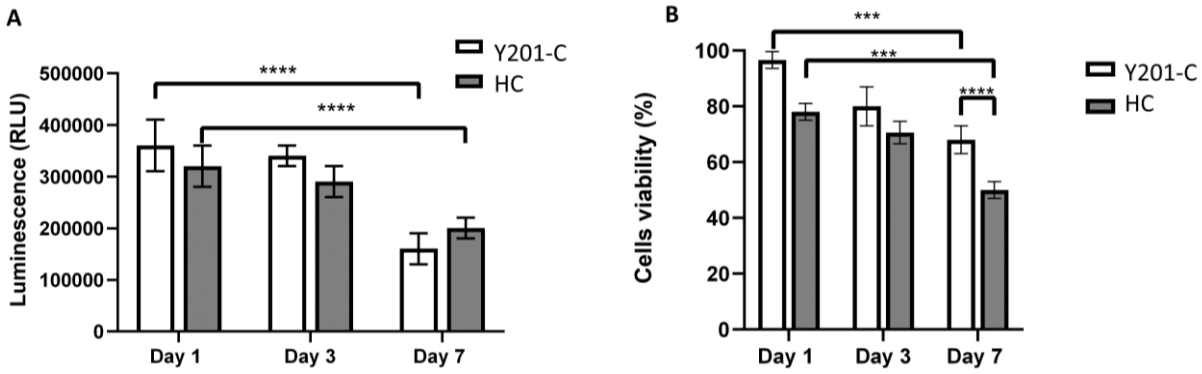

Figure 4.8: HC and Y201-C spheroids metabolic activity via CellTiter-Glo® 3D assay at days 1, 3 and 7 for both cells type (**A**). Cells viability percentage obtained by CellTox™ Green Assay (**B**). Statistics: **** $p<0.0001$, *** $p<0.001$.

4.3.4 Analysis on spheroids apoptosis and necrosis

Analyses of ultrathin sections were performed with TEM to estimate the preservation of cells ultrastructure within the spheroids over culture (**Figure 4.9**). At day 2 of incubation, in both HC (**Figure 4.9A-C**) and (**Figure 4.9G-I**) spheroids, cells were closely contacting and tightly packed with a well-developed intracellular structure, retaining cells their nuclei (N), mitochondria and endoplasmic reticula (ER) both in the spheroids core (**Figure 4.9A,B,G,H**) and in the peripheral regions (**Figure 4.9C,I**). Interestingly, lots of dividing cells were observed at day 2 in the Y201-C samples (**Figure 4.9H,I**). However, after 7 days, cells degeneration within the spheroids was observed with convolution of cellular surface, nuclear fragmentation, and chromatin clumping (red arrows) and the presence of vacuoles (purple arrows). This phenomenon was much more evident in the HC spheroids (**Figure 4.9D-F**) compared to the

Y201-Chondro (**Figure 4.9J-L**). Furthermore, signs of ECM accumulation were observed at this stage in core of spheroids (**Figure 4.9D,E,J,K**).

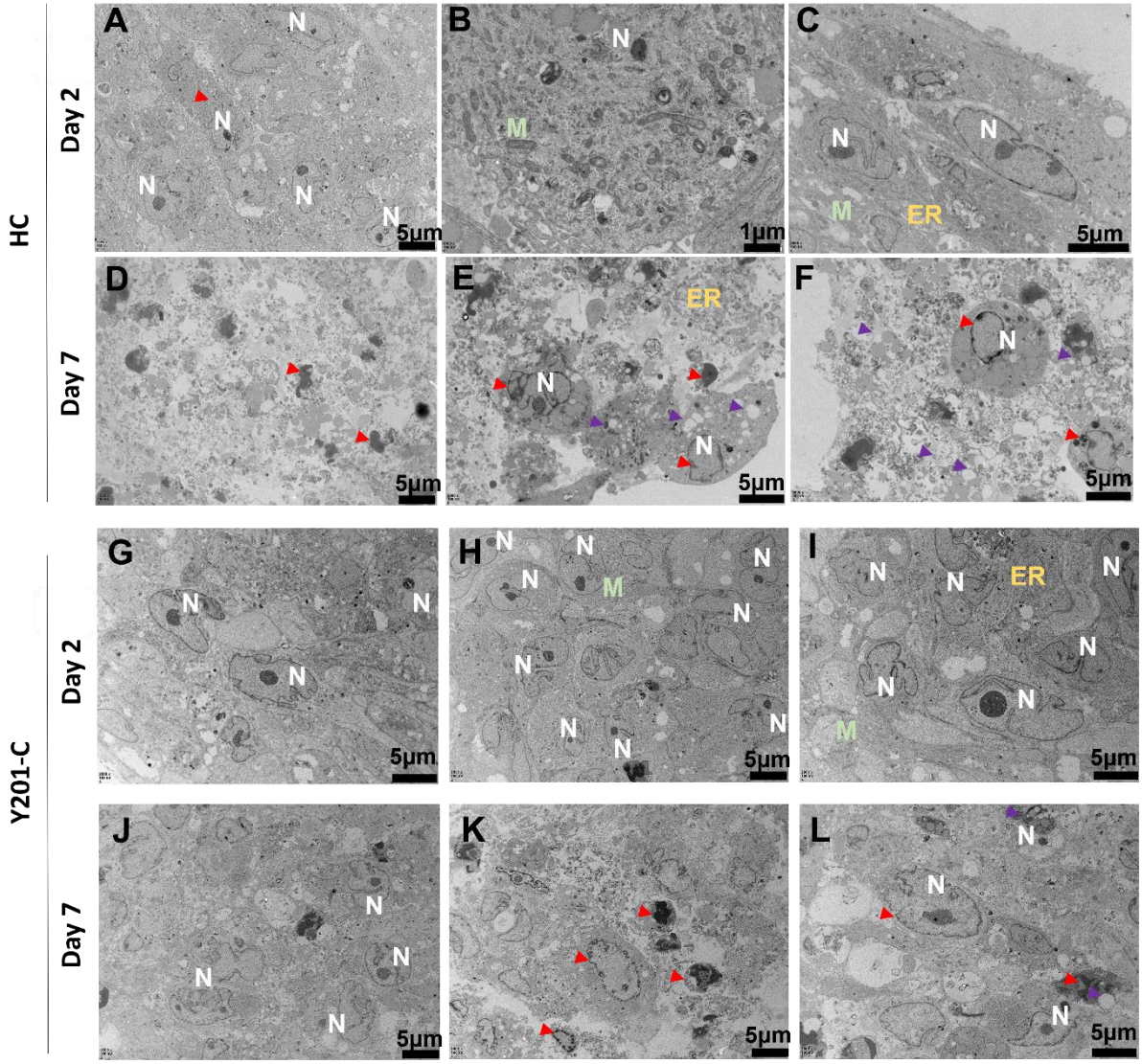

Figure 4.9: TEM images of changes to cellular ultrastructure during spheroids maturation *in vitro* at day 2 and day 7 for HC (**A-F**) and Y201-C (**G-L**) in the core (**A,B,D,E,G,H,J,K**) and in the peripheral zone (**C,F,I,L**); specific organelles are reported: nuclei (N), mitochondria (M) and endoplasmic reticula (ER) and cellular degeneration in form of chromatin clumping and nuclear fragmentation (red arrow) and vacuolisation (purple arrow).

To quantify the necrotic and apoptotic cells within spheroids over culture, a real-time Apoptosis and necrosis assay was performed, and graphs reported in **Figure 4.10.** This analysis allows to discriminate apoptosis from necrosis, measuring Annexin V binding happening in early-stage apoptosis (luminescence) and loss of membrane integrity indicating an apoptotic phenotype that leads to secondary necrosis (fluorescence). This assay was performed at early stage (day 1 - day 3) resulting in an increase in the apoptosis for both HC and Y201-C (**Figure**

4.10A) over the 72 h of monitoring, reaching a value of around 90 % for HC and 50 % for Y201-C with respect to the starting time point of analysis (time = 0 h). The assay was repeated at late stage (day 5 - day 7) confirming the TEM results, showing a higher increase of apoptosis in HC, which reached a value of 150 % compared to a 90 % of Y201-C spheroids. The necrosis process instead appeared to be slower with values that did not overpass the 50 % in early-stage and 60 % in late-stage for both cells (**Figure 4.10B**).

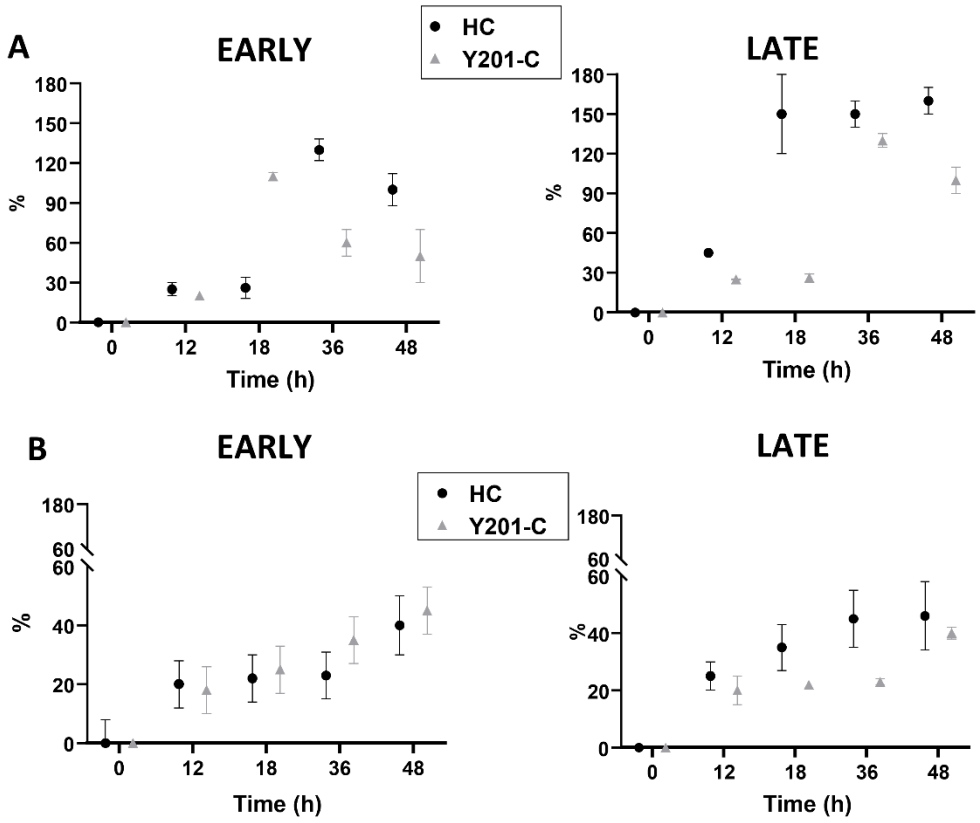

Figure 4.10: Apoptosis-Necrosis assessment via Real-time assay at early stage (day 1 - day 3) and late stage (day 5 – day 7) for HC and Y201-C. Graphs for HC and Y201-C at early and late stages reporting the apoptosis percentage (**A**) and the necrosis percentage (**B**).

4.3.5 Evaluation of spheroids morphology

SEM analysis was performed to assess HC and Y201-C spheroids morphology at day 2 (**Figure 4.11A,C**) and day 7 (**Figure 4.11B,D**). At early stage (day 2), spheroids exhibited a very smooth surface formed by intimately contacting compact cells. Also, HC spheroid showed to not be assembled yet in a 3D sphere (**Figure 4.11A**), while Y201-C had already formed an organised ovoidal shape (**Figure 4.11C**). After 7 days of culture the morphology of both aggregates changed. In fact, HC and Y201-C cells formed a regular round-shaped spheroid and the surface appeared to be rougher, with the presence of vesicles and microvilli. Interestingly, at day 7 the HC spheroids presented cells organising in lacunae (**Figure 4.11B insert**).

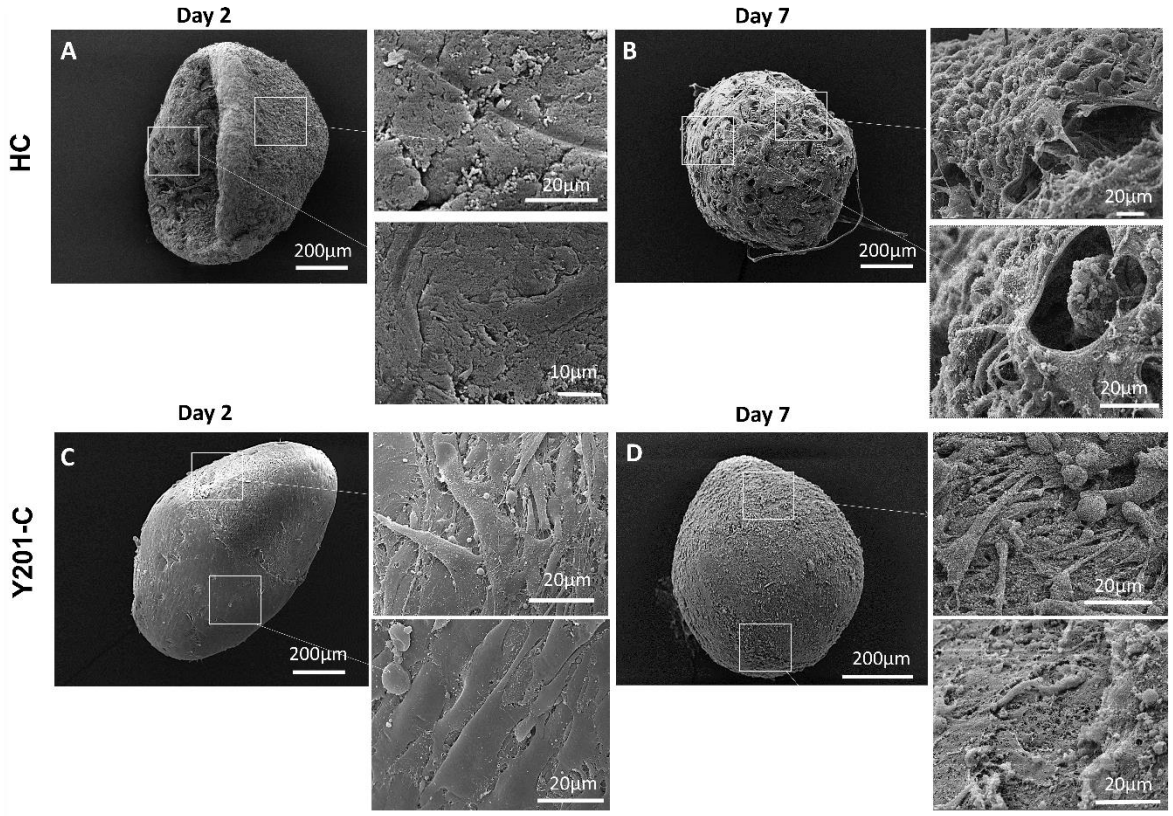

Figure 4.11: SEM analysis of HC and Y201-C spheroids at day 2 (**A,C**) and day 7 (**B,D**). Inserts report a higher magnification on the surface morphology of spheroids.

4.3.6 Chondrosphere formation and maturation assessment

For the formation of chondrospheres, after 7 days of spheroids culture, multiple trials were exploited. The first experiment was based on combining 10 - 15 spheroids to form a chondrosphere, suspending cells in DMEM/F12 loaded with 0.25 % MC having as a control the suspension of spheroids in DMEM/F12 without the presence of MC (**Figure 4.12**). Both with and without MC, spheroids were not able to agglomerate and fuse after 14 days of culture, when seeded in the 24 - well plate. In the trial with DMEM/F12 with MC, spheroids appeared totally disrupted, whilst in the experiment with the absence of MC, spheroids didn't agglomerate but remained intact and the only defect present was a hole in their middle, probably related to their handling.

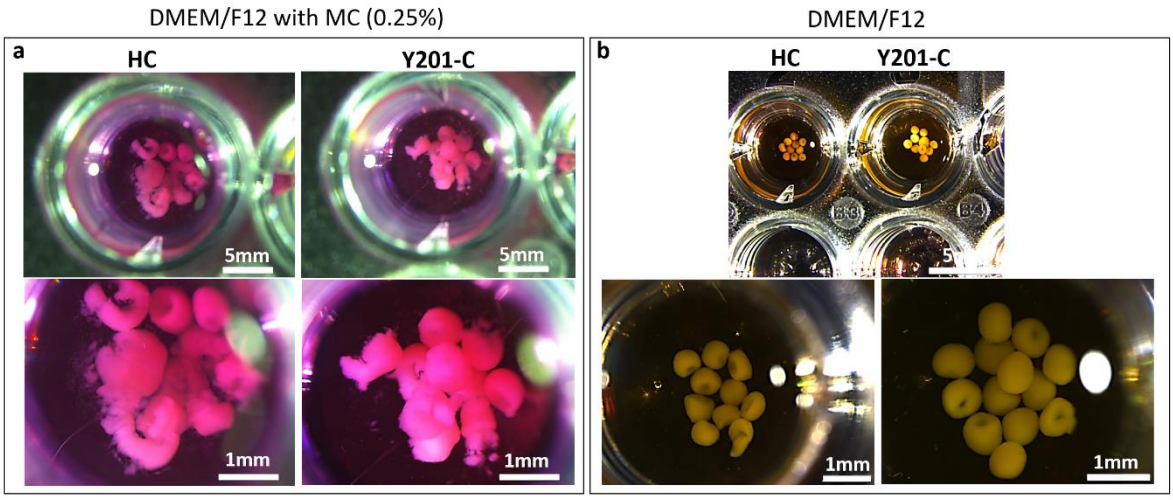

Figure 4.12: Chondrosphere fusion trial after 21 days of culture in 48-well plate with (**A**) or without (**B**) the addition of MC.

The third trial was based on the use of GEL coated PLGA - membrane which allowed spheroids fusion (**Figure 4.13**), as evidenced after 21 days of culture. From day 0 of spheroids seeding on the membrane, it was observed the presence of spheroid migration and agglomeration between each other's and with the membrane, as showed by light microscopy images. This result was confirmed by SEM, where it was visible the fusion of near spheroids and their adhesion to the GEL-coated membrane. The membrane appeared covered by a cells sheet suggesting that these like the environment and adapting themselves to it.

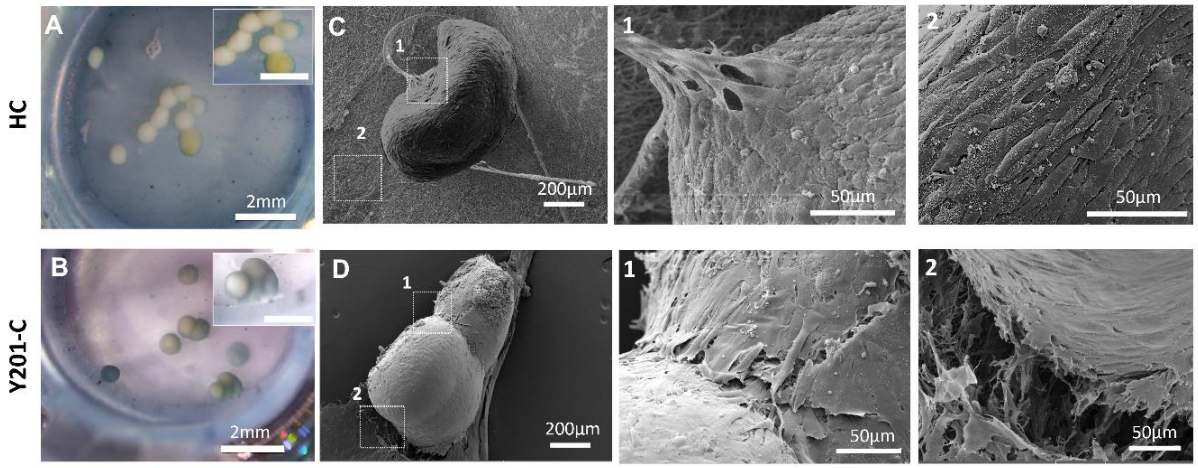

Figure 4.13: Chondrosphere formation and maturation after 21 days of culture. Brightfield images taken of spheroids seeded on the membrane and some higher magnifications in inserts for HC (**A**) and Y201-C (**B**). SEM images of chondrosphere after 21 days of culture on PLGA-GEL membrane of HC (**C**) and Y201-C (**D**). Higher magnification in the areas of interest (1, 2).

4.3.7 Chondrogenic potential and neo-cartilaginous tissue production

As a first step in the evaluation of cartilaginous tissue production, a quantitative assay to assess the production of GAGs by cells was performed with Alcian Blue and guanidine-hydrochloride (**Figure 4.14)**. HC chondrospheres showed a great increase in GAGs produced by cells at 21 days (0.30 ± 0.02 μg) compared to day 7 (0.14 ± 0.02 μg) and day 0 (0.09 ± 0.01 μg) ($p<0.0001$); cells produced a three-fold enhanced GAGs content with the increase of chondrospheres culture time (**Figure 4.14A)**. A similar trend was exhibited by Y201-C chondrospheres, with a more gradual increase of GAGs production over culture time: GAGs amount doubled in the first 7 days of chondrosphere culture, from 0.09 ± 0.01 μg at day 0 to 0.20 ± 0.02 μg at day 7 ($p<0.001$), reaching a value around 0.25 ± 0.01 μg ($p<0.0001$) at day 21 (**Figure 4.14B)**. No statistical differences were observed between GAGs production by HC and Y201-C at days 1 and 21, whilst at day 7 Y201-C showed an increased GAGs accumulation compared to HC ($p<0.01$).

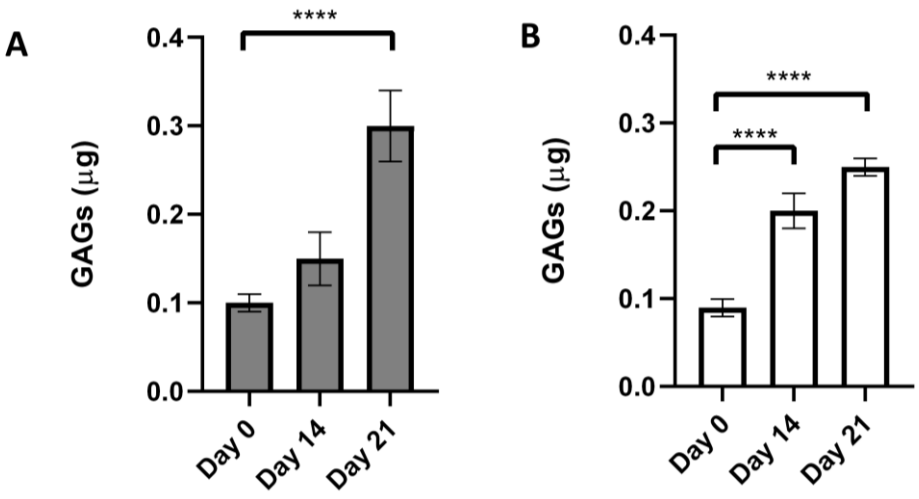

Figure 4.14: GAGs quantification analysis on HC (**A**) and Y201-C (**B**) for the chondrospheres at day 0,14 and 21 of culture. Results are normalised to spheroids at day 1. Statistics: **** $p<0.0001$.

Also, for evaluating the chondrogenic potential, the genes *sox9, col2a1, acan* were analysed with housekeeping gene *gapdh*. HC chondrospheres showed a 160 ± 60-fold and 220 ± 10-fold changes at days 1 and 21 (**Figure 4.15A**). Y201-C chondrospheres showed a statistically different fold change of *sox9* expression at day 21 (205 ± 30-fold) compared to day 1 (5 ± 1-fold) ($p<0.0001$) (**Figure 4.15D**). *Acan* expression of HC was significantly higher at day 21 (1800 ± 300-fold) compared to day 1 (490 ± 400-fold) ($p<0.0001$) (**Figure 4.15B**). Same trend was observed for Y201-C chondrospheres with a value of 7000 ± 250-fold at day 21 compared to

250 ± 200-fold at day 1 (**Figure 4.15E**). Similarly, the fold increase in *col2a1* expression was significantly higher at day 21 for both HC and Y201-C chondrospheres, compared to day 1: 20000 ± 200-fold vs. 60 ± 40-fold for HC ($p<0.0001$) (**Figure 4.15C**) and 4.0 ± 0.6-fold vs 2.2 ± 0.2-fold for Y201-C ($p<0.0001$) (**Figure 4.15F**).

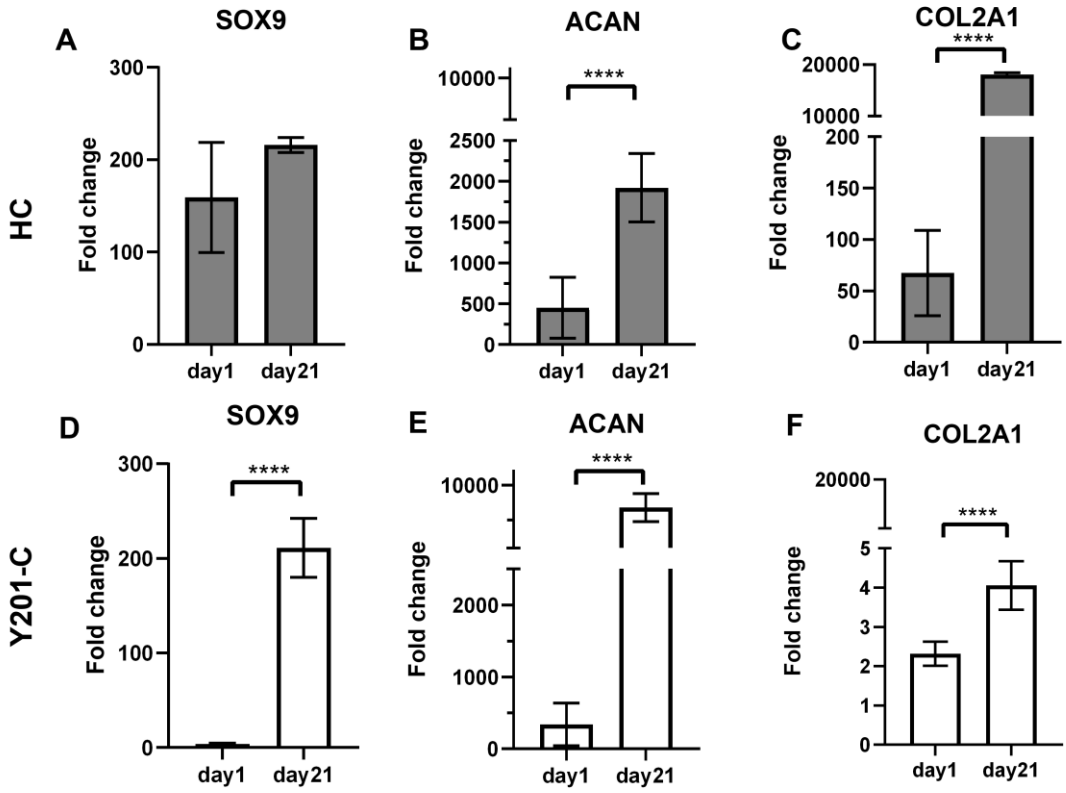

Figure 4.15: RT-qPCR analysis graphs showing the fold-change ($2^{-\Delta\Delta Ct}$) at days 1 and 21 of chondrospheres culture relative to spheroid at day 1: *sox9* for HC (**A**) and Y201-C (**D**), *acan* for HC (**B**) and Y201-C (**E**) and *col2a1* for HC (**C**) and Y201-C (**F**). Statistics: ****$p<0.0001$.

4.3.8 Spheroids growth in healthy and OA conditions

The growth dynamics of HC and Y201-C spheroids in Healthy, LC-OA, and HC-OA environments were studied on days 1, 4, and 10.

Figure 4.16 shows the results for HC: it was visible a progressive decrease in the size of Healthy spheroids from day 1 (**Figure 4.16A**) to day 4 (**Figure 4.16B**) and, particularly, to day 10 (**Figure 4.16E**). On the other side, during the on-set of OA, the growth dynamic of spheroids revealed a unique pattern, with spheroids of constant size throughout cultures at low (**Figure 4.16C,F**) and high cytokine concentrations (**Figure 4.16D,G**). This qualitative assessment was confirmed by quantitative analyses of spheroid diameter measurement over culture (**Figure 4.16H**). Healthy HC spheroids showed significant decrease in diameter from 1610 ± 100 µm at day 1

to 1450 ± 45 µm at day 4 and to 1050 ± 50 µm at day 10 ($p<0.0001$). In OA condition, a different tendency was detected, with the maintenance of a more constant diameter: LC-OA spheroids showed a diameter of 1480 ± 100 µm at day 4 and 1450 ± 50 µm at day 10 whereas HC-OA spheroids displayed a diameter of 1505 ± 70 µm at day 4 and 1650±50 µm at day 10. At day 10 HC spheroids diameter in healthy conditions were statistically different from both LC-OA and HC-OA ($p<0.0001$).

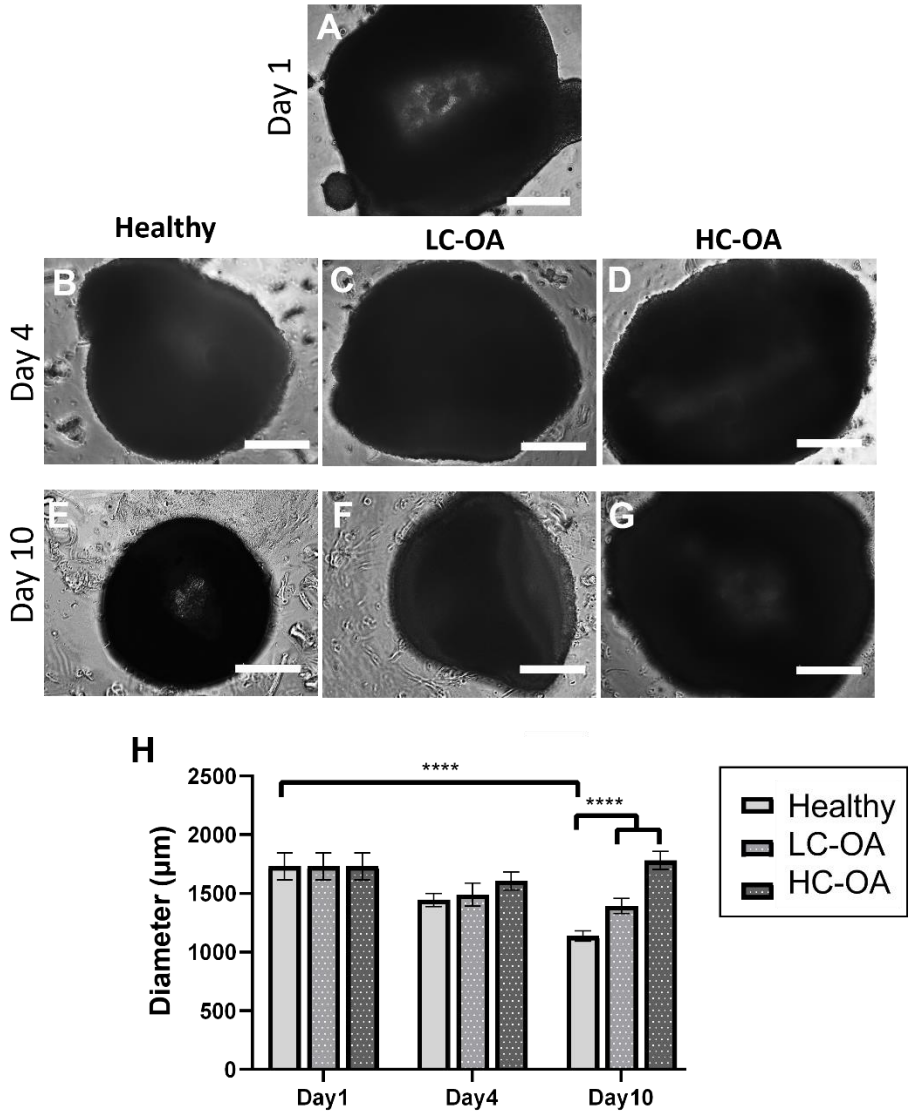

Figure 4.16: Spheroids growth. Images of HC spheroids at day 1 (**A**), day 4 (**B-D**) and day 10 (**E-G**) in Healthy (**A,B,E**) LC-OA (**C,F**) and HC-OA (**D-G**) conditions. Bars: 300 µm. Diameter length analysis (**H**). Statistics: ****$p<0.0001$.

Y201-C showed an analogous behaviour, where considerable reduction in the spheroids size in healthy conditions, from day 1 (**Figure 4.17A**) to day 10 (**Figure 4.17E**), was observed. Conversely, LC-OA and HC-OA samples showed the maintenance of a stable diameter over

culture (**Figure 4.17C,F** and **Figure 4.17D,G**, respectively for LC-OA and HC-OA). **Figure 4.17H** shows the diameter dimensions measurement. Healthy spheroids showed a clear decrease of diameter (from 1750 ± 50 µm at day 1 to 1490 ± 70 µm at day 4 and 1200 ± 20 µm at day 10) ($p<0.0001$) compared to LC-OA (1650 ± 55 µm at day 4 to 1490 ± 70 µm at day 10) and to HC-OA (1780 ± 100 µm at day 4 and 1850 ± 50 µm at day 10). At day 10 healthy samples showed a smaller diameter compared to OA conditions ($p<0.0001$).

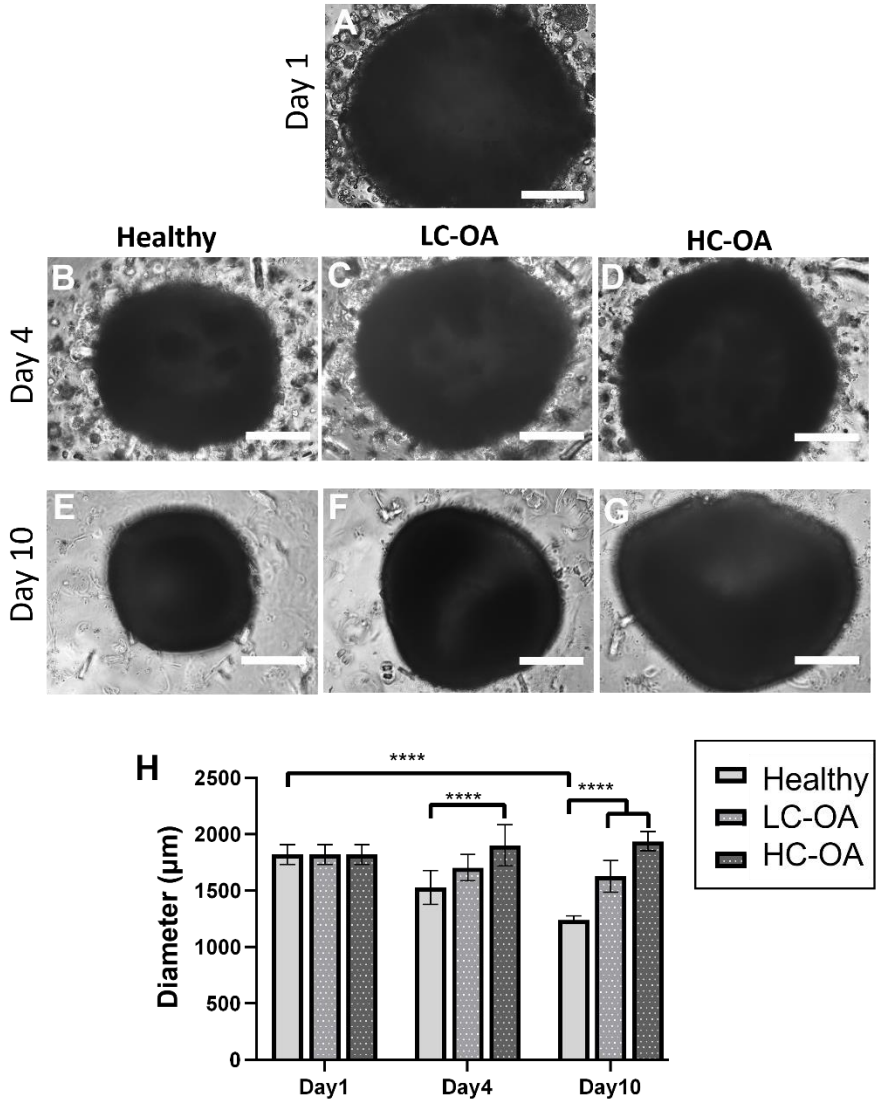

Figure 4.17: Spheroids growth. Images of Y201-C spheroids at day 1 (**A**), day 4 (**B-D**) and day 10 (**E-G**) in Healthy (**A,B,E**) LC-OA (**C,F**) and HC-OA (**D-G**) conditions. Bars: 300 µm. Diameter length analysis (**H**). Statistics: ****$p<0.0001$.

4.3.9 Cell metabolic activity, proliferation, and apoptotic tendency during OA progress

MTS assay was used to determine the mitochondrial activity of cells within spheroids of HC (**Figure 4.18A**) and Y201-C (**Figure 4.18B**). The metabolic activity of HC spheroids decreased

with time in both cases: from 0.072 ± 0.003 at day 1 to 0.04 ± 0.002 in healthy, ($p<0.0001$) 0.049 ± 0.001 in LC-OA ($p<0.0001$) and 0.053 ± 0.002 in HC-OA ($p<0.001$) conditions at day 10. On the contrary, Y201-C spheroids metabolic activity increased significantly from days 1 and 4 to day 10 in all conditions ($p<0.0001$). From the value of 0.079 ± 0.001 at day 1, healthy samples showed an increase of absorbance to 0.138 ± 0.002, LC-OA to 0.142 ± 0.005 and HC-OA to 0.152 ± 0.005. For HC at day 10, HC-OA and LC-OA samples showed higher metabolic activity compared to healthy ($p<0.001$) and for Y201-C, HC-OA showed higher metabolic activity compared to LC-OA ($p<0.05$) and healthy ($p<0.01$).

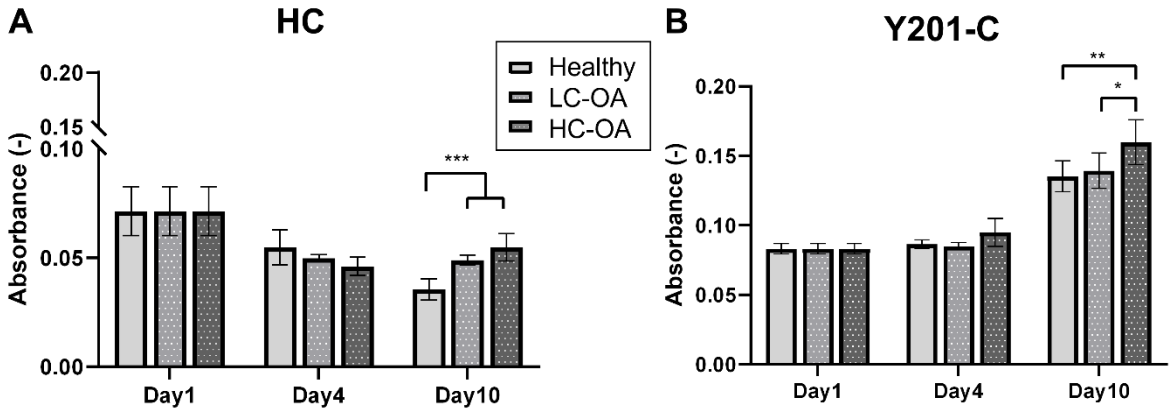

Figure 4.18: HC (**A**) and Y201-C (**B**) cells metabolic activity evaluated with MTS assay at day 1, day 4 and day 10 of spheroids culture in Healthy, LC-OA and HC-OA. Statistics: *$p<0.05$, **$p<0.01$ and ***$p<0.001$.

The spheroids collected and assembled on a GEL-coated PLGA membrane (as showed in **Figure 4.19**) were cryosectioned to assess proliferation and apoptotic tendencies after 21 days of culture in the three conditions, compared to control at day 1. Immunostaining for Ki-67, an antigen associated with cellular proliferation, was used to stain proliferative cells (green) and cells nuclei were counterstained with DAPI (blue) (**Figure 4.19**). At day 21, the signal corresponding to Ki-67 staining was increased in both HC (**Figure 4.19A**) and Y201-C (**Figure 4.19B**) in the pathological samples, compared to the healthy samples at day 21 and to the control at day 1. On the edges of the spheroids, few proliferative cells were observed in Y201-C samples at day 1, as well as in Healthy samples at day 21 (**Figure 4.19B**). Few proliferative cells were observed in healthy sample of HC cells at day 21, likewise: however, no Ki-67-stained cells were observed in control at day 1 for HC (**Figure 4.19A**).

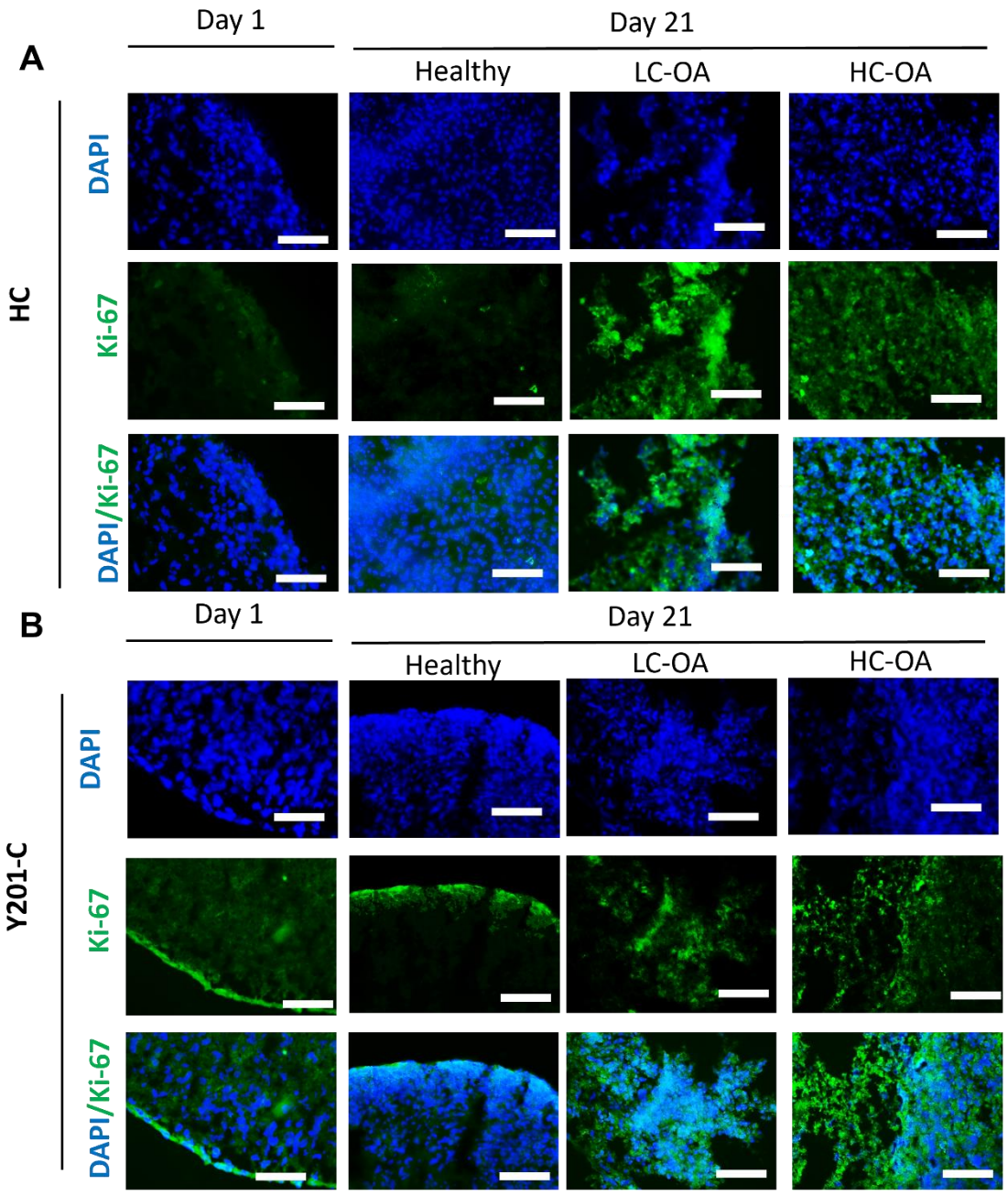

Figure 4.19: Analysis upon cells proliferation at day 1 and day 21 in healthy, LC-OA and HC-OA conditions by staining of Ki-67 (green) proliferation marker; cells nuclei are counterstained with DAPI (blue), for HC (**A**) and Y201-C (**B**). Bars: 150 µm.

Chondrocyte apoptosis were examined on cryosections at 21 days using a high magnification (63 x) and staining cells nuclei with DAPI (**Figure 4.20**). Both HC and Y201-C cells revealed predictable rounded shaped nuclei homogeneously dispersed within the tissue slices in healthy state (**Figure 4.20A,B**). In OA conditions, heterogeneous cell distribution was instead observed: particularly, HC and Y201-C cells showed a propensity to agglomerate and form clusters. Furthermore, cells in pathological conditions had fractured and smaller nuclei: this

feature was observed in HC-OA condition, especially for HC cells (**Figure 4.20C**) and slightly less for Y201-C (**Figure 4.20F**).

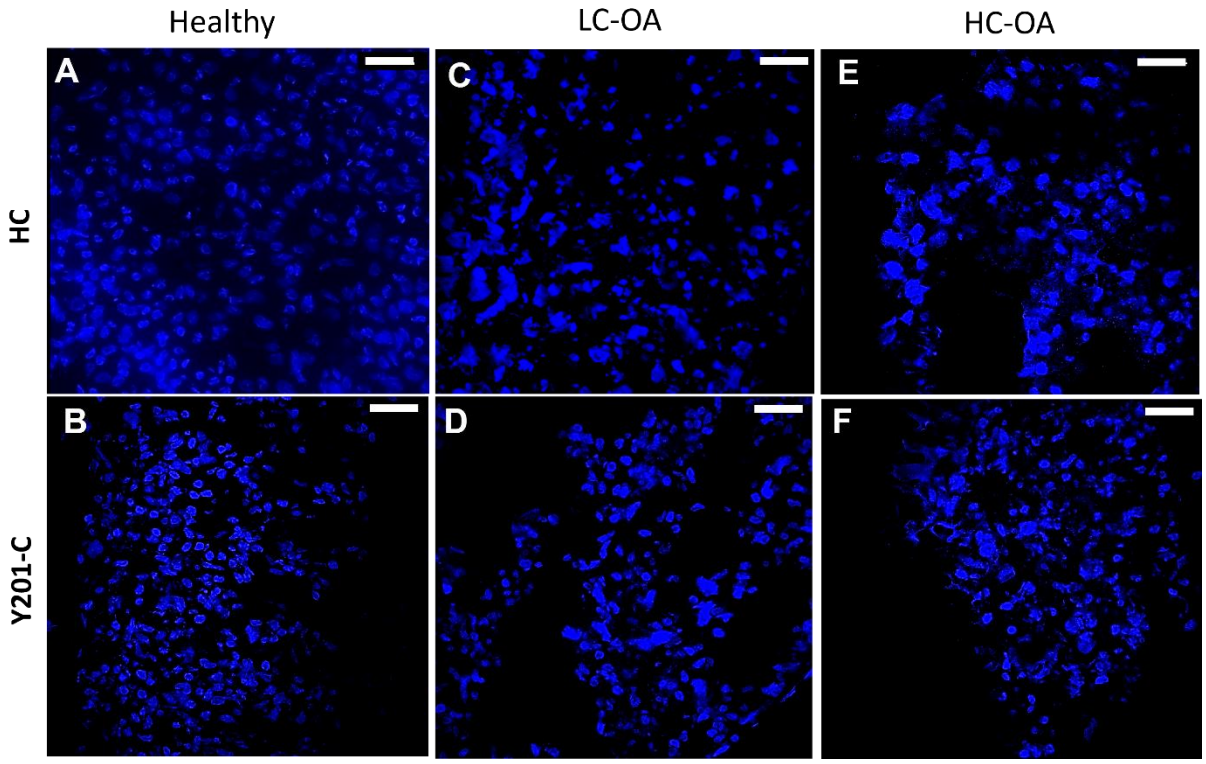

Figure 4.20: Evaluation of HC and Y201-C cells nuclei (stained with DAPI) morphology at 21 days in healthy, LC-OA and HC-OA conditions 63 x magnification. Bars: 20 µm.

4.3.10 Analysis on gene expression of anabolic and catabolic markers

For HC and Y201-C under the three conditions, it was investigated the expression of anabolic (*sox9, col2a1* and *acan*) (**Figure 4.21**) and catabolic (**Figure 4.22**) (*mmp13* and *adamts-5*) markers. Also, the ratio between *col2a1* and *col1a2* was assessed.

Starting from the anabolic markers, over the course of 21 days of culture in healthy conditions, both HC and Y201-C demonstrated a considerable increase in the expression of *sox9, acan,* and *col2a1* markers. Regarding *sox9*, both cells in the healthy condition at day 21 showed an up-regulation of the expression of this marker compared to both OA conditions ($p<0.0001$): HC displayed a change of 56.0 ± 4.0-fold in healthy samples compared to 0.2 ± 0.1-fold and 0.9 ± 0.1-fold respectively in LC-OA and HC-OA samples (**Figure 4.21A**); Y201-C showed a fold-change of 19.9 ± 2.6 in Healthy conditions compared to 1.2 ± 0.1-fold and 1.5 ± 0.5-fold respectively in LC-OA and HC-OA conditions (**Figure 4.21B**). *Acan* expression showed a similar trend and both HC and Y201-C showed an up-regulation of its expression already from day 10 in Healthy condition compared to both OA conditions. Specifically, at day 10 HC cells showed

a fold-change of 2.2 ± 0.3, statistically different from 0.3 ± 0.0-fold in LC-OA and 0.3 ± 0.1-fold in HC-OA ($p<0.0001$). At day 21, instead, healthy samples displayed a very high value of fold-change (895.7 ± 158.0) compared to approximately 0-fold in LC-OA and HC-OA ($p<0.0001$) (**Figure 4.21C**). Y201-C showed the same trend, with a statistically significant increment of gene expression at day 10 in healthy conditions (75.4 ± 11.9-fold) compared to LC-OA (47.8 ± 13.1-fold) ($p<0.05$) and HC-OA (28.1 ± 4.8-fold) ($p<0.01$) (**Figure 4.21D**). *Col2a1* followed the same tendency of the two others anabolic markers at day 21. For HC, healthy samples showed a value of 15921.9 ± 4653.0-fold compared to 491.5 ± 24.1-fold and 54.7 ± 1.3-fold of LC-OA and HC-OA respectively, all statistically different from each other's ($p<0.0001$) (**Figure 4.21E**); similarly, for Y201-C, healthy samples at day 21 displayed a value of 206.7 ± 8.5-fold compared to 76.4 ± 1.5-fold for LC-OA and ~1 HC-OA (**Figure 4.21F**). At day 10, both cells showed values around 0 for OA conditions. HC in healthy condition, already at day 10, showed a fold-change *col2a1* gene of 277.7 ± 96.8.

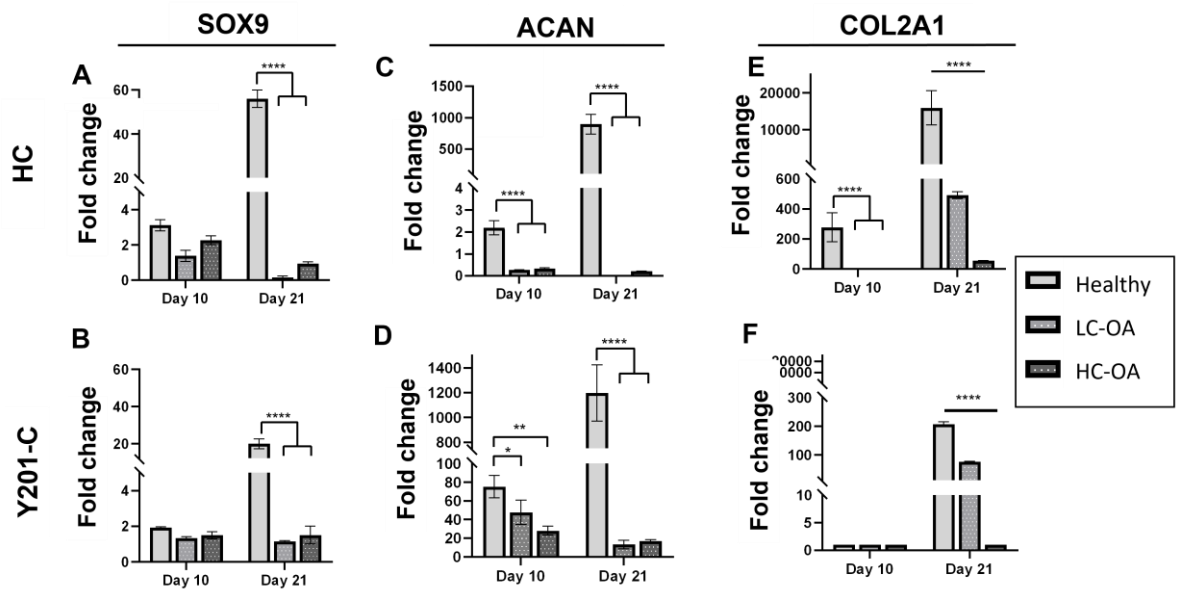

Figure 4.21: Gene expression of anabolic markers via RT-qPCR analysis for HC and Y201-C: fold change of *sox9* (**A,B**), *col2a1* (**C,D**) and *acan* (**E,F**) in Healthy, LC-OA and HC-OA conditions. Statistics: **** $p<0.0001$, **$p<0.01$, $p<0.05$.

For catabolic markers instead, **Figure 4.22A,B** shows *mmp13* expression for HC and Y201-C. *Mmp13* expression increased from day 1 to day 10 for HC sample in all condition and then, decreased after 21 days (**Figure 4.22A**): HC-OA showed a much higher expression at both day 10 and day 21 compared to the LC-OA and Healthy samples (206417.9 ± 24351.0-fold vs. 154465.8 ± 31918.0-fold and 5773.6 ± 991-fold respectively at day 10; 132390.8 ± 9734.0-fold vs. 9767.9 ± 466.1-fold and 10036.4 ± 1609.2-fold respectively at day 21). For Y201-C, instead,

a similar trend was observed for LC-OA and healthy condition. *Mmp13* fold-change decreased from 50.9 ± 22.2 at day 10 to 23.5 ± 8.0-fold at day 21 in Healthy samples, and from 57.9 ± 12.4 at day 10 to 40.5 ± 1.2-fold at day 21 in LC-OA samples. *Mmp13* expression significantly increased over culture in the case of HC-OA, showing values significantly higher (73.4 ± 10.9-fold at day 10 and 396 ± 61.9-fold at day 21) compared to the other two conditions ($p<0.0001$) (**Figure 4.22B**). *Adamts-5* catabolic marker expression increased at day 10 for both cell types in each condition. HC cells showed statistically significant different values between the three conditions at day 10 and day 21, with LC-OA showing the highest values of fold-change at day 10 (20.1 ± 2.7-fold, compared to 3.3 ± 0.2-fold for Healthy and 13.1 ± 0.3-fold for HC-OA ($p<0.0001$)) and the lowest at day 21 (1.2 ± 0.4-fold, compared to 14.0 ± 0.9-fold for healthy and 33.3 ± 1.1-fold for HC-OA ($p<0.0001$)) (**Figure 4.22C**). Y201-C showed statistically significant differences in *adamts-5* expression between the three conditions, with LC-OA showing the highest fold-change. Indeed, LC-OA *adamts-5* expression was 149.2 ± 7.6-fold at day 10, compared to 76.4 ± 10.7-fold for healthy and 96.4 ± 20.3-fold for HC-OA ($p<0.01$), while at day 21 it was 157.9 ± 28.5-fold, compared to 77.4 ± 6.9-fold for healthy and 6.5 ± 1.2-fold for HC-OA samples ($p<0.001$) (**Figure 4.22D**).

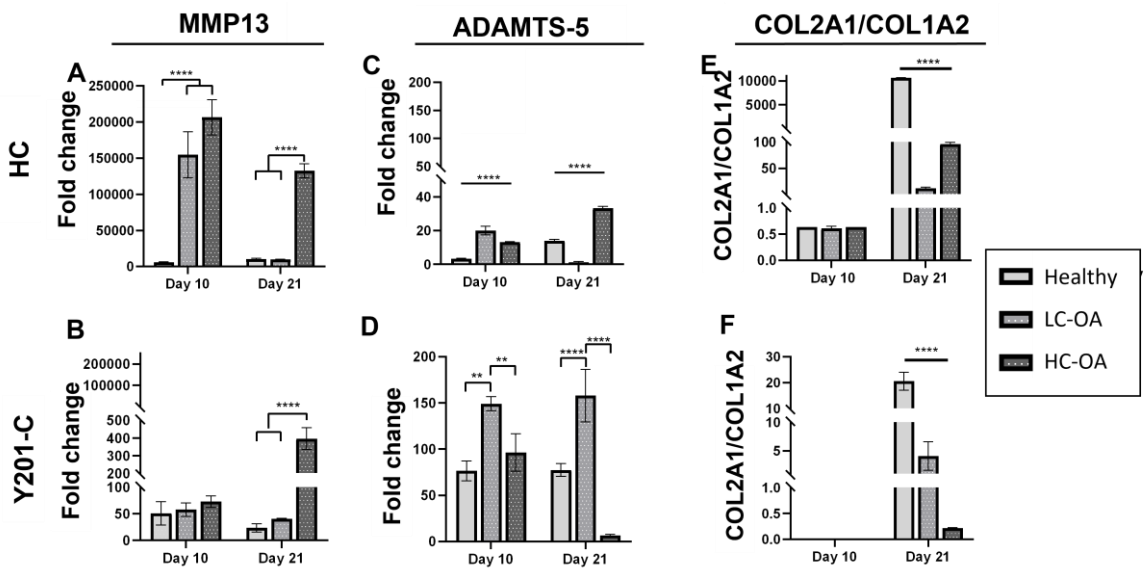

Figure 4.22: Gene expression of catabolic markers via RT-qPCR analysis for HC and Y201-C: fold change of *mmp13* (**A,B**), *adamts-5* (**C,D**) in Healthy, LC-OA and HC-OA conditions. Report of the *col2a1/col1a2* ratio for HC (**E**) and Y201-C (**F**) Statistics: **** $p<0.0001$, ** $p<0.01$, $p<0.05$.

Col2a1/Col1a2 ratio did not differ between the three conditions after 10 days of culture (~0.65 for HC and ~0 for Y201-C), while it showed statistically significant differences at day 21: HC displayed a value of 10614.0 ± 32.7 in healthy condition vs. 12.3 ± 2.5 and 96.4 ± 3.2

respectively in LC-OA and HC-OA; Y201-C displayed a value of 20.66 ± 3.5 in healthy samples vs. 4.1 ± 2.5 and 0.2 ± 0.1 respectively in LC-OA and HC-OA.

4.3.11 Assessment of the tissue obtained in Healthy and OA state

Histological and Immunohistochemical analyses were performed at days 1 and 21 for healthy, LC-OA and HC-OA conditions in HC (**Figure 4.23A**) and Y201-C cells (**Figure 4.23B**).

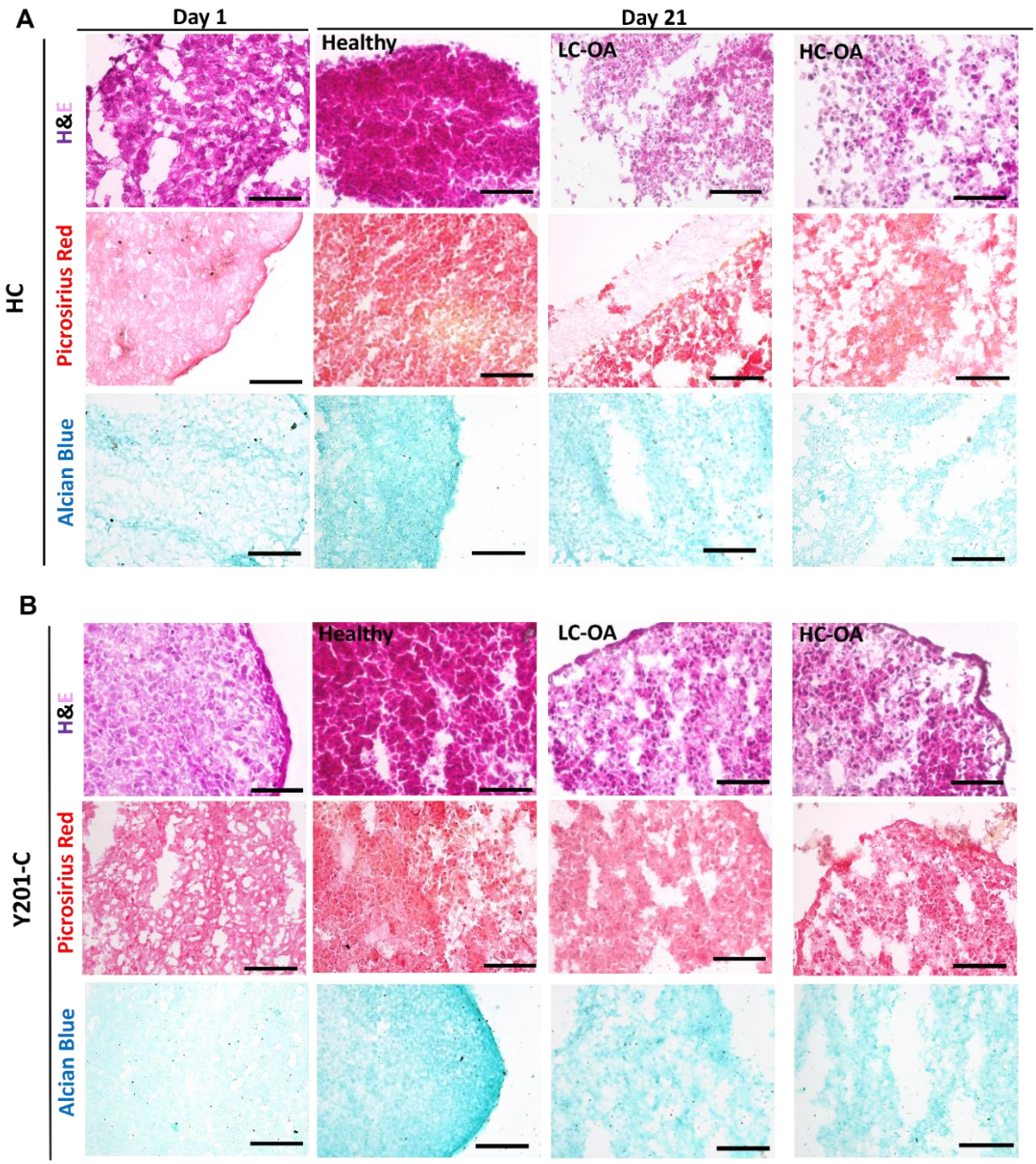

Figure 4.23: Histological staining of H&E, Alcian Blue and Picrosirius Red on obtained cryosection of HC (**A**) and Y201-C (**B**) samples in Healthy, LC-OA and HC-OA condition at days 1 and 21. Bars = 150 µm.

Starting from Histology, H&E staining intensity was higher for both HC and Y201-C in healthy samples at day 21 compared to day 1; however staining intensity at day 21 was lower for both OAs conditions compared to healthy and to day 1 control conditions. In addition, both cell types demonstrated a reduction in cellularity in OA microtissues, with this feature being more noticeable in the centre of the construct compared to the margins, especially for HC samples. Regarding the collagen deposition (stained with Picrosirius Red), HC and Y201-C showed a very intense red colouration at day 21 in healthy condition compared to day 1. Even if the collagen staining was observed at 21 days in OA conditions, the tissue was more compact, and the collagen more homogenously distributed within the tissue slice in the case of healthy samples at day 21. Finally, the mucopolysaccharides deposition (stained with Alcian Blue), showed similar results to the collagen, for both cells: healthy samples of HC and Y201-C showed at day 21 a more intense staining compared to day 1 control and to both LC-OA and HC-OA conditions at day 21.

Regarding IHC analyses, microtissues revealed an increase in Coll II and aggrecan staining in healthy condition at 21 days, compared to both control at day 1 and OAs conditions at day 21, for both HC and Y201-C cells (**Figure 4.24**). Coll II and aggrecan staining were less prominent in the OA-HC and OA-LC samples compared to Healthy condition at day 21 and to control at day 1. In addition, IHC results showed the presence of a more fragmented tissue, as anticipated by Hhstology analysis in LC-OA and HC-OA for both cell type, with a prevalence of this feature observed in HC-obtained tissues (**Figure 4.24B**).

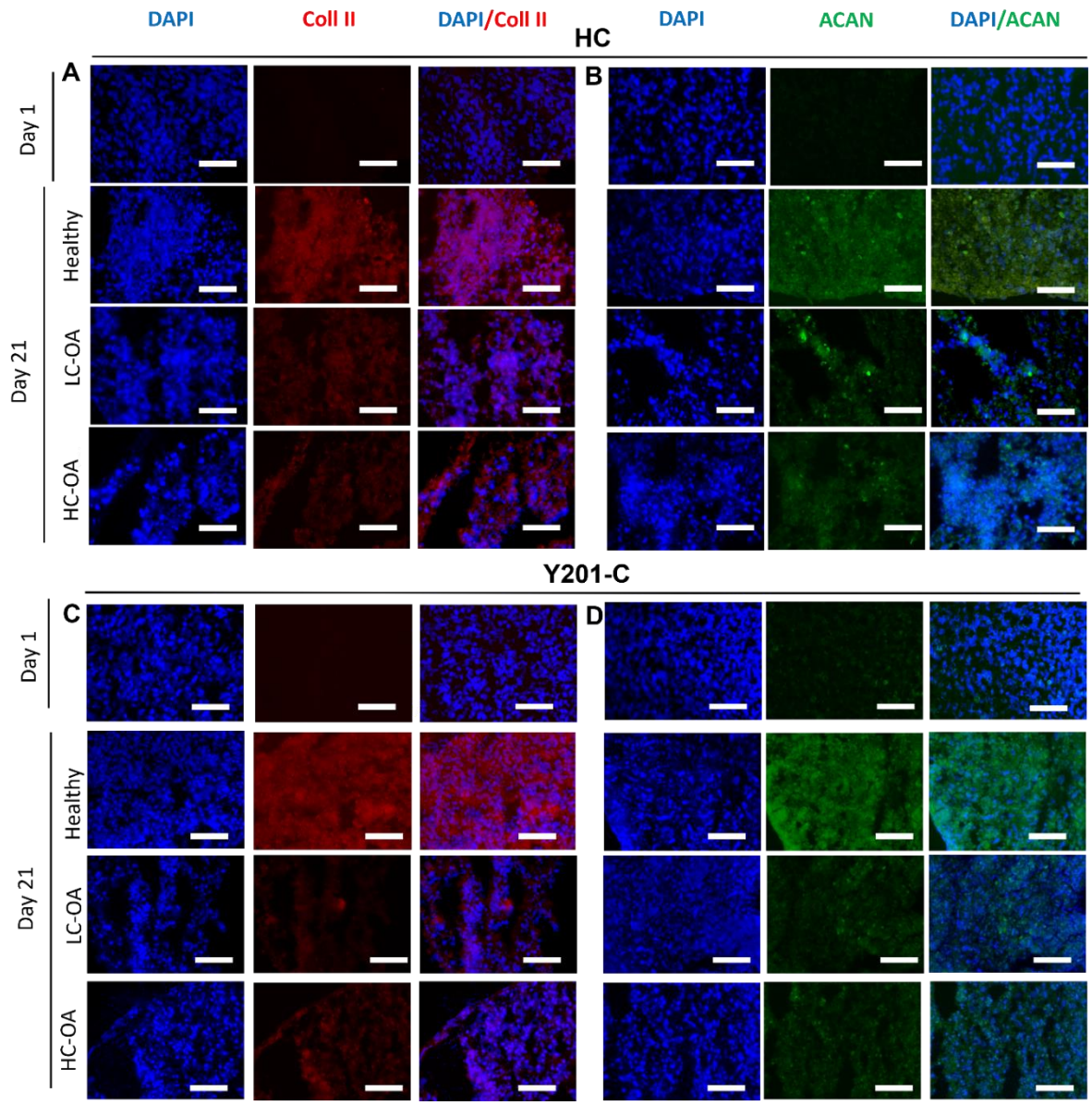

Figure 4.24: IHC on cryosection of HC (**A,B**) and Y201-C (**C,D**) in Healthy, LC-OA and HC-OA conditions: Coll II (AlexaFluor594 - Red) (**A,C**) and ACAN (Fluorescein - Green) (**B,D**). Nuclei are counterstained (DAPI- Blue). Bars = 150 µm.

4.4 Discussion

In accordance with the objectives of this chapter, three main points are discussed: the optimisation of a standard production of spheroids with primary chondrocytes and a bankable cell type (Y201-C), the ability of spheroids to assemble to form a few mm thick construct and the optimisation of a cytokines-induced OA model.

4.4.1 Optimisation of standardizable production of spheroids

The protocol used for the spheroids manufacturing allowed to obtain a standardizable process, which is of great utility for the translational potential of this technique. Among the

four different cell types tested, HC and Y201-C cells were the only ones being able to form a compact aggregate within 3 days of culture and for this reason, these were selected for further experiments. Both cells showed a similar trend in terms of growth kinetics and were able to form compact sphere after 7 days of culture (**Figure 4.6**), suggesting that cells adapt their packing density during spheroid's formation (Gionet-Gonzales & Leach, 2018). Spheroids dimension changed over the 7 days of culture reaching a value of approximately 600 µm for HC and 800 µm for Y201-C. Interestingly, for spheroid size, the efficacy was demonstrated in the Chondrosphere® clinical trial batches for spheroids with a diameter in the range 200 - 850 µm (EMA, 2017). The main difference between the two cells population was the variability of the diameter of HC spheroids in the first 24 h of culture, in fact HC cells were able to form a well-shaped sphere only after 3 days of culture, compared to the Y201-C that formed a spheroid already within 24 h. This delay in the formation of a rounded-shape construct was confirmed by the circularity and roundness analysis, important to assess spheroids morphological stability and homogeneity over time (Bellotti et al., 2016).

Multiple methodologies were used to examine the spheroids' time-dependent vitality. Live/Dead assay revealed a steady drop in the live/dead cell ratio in both cell types during the 7 days of culture, as well as the CellTiter-Glo® 3D assay, which revealed a considerable reduction in HC and Y201-C ATP generation from day 1 to day 7. However, CellTox™ Green assay, which measures cell membrane integrity and so reveals the dead cells with damaged border, showed that Y201-C maintained their viability (> 60 %) up to 7 days of culture, whereas HC spheroids viability dropped off the 50 % at day 7 (**Figure 4.8**). At this regard, literature studies demonstrated that, while MSCs-derived spheroids can be formed with diameters as large as 700-800 µm without a drastic cells' death, spheroids formed of other cells may be more vulnerable to limitations in nutrient transport (Gionet-Gonzales & Leach, 2018). Indeed, the decrease in Y201-C metabolic activity could be related to the change of cellular state over time, which is closely correlated to their metabolic activity and therefore ATP level (Anderer & Libera, 2002).

TEM analysis (**Figure 4.9**) was performed to evaluate the behaviour and state of cells within spheroids both in the core and in the peripheral region, since cells at different depths from the surface of the spheroid/aggregate are in different nutritional states and, thus, at different stages of the cell cycle: oxygenation gradients have been estimated to drop from 6 – 10 % at the surface to less than 1 % at the deepest layers (Bellotti et al., 2016). Both HC and Y201-C

spheroids, at early stage of incubation (day 2), showed that chondrocytes were tightly packed with well-developed intracellular structure retaining nuclei and cellular membrane and organelles. Also, Y201-C cells were undergoing mitotic division, meaning that were still in the proliferation state (Strunov et al., 2016). Viable cells and round nuclei in the interior of both HC and Y201-C spheroids suggest that sufficient nutrient supply was available for all cells (Anderer & Libera, 2002). Indeed, RealTime apoptosis/necrosis assay confirmed, at this early stage of culture the presence of few apoptotic or necrotic cells. However, after 7 days of culture, TEM images showed the presence of convolutions in cells surface, clumped chromatin, and its marginalisation as well as nuclei fragmentation (red arrows), indication of cell's apoptosis, mainly present in peripheral region for HC spheroids and to a less extent in Y201-C spheroids. These apoptotic cells were concentrated at spheroid's surface, because according to Malcolm Steinberg's differential adhesion hypothesis, the sorting-out behaviour of nonviable cells due to the loss or shedding of cell adhesion receptors during apoptosis, cannot be completely excluded and non-viable apoptotic cells were pushed out at peripheral zone (Steinberg, 1996). Quantitative analysis confirmed the presence of apoptotic cells in HC spheroids at a late stage and a low number of necrotic cells, in fact just few HC and Y201-C cells lost membrane integrity or showed swelling and vacuolisation, which are indexes of necrosis. Furthermore, in the spheroids core the start of ECM production and accumulation by cells was observed, as noticed in previous literature works, paralleled by a reduction of the cell-matrix-ratio (Anderer & Libera, 2002). This suggests that the restricted oxygenation and nutrition environment in 3D spheroids/aggregates mimics the microenvironment of *in vivo* tissues to a certain extent, being potential for matrix maturation, confirming the ability of chondrocytes ability to produce AC ECM hypoxic condition (Omelyanenko et al., 2018). However, it is important to mention that this *in vitro* model was used as a control condition in the following experiments performed, and it is referred to as "healthy", due to the lack of cytokines addition, compared to the pathological model. In fact, the drop in cells viability would suggest that we can't consider this model fully healthy.

Regarding the morphology, spheroids had a smoother surface at day 3, while it results to be rougher at day 7, when it is easier to recognise the chondrocytes morphology and the matrix is more like the hyaline cartilaginous tissue (Scalzone et al., 2019a). Furthermore, the SEM confirmed the HC spheroids delayed formation of a sphere, in fact these presented a 2D-folded shape at day 2 of analysis, compared to Y201-C (**Figure 4.11**).

4.4.2 In vitro chondrospheres-based AC tissue analysis

It was developed a repeatable scaffold-free *in vitro* model of AC with a novel approach inspired by the recent clinically approved Chondrosphere® technique: the optimised technology demonstrated its suitability for the obtainment of a reliable and predictive validation model to be used for clinical translation of *in vitro* models.

Two unsuccessful trials were performed before the optimisation of this protocol, without the membrane support, just combining 10-15 spheroids in a well of a 24-well plate with or without the presence of MC, with the aim of obtaining the spheroids fusion and the formation of a few mm construct: the presence of MC brought to the spheroid's disruption (**Figure 4.12A**), whilst its absence led to have the independent spheroids which didn't fuse among each other's (**Figure 4.12B**). Therefore, according to the optimised protocol, after 7 days of spheroids culture, 10 spheroids were seeded on ≈ 1 cm^2 of GEL-coated PLGA membrane to create a chondrosphere, using the minimum concentration required for the chondrosphere protocol (10-70 spheroids/cm^2 defect). The substrate selected as support for spheroids, was able to emulate the *in vivo* environment that cells find in the moment that spheroids are injected within the cartilaginous defect, according to the Chondrosphere® procedure (National Institute for Health and Care Excellence, 2017a; T. et al., 2009). In fact, when in contact with each other and with the adhesive substrate (GEL -coated membrane), similar to the native ECM environment, spheroids arrange themselves in bigger aggregates, and produce a few mm thick construct after 21 days of culture. The fusion process was mediated by the surface cells of adjacent spheroids and single cells were observed to be leaving chondrospheres, migrating to the GEL-coated membrane, stretching between matrix filaments to synthesize cartilage-specific proteins and matrix components, and to deposit the components in the intercellular space (**Figure 13**) (Koudan et al., 2020).

In fact, the *in vitro* generated AC-like tissues generated both by HC and Y201-C were characterized by a time-dependent increased expression of *sox9*, *acan*, and *col2a1*, chondrogenic markers, which reached their highest expression at day 21 in chondrospheres, indicating the cells potential to produce essential proteins (mainly aggrecan and Coll II) for the formation, maturation, and maintenance of AC ECM (**Figure 4.15**) (Caron et al., 2018). The observed protein expression underlines that the Chondrosphere® system is generating cells that can support and to promote the function necessary to foster growth of hyaline-like cartilage (EMA, 2017). Particularly, at day 21 it was detected a higher expression of *col2a1* in

the HC compared to Y201-C, whereas an increased *acan* expression was observed in the Y201-C chondrospheres compared to HC. This result is of interest because *acan* expression levels are used as surrogate potency assay for the Chondrosphere® technique, to predict cells regenerative capacity in human patients. The prevalence of *col2a1* over the *acan* expression, as in the case of HC, indicates the obtainment of a more mature tissue, while high expression and production of *acan* is an index of fully differentiated chondrocytes, important for higher regenerative capacity (Libera et al., 2012; Anderer & Libera, 2002; Akkiraju & Nohe, 2015). Also, quantification of GAG content showed that ECM was continuously accumulated within the constructs during the entire culture period in both HC and Y201-C chondrospheres (**Figure 4.14**). Interestingly at day 0 of HC and Y201-C chondrosphere culture, which corresponds to the moment in which the spheroids were put together (day 7 of spheroids cultivation), the value of GAGs produced was higher compared to day 1 of spheroids, used as a normalisation control. This result confirmed the TEM analyses at day 7 of spheroids culture, where it was observed the start of deposition of ECM in the core of spheroids (**Figure 4.11**).

4.4.3 Study and optimisation of OA-induction in vitro

The optimised cytokines-induced methodology produced a reliable *in vitro* model of OA at early stage. Spheroids of Y201-C and HC were formed in the same way as for the first part of this chapter and their growth kinetics assessed accordingly. While in healthy condition, HC (**Figure 4.16**) and Y201-C (**Figure 4.17**) spheroids showed a decrease in size over the course of 10 days of culture, as scattered cells became closely packed aggregates owing to cell-cell contact and condensation, the exposition to cytokines led to a substantial difference in growth kinetics in both LC-OA and HC-OA groups. Spheroids did not shrink in size under diseased settings over culture and at day 10 their diameter was statistically bigger than healthy conditions for both cells. The obtained results could be probably related to the increase of cell proliferation, a common characteristic of OA at early stage of disease evolution, as well as to the interference of cytokines within intercellular interactions (Wojdasiewicz et al., 2014; Gao et al., 2014). HC exhibited a reduction in cell metabolic activity within spheroids (**Figure 4.17A**), whereas Y201-C showed an increase over culture (**Figure 4.17B**). However, at 10 days, they revealed a similar trend: under the impact of cytokines, both cells increased their metabolic activity, which might be associated to the synthesis of inflammatory and degradative enzymes, as well as an attempt to repair ECM which started to get damaged, typical feature of early-stage OA (Goldring et al., 2008).

Then, the spheroids were assembled and cultured for further 11 days on a GEL-coated PLGA electrospun membranes (10 spheroids/cm^2), as explained earlier and reported in a publication related to this PhD (Scalzone, Wang, et al., 2022).

Early OA is defined by three main events: a hardly ever recognised early-phase of cartilage-resident cell proliferation, in contrast to well-established enhanced production, breakdown of extracellular matrix components, and inflammation, all of which are linked to OA development (Boehme & Rolauffs, 2018). Cells proliferation was assessed via staining Ki-67, which is a nuclear protein highly expressed when cells are in proliferative state (Miller et al., 2018). When compared to the healthy samples at day 21 and to the control at day 1, in OA conditions both cell types showed a high staining of Ki-67 at day 21 (**Figure 4.19**), suggesting that cells in OA state have a predisposition to proliferate. In fact, OA-induced cells form a cell population with anomalous proliferation, which is a frequent chondrocyte response to altered joint environments (Dreier, 2010; Sandell & Aigner, 2001). Following that, it was studied the apoptotic tendency of cells, by evaluating cells nuclei stained with DAPI at high magnification (**Figure 4.20**). Both cells in OA conditions, showed a reduction in the size of nuclei, as well as their clusterisation and anomalous shape due to the presence of apoptotic bodies, nuclear condensation, and fragmentation: these events are related to the shift of cells towards the hypertrophic pathway which may cause chondrocytes apoptosis and, as a result, AC loss (Elmore, 2007a; Blanco et al., 1998; Muldrew et al., 2001). Apoptosis is a key event during OA pathogenesis, in fact *in vitro* studies on AC demonstrated that OA cartilage shows a higher rate of apoptotic chondrocytes (51%) compared to the healthy one (11%) (Blanco et al., 1998). The correlation between OA and apoptosis was found to be mediated by synovial inflammation and the increase in cytokines concentration in a dose-dependent manner. However, since OA chondrocytes seem more sensitive to IL-1β than normal chondrocytes, because they express higher level of IL1-β receptors compared to healthy ones, probably it is needed a long-term exposure to pro-inflammatory mediators before it can be seen apoptotic degeneration of HC and Y201-C cells (Hashimoto et al., 1997; Bosman et al., 1996)(Heraud et al., 2000).

Regarding gene expression analysis, anabolic markers (*sox9*, *acan*, and *col2a1*) were up-regulated in the healthy model of HC and Y201-C after 21 days of culture, compared to both diseased models, in which their expression decayed throughout culture, as predicted (**Figure 4.21**). On the other hand, the expression of *mmp13*, the main collagenase responsible for the

degradation and cleavage of Coll II, was greater in the HC-OA for both cell types at day 21 compared to the less inflamed (LC-OA) and Healthy environments. The other catabolic marker studied was *adamts-5*, responsible for *acan* cleavage, which, being constitutively produced by chondrocytes, did not showed a constant trend in the different conditions for the two cell types (Verma & Dalal, 2011) (Jiang et al., 2021). Another important discriminator between healthy and OA cartilage is the ratio between *col2a1* and *col1a2*, which was showed to be significantly higher in Healthy condition compared to LC-OA and HC-OA for both HC and Y201-C cells after 21 days of culture. The decrease in the *col2a1/col1a2* ratio in OA conditions was mainly caused by a change in, and constant downregulation, of expression of *col2a1*, whereas that of *col1a2* changed much less (in fact it did not give conclusive results regarding significant alterations among different conditions). This feature is in concordance with previous literature studies (Marlovits et al., 2004).

The quality of tissue and its degree of degradation was determined by histology (**Figure 4.23**) and HIC stainings (**Figure 4.24**). H&E staining reveals the existence of nucleated cells with high cytoplasmic content for both HC and Y201-C, in all conditions. However, weaker staining of collagen (stained with PicroSirius Red) and proteoglycans (stained with Alcian Blue) under OA conditions was observed. Also, all the stainings revealed that, in OA conditions, tissues were less compact and more fragmented. IHC confirmed histology and gene expression results: HC and Y201-C cells produced a tissue rich in Coll II and ACAN, as evident from the brighter staining and the compactness of the tissue slice, when compared to LC-OA and HC-OA conditions. This result is related to the inhibition of the biosynthetic activity of chondrocytes during the OA progression and matrix degradation by proteinases (Matyas et al., 2002; Roughley & Mort, 2014).

In conclusion, even using a low concentration of cytokines (in accordance with values present in human synovium during OA progression) it was possible to observe these features and therefore the LC-OA, was the cocktail used for the next step of this PhD research. Also, it was demonstrated that a bankable cell type, the Y201-C, could be used to produce an engineered AC-like construct, not only in healthy condition, but as well for studying the progression of OA with future insight into treatment strategies. Therefore Y201-C were used as cell source in the next step of this PhD research.

Chapter 5. Evaluation of novel therapeutic treatments for OA: proof-of-concept

STATEMENT OF SIGNIFICANCE

In line with the 3R's philosophy, the importance of developing reliable and reproducible models of early-stage OA lies in the possibility of testing novel therapeutic treatments, able to interrupt the disease progression (Benam et al., 2015). *Amongst novel therapeutic strategies, biophysical stimuli, such as biochemical cues or mechanical stress, show great potential in OA therapy, being able to increase cell proliferation and to stimulate the release of molecules associated with hyaline cartilage ECM maintenance* (Massari et al., 2019). *As biomechanical cues, chondrocytes can sense and respond to different mechanical loads (e.g., compression or shear stress), by changing their conformation and their anabolic and catabolic activity* (Gilbert et al., 2021). *As a biochemical cues, miRNA, by directing post-transcriptional regulation of a network of genes by targeting mRNA, have varying effects on cartilage homeostasis in the progression of OA* (Li et al., 2015). *Herein, the optimised in vitro spheroids-based OA platform was used to evaluate the effect of two different therapeutic strategies as proof-of-concept studies: biomechanical and biochemical stimulations.*

5.1. Introduction

The primary goal of this chapter was to test the effect of novel therapeutic treatments for OA disease, by using the optimised OA-induced scaffold-free model as *in vitro* platform, proved to be a reliable testing model in *Chapter 4*. More in details, two different strategies were explored, which represent the two objectives of this chapter:

OBJ 1: To assess the effect of the mechanical load on Y201-C fate within a magnetic-field bioreactor, induced by the movement of ferrite-based PLLA magnetic microspheres.

OBJ 2: To evaluate the therapeutic effect of miRNA-loaded chitosan polyplexes on HC cells fate within an OA-induced in vitro model of AC.

5.2 Materials and Methodology

5.2.1 Manufacturing and analysis of ferrite loaded PLLA microspheres

The manufacturing of the ferrite-loaded PLLA microspheres (MS) was performing with an oil in water (O/W) emulsion technique (**Figure 5.1**): the oil phase was constituted by medical grade PLLA (Corbion Purac, Purasorb PL-18, Spain) dissolved in Chloroform (Scharlab, Spain) at 2% w/v, while the water phase was constituted by Poly(vinyl alcohol) (PVA) (MW = 130,000 Da, Sigma Aldrich, Spain) dissolved in dH_20 at 4% w/v. Ferrite- based magnetic nanoparticles (Fe_2O_3, Ferrotec, Ferrofluid, US) were dispersed in the homogenous oil phase of PLLA/chloroform at 5% w/w, with respect to the weight of PLLA. The PLLA used was in amorphous phase and it was obtained by pouring the PLLA in a Teflon mould, leaving it for 1 hour at 210 ° C and cooling it down at RT. Once obtained the PLLA and PVA solutions, 200 mL of PVA were filtered by using filter papers (Whatman, UK). Then, 20 mL of PLLA/ferrite solutions were added dropwise at 1 mL/min, via a syringe pump (NE-1000, New Era Pump Systems Inc., US), to the PVA solution under agitation at 750 rpm, via a helix agitator (Ika Eurostar, Germany). Once completed the procedure, 150 mL of dH_20 were added to the final solution for assisting the evaporation of the solvent. The obtained solution was let under agitation overnight at 750 rpm, before performing multiple washes: four times in dH_20 (200 mL each time) and two times in 100% Ethanol (150 mL each time). Then, the solution was filtered (with a 100 μm filter) and the remaining ethanol was removed and let evaporate under chemical hood, before storing the obtained MS at -80 °C. The freeze-drying process was performed with a LyoQuest 85 (TELSTAR, Spain) freeze-dryer for 48 h, for removing all the water from the MS. Also, to improve the hydrophilic properties of the microparticles, these were treated with Argon in a plasma chamber at a gas pressure of 50 Pa, flow rate of 160 sccm and potency 300 W for 300 s. The treatment was performed twice, to ensure that the surface of all the particles were cured, mixing them between the two processes.

The morphology of the obtained microspheres was analysed by SEM (Ultra 55, Zeiss Auriga Compact, Germany) and images were taken at 30 kV and at 144 x, 426 x, 862 x and 2700 x magnifications. Particles were coated with platinum before the visualisation, via ionic beam (JFC 1100, JEOL, Japan). The size of the obtained particles was measured by analysing the images obtained via three different syntheses, with Image J.

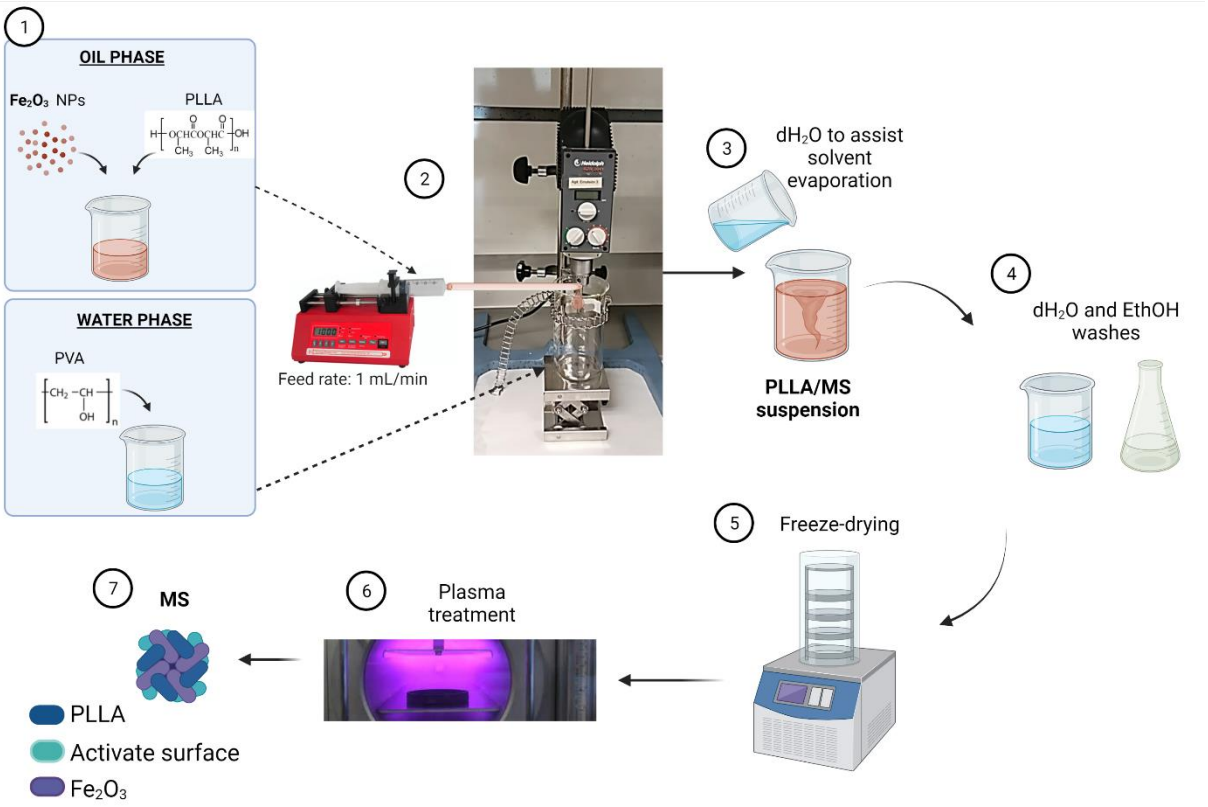

Figure 5.1: Manufacturing process of PLLA/Fe_2O_3 MS, via an Oil/Water emulsion process (1-4), followed by freeze-drying (5) and plasma treatment (6), to activate the surface of the MS (7).

5.2.2. Analysis upon the formation of the spheroids and MSP cytotoxicity

MS-loaded spheroids were manufactured with the same protocol used in *section 4.2.1.* Y201-C at concentration of 2 x 10^5 cells/spheroid were selected, and multiple ratios of Y201-C:MS were evaluated, as reported in **Table 5.1.** Y201-C/MS suspended in 150 µL of DMEM/F12 supplemented with MC (0.25 % w/v), were seeded in a round bottom 96-well plate. Cells ability to form spheroids was qualitatively evaluated by observing the spheroids formation within 48 hours of culture and the ratio Y201-C:MSP 5:1 was selected for further analysis.

Cells viability was evaluated via staining of Hoechst and Propidium Iodide (PI), using an IN Cell Analyzer 6000 microscope (GE Healthcare), at "La Fe" University and Polytechnic Hospital of Valencia. Also, the morphometric analysis of spheroids dimensions after 48 h of culture was assessed in brightfield images, as reported in *section 4.2.2*.

The organisation of the cells within the spheroids, in presence or in absence of MS, was analysed by TEM at day 7, (FEI Tecnai G2 Spirit Biotwin 120 kw TEM) at Centro de Investigacion Principe Felipe of Valencia, according to routine procedures. Images were taken both in the middle and in the peripheral region of the spheroids.

Y201-C:MS	MS per spheroid (mg)
1:0	0
1:1	1.2
2:1	0.6
3:1	0.2
4:1	2.4
5:1	0.2
10:1	0.1

Table 5.1: Ratios of Y201-C:MS and the correspondent mg of MS per each spheroid.

5.2.3. Assessment of the magnetic field stimulation on cells fate

In **Figure 5.2** it is schematised the process for the set-up of the bioreactor experiment.

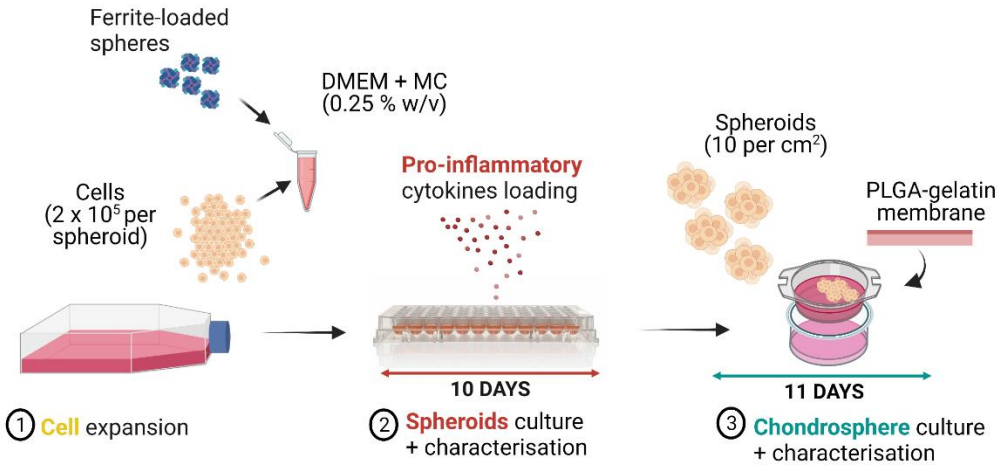

Figure 5.2: Manufacturing process of the PLLA/MS loaded OA *in vitro* model: Y201-C cells expansion (1), Spheroid's culture and characterisation in a round bottom 96-well plate for 10 days (2) with the addition of IL-6, IL-1ß, TNF-α proinflammatory mediators (3), Chondrospheres culture and characterisation for further 11 days on a GEL-coated electrospun PLGA membrane (4).

Y201-C were suspended with Ferrite-loaded MS (Y201:MS ratio of 5:1) and seeded in a round bottom 96-well plate, with or without the presence of MS and with/without the presence of cytokines. After 10 days of spheroids culture, 10 spheroids per cm^2 of PLGA/GEL membrane were seeded on the membrane and cultured in the bioreactor (EXP-H and EXP- P) or in static

conditions, outside the bioreactor (CTRL-H, CTRL-P, MSP-H and MSP-P). The bioreactor was maintained at 37 ° C and 5% CO_2 for 11 days: the stimulation performed was at 1 Hz for 16 h per day, with an activity of 5 minutes each 25 minutes, to simulate the human activity. The samples outside the bioreactor were cultured, as well, at 37 ° C and 5% CO_2 for 11 days.

Six different conditions were analysed and summarised in **Table 5.2.** The effect of the magnetic field was evaluated in healthy (EXP-H) and pathological conditions (EXP-P) in presence of cytokines. The controls were: Y201-C/MS without the stimulation from the bioreactor (MS – H and MS- P) and Y201-C without MS (CTRL-H and CTRL-P).

NOMENCLATURE	BIOREACTOR	CYTOKINES
CTRL – H	NO	NO
CTRL – P	NO	YES
MS – H	NO	NO
MS – P	NO	YES
EXP – H	YES	NO
EXP - P	YES	YES

Table 5.2: Table reporting the condition analysed, with the correspondent nomenclatures.

The effect of the bioreactor on cells fate was analysed by gene expression analysis of *sox9, col2a1, acan, mmp13* and *adamts-5,* as reported in *section 3.13.*

5.2.4. Manufacturing and characterisation of miRNA-140-5p / chitosan polyplexes

For the manufacturing of the polyplexes, chitosan (CH) (MW = 100kDa, DD= 95 %, HMC +, Germany), was dissolved in sodium acetate buffer (pH 4.3, 0.2 M) overnight at concentration of 1 % w/v, to obtain the stock solution of 10 mg/mL. After the dissolution, the pH was raised to 5.5 and the stock solution was diluted to obtain solutions at different concentration of CH: 5, 10, 15, 20, 100, 250, 500, 2000 µg/mL.

To obtain the polyplexes, 1 mL of each CH solution was added to a 1.5 mL eppendorf tube and mixed with 20 µL of 20 µM Dharmacon™ miRIDIAN microRNA human hsamiR-140-5p – Mimic (Horizon Discovery, US) (miRNA-140-5p), according to a protocol from Liu et al (Andersen et

al., 2008; Liu et al., 2007). The CH concentrations was varying the N:P ratios, whilst the concentration of miRNA remained 10 nM in each formulation.

The surface charge and the size of the obtained NPs was measured using a Zetasizer Nano ZS (Malvern Instruments, Malvern, UK) at 25 °C. 100 µL of CH polyplex solution were taken from each eppendorf tube and added to a 7 mL sterile bijou vial. Afterwards, 900 µL of dH_2O were added, mixed thoroughly and 800 µL of the CH/miRNA solution was added to the DTS-1070 cuvette. The cuvette was put into the DLS machine and, finally, three measurements for with a least 10 runs were performed.

The concentrations of CH 5 µg/mL and 250 µg/mL were selected for biological assessment, using the naked miRNA-140-5p as control.

5.2.5. Assessment of polyplexes cytocompatibility and cellular uptake

Cell viability was determined using a ReadyProbes® Cell Viability Imaging Kit (Thermo Fisher, UK), as reported in *section 3.9.1*. HC cells (30 000 cells in 48 well-plate) were seeded with CH/miRNA-140-5p polyplexes at 3 different concentrations of CH: 0 µg/mL (naked miRNA), 5 µg/mL and 250 µg/mL. Images were recorded using EVOS M5000 inverted microscopes (10 x and 20 x magnifications) at 24 hours and 48 hours in the three conditions.

HC metabolic activity was analysed via MTT assay at 48 h, as reported in *section 3.10.1,* for 0, 5 and 250 µg/mL of CH.

Immunostaining analyses were performed to assess the uptake of polyplexes by HC, in the three conditions: 0, 5 and 250 µg/mL of CH. The polyplexes were prepared using a FITC labelled miR (miridian microRNA Human hsa-miR-140-5p-FI, Horizon Discovery, US) and fixed with 4% w/v PFA then washed with PBS and stained, as reported in *section 3.12*. Images were captured using EVOS M5000 fluorescence microscope.

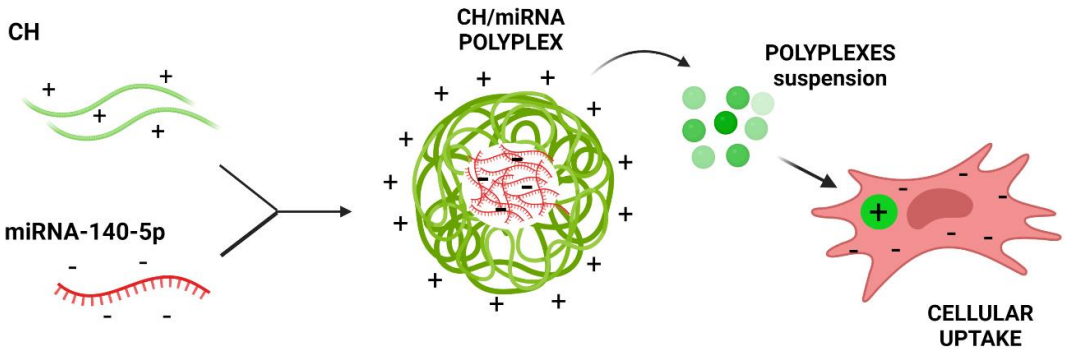

Figure 5.3: Manufacturing of the CH/miRNA polyplexes, starting from CH (5, 10, 15, 20, 100, 250, 500, 2000 µg/mL) and miRNA-140-5p (20 µM). Representation of the cellular uptake of the positively charged polyplexes, through the negatively charged cells membrane.

5.2.6. Evaluation of polyplexes therapeutic effect within an in vitro model of OA

The concentration of CH of 250 µg/mL, corresponding to a N:P ratio of 50, was used for the evaluation of the therapeutic effect of the manufactured CH/miRNA-140-5p polyplexes. For the experiment set-up, HC spheroids were manufactured as reported in *section 4.2.1,* and cultured in healthy, OA condition (at low concentration of cytokines: 1 ng/mL of IL-1ß and TNF-α, and 10 ng/mL of IL-6) and OA condition with the presence of CH/miRNA, which were added to the cells suspension before seeding the spheroids. Gene expression of anabolic and catabolic markers (*sox9, col2a1, acan, mmp13* and *adamts-5*) was evaluated at day 10 of culture, as reported in *section 3.13,* and the results were reported as the fold change at day 10 with respect to day 1.

Histological analysis of H&E, Picrosirius Red and Alcian Blue stainings was performed at day 10 and at day 1 in the three conditions, as reported in *section 3.16*.

5.3 Results on the effect of shear stress induced by magnetic field on cells

5.3.1 Characterisation of the PLLA/Fe_2O_3 microspheres

SEM was performed to assess the morphology of the MS and their dimension. From **Figure 5.4A,** it is noticeable that the surface of the MS was a bit rough and very porous: especially at high magnification, the presence of pores distributed overall the surface of the spheres was visible. Regarding the diameters of MS, it ranged between 0 – 100 µm, with most of the MS

having a diameter within 10 – 70 µm. The average diameter obtained was 37 ± 6 µm (**Figure 5.4B**).

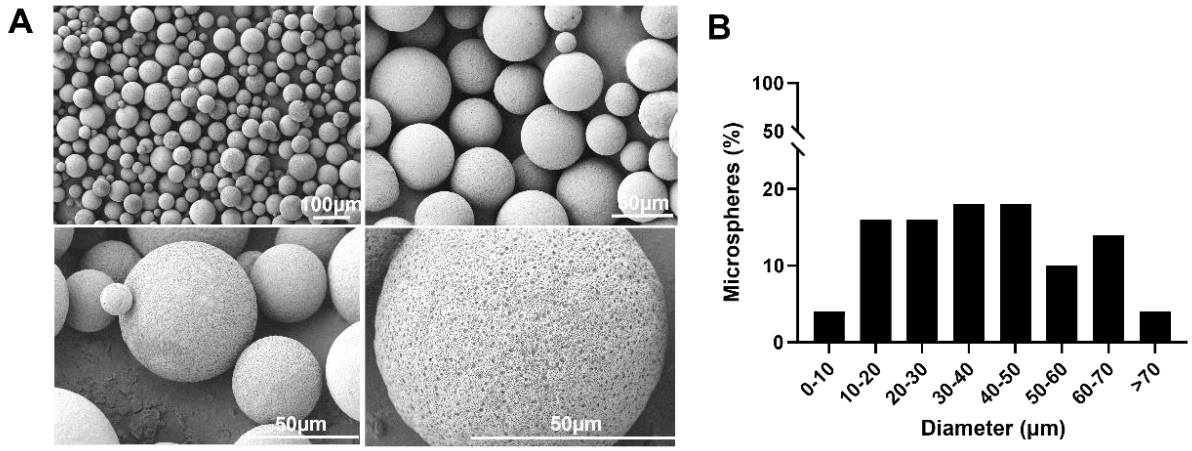

Figure 5.4: SEM images of the obtained PLLA/MS at different magnifications: 144 x, 426 x, 862 x and 2700 x (**A**) and analysis of the percentage of the microspheres with a diameter in the ranges: 0 – 10, 10 – 20, 20 – 30, 30 – 40, 40 – 50, 50 – 60, 60 – 70, > 70 µm. Analysis performed from 3 images from each batch of MS (**B**).

5.3.2 Evaluation of MS cytocompatibility and ability to induce the spheroid formation

Multiple ratios of Y201-C:MS were evaluated in terms of ability to form the spheroids. In **Figure 5.5**, there are reported some attempts to obtain a good spheroid, compared to the control of bare Y201-C (first line, 1:0). In all cases (ratio Y201-C:MS 1:1, 2:1, 3:1 and 2:1) it was not possible to obtain a homogenous distribution of cells and MS. Indeed, at ratios 1:1-2:1-3:1 the number of particles appeared very high, and the MS precipitated at the bottom of the spheroids, before the cells, leading to the obtainment of two phases: MS at the bottom of the well and the Y201-C above. On the other side, at ratio 1:2, it was impossible to obtain an aggregate and both Y201-C and MS appeared scattered in the well.

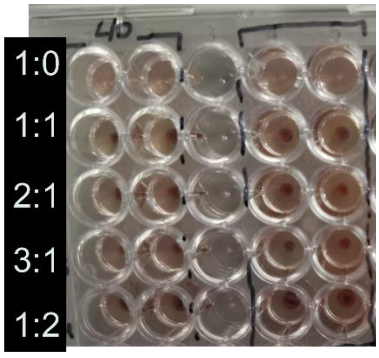

Figure 5.5: Image of the round bottom 96 multi-well plate and the obtained spheroids after 48 h of culture in DMEM/F12 with 0.25 % MC. Ratios of Y201-C: MS exploited: 1:0, 1:1, 2:1, 3:1 and 1:2.

Therefore, two new ratios were exploited: Y201-C:MS 5:1 and 10:1. For the ratio 10:1, Y201-C precipitated at the bottom of the well with the and MS forming a layer on the top of cells precipitate, leading to a non-homogenous spheroid. Finally, the ratio 5:1 gave good results in terms of homogenous dispersion of cells and MS and thus, it was used for further analysis.

The ability of Y201-C/MS to form spheroids and the analysis of the morphology of the obtained spheroids was evaluated at 48 h in healthy and pathological conditions, with the presence of cytokines, to assess if the combination of MS and cytokines could affect the formation of the spheroids. Compared to the controls in healthy (CTRL-H) and in pathological (CTRL-P) conditions, no big differences were observed in terms of spheroids size (**Figure 5.6A,B**). However, MS-P samples, apart from showing a significant statistical bigger diameter, compared to the CTRL-P ($p < 0.01$), it also presented an indented surface (pointed by the arrows), compared to spheroids in all the other three conditions, which presented a smoother surface. Indeed, MS-P showed the lowest value of circularity (~ 0.8), compared to the other conditions where this value was more proximal to 1; whilst the roundness was around 0.8-0.9 in all the conditions (**Figure 5.6C**).

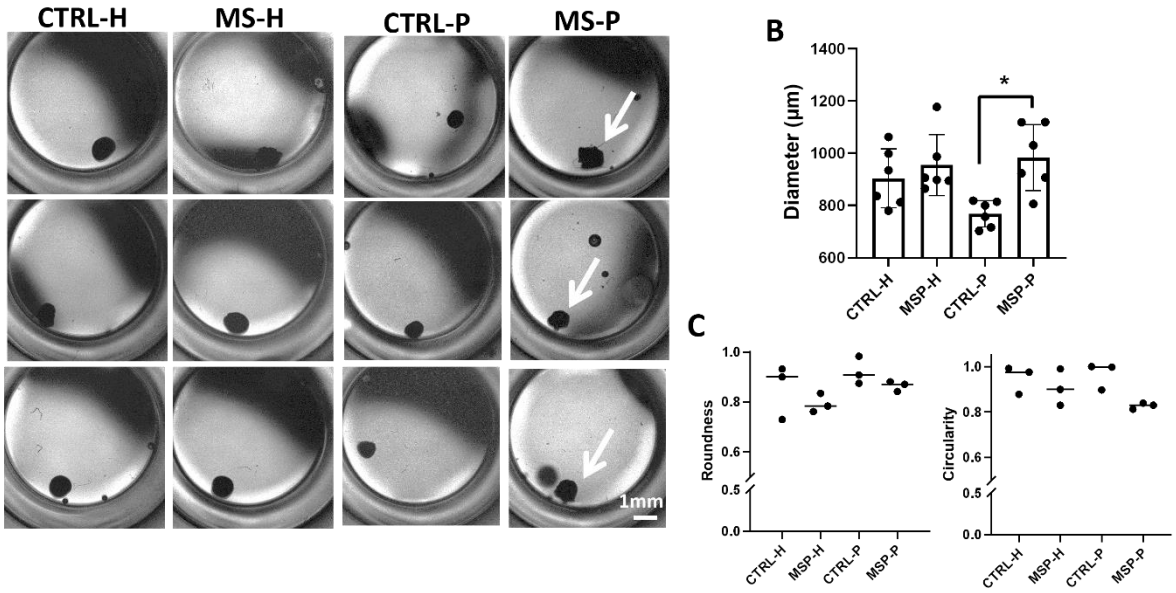

Figure 5.6: Analysis of the morphology of the obtained spheroids after 48 hours of culture, in healthy and pathological conditions and with (MS) and without (CTRL) the presence of MS. Images of the spheroids (**A**), analysis of the average diameter in each condition (**B**), morphometric analysis of spheroids roundness and circularity (**D**). Arrows pointing at the inhomogeneous surface of the MS-P spheroids in (**A**).

Then, the viability of the spheroids was assessed in the same four conditions at 48 h. It was discovered that Y201-C remained viable in all cases and only few dead cells (stained in red with PI) were found (**Figure 5.7A**). It is also interesting to note the presence of the microspheres homogenously dispersed in the spheroids after 48 h of culture in the MS-H and MS-P samples (pointed by the white arrows). Regarding the metabolic activity of the cells, which was evaluated via MTS, no statistical differences were observed up to 3 days. However, after 7 days of culture, statistical differences were observed between CTRL-H and CTRL-P, and between MS-H and MS-P, with both pathological controls showing a higher value of absorbance, compared to the respective healthy ones ($p<0.0001$). Also, the presence of MS in healthy conditions led to an increase of cells metabolic activity, compared to the CTRL-H ($p<0.0001$).

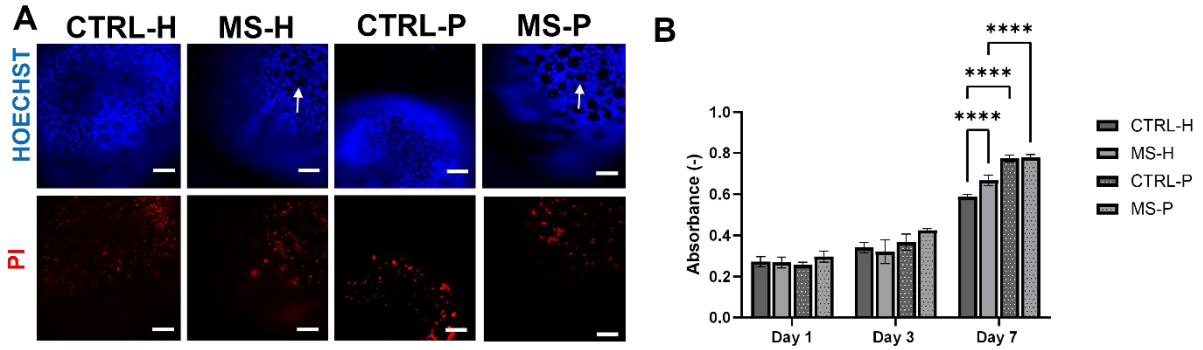

Figure 5.7: Analysis of cells viability via staining of all cells nuclei with HOECHST (blue) and dead cells with propidium iodide (PI) (red). Arrows pointing at the MS. Bars = 100 µm (**A**). Metabolic activity evaluation for Y201-C (**B**). The conditions exploited were CTRL-H, MS-H, CTRL-P, MS-P. Statistics: ****$p<0.0001$.

In addition, TEM analysis was performed at day 7, to assess the Y201-C organisation within the spheroids and around the MS. From the images taken in the peripheral region of the spheroids, it is noticeable in both cases that cells appeared flattened, elongated and organised in layers, adhering among each other's (**Figure 5.8A,B,E,F**). Especially, in **Figure 5.8F**, cells were tightly packed towards the external surface of the spheroids and between the spheroids and the MS nearby the surface. Inside the spheroids, a clear difference can be observed: cells appeared more rounded in the CTRL-H (**Figure 5.8C,D**), while they seemed to be adhering to the MS and organising themselves around them, in the MS-H samples. Also, in MS-H samples, cells appeared more elongated nearby the MS and more rounded in the free space between the MS (**Figure 5.8G,H**). As anticipated by SEM, the manufactured MS appeared very porous

(**Figure 5.8G,H**). In all the conditions and within the all spheroids, Y201-C cells appeared alive, preserving their organelle and nuclear content (darkest part).

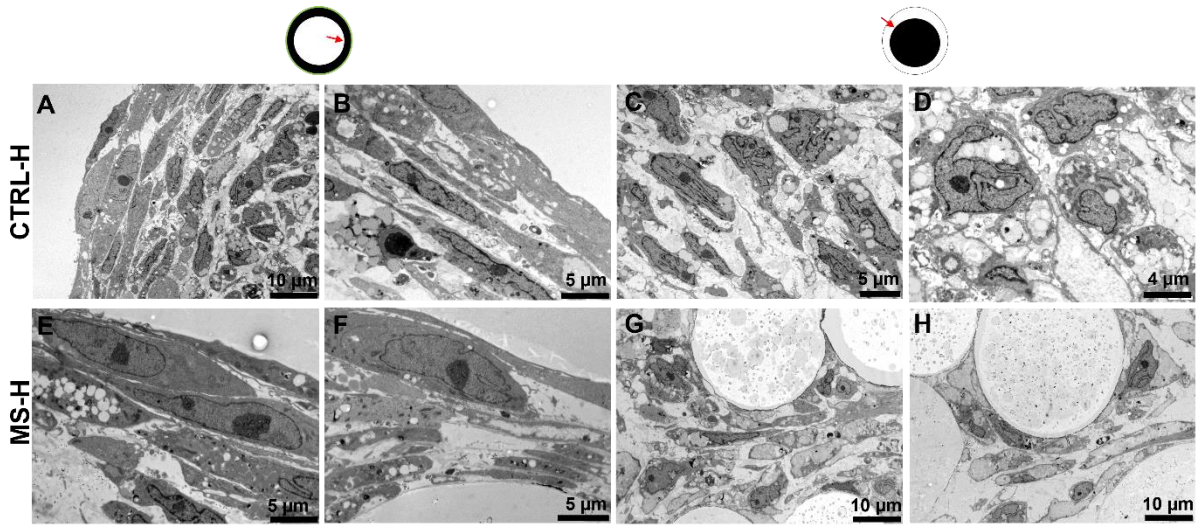

Figure 5.8: TEM analysis performed for CTRL-H and MS-H at day 7. Images taken at the peripheral region of the spheroids (**A,B,E,F**) and in the middle of the spheroid (**C,D,G,H**).

5.3.3 Evaluation of magnetic field stimulation – induced therapeutic effect within an OA in vitro platform

After 11 days of Y201-C/MS spheroids within the bioreactor, the gene expression of anabolic (*sox9, col2a1, acan*) and catabolic (*mmp13, adamts-5*) markers was exploited. The expression of *sox9* (**Figure 5.9A**) showed significant differences between the six conditions ($p<0.0001$): CTRL-H displayed the highest fold-change at day 21 (~ 22-fold), compared to CTRL-P, MS-P, EXP-H, EXP-P, whose fold-change was proximal to 1; instead, MS-H samples exhibit a fold change of ~ 4-fold. Similarly, *acan* (**Figure 5.9C**) expression, which followed the same trend, showing its highest fold change in CTRL-H samples (~ 500-fold), followed by CTRL-P (~4-fold); all the other conditions showed a fold-change value lower than 1 ($p<0.0001$). Gene expression of *col2a1* (**Figure 5.9B**) displayed a different behaviour, with all the samples showing statistical differences amongst each other's ($p<0.0001$): EXP-P displayed the highest fold-change (~ 340-fold), which was followed by CTRL-H (~ 200-fold), MS-H and EXP-H (~ 100-fold), and CTRL-P (~60-fold) and MS-P (~ 20-fold). For the *mmp13* catabolic marker (**Figure 5.9D**), instead, a significant statistical difference was observed in the CTRL, MS and EXP, between the healthy and pathological conditions, with the pathological conditions showing higher expression ($p<0.0001$). EXP-P showed the highest expression of *mmp13* (~ 22-fold). Finally, gene expression of *adamts-5* (**Figure 5.9E**), while showing the same trend of *mmp13* for the CTRL

and MS, displaying a higher fold-regulation in pathological conditions compared to healthy ones ($p<0.0001$), it did not show the same behaviour for the EXP, where no significant differences were observed in healthy (EXP-H) and pathological conditions (EXP-P). However, a decrease in the expression of *adamts-5* was observed after the bioreactor culture (EXP-P), compared to its absence in the CTRL-P.

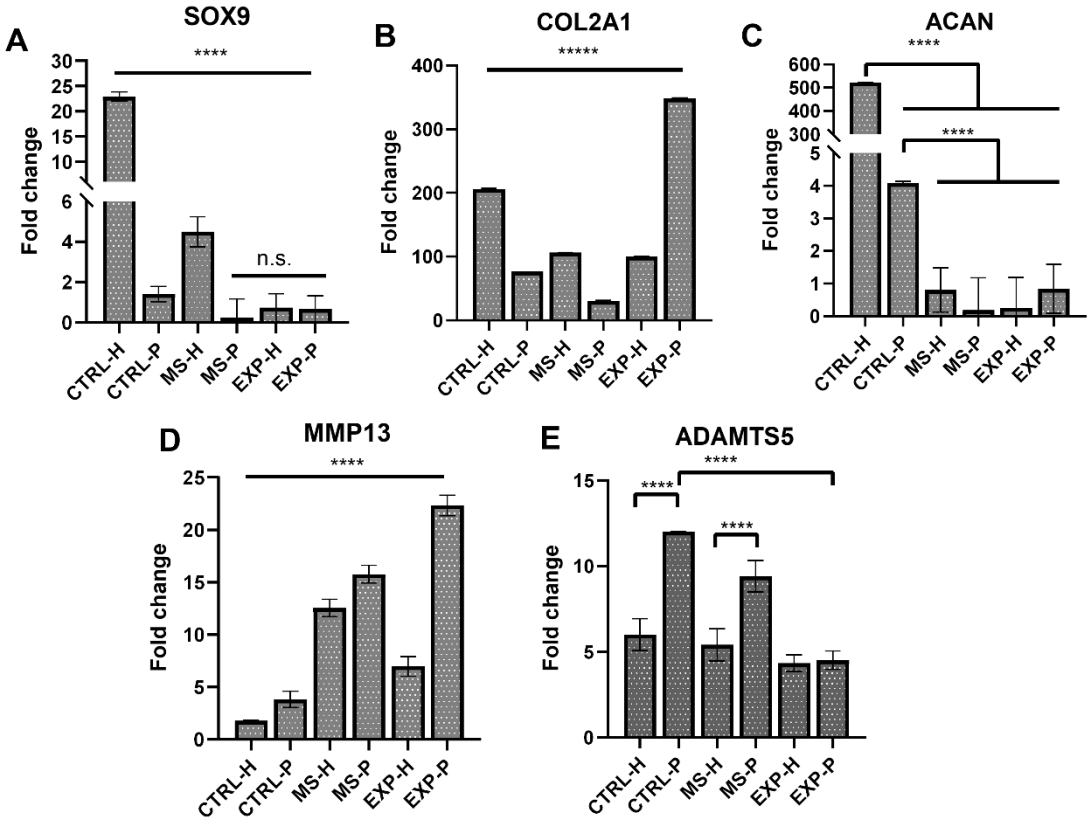

Figure 5.9: RT-qPCR results showing the fold change of *sox9* (**A**), *col2a1* (**B**), *acan* (**C**), *mmp13* (**D**) and *adamts-5* (**E**) at day 21, with respect of day 1. Conditions analysed: CTRL-H and CTRL-P, Y201-C without the MS and without the bioreactor stimulation; MS-H and MS-P, Y201-C with the MS and without the bioreactor stimulation; EXP-H and EXP-P, Y201-C with the MS and with the bioreactor stimulation. Statistics: ****$p<0.0001$.

5.4 Results on the effect of miRNA-loaded chitosan polyplexes on cells

5.4.1 Analysis of the CH/miRNA polyplexes charge and ζ-potential

After the CH/miRNA polyplexes manufacturing, their charge (ζ-potential) and their size were evaluated at different CH concentrations and reported in **Figure 5.10**. The values of ζ-potential seemed slightly increased from the 0 µg/mL concentration of CH (naked miRNA), showing a value of ~-20 mV, to 250 µg/mL of CH (corresponding to N:P ratio of 50), where the ζ-potential stabilized to the value of ~+40 mV. After that concentration, there was a plateau and stable ζ-

potential up to 2 mg/mL of CH concentration (**Figure 5.10A**). It is interesting to notice that, even the lowest concentration of CH (5 µg/mL) was sufficient to obtain a positive superficial charge of around 22 mV. All the results obtained for the polyplexes were not statistically different.

Figure 5.10B shows the size distribution of the polyplexes. The smallest size of the polyplexes (about 90 nm) was obtained by the lowest concentration of chitosan, which was 5 µg/mL; the size continued to increase with the increase in concentration: the largest size was slightly above 3000 nm at the maximum concentration of 2 mg/mL. All the particle sizes were significantly different from one another ($p < 0.0001$).

The CH concentration of 250 µg/mL, which was the first concentration to give a plateau in the ζ-potential curve was selected for further analysis and compared with the lowest concentration of 5 µg/mL and with naked miRNA-140. From the DLS curves of the size distribution of CH 250 µg/mL (**Figure 5.10C**), three peaks were observed: it is worth noticing that before cells culture the solution were filtered with 0.22 µm filter and, therefore, the only remaining nanoparticles were the ones with a size around 100-200 nm.

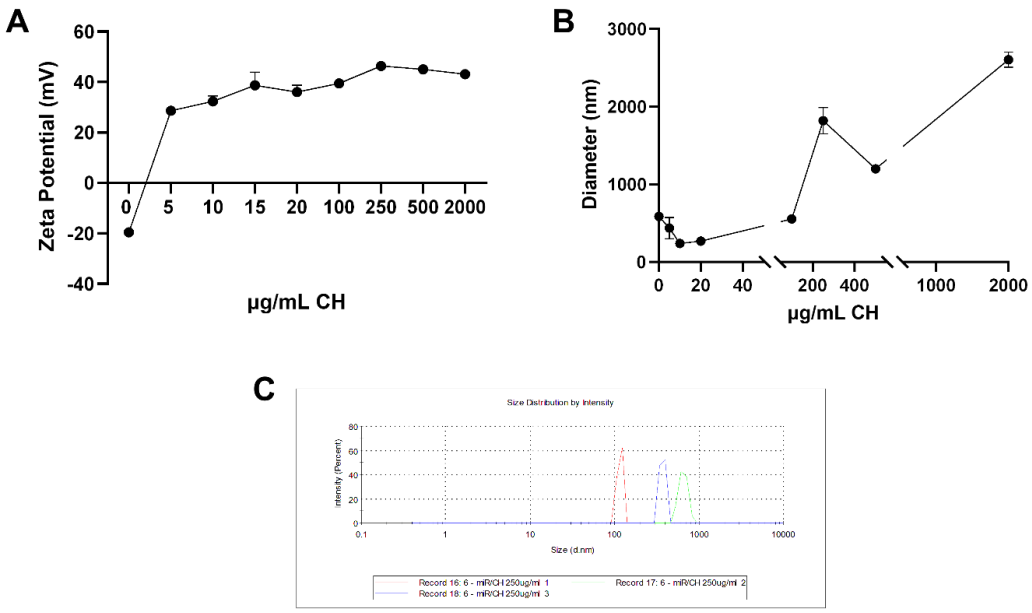

Figure 5.10: Graphs representing the ζ- potential and size distribution of the different polyplexes at 0, 5, 10, 15, 20, 199, 250, 500, 2000 µg/mL of CH.

5.4.2 Polyplexes cytocompatibility and cellular uptake assessment

HC cells viability, when cultured in presence of polyplexes at 0, 5 and 250 µg/mL of CH, was assessed at 24 and 48 hours. The results in **Figure 5.11A** showed that almost no dead cells (red) in both time frames were found, compared to the total amount of cells (blue). Also, HC metabolic activity, evaluated with MTT assay, showed an increase in the number of metabolically active cells after 48 h (38000 ± 5000), compared to 24 h (28000 ± 1000) in CH 250 µg/mL samples; in the other conditions no significant differences were observed.

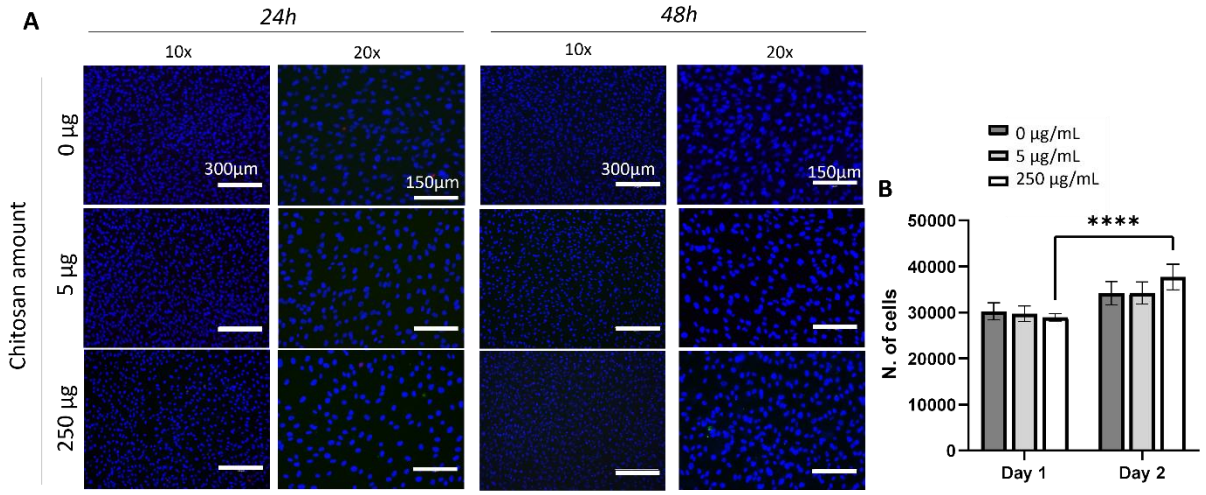

Figure 5.11: Cell viability performed at 24 and 48 hours using CH at 3 different concentrations (0 µg/mL, 5 µg/mL, and 250 µg/mL). In blue are stained cells nuclei (HOECHST) and in red dead cells (EthBrom) (**A**). Cells metabolic activity assessment at day 1 and day 2 in the same three conditions (**B**). Statistics: ***p<0.001.

To evaluate the cellular uptake of the CH/miRNA polyplexes, samples (CH 0, 5 and 250 µg/mL polyplexes) were stained with DAPI to visualise the nuclei and Rhodamine Phalloidin to visualise the cytoskeleton. For this assay, FITC-labeled miRNA (mirFI) was used. The obtained images revealed that there were no apparent signals of miRNA at any magnification of the test at both days, at 0 and 5 µg/mL of CH. mirFI (in yellow, due to the overlap with the other stainings), was visible at both 24 and 48 hours at the maximum concentration of CH (250 µg/mL), indicating the presence of miRNA polyplexes, localised within in cells cytoplasm (**Figure 5.12**). The findings reveal that miRNAs were successfully encapsulated within the CH polyplexes and delivered to HC at 250 µg/mL of CH, corresponding to N:P ratio of 50.

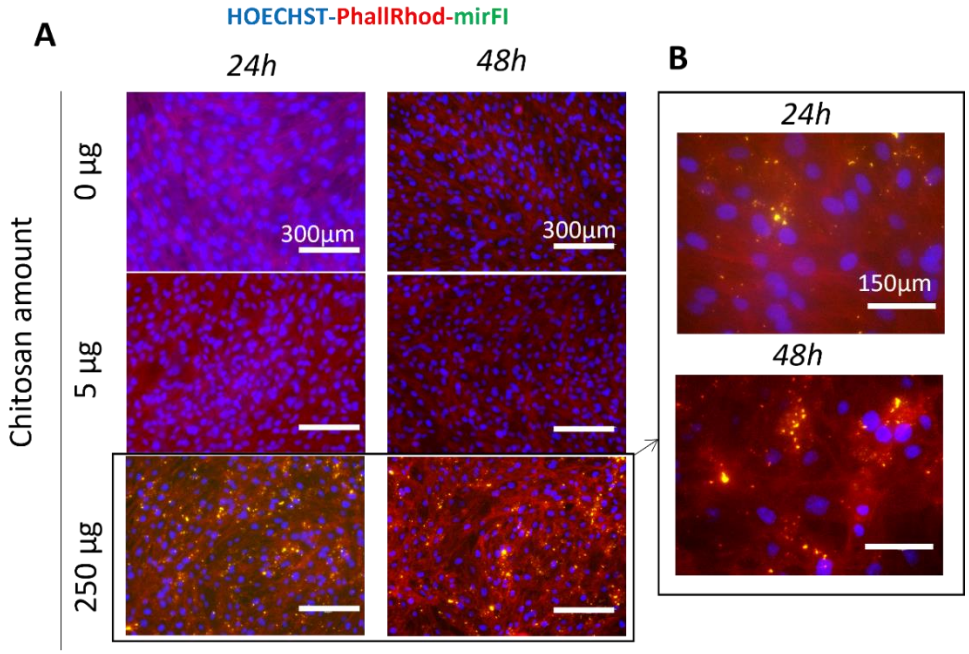

Figure 5.12: Immunostaining images of CH/miR-140 polyplexes at 24 and 48 hours. The images shown are a merge of DAPI, Phalloidin Rhodamine (PhallRhod) and labelled mirna (mirFI). Images are taken at 20 x at 24 and 48 h for the three conditions (**A**) and at 20 x and 40 x at 48 h for the CH 250 µg/mL condition.

5.4.3 Evaluation of miRNA therapeutic effect within an OA in vitro platform

Therapeutic effect of miRNA-140-5p loaded polyplexes was assessed via gene expression analysis and histology, within the HC spheroid-based *in vitro* model of OA, over 10 days of culture.

For the PCR, results are reported as the fold change at day 10, with respect of day 1 (**Figure 5.13**). No statistical differences were found in *sox9* gene fold-change between the healthy spheroids, the spheroids cultured with cytokines (OA) and the spheroids cultured with cytokines and the supplement of CH/miRNA polyplexes (at 250 µg/mL concentration of CH) (OA+polyplexes). However, *acan* expression showed differences between the three conditions: the fold change in healthy condition and OA+polyplexes were statistically different from the fold change in OA condition, which was lower than 1-fold. Similarly, for *col2a1,* but in this case, the three conditions showed statistical different values between each other's ($p<0.0001$). The fold-change of *col1a2* was not displaying significant difference amongst the three conditions. The analysis of catabolic markers *mmp13* and *adamts-5*, showed a different trend amongst the conditions. *Mmp13,* showed its highest expression in OA condition, compared to the healthy one and the OA+polyplexes, while *adamts-5* gene did not show statistical difference between the OA samples, both untreated and treated with polyplexes,

but in both cases, the fold-change was higher compared to the healthy control. Also, *col2a1/col1a2* ratio was evaluated, displaying its highest expressions in healthy and OA+polyplexes conditions, compared to OA ($p<0.0001$).

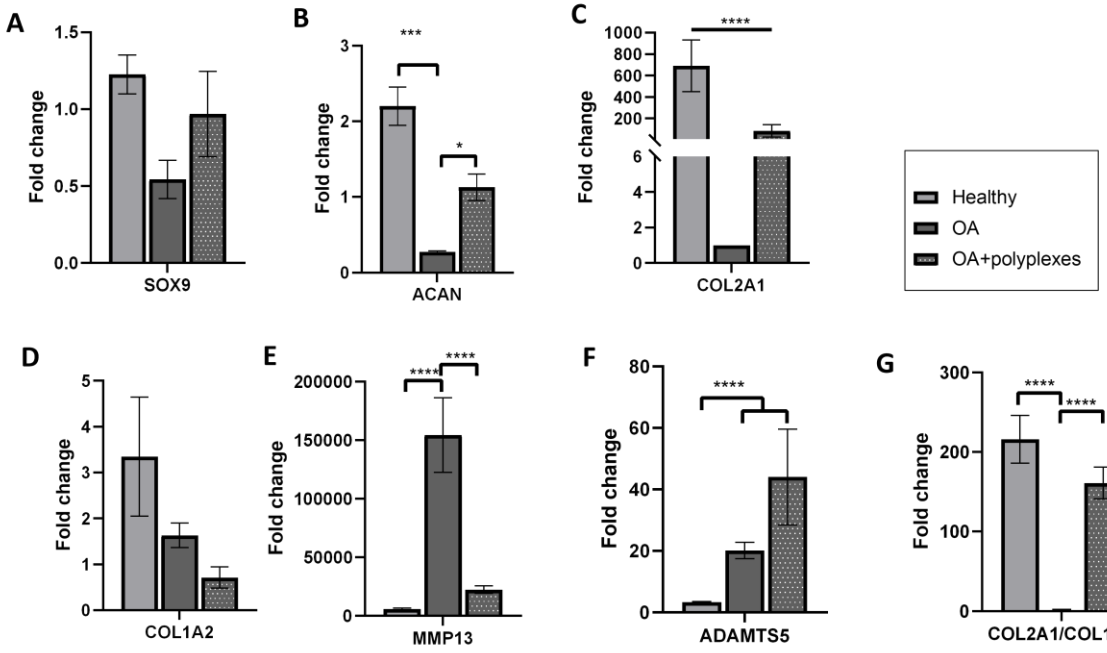

Figure 5.13: Gene RT-qPCR analysis to evaluated the expression of *sox9* (**A**)*, acan* (**B**)*, col2a1* (**C**)*, mmp13* (**D**) and *adamts-5* (**E**)*,* for assessing the therapeutic treatment of CH/miRNA based polyplexes in an OA *in vitro* model, compared to OA conditions and healthy conditions. The fold change at day 10 with respect to day 1 is reported in the graphs. A graph reporting the *col2a1/col1a2* ratio is reported as well (**G**). Statistics: *p<0.05, ***p<0.001, ****p<0.0001.

Finally, histological analysis of cells nuclei and cytoplasm (H&E), did not show great differences at day 10 in the three conditions (**Figure 5.14 B-D**), compared to day 1 (**Figure 5.14A**), as well as Alcian blue staining, which was very weak in all conditions (**Figure 5.14I-L**). However, some clear differences in terms of staining intensity can be observed at day 10 in OA condition, compared to both healthy and OA+polyplexes for PicroSirius Red: in OA condition the staining was more light orange (**Figure 5.14G**), while in both healthy and OA+polyplexes the red colouration was very intense (**Figure 5.14F,H**), even more intense than the one observed at day 1 (**Figure 5.14E**)

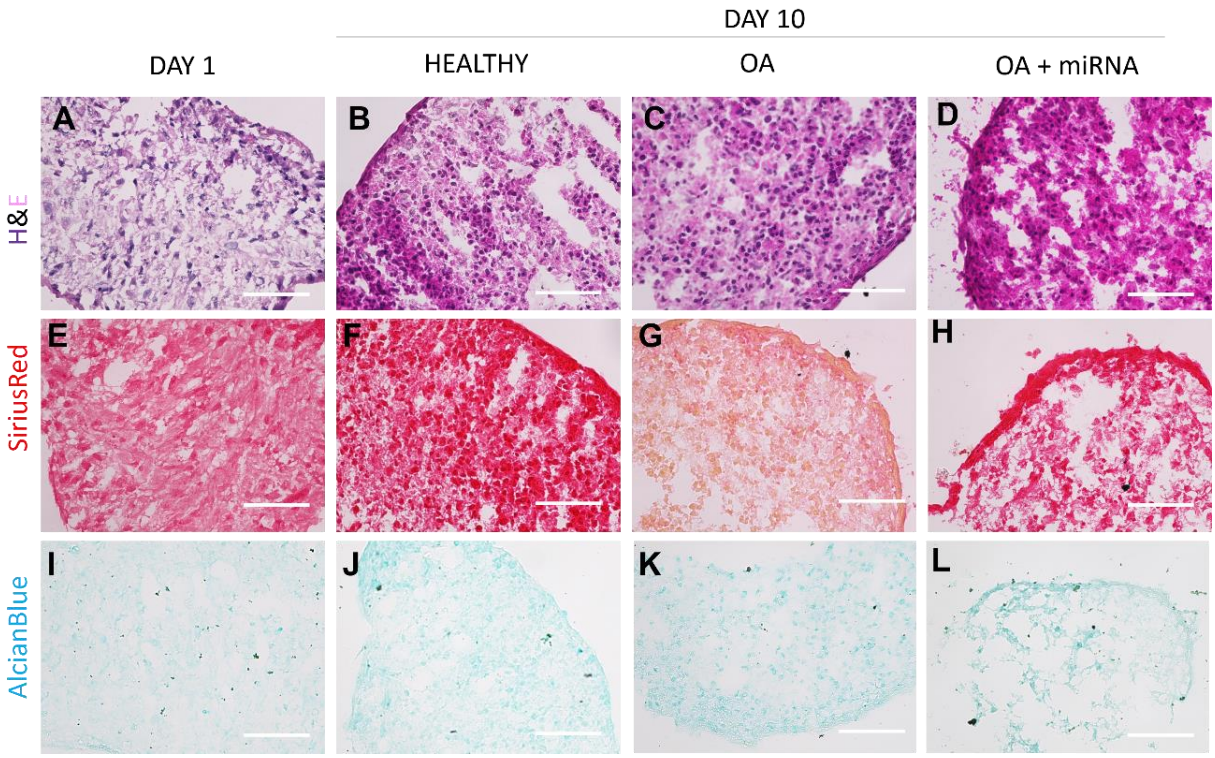

Figure 5.14: Histological analysis of cryosections of HC spheroids at day 1 and at day 10 in healthy, OA and OA+polyplexes conditions. H&E staining of cells nuclei and cytoplasm (**A-D**), Picrosirius red staining of collagen (**E-H**), Alcian blue staining of GAGs (**I-L**).

5.5 Discussion

5.5.1 Evaluation of shear stress via magnetic particles on HC

The first objective of this chapter was to evaluate the effect of the biomechanical stimulation of cells, as potential therapeutic treatment for OA. This is the first study assessing the use of magnetically induced stimulated cells within an OA model. As first step, magnetic PLLA/Fe_2O_3 microspheres were manufactured according to a previously optimised protocol (**Figure 5.1**) (Vikingsson et al., 2016). Magnetic nanoparticles (MNPs)-based techniques are an intriguing options for treating musculoskeletal tissues, remarkably bone and cartilage tissues, by stimulating intracellular pathways and influencing cell activity at the cellular level (Lima et al., 2015).The obtained microspheres showed a range of size of 10 – 70 µm, proximal to cells dimension, which was good in order to be able to be suspended with cells, as well as, to interact with them (**Figure 5.4**). Also, the presence of ferrite led to a higher crystallinity of the PLLA, visible from the presence of superficial roughness (**Figure 5.4**), as demonstrated in a previous work (Vikingsson et al., 2016).

For the manufacturing of the spheroids, the ratio of Y201-C:MS of 5:1 was the only one leading to the obtainment of a homogenous distribution of MS within the spheroid, which was

fundamental for making sure that all the cells are exposed to the same conditions: both in terms of interactions of Y201-C with the MS, and in terms of mechanical stimulation received once exposed to the magnetic field. The presence of MS did not affect cells viability at 48 h (**Figure 5.7**), while it affected cells shape within the spheroids (**Figure 5.8**): while in presence or absence of MS, cells appeared flattened in the outer region of the spheroid, as is usually observed in the superficial region of AC, in the inner region the presence of MS modified cells arrangement and morphology, which appeared adherent to the MS and elongated in MS samples, while these appeared rounded in the samples without MS (Wehland et al., 2020).
Furthermore, in presence of microsphere there was more inhomogeneity in the shape of the spheroids between healthy and pathological conditions, as demonstrated by the circularity analysis, which displayed the lowest value in MS-P samples (around 0.8), suggesting a low symmetry of the spheroid (Leung et al., 2015) (**Figure 5.6**)**.** This result highlighted that, not only, as anticipated in the *Chapter 4,* cytokines are involved in cell/cell interaction, and could, therefore, interfere with the cellular packing during the spheroids culture; also, cytokines were found to affect cells interaction with extra cellular material, in this case the MS, due to their direct effect on integrins and, therefore, on cells adhesion to the MS (Jin et al., 2021; Loeser, 2014).

After 10 days of Y201-C/MS spheroids culture, for the following 11 days, the Y201-C/MS spheroids were combined in chondrosphere and exposed to the magnetic field, by mounting the multi-well culture plate above the permanent magnets of the magnetic field bioreactor. As a control, apart from MS-free spheroids in healthy and OA conditions, spheroids loaded with MS, without exposure to magnetic field were studied, to determine if MS alone were able to affect cells fate. The hypothesis behind this study was that the cells mechanical stimulation associated with the movement of the PLLA/Fe_2O_3 MS, could affect chondrocytes through changes in the membrane potential, solute transport, or cellular fate, by activating specific cellular pathways able to convert mechanical stress into chondrogenic potential. However, controversial results were observed about the effect of MPs on cells chondrogenic activity (Dikina et al., 2017; Hu et al., 2013; Gemmiti & Guldberg, 2009a).
Sox9 expression showed higher fold-change in the healthy controls (CTRL-H and MS-H), compared to the pathological controls (CTRL-P and MS-P), as already expected from the results obtained in the previous *Chapter 4* and *Chapter 5*. However, in the magnetically stimulated samples in both healthy and OA conditions, *sox9* was not detected. The same

behaviour was observed by *acan* expression, which appeared to be negatively affected by the stimulation, but as well as by the presence of MS. Only in the CTRL samples, in fact, it was detected *acan*. This outcome suggested that the introduction of the magnetic field, as well as the introduction of MS, could be associated with the loss of cells phenotype and therefore these are not beneficial on cells chondrogenesis and, as well, in reversing the effect of cytokines. *Adamts5* expression, showed a decrease in OA condition in presence of the stimulation, suggesting that the dynamic culture had a positive effect in downregulating this catabolic gene. This outcome could be explained as the effect of a moderate stress on cells (Chen et al., 2020).

Shear stress is known to primarily have effect on Coll II fibrils and on *col2a1* gene expression and some studies demonstrated that fluid induced shear stress could promote Coll II secretion (Zhou et al., 2010; Sharifi & Gharravi, 2019). In this work, *col2a1* was very high in pathological condition, when stimulated, compared to the healthy condition stimulated. However, these results could be due to a combination of the mechanical stimulation of the cells and the chemical stimulation, by the presence of cytokines. This combination could result in an increased expression of *mmp13*, via COX-2-derived PGE2 at the early stage of OA (Wang et al., 2013). Chondrocytes tend to show an increased synthetic activity in early OA, which is thought to be an effort to rebuild the matrix with cartilage-specific components such as types II, to counteract the effect of the collagenases (Thibault et al., 2002). Therefore, the *col2a1* high expression in EXP-P could be associated with the very high expression of *mmp13* in the same condition (**Figure 5.9**).

Overall, the results obtained in this part of the work, suggested that the mechanical stimulation via magnetic particles, while exerting an effect of gene expression, still needs to be totally understood. The lack of enhanced cartilage formation and the increase in the proteases effect could be due to, for example, to an inadequate activation of mechanoreceptors such as stretch-activated ion channels or integrins. Therefore, follow-up studies for optimising the amounts of particles added to the culture conditions, or modification of magnetic field gradient magnitudes (Hu et al., 2013). Also, more analyses should be performed to evaluate and quantify which is the mechanical effect produced by the microspheres on cells within this *in vitro* model.

5.5.2 Evaluation of miRNA-based polyplexes effect on Y201-C

The second objective of this chapter was to exploit the use of miRNA-based polyplexes, as potential therapeutic treatment. The hypothesis behind that was that, once the polyplexes are uptaken by the cells, these can regulate the post-transcriptional gene expression. Since increasing evidence indicates that miRNA-140 is downregulated during OA pathogenesis (Li et al., 2015; Ghafouri-Fard et al., 2021), it would be of great interest to evaluate if its presence could interrupt the disease progression, once internalised by the cells. However, being the miRNAs negatively charged nucleic acids, these cannot penetrate the cellular membrane by passive endocytosis, and rapid clearance of naked miRNA in the blood stream renders its systemic delivery highly inefficient. Therefore, the successful application of miRNA largely depends on the development of effective delivery platforms (Prabu et al., 2015).

Herein, miRNA-140-5p were combined with CH, a polycation widely used in AC TE applications, to obtain a positively charged polyplexes, by the electrostatic interaction of the negatively charged phosphate group of miRNA and the positive charge of the CH amine groups, known as the N:P ratio (ratio of the number of atoms of nitrogens over phosphorus) (Zhou et al., 2018; Scalzone et al., 2019b). The charge of the polyplexes increased, with the increase of the CH concentration, up to 40 mV, obtained at 250 μg/mL; after that value the charge remained stable. The CH 250 μg/mL, which corresponded to an N:P ratio of 50, was selected to further analysis since it offered a reasonable charge for the application as a cargo system (Boussif et al., 1995; Richards Grayson et al., 2006). Regarding the size of the polyplexes analysed, the results obtained are similar to other works in literature : it has been shown that transfection complexes with particle sizes between 50 and 200 nm were optimal for an efficient endocytosic uptake into the cell (Boussif et al., 1995). The particles obtained were therefore filtered with a 0.22 μm filter, to ensure that all the particle of a superior size would have been removed (**Figure 5.10**).

The transfection efficiency of the obtained polyplexes with 250 μg/mL of CH was analysed in HC and compared with CH 5 μg/mL and with naked miRNA. While cells remained viable in all conditions and metabolically active (**Figure 5.11**), transfection complexes of FITC-labelled miRNA with CH 250 μg/mL were the only ones showing highly efficient uptake (**Figure 5.12**) (Bakhshandeh et al., 2012). Even if the CH 5 μg/mL polyplex showed a positive charge, meaning that CH was able to condense all miRNA, thus protecting it from enzymatic degradation by nucleases, however it was not sufficient to be uptaken by HC (Schade et al.,

2013). Moreover, high positive surface charge of complexes provides better binding to negatively charged cell membranes, facilitating subsequent cellular uptake, due to the "proton sponge effect" (Godbey et al., 1999; Freeman et al., 2013). Also, for effective gene knockdown, cytoplasmic release of miRNA is required: in **Figure 5.12B** it is noticeable that the fluorescent miRNAs were distributed in the cytoplasm and in the pericellular region of the cells and not in the nucleus, which may provide a better accessibility of miRNA to further processing. On the contrary, when using other polymers, such as PEI, complexes were found inside the nucleus. On the other side, naked miRNA, as expected due to their negative charge, were not uptaken by cells.

Then, the anabolic effect of miRNA-140 on HC during the progression of OA was assessed within the first 10 days of spheroids formation, since the effect of reversing the inflammation is usually assessed over a short time of culture (Ghafouri-Fard et al., 2021). The presence of miRNA-140 resulted in an increased expression of the anabolic genes, compared to their absence in the *in* vitro OA model, and a decreased expression of *mmp13* anabolic marker. In fact, one of the main mechanisms of action of the miRNA-140 is to inhibit *mmp13* and *adamts-5* expression (Si et al., 2017). Also, the fold-change results obtained in the OA model with the presence of polyplexes, were comparable with the healthy control, confirming that, not only miRNA-140 were able to interrupt the disease progression and cartilage degradation, but they were also able to inhibit the inflammatory response, reversing the cytokines action (**Figure 5.13**). This was confirmed by histological analysis of collagen: collagen production in the miRNA-loaded OA model was similar to the one in the healthy tissue, while it drastically decreased in the OA model (**Figure 5.14**). These results were consistent with other studies based on the use of miRNA-140 as a therapeutic molecule (Zhao et al., 2019).

Altogether the obtained results showed the efficacy of using miRNA-140 to interrupt the disease progression, by downregulating the expression of catabolic markers; to stimulate the production of a hyaline-like cartilage tissue, given by the expression of AC-specific chondrogenic markers and this was possible thanks to the combination of miRNA-140 with CH in polyplexes, to obtain an effective transfection.

CHAPTER 6. Engineering of an *in vitro* tissues with a zonal composition and organisation mimicking native AC in healthy state and during Osteoarthritis

STATEMENT OF SIGNIFICANCE

AC is a zonal tissue with a depth-dependent gradient of cells and ECM, whose functional properties are correlated to its structural variation, according to depth from the superficial layer to the subchondral bone. Aiming to mimic the AC structure and function, the emphasis of recent research has shifted from homogeneous engineered cartilage to zonal engineered cartilage (Ren et al., 2016)*. Despite the importance of this zonal organisation, to date relatively few studies have attempted to engineer a zonal in vitro construct with a structure and composition reliably mimicking that of the native tissue* (Kock et al., 2012)*. Also, there is a topographical variation in the zonal properties of AC during OA, which was never studied in a zonal in vitro model* (Lee et al., 2016)*. Thus, this chapter reported an in vitro model of zonal AC in healthy and OA conditions, focusing on each layer with a particular interest in cells morphology and organisation, as well as the ECM composition and structure.*

6.1. Introduction

The aim of this chapter is to develop an engineered biomimetic zonal model of AC, by taking into account several properties of AC: *(i)* biochemical composition (decreasing Coll II and increasing PGs content from the surface to the deep zone), *(ii)* matrix organisation (aligned collagen fibre in the superficial zone) *(iii)* cellular morphology (flattened and organised alongside the collagen fibres in the superficial layer, rounded and randomly distributed within the ECM matrix in the middle layer and piled up within vertical channels in the deep layer) and number (decreasing from the superficial layer to the subchondral bone), and mechanical properties (Young's modulus increasing with the depth). The approach exploited was based on multiple objectives:

OBJ 1: Manufacturing of each single layer of AC, by optimising the materials, cells, and manufacturing technique, by considering the properties of each layer (Table 2.1).

OBJ 2: Analysis of cells fate in healthy and pathological condition within each layer. The pathological condition was obtained by emulating the OA environment with the addition of pro-inflammatory cytokines (according to the optimised protocol presented in Chapter 4) to

the culture. Particularly cells anabolic and catabolic activity was evaluated in terms of gene expression and ECM production.

OBJ 3: Study of the zonal model in healthy and OA conditions, by combining all the optimised layers.

The development and characterisation of the two hydrogels formulation, GGMA and CSDP, were reported and published in two articles (Scalzone et al., 2020; Scalzone et al., 2022).

6.2 Materials and Methodology

Different materials and methodology were used for each layer, as reported in **Table 6.1**.

ZONE	BIOMATERIALS	CELLS	FABRICATION TECHNIQUE
SUPERFICIAL LAYER (SL)	PCL/GEL (80:20 w/w)	Y201-C 14 x 10^6 cells/mL	Electrospinning
MIDDLE LAYER (ML)	GG2 (GG (2% w/v) & GG2-MH (GG (2% w/v)-MH (5% w/v))	Y201-C 7 x 10^6 cells/mL	Bioprinting
DEEP LAYER (DL)	GG3 (GG (3% w/v)) & CSDP (15% w/v)	Y201-C 3.5 x 10^6 cells/mL	Soft lithography
SUBCHONDRAL BONE (SB)	PLA/GEL & PLA/GEL/nHA	Y201 8.75 X 10^5 cells/mL	Fusion deposition modelling

Table 6.1: Biomaterials, cells, and manufacturing techniques, selected for each layer of the zonal model.

6.2.1 GGMA: synthesis and assessment of methacrylate efficiency

GGMA was synthetised, lyophilised, and stored as reported in *section 3.1.1* and **Figure 3.1**. To assess the methacrylation efficiency FTIR-ATR, h-NMR and XPS analyses were performed on GG raw powder and lyophilised GGMA, as reported in *section 3.3*.

6.2.2 GGMA hydrogels preparation and characterisation

Multiple GGMA-based hydrogels formulations were prepared, as reported in *section 3.2.1* and **Table 3.1**. Amongst them, GGMA 2%, GGMA 3%, GGMA 2% - MH 5% were selected for further analysis. Briefly, GGMA freeze-dried powder, with or without the addition of MH, was

dissolved at the appropriate concentration in dH_2O, together with LAP photoinitiator (0.1 % w/v) overnight, prior to photocuring.

Several characterisation tests were performed on these formulations: gelation time and water uptake kinetics analysis, as reported in *section 3.4;* morphological analysis and evaluation of the frequency of the diameter of the hydrogel pores, as reported in *section 3.6*; unconfined compression tests and rheological analysis, as reported in *section 3.5.*

6.2.3 CSDP: synthesis and evaluation of Catechol conjugate characterisation

CSDP was synthetised, lyophilised, and stored, as reported in *section 3.1.2* and in **Figure 3.2**. FTIR-ATR and XPS were carried out to study the elemental composition of the CSDP conjugate, in comparison with bare CS, as explained in *section 3.3.*

6.2.4 CSDP hydrogel preparation and characterisation

Catechol groups were chemically crosslinked to CS obtain the CSDP hydrogels, as reported in *section 3.2.2*. Briefly, CSDP10 and CSDP20 solutions were prepared by dissolving the CSDP in PBS. To obtain the sol/gel transition, $NaIO_4$ was introduced to the CSDP solutions at pH adjusted to 8-9, considering a molar ratio of $NaIO_4$/Catechol 1.5:1.0. When the solution flow stopped inverting the vial, the gelation time was calculated.

Water uptake analysis was performed on CSDP freeze-dried samples, as reported in *section 3.4.2*. Mechanical properties were evaluated via unconfined compression test, as reported in *section 3.5.1.* SEM was used to examine the morphology of hydrogels on freeze-dried materials and evaluate the frequency of the diameter of the hydrogel pores, as reported in *section 3.6*.

6.2.5 Cell culture and pathological environment set-up

The cells used in this chapter were Y201 and Y201-C. Both cells culture conditions are reported in *section 3.7.*

To set-up the AC pathological model, a cocktail of pro-inflammatory cytokines was introduced to the culture media at day 1 of samples culture, to emulate the OA environment (as reported in *section 3.8*). A low concentration of cytokines was used for the zonal model (LC-OA): 1 ng/ml of IL-1β and TNF-α and 10 ng/mL of IL-6.

6.2.6 Subchondral bone manufacturing

For the SB manufacturing, it was selected a thermoplastic polymer, PLA (Ingeo™ Biopolymer, NatureWorks), which was extruded via the FDM head of the Rokit INVIVO 3D bioprinter (Rokit Healthcare), to obtain a 13 x 13 x 1 mm (W x L x H) grid with a 45 ° rotate angle between consecutive layers. The printing parameters are reported in **Table 6.2**.

NOZZLE SIZE	EXTRUSION TEMPERATURE	BED TEMPERATURE	TRAVEL SPEED	PRINTING SPEED	ROTATE ANGLE
400 µm	215 °C	25 °C	2 mm/s	2 mm/s	45°

Table 6.2: Printing parameters for the FDM processing of PLA with Rokit INVIVO bioprinter.

PLA scaffolds were functionalised with nHA and GEL via polydopamine coating. Briefly, the scaffolds were incubated in polydopamine solution, obtained by dissolving DP hydrochloride (MW= 189.64 g/mol) in TRIS buffer (0.1 M, pH 8.5) overnight and then washed in dH_2O and incubated for 7 hours in GEL (1.5 % w/v in TRIS buffer) and nHA (5 % w/w with respect to the weight of GEL) solution. The morphology of the PLA, PLA with DP (PLA/DOPA), PLA with DOPA and GEL (PLA/GEL) and PLA with DOPA, GEL and nHA (PLA/GEL/nHA) were assessed via SEM, as reported in *section 3.6*. All the tests were performed on 6 x 6 x 1 mm (W x L x H) grids.

PLA, PLA/GEL and PLA/GEL/nHA scaffolds were sterilised by immersion in 70 % ethyl alcohol solution (ETOH; Sigma Aldrich, UK) for 20 min and treated with Sudan Black (0.3% w/v in 70 % EtOH) to limit auto-fluorescence, for further 20 min at 37 °C. Scaffolds were washed three times with PBS and then sterilized under a UV lamp for 30 min and placed in 48-well plates. Y201s were suspended in DMEM/F12 and seeded on each sample at a concentration of 2.8 x 10^5 cells/scaffold (considering a ratio 1:4 compared to DL) and incubated at 37 °C, 5 % CO_2 for 30 min. Then, 500 µL of fresh DMEM/F12 was added to each well. For the set-up of OA conditions (SB-OA) the cocktail of cytokines was added at day 1 of culture, as reported in *section 5.2.5*. Samples were cultured up to 21 days with a change of media every two days.

6.2.7 Subchondral bone cytocompatibility assessment

Live/Dead assay was performed to assess the cytocompatibility of PLA and PLA/Gel at day 3 and PLA/GEL/nHA at day 3 and day 7, as reported in *section 3.9.1*. Y201s distribution onto PLA/GEL/nHA was evaluated after 3 and 7 days of culture via Immunostaining analysis of cells

nuclei and cytoskeleton, following the protocol reported in *section 3.12.* Images were collected with EVOS M5000 microscope in GFP and RFP for Live/Dead and in DAPI/RFP for the Immunostaining with a 10 x or 20 x objective lens. Y201s morphology at day 1 of culture onto PLA/GEL/nHA was performed via SEM: samples preparation is reported in *section 3.15.*

MTT assay was performed to assess the metabolic activity of Y201s, as reported in *section 3.10.1*. Measurements were taken after 1, 7 and 21 days.

6.2.8 Y201s osteogenic commitment onto PLA/GEL and PLA/GEL/nHA scaffolds

PLA/GEL and PLA/GEL/nHA were evaluated in terms of osteogenic commitment of Y201s: protein expression analysis was performed for RUNX2, ALP (200kDa) and ON via Western blotting analysis at days 1,7,14,21. Protein densitometric quantification, normalised to GAPDH, and antibody binding onto the Western blotting membranes, were obtained and reported as reported in *section 3.19.*

Gene expression analysis was performed via RT-qPCR at day 1 and day 21, according to the protocol reported in *section 3.13.* TaqMan qRT-PCR *runx2, alpl, sparc* and *gapdh* probes were quantified. Results are presented at day 1 and day 21, as the relative expression of *runx2, alpl, sparc*, normalized to *gapdh,* and expressed relatively using the $2^{-(\Delta Ct)}$ method of Livak (Livak & Schmittgen, 2001b).

Immunofluorescence of Osteonectin (anti-*sparc*) (ON) was performed as well at day 21 of PLA/GEL and PLA/GEL/nHA, as reported in *section 3.17*.

Alizarin red analysis was quantitatively and qualitatively performed, according to the protocol in *section 3.18* at days 1, 7, and 21. Images of stained samples were collected with a stereomicroscope (Leica Microsystems), while Alizarin red quantification was performed with a Filter-based FLUOstar® Omega multi-mode reader.

6.2.9 Study of Subchondral bone in healthy and OA conditions

SB was evaluated in Healthy (SB-H) and pathological (SB-P) conditions, following the same characterisation performed in *section 6.2.8*. However, for the protein expression RANKL, OPG and GAPDH were analysed, while for the gene expression, the analysis was performed at days 1,7 and 21, for *runx2, coll1a2, spp1, vegf* and *gapdh* genes. Alizarin Red analysis was performed qualitatively and quantitatively at days 1, 7, 14, 21.

6.2.10 Soft lithography for manufacturing a multi-channelled gellan gum

For the manufacturing of a multi-channelled DL biomimetic construct, a soft lithography approach was used. A PLA (Filamentive, UK) structure of 14 x 14 x 2 mm (W x L x H) with 16 channels (1 mm diameter each) was designed with autoCAD Inventor software and manufactured with a FDM 3D printer (Ultimaker 3, Netherland). Printing parameters are reported in **Table 6.3**. Once the final mould was printed, it was analysed through a stereomicroscope (Leica Microsystems) and all dimensions were recorded.

NOZZLE SIZE	EXTRUSION TEMPERATURE	BED TEMPERATURE	MATERIAL INFILL	PRINTING SPEED	LAYER HEIGHT
400 µm	200 °C	25 °C	100 %	40 mm/s	60 µm

Table 6.3: Printing parameters for the FDM processing of PLA with Ultimaker 3.

The obtained structure served as a positive template for the creation of a negative PDMS-based silicone mould, with 16 pins each. PDMS was casted onto the PLA by using Dowsil sylgard 184 silicone (Dow, USA) elastomer kit. The pre-polymer base and the cross-linking curing agent were combined at mixing ratio of 10:1 and the obtained solution was mixed using a vortex shaker until homogeneous. Pro anti-adhesive spray (RS Components, UK) was faintly applied to the PLA moulds from 30 cm distance, then left for 20 min under the fume hood, and this was repeated twice before the PDMS mixture was poured into the PLA moulds. To remove the bubbles, samples were placed in a vacuum desiccator and degassed for 2 minutes using a pump, prior to let the PDMS curing at RT for 48 hours. Once the samples were cured, the PDMS mould was carefully detached from the PLA mould by using tweezers, sterilised using UV (254 nm) and placed in a 12 well plate.

2 mL of GG3 were poured on top on the PDMS mould in sterile conditions and the multi-well was exposed to UV light (254 nm) for photocuring for 10 minutes before being filled with 500 µL of DMEM/F12 to complete the physical crosslinking. The PDMS mould was then removed, revealing a multi-channelled GG. At this time, 20 µL of pre-crosslinked CSDP with half of the amount of needed $NaIO_4$, according to the counts explained in *section 3.2.2*, embedded with Y201-C (3.5 x 10^6 cells/mL) was introduced to each channel of the GG structure. The structure was incubated at 37 °C, 5 % CO_2 for few minutes to complete the crosslinking, before the addition of DMEM/F12. For the set-up of OA conditions (DL-OA) the cocktail of cytokines was

added at day 1 of culture, as reported in *section 6.2.5*. Samples were cultured up to 21 days with a change of media every two days.

6.2.11 Deep layer cytocompatibility assessment

Live/Dead assay was performed to assess the cytocompatibility of DL at days 1 and 7 and images of the GG3-CSDP channels were taken with a Nikon A1R confocal laser with a 10 x objective lens, as reported in *section 3.9.1.*

Y201-C distribution within the DL hydrogel was evaluated after 3 and 7 days of culture via Immunostaining analysis of cells nuclei and cytoskeleton and images were collected with a Nikon A1R confocal laser with a 10 x objective lens, as reported in *section 3.12*. Y201-C morphology at day 1 of culture within the DL was performed via SEM: samples preparation is reported in *section 3.15.*

MTS assay was performed to assess the metabolic activity of Y201-C, as reported in *section 3.10.2*. Measurements were taken after 1, 3 and 7 days of culture.

6.2.12 Study of Deep layer in healthy and OA conditions

To observe the behaviour of Y201-C in terms of chondrogenic behaviour and hypertrophy tendency, immunofluorescence staining was applied to the DL-H and DL-P at days 1 and 21. Samples were fixed using 4% PFA for 1 h at 4 °C, as reported in *section 3.17.* Samples were incubated for 2 hours with Anti-Collagen X or and Anti-Aggrecan primary antibodies and Fluorescein-labelled goat anti-rabbit IgG (H + L) for Anti-Aggrecan and Goat Anti-Mouse IgG (H&L) Alexa Fluor® 594 for Anti-Collagen X were used as secondary antibodies. Cell nuclei were counterstained with Hoechst. Samples were imaged with a Nikon A1R confocal microscope and analysed with NIS Nikon software. The percentage of Aggrecan and Coll X positively stained cells was quantified with Image J software in all conditions.

GAGs were quantified at days 1, 14 and 21, as reported in *section 3.14.* Stress relaxation analysis was performed on DL-H and DL-OA samples at days 1 and 14, as reported in *section 3.5.2*. Y201-C morphology was evaluated at day 21 of culture within GG3 channels in healthy (DL-H) and OA (DL-P) condition via SEM: samples preparation is reported in *section 3.15.*

6.2.13 Middle layer manufacturing: bioprinting process optimisation

Multiple bioinks formulations were prepared by varying the GGMA polymer and MH concentrations (as reported in *section 3.2.1*). 3 mL of each formulation was loaded in a 10 mL

Luer-Lock syringe with a 27-gauge metal needle (Intertronics, UK) and placed in the Rokit INVIVO biodispenser. X, y, and z calibrations were done manually before printing, and the NewCreatorK programme was used to create a multi-layered squares grid structure (6 mm x 6 mm x 2 mm) (Rokit Healthcare). During the printing process, the UV-led (wavelength 365 nm) was kept switched on for the photo-curing. Printing parameters are reported in **Table 6.4**. The ability of each bioink to be extruded was evaluated, and GG2 and GG2-MH were selected for further analysis.

NOZZLE SIZE	DISPENSER TEMPERATURE	BED TEMPERATURE	MATERIAL INFILL	PRINTING SPEED	LAYER HEIGHT
27 G	36 °C	25 °C	20 %	5 mm/s	150 µm

Table 6.4: Printing parameters for the bioprinting of GGMA-based bioinks with Rokit INVIVO bioprinter.

GG2 or GG2-MH solutions were loaded with Y201-C at a concentration of 7×10^6 cells/mL. These bioinks were then transferred to the Rokit INVIVO printing cartridge, which was fitted with a bio-dispenser to extrude bioinks in a sterile environment (HEPA filters), with regulated temperature. The constructs were printed on a layer of sterile DMEM/F12 upon a glass Petri dish (diameter 9 cm) to allow physical crosslinking. The printability was investigated on images captured with an EVOS M500 microscope, by analysing the filament spreading ratios, determined as the width of the printed filament divided by the needle diameter, and the filament diameter after the deposition post-crosslinking. Image J was used to process the images. After bioprinting, the samples were transferred to 48-well plate plates containing 500 µL of DMEM/F12 and kept in the incubator for 21 days for analysis. For the set-up of OA conditions (ML-OA) the cocktail of cytokines was added at day 1 of culture, as reported in *section 6.2.5*. Samples were cultured up to 21 days, with a change of media every two days.

6.2.14 Middle layer cytocompatibility assessment

Cells viability was evaluated after 1 and 3 days from the bioprinting process with ReadyProbes® Cell Viability Imaging Kit, as reported in *section 3.9.1.* Total cells were stained in blue and dead cells in red. Images were taken with a Nikon A1R confocal laser with a 10 x objective lens, as reported in *section 3.9.1.*

Y201-C distribution within the GG2 and GG2-MH bioprinted constructs was evaluated at days 1, 3 and 7 via Immunostaining analysis of cells nuclei and cytoskeleton and images were collected with a Nikon A1R confocal laser with a 10 x objective lens, as reported in *section 3.12.* Y201-C morphology at day 1 and day 21 of culture, within the GG2 and GG2-MH, was performed via SEM, as reported in *section 3.15.*

MTS assay was performed to assess the metabolic activity of Y201-C, as reported in *section 3.10.2*. Measurements were taken after 1, 3 and 7 days of culture.

6.2.15 Study of Middle layer in healthy and OA conditions

ML was evaluated in Healthy (GG2-H, GG2-MH-H) and pathological (GG2-P, GG2-MH-P) conditions.

Histological analyses were performed on fresh tissue slices, as reported in *section 3.16,* via H&E, Alcian Blue and PicroSirius Red stainings. Images were taken with EVOS M5000 microscope at 20 x. HIC was performed as well on fresh tissue slices, as reported in *section 3.16.6,* for staining Aggrecan and Coll II.

Gene expression analysis was performed at days 1 and 21, for *sox9, acan, col2a1, col1a2, mmp13, adamts-5* and *gapdh* genes, as reported in *section 3.13*. Results are reported as the fold change at day 21, using the day 1 as calibrator. GAGs were quantified at days 1, 7 and 21, as reported in *section 3.14.*

6.2.16 Superficial layer manufacturing: electrospinning of PCL/Gel membranes

The PCL/GEL solution (15% w/v) was obtained by mixing PCL (80 kDa, Sigma Aldrich UK) and GEL (Porcine skin type A, Sigma Aldrich) at ratio 80:20 w/w in a 5 mL solution of acetic acid and formic acid (50:50). The solution was stirred for 24 h at RT at 200 rpm. The γ-glicidossipropiltrimetossisilano (gptms) (3.68 % (v/v)) was added to the PCL/Gel solution at a concentration of 3.68 % (v/v) and the final solution was stirred for further 30 minutes. Then, PCL/Gel was then inserted in a 5 mL syringe and electrospun with voltage of 20 kV, distance of 12 cm and flow rate of 500 µL/min. The membranes were cut to obtain a dimension of 6 x 6 x 1 mm.

FTIR-ATR was carried out to study the elemental composition of the PCL/GEL electrospun membrane, in comparison with bare PCL membrane, as explained in *section 3.3.* Also, the morphology of random (PCL/GEL-Random) and aligned (PCL/GEL-Aligned) membranes was

assessed via SEM, as reported in *section 3.6*, at different magnifications (5000 x, 6000 x and 9000 x).

6.2.17 Superficial layer cytocompatibility assessment

Live/Dead assay was performed to assess the cytocompatibility of PCL/GEL random and aligned membranes, as well as cells organisation upon the membranes, at days 1 and 3, as reported in *section 3.9.1.* Y201-C distribution and proliferation onto PCL/GEL-Random and PCL/GEL-Aligned membranes was evaluated after 7 days of culture via Immunostaining analysis of cells nuclei, cytoskeleton, and staining of Ki-67 proliferation marker, following the protocol reported in *section 3.12.* Images were collected with EVOS M5000 microscope in GFP and RFP for Live/Dead and in DAPI/RFP/GFP for the Immunostaining with a 20 x objective lens.

MTT assay was performed to assess the metabolic activity of Y201-C, as reported in *section 3.10.1*. Measurements were taken after 1, 3 and 7 days of culture.

6.2.18 Study of superficial layer in healthy and OA conditions

PCL/GEL-Aligned membranes were used to study SL in Healthy (SL-H) and pathological (SL-P) conditions.

Histological analyses were performed on fresh tissue slices, as reported in *section 3.16,* via H&E, Alcian Blue and PicroSirius Red stainings. Images were taken with EVOS M5000 microscope at 20 x magnification. HIC was performed on fresh tissue slices, as reported in *section 3.16.6,* for staining Aggrecan (ACAN) and Coll II (Coll II).

Gene expression analysis was performed at days 1 and 21, for *sox9, acan, col2a1, col1a2, mmp13, adamts-5* and *gapdh* genes, as reported in *section 3.13*. Results are reported as the fold change at day 21, using the day 1 as calibrator. Also, the ratio of COL2A1/COL1A2 was reported and plotted.

Immunofluorescence of Coll II and Aggrecan (ACAN) was performed on membranes at days 1 and day 21 (SL-H and SL-P) of culture, as reported in *section 3.17*.

Y201-C morphology in SL-H and SL-P at day 21 and at day 1 was evaluated was evaluated at different magnifications (400 x, 750 x or 1000 x) via SEM, as reported in *section 3.15.*

6.2.19 Zonal model manufacturing and characterisation

The zonal model of AC and SB was manufactured by combining all the fabrication techniques reported in this chapter, as reported in **Figure 6.** First it was manufactured and functionalised with GEL and nHA the SB via FDM, which was merged with the DL made via soft-lithography; following, the ML was bioprinted and merged with the SL. The two parts (SB-DL and ML-SL) were made adhere, by using the CSDP15 hydrogel.

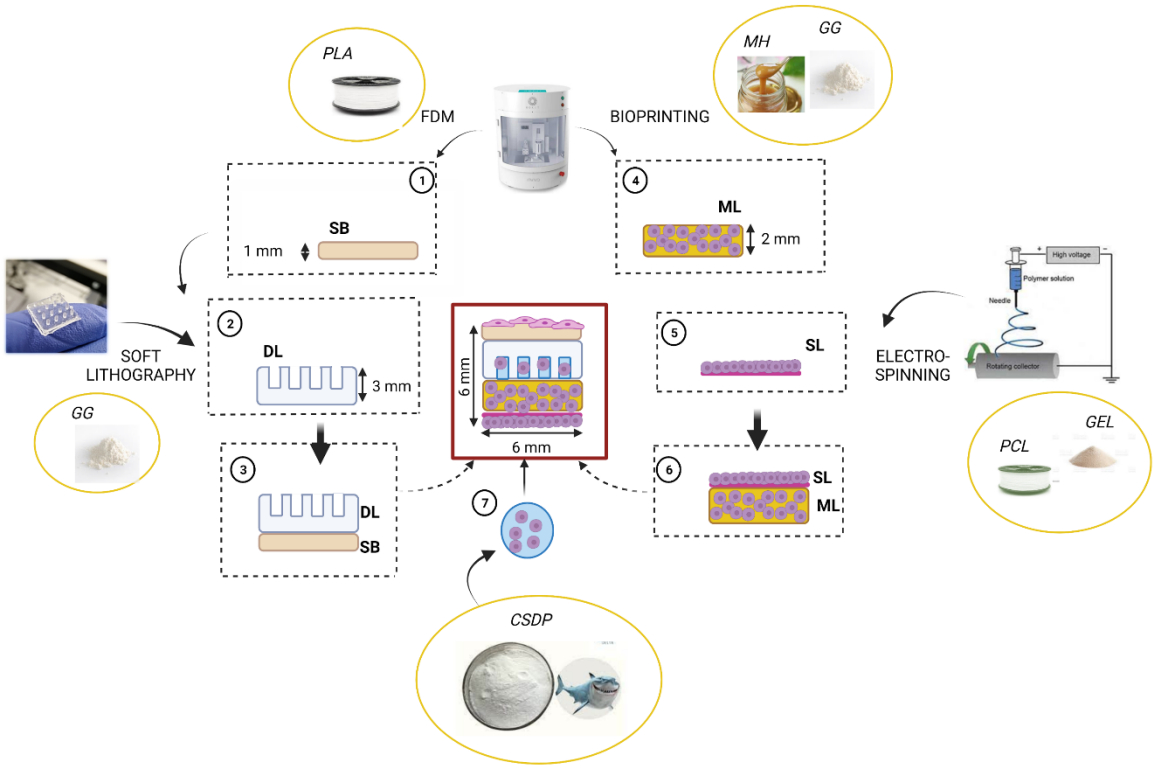

Figure 6.1: Scheme of the manufacturing process for the zonal model: (1) manufacturing of SB via FDM of PLA with Rokit INVIVO bioprinter (6 x 6 x 1 mm); (2) DL manufacturing, based on GG3, via soft-lithography, with PDMS moulding (6 x 6 x 3 mm); (3) combination of SB and DL constructs, during UV exposure; (4) bioprinting of Y201-C-loaded GG2-MH bioink for the obtainment of the ML (6 x 6 x 2 mm); (5) electrospinning of PCL/GEL membranes and seeding with Y201-C for the manufacturing of the SL (6 x 6 mm); (6) combination of SL and ML; (7) formation of the zonal construct by merging the SL-ML construct with the SB-DL construct, via CSDP hydrogel loaded with Y201-C and seeding of the SB with Y201.

The whole zonal model was incubated for 10 minutes to ensure the adherence of the Y201s to the PLA scaffold and then turn upside down in the 12 well-plate and each well was filled with 2 mL of DMEM/F12 culture medium. For the set- up of OA conditions, DMEM/F12 supplemented with the cocktail of pro-inflammatory cytokines (LC-OA) (as reported in *section 6.2.5*) was added after 1 day of culture.

6.2.20 Zonal model characterisation in healthy and OA conditions

The viability of cells within the zonal model in Healthy conditions was evaluated after 24 h of the manufacturing, with ReadyProbes® Cell Viability Imaging Kit, as reported in *section 3.9.1.* The nuclei of all cells were stained in blue and dead cells in red. Images were taken with a EVOS M5000 microscope with a 10 x objective lens, as reported in *section 3.9.1.*

MTS assay was performed to assess the metabolic activity of cells within the construct, as reported in *section 3.10.3*. Measurements were taken after 1, 3 and 7 days of culture.

Cells distributions within the construct was assessed at day 1 and day 7 of culture via Immunostaining analysis of cells nuclei and cytoskeleton and images were collected with a EVOS M5000 microscope with a 10 x objective lens, as reported in *section 3.12*.

Histological analyses of the zonal model were performed on fresh tissue slices at day 1 and day 21 in Healthy and OA conditions, as reported in *section 3.16,* via H&E, Alcian Blue and PicroSirius Red stainings. Images were taken with EVOS M5000 microscope at 20 x. The zonal model and cells morphology at day 1 and day 21 in Healthy and OA conditions were evaluated with SEM: samples preparation is reported in *section 3.15.*

6.2.21 Statistical analysis

All tests were performed at least in triplicate for each sample in each condition. The results were represented as mean ± standard deviation. Differences between groups were determined using One-way analysis of variance (ANOVA) with Tukey's multiple comparison test using levels of statistical significance of $p<0.0001$ (****), $p<0.001$ (***), $p<0.05$(**) and $p<0.01$(*).

6.3 Results

6.3.1 GGMA chemical characterisation

In **Figure 6.2A** are reported the FTIR-ATR spectra for GG and GGMA. From the GG spectrum, the main peaks are the C-O stretching around 1050-1000 cm^{-1}, the COO- symmetric stretching at 1412 cm^{-1} and the asymmetric stretching at 1618 cm^{-1}, the stretching vibration of $-CH_2$ and $-CH_3$ aliphatic groups at 2970–2880 cm^{-1} and the stretching of O-H at 3420 cm^{-1}. In the GGMA spectrum, instead, in addition to the GG characteristic peaks, the ones typical of the methacrylate group: at 1645 cm^{-1} the typical double bond (C=C) stretches, partially

overlapping with the GG asymmetric COO− stretching band; at 1536 cm^{-1} the C-C stretching and at 1738 cm^{-1} the carbonyl stretching vibration of an ester (Oliveira et al., 2011; Daniela F Coutinho et al., 2010).

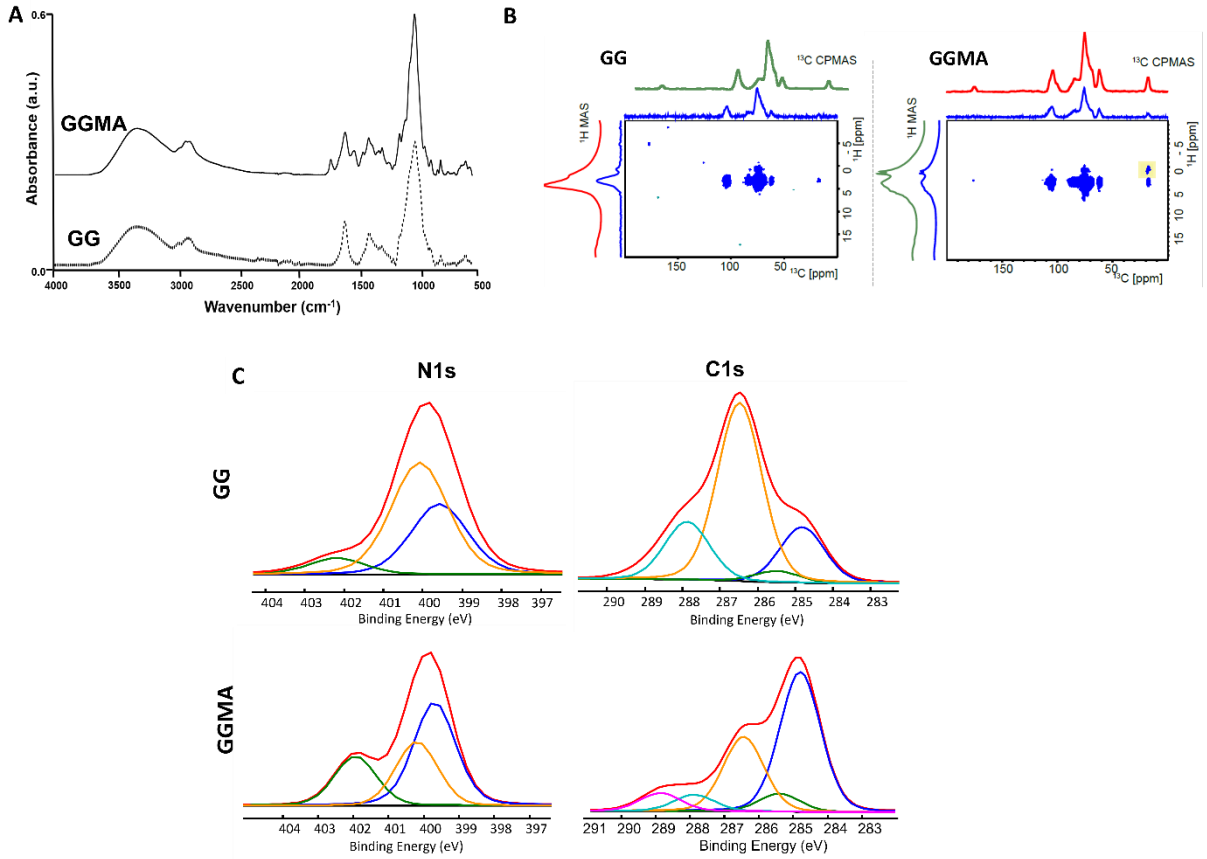

Figure 6.2: Chemical characterisation of GG and GGMA. FTIR-ATR spectra of low-acyl GG and GGMA freeze-dried samples **(A);** NMR graph of GG before and after the methacrylation, relative to the ^{13}C CP, ^{1}H MAS and 2D ^{1}H-^{13}C heteronuclear correlation spectra with related ^{1}H and ^{13}C projections (**B**); XPS data relevant to C1s curve fittings of GG and GGMA samples, whose attributions and atomic percentages were reported in **Table 6.5** (**C**).

h-NMR analysis was used to verify the inclusion of methacrylate groups in the GG structure, as shown in **Figure 6.2B**. Chemical shifts were observed in GG at 5.15 and 1.32 ppm, which corresponded to H-1 and H-6 of the α-anomers of L-rhamnopyranosyl residues, respectively, and at 4.73 and 4.55 ppm, which corresponded to D-glucopyranosyl and D-glucuropyranosyl residues, respectively. Furthermore, these distinct signals may be found in the chemical shift of GGMA. Singlets seen in the GGMA spectra at 1.96, 5.77, and 6.18 ppm, are attributed to the methyl proton of methacrylate and the two peaks from vinyl proton, respectively. In addition, methacrylate's heteronuclear ^{1}H-^{13}C correlation spectra revealed an additional peak at ~18 ppm for ^{13}C and ~1 ppm for ^{1}H (Xu et al., 2018).

XPS was used to further characterise the chemical composition. The elemental compositions of GG and GGMA were investigated, and the findings are presented in **Table 6.4**. Carbon (C1s) and oxygen (O1s) were the most abundant elements found in both samples, together with a low percentage of nitrogen (N1s) and sulphur (S2p). Furthermore, after the methacrylation, a considerable rise in the C/O atomic area ratio (equivalent to 1.4 and 2.9 for GG and GGMA, respectively) was found.

	Atomic %					
Sample	C1s	O1s	N1s	S2p	Na1s	Ca2p
GG	56.9	40.1	1.9	0.5	0.3	0.3
GGMA	71.9	25.2	2.0	0.9	-	-

Table 6.5: XPS Atomic percentage of each element for GG and GGMA samples.

As indicated in **Table 6.6**, an accurate curve fitting the C1s spectra (**Figure 6.2C**) revealed for GG and GGMA samples five-components. The same components were found in GGMA samples, albeit at different relative percentages. Indeed, the C-OR/COOR and O-C-O/COOR area ratios in the GG sample were 16:1 and 5:1, respectively, whereas similar ratios in the GGMA sample were 4:1 and 0.9:1.

	BE (eV)/ At%							
Sample	**CH_x**	**C-COOR, C-NH**	**C-OH, $CH\text{-}NH_3^+$**	**O-C-O, $C\text{-}O\text{-}SO_3^-$, CO-NH**	**COOR**	**NH_2**	**NH-C=O**	**NH_3^+**
GG	284.8/ 17.7%	285.5/ 3.6%	286.5/ 56.6%	287.9/ 18.4%	288.8/ 3.6%	399.6/ 35.2%	400.1/ 56.2%	402.2/ 8.6%
GGMA	284.8/ 52.6%	285.4/ 6.7%	286.5/ 27.9%	287.9/ 6.1%	288.9/ 6.7%	399.7/ 49.0%	400.0/ 28.2%	401.9/ 22.7%

Table 6.6: XPS high resolution C1s and N1s peaks for GG and GGMA samples.

6.3.2 GGMA-based hydrogels characterisation

The experiment was conducted under two conditions using the tube inversion test (**Figure 6.3A,B**). First, the solutions were exposed to UV light to determine the gelation time related to the sole photo-crosslinking, which was found to be 10 minutes for the three formulations: in fact after 3 minutes GG2, GG3 and GG2-MH solutions were still liquid and flowing in the vial (**Figure 6.3C**), even if their flowability was lower compared to the start of the experiment; after 10 minutes the three formulations underwent the sol/gel transition and no flow of solution was observed in the vial (**Figure 6.3E**). Particularly, GG3 showed sol/gel transition already after 5 minutes of UV exposure (**Table 6.7**). The second condition explored was the combination of photo and ionic crosslinking mechanisms, by adding divalent ions present in DMEM/F12 cell media, to the solutions, after 1 minute of UV light exposure: the addition of these ions anticipated the crosslinking and, after 3 minutes, the three formulations showed sol/gel transition, as observed in **Figure 6.3D**. A clear separation between the transparent gels and the pink liquid DMEM/F12 medium can be noticed and kept up to 10 minutes, when the experiment was stopped (**Figure 6.3F**).

	Gelation time	
	Photo	**Ionical + Photo**
GG2	10 min	3 min
GG3	5 min	3 min
GG2-MH	10 min	3 min

Table 6.7: Report of the gelation times for the GG2, GG3 and GG2-MH formulations with Photo-crosslinking or a combination of Photo and Ionical crosslinking.

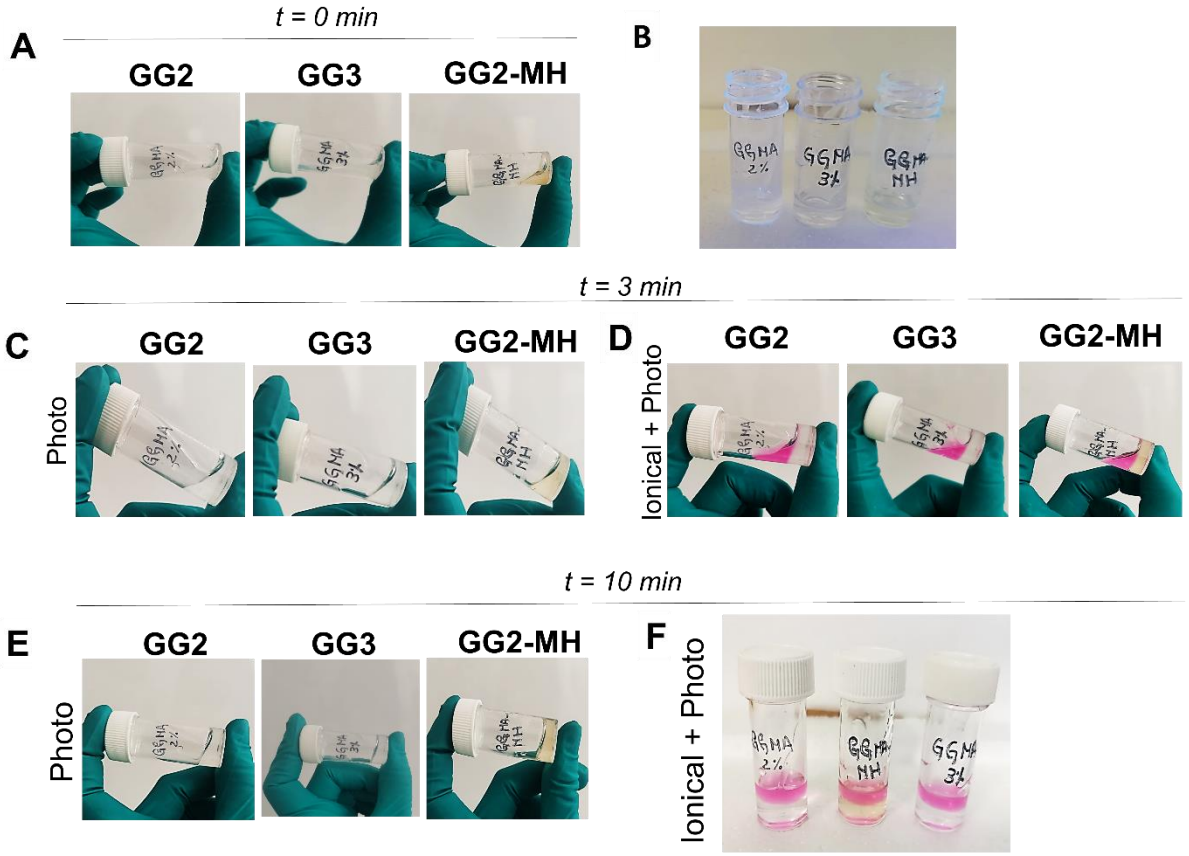

Figure 6.3: Analysis of Gelation time for GG2, GG3 and GG2-MH hydrogels with Photo-crosslinking or a combination of Ionical and Photo-crosslinking: Tube inverted vial test at 0 minutes (**A,B**), 3 (**C,D**) and 10 minutes (**E,F**).

The capacity of the GG-based hydrogels to absorb water, when soaked in PBS at 37 °C, is shown in **Figure 6.4**. Within one hour, GG2 samples showed a ~1400 % fast water absorption and the WU then gradually rose over time, peaking at around 1800 ± 20 % after 8 hours and remaining stable for the next 48 hours. GG3 showed an increase in WU percentage up to ~1200 %, and this value gradually increased up to 1433 ± 57% within 3 hours, remaining stable at this value up to 48 hours. GG2-MH samples, on the other hand, displayed a rapid initial water absorption, reaching a value of 500 ± 60 % within 60 minutes and stabilising at that level for the following 48 hours.

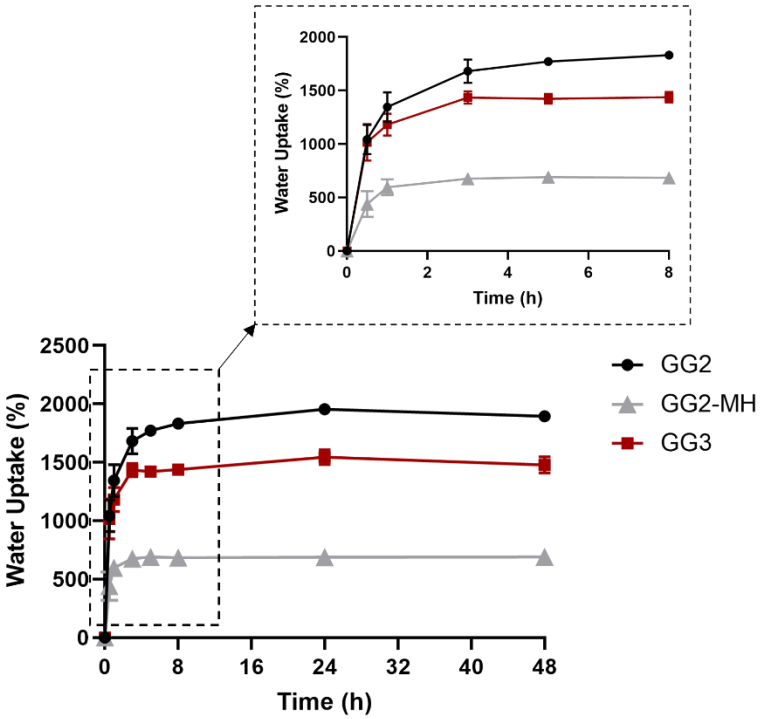

Figure 6.4: Water Uptake study of GG2, GG3 and GG2-MH at different time points up to 48 hours (insert: zoom on the first 8h of uptake).

In **Figure 6.5** are reported the morphology of the freeze-dried samples after the formation of hydrogels, together with the calculation of the frequency of pores dimension. The three formulations showed a good porosity, with a typical spongy three-dimensional morphology, with open macropores, a high degree of interconnectivity, and anisotropic porosity, as seen in photos of typical cross-sections (**Figure 6.5A-F**). Although variances in the pores dimension distribution were discovered, no changes in the morphological structure of the interior of any GG-based hydrogels were found. For GG2 samples, the 88 % of the pores showed a diameter with a dimension lower than 150 µm: 47 % of diameters in the range 100-150 µm and 41 % of pores with a diameter below 100 µm. The 6 % of the pores for the GG2 samples showed a diameter dimension higher than 200 µm and the 6 % between 150 and 200 µm. GG2-MH samples showed the 73 % of pores with a diameter lower than 150 µm: 44 % of them in the range 100-150 µm and 29 % with a diameter below 100 µm. The 3 % of the pores for the GG2-MH samples showed a diameter dimension higher than 200 µm and the 24 % between 150 and 200 µm. GG3 samples instead, showed ~ 56 % of pores with a diameter dimension lower than 150 µm: 25 % with a diameter lower than 100 µm and 32 % with a diameter in the range 100-150 µm. The 18 % of the pores for the GG3 samples showed a diameter dimension higher than 200 µm and the 25 % between 150 and 200 µm. The average pores diameter dimension

for GG2, GG2-MH and GG3 was respectively 77.4 ± 17.6 µm, 87.2 ± 9.5 µm and 147.8 ± 16.3 µm.

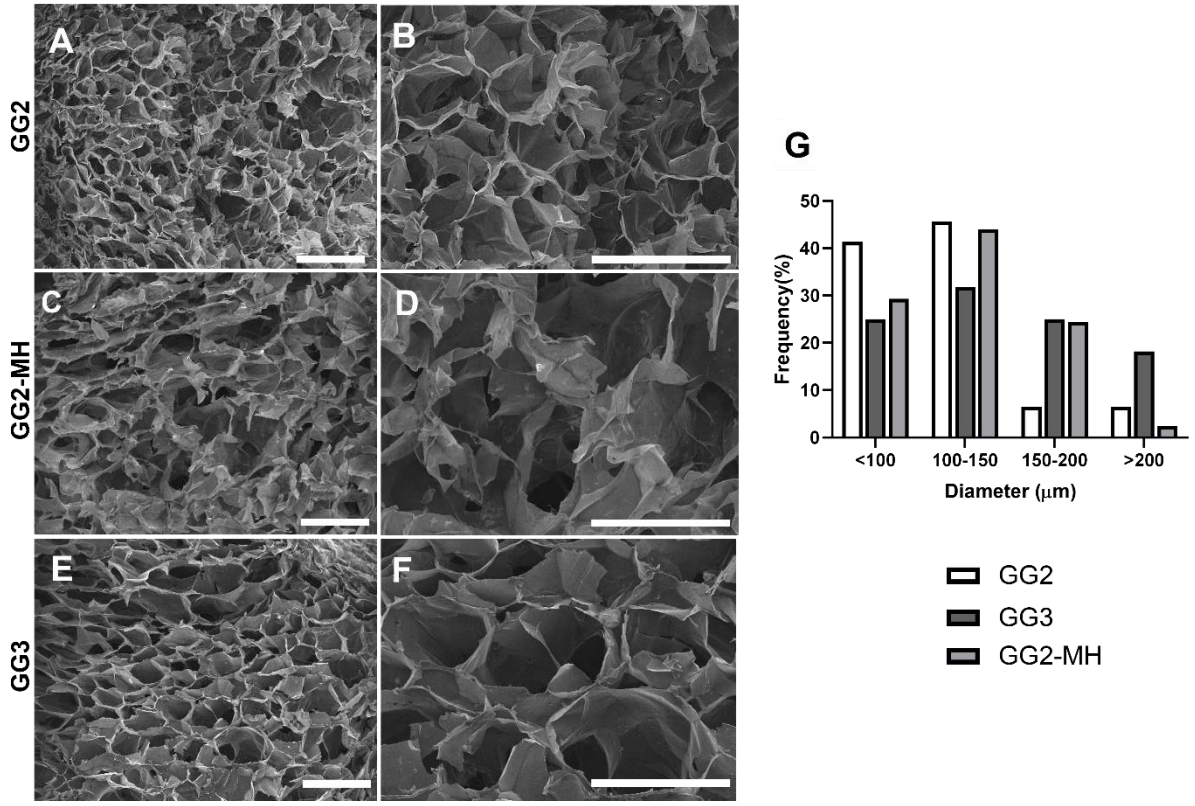

Figure 6.5: Morphological analysis of GG2, GG3 and GG2-MH hydrogels. SEM images representing cross-section microstructure of: GG2 at 35 x (**A**) and 100 x (**B**); GG2-MH at 35 x (**A**) and 100 x (**B**) and (C,D) GGMA-MH hydrogels at magnifications 35 x (A,C) and 100 x (B,D). Bars=500 µm; (E) Distribution analysis of the pores within the ranges <100 µm, 100–1500 µm, 150–200 µm, >200 µm for GGMA (black) and GGMA-MH (grey).

Static and dynamic mechanical analysis were performed on the manufactured GG2, GG3 and GG2-MH hydrogels. Regarding the unconfined compression test, **Figure 6.6A-C** shows a characteristic stress-strain (σ/ ε) curve obtained for the three hydrogels. The recorded Young's modulus, calculated in the linear component of the curve (0-10 % strain), were 26.3 ± 3.0 kPa, 31.4 ± 4.2 kPa, and 23.6 ± 5.0 kPa, respectively for GG2, GG3 and GG2-MH (**Figure 6.6D**). After the linear zone, the densification was recognised for all the samples, followed by the samples breaking, which was observed at 25-30% for the GG2 sample (**Figure 6.6A**) and ~ 60% for GG3 (**Figure 6.6B**) and GG2-MH (**Figure 6.6C**) hydrogels.

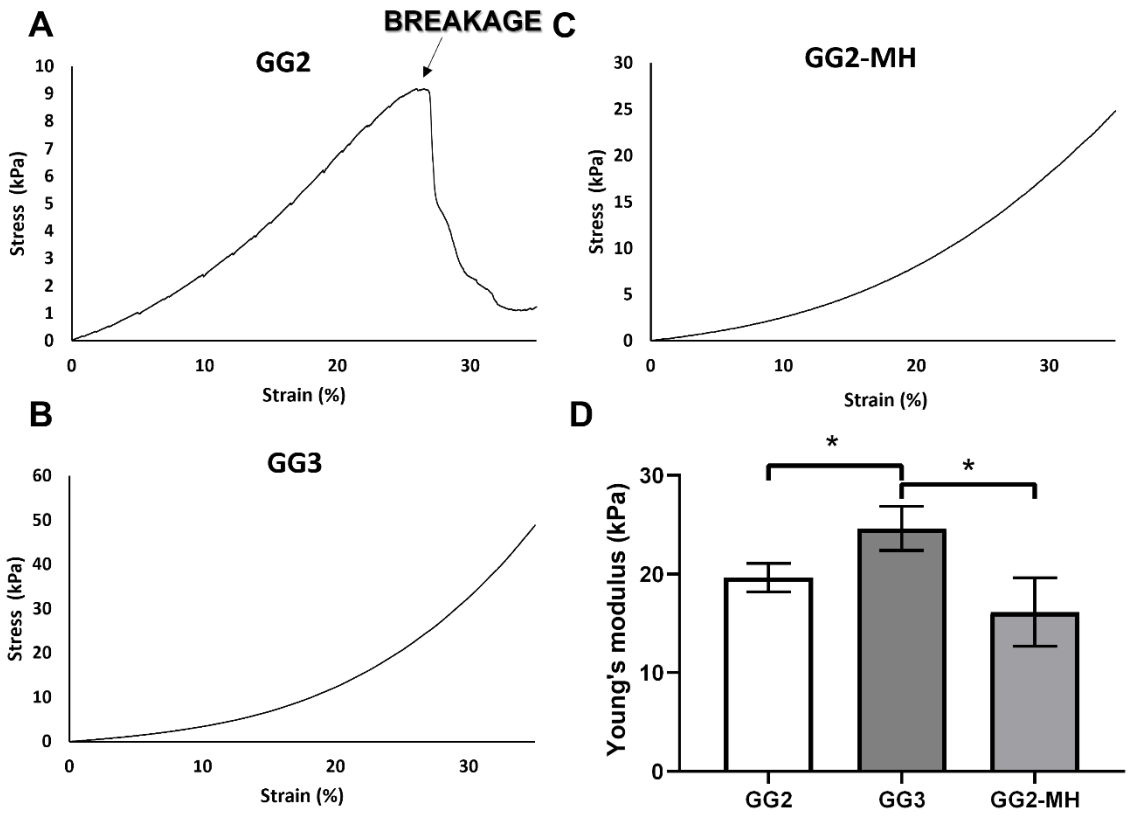

Figure 6.6: Unconfined compression test of GGMA-based hydrogels. Example of stress(σ) vs. strain (ε) curves for GG2 (black arrow pointing at the breakage point) (**A**), GG3 (**B**) and GG2-MH (**C**). Report of the Young's Modulus for GG2, GG3 and GG2-MH. Statistics: *p<0.05.

The strain sweep test, performed at 37 °C, shows the LVER regions of GG2, GG2-MH and GG3 hydrogels, whose limits were respectively 8.0 ± 0.3 %, 10.5 ± 0.2 % and 25.1 ± 1.5 % (**Figure 6.7A,D**). In the LVER, all hydrogels demonstrated G'>G" of at least one order of magnitude. Also, the complex moduli (G*) were plotted for GG2, GG2-MH and GG3 (**Figure 6.7B**) and their values were recorded in the LVER: 730.3 ± 50.2 Pa for GG2, 1042.1 ± 30.3 Pa for GG2-MH and 1304.2 ± 13.8 Pa for GG3. The apparent viscosity (η) was also measured for the hydrogels: 111.2 ± 20.0 Pa·s for GG2, 181.4 ± 10.6 Pa·s for GGMA-MH and 202.8 ± 8.1 Pa·s for GG3 (**Figure 6.7D**). The temperature sweep test curves were reporting the storage (G') and loss (G") moduli values in the temperature range 15-50 °C. Up to roughly 35 °C, the temperature sweep test graph in **Figure 6.7C** demonstrates that G'>G" by at least one order of magnitude for GG2, GG2-MH and GG3. Around 45 °C, it can be observed the crossing point of G' and G" for the GG2 samples, index of gel/sol transition. GG2-MH followed a similar pattern, reaching the crossing point at 50 °C. GG3, instead, did not reach the gel/sol transition point in this temperature range.

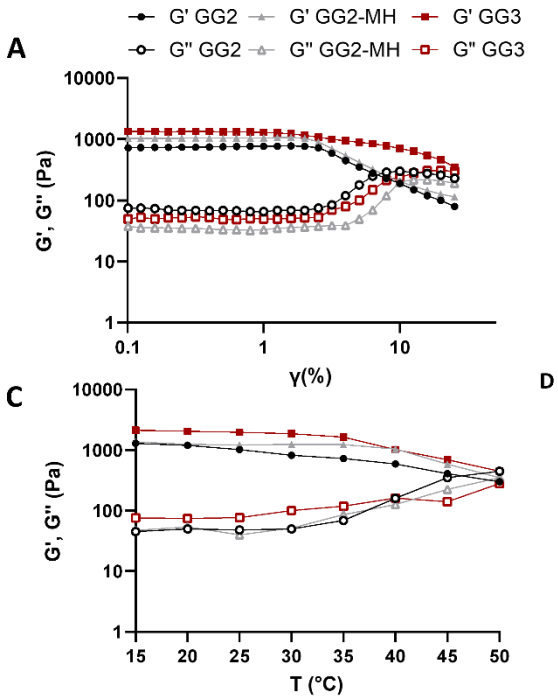

D

	GG2	GG2-MH	GG3
G* (Pa)	730.3 ± 50.2	1042.1 ± 30.3	1304.2 ± 13.8
η (Pa·s)	111.2 ± 20.0	181.4 ± 10.6	202.8 ± 8.1
Yield γ (%)	8.03 ± 0.3	10.5 ± 2.1	25.1± 1.5

Figure 6.7: Rheological analysis of GG2, GG2-MH and GG3 hydrogels. Strain sweep test at 37 °C showing Storage (G') and Loss (G") moduli as a function of the strain in the range 0.1 -20 % (**A**); Complex modulus (G*) as a function of the strain (0.1-20%) (**B**); Temperature sweep test in the temperature range 15-50 °C and record of G' an G" in LVER at each temperature (**C**); Report of G* at 2% strain, apparent viscosity (η) and strain value at yield point (Yield γ %) (**D**).

6.3.3 CSDP chemical characterisation

EDC coupling process was employed to bind dopamine to the carboxyl group of CS, to make the CSDP conjugate. FTIR-ATR, XPS and NMR analyses were performed to evaluate the successful conjugation of DP to CS.

From FTIR-ATR, CS characteristic peaks can be observed: phenol (-O-H) and amine (-N-H) stretching vibration at 3640-3350 cm^{-1}; asymmetric and symmetric vibration of C-H in $-CH_3$ and $-CH_2$ groups at 2940-2920 cm^{-1} and 2860-2850 cm^{-1}; C=O stretching vibration and O-H variable-angle vibration in free COO- groups at 1700-1250 cm^{-1}; N-H deformation of amide II signal was recorded at 1559 cm^{-1}, stretching vibration of S=O bond in sulfate groups at 1125-1031 cm^{-1} and ethers' contribution (-C-O-C-) of sulfate groups was observed at 1100 cm^{-1} (Mallet et al., 2016). The addition of DP brought new peaks: the aromatic C-H stretching at 3050.77 cm^{-1}, the bending of amine N-H at 1616 cm^{-1}, the aromatic stretching of C=C at 1519 cm^{-1} and the stretching of C-N amine at 1245 cm^{-1} (amine C–N stretching) (**Figure 6.8**) (Thakur et al., 2018).

Regarding NMR spectra (**Figure 6.8B**), both CS and CSDP sample showed some peaks between 1.9 and 2.3 ppm (*i*) representative of the N-acetyl methyl group characteristic of CS, two peaks at 3.6 ppm and 4.43 ppm (*ii*) representative of the d-glucuronic acid, and at 4.6 ppm and 4.75 ppm (*iii*) representative of the N-acetyl-D-galactosamine, which are specifics of the chondroitin-4-sulfate (Scalzone et al., 2020). After the conjugation with DP, new peaks were observed in CSDP spectra: the two methylene groups introduced by dopamine after they were grafted onto the CS backbones are represented by the multi-peaks centred at 2.75 ppm (*i*) and 3.2 ppm (*ii*). The equivalent methine groups on the benzene ring of grafted dopamine are represented by the multi-peaks centred at 6.75 ppm (*iii*) and 6.89 ppm (*iv*). Also, a little quantity of NHS residue was observed in CSDP polymers after the chemical interaction between CS and dopamine (peaks centred at 0.8-0.9 ppm; *v*).

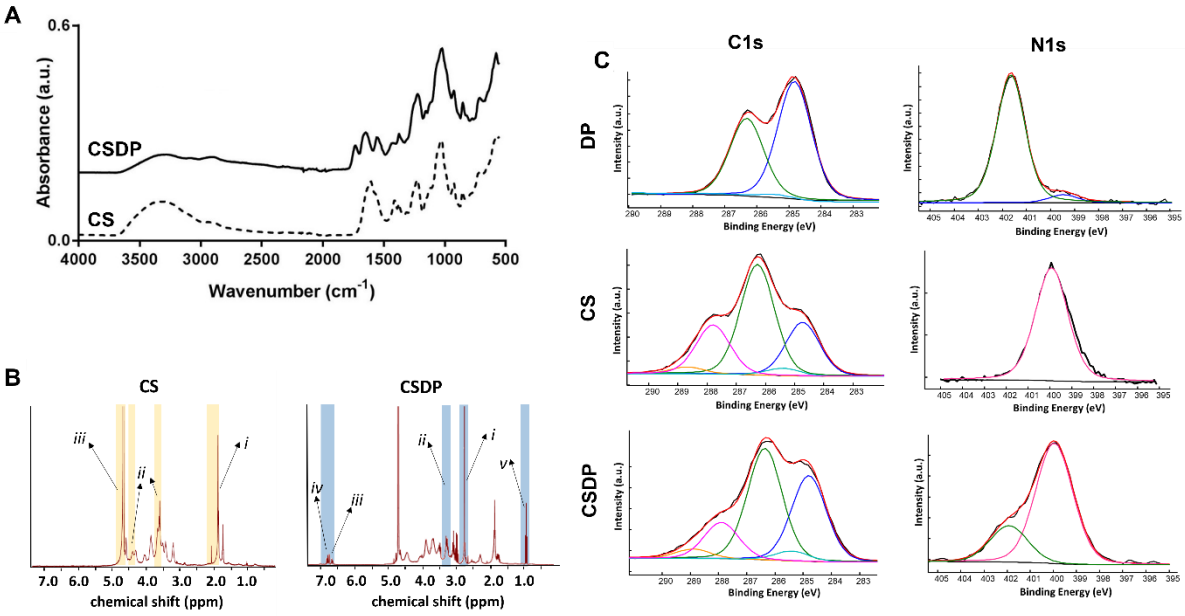

Figure 6.8: Chemical characterisation of CS and CSDP. FTIR-ATR spectra of CS powder and freeze-dried CSDP samples **(A);** NMR graph of CS and CSDP (**B**); XPS data relevant to C1s and N1s curve fittings of CS, DP and CSDP samples (**C**).

Finally, XPS analysis was performed on DP and CS raw powders and freeze dried CSDP. The experimentally observed C/O and C/N ratios of DP were 4.3:1 and 9.7:1, respectively, according to the elemental composition analysis. In terms of identified components, the XPS compositions of CS and CSDP surfaces were quite comparable (**Table 6.8**).

	Atomic %					
Sample	C1s	O1s	N1s	S2p	Na1s	Cl2p
DP	68.8	16.0	8.1	-	-	7.1
CS	51.0	36.1	5.8	2.2	4.3	0.6
CSDP	56.7	30.3	7.8	1.7	2.6	0.9

Table 6.8: XPS Atomic percentage of each element for DP, CS and CSDP samples.

An accurate curve fitting the C1s spectra (**Figure 6.8C**) revealed for CS a deconvolution in five-components. The same components were found in CSDP samples and the relative atomic percentages of each contribution (reported in **Table 6.9**). Also, N1s spectra fitting was explored (**Figure 6.8C**). The N1s spectra of DP showed essentially protonated amine groups, as demonstrated by the peak at 401.7 eV, with a low presence of neutral amine groups, which was in good agreement with C1s curve fitting. Only amide contribution was seen in the CS specimen, which fell at 400.0 eV. Finally, CSDP showed two contributions: the first at 400.0 eV, due to amide groups already present in CS, in addition to those produced by DP grafting; the second, at 401.8 eV, due to unloaded DP as well as residue ester connection between NHS and CS (**Table 6.9**).

	BE (eV)/ At%							
Sample	**CH_x**	**C-COOR, C-NH**	**C-OH, $CH\text{-}NH_3^+$**	**O-C-O, $C\text{-}O\text{-}SO_3^-$, CO-NH**	**COOR**	**NH_2**	**NH-C=O**	**NH_3^+**
DP	284.8/ 59.3%	285.4/ 0.9%	286.3/ 39.8%	-	-	399.5/ 5.8%	-	401.7/ 94.2%
CS	284.8/ 23.6%	285.4/ 3.5%	286.3/ 49.6%	287.9/ 20.4%	288.8/ 3.0%	-	400.0/ 100.0%	-
CSDP	284.8/ 34.0%	285.4/ 3.9%	286.3/ 44.1%	287.9/ 14.4%	288.9/ 3.6%	-	400.0/ 77.3%	401.8/ 22.7%

Table 6.9: XPS high resolution C1s and N1s peaks for DP, CS and CSDP samples.

6.3.4 CSDP hydrogels characterisation

At the selected molar ratio of $NaIO_4$/catechol 1.5:1, CSDP10 developed a gel in 50-60 seconds and CSDP20 in less than 30 seconds.

After freeze-drying, the porosity structure and pore size of the resulting hydrogels were investigated using SEM (**Figure 6.9A**). CSDP10 and CSDP20 showed good porosity, with an average pore size of 140 ± 67 µm and 93 ± 58 µm, respectively.

CSDP hydrogels showed a rapid increase of WU (%) within 10 hours, reaching values of 1571 ± 139 % and 987 ± 157 %, respectively for CSDP10 and CSDP20. After that, the water uptake slowly increased and stabilised up to 48 h at the values of 1747 ± 257 % for the CSDP10 and 1092 ± 159 % for the CSDP20 (**Figure 6.9B**).

The stress/strain curves obtained for CSDP10 and CSDP20, reported in **Figure 6.9C,** show the linear starting region (0-10 % strain) where the compressive elastic Young's moduli were calculated: CSDP10 reported a value of 4.6 ± 1.8 kPa, whereas the CSDP20 reported a value of 7.8 ± 1.0 kPa.

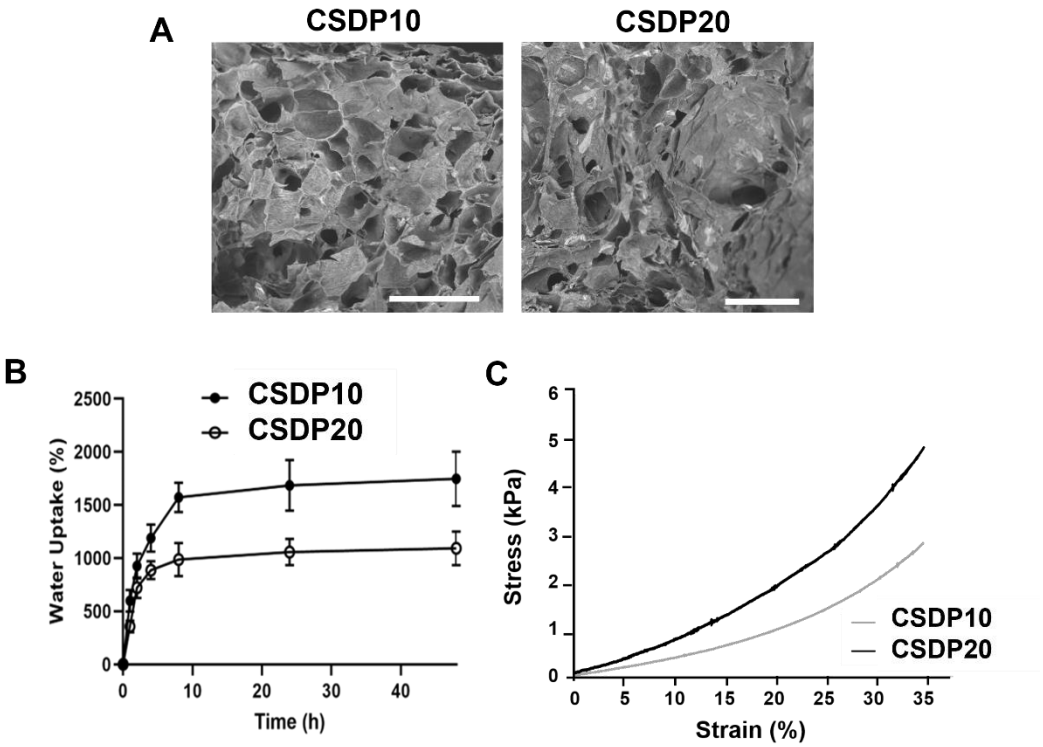

Figure 6.9: Physico-chemical characterisation of CSDP10 and CSDP20 hydrogels: SEM images of the freeze-dried hydrogels. Bars= 500 µm. (**A**) Water Uptake study of at different time points up to 48 hours (**B**); Unconfined compression test of CSDP hydrogels: example of stress(σ) vs. strain (ε) curves (**C**).

6.3.5 Subchondral bone: manufacturing and characterisation

For the manufacturing of the SB, a 3D grid of PLA was obtained via FDM technology. The obtained structure showed high interconnected porosity and a structure like the trabecular bone by printing subsequent layers with an infill rotating angle of 45 ° (**Figure 6.10**).

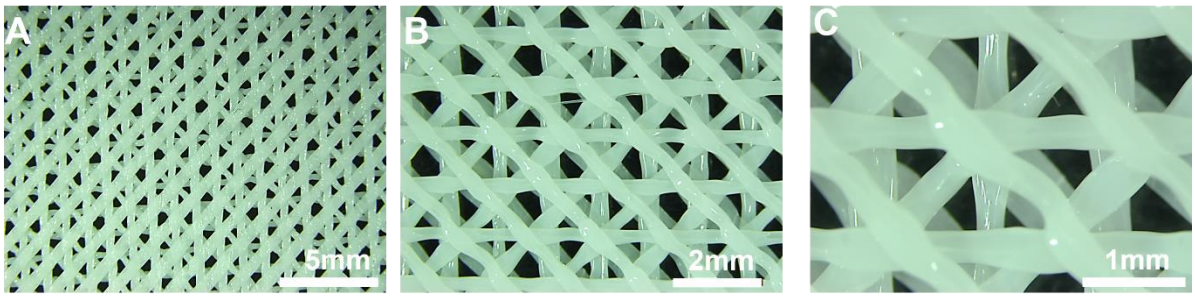

Figure 6.10: Images of the 3D-printed PLA grid for the SB manufacturing, at different magnifications.

PLA grids were functionalised with GEL and nHA through DOPA coating. To investigate the morphology of the 3D printed scaffold and the effect of the functionalisation, SEM analysis was done on PLA, PLA/DOPA, PLA/GEL, and PLA/GEL/nHA. The unfunctionalized extruded filament showed a smooth and uniform surface (**Figure 6.11A,B**). No differences were observed with the sole addition of DOPA (**Figure 6.11C,D**), whereas the filament developed crest-like structures on its surface after being immersed in DOPA and functionalised with GEL (**Figure 6.11E,F**). Furthermore, the addition of nHA to the scaffold (PLA/GEL/nHA) resulted in the appearance of a homogeneous roughness (pointed by the arrows) with no changes in filament structure (**Figure 6.11G,H**). No macrostructural variation was observed by average filament's dimension analysis: 332 ± 56 µm for PLA, 342 ± 70 µm for PLA/DOPA, 378 ± 46 µm for PLA/GEL and 380 ± 15 µm for PLA/GEL/nHA. All the samples showed a pore size in the range 100-250 µm. In addition, µ-CT analysis was performed on the four samples (**Figure 6.11I-L**), obtaining an overall total porosity not statistically different between the three samples (**Figure 6.11M**).

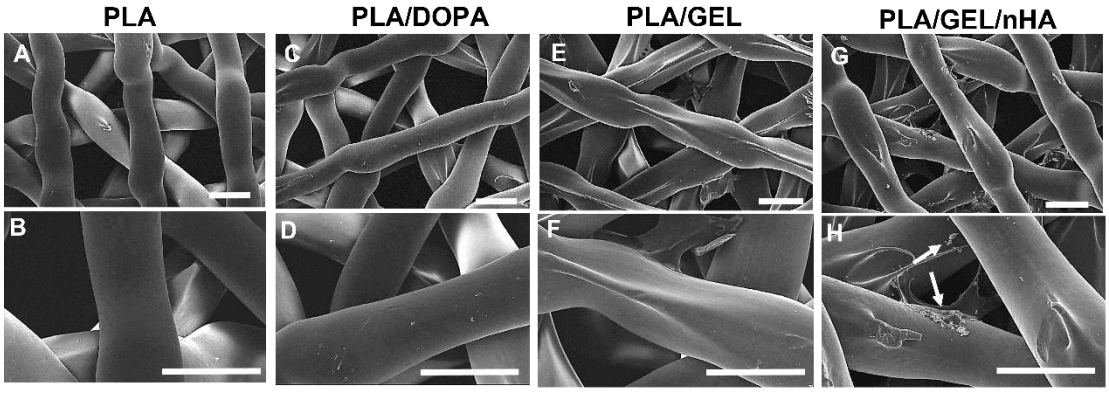

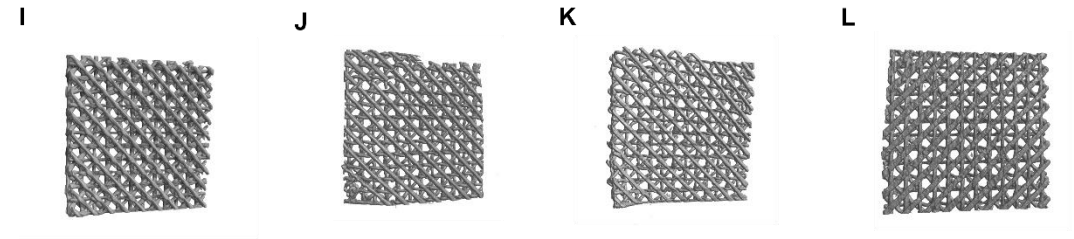

M

	PLA	PLA/DOPA	PLA/GEL	PLA/GEL/nHA
Total porosity (%)	54	58	56	53

Figure 6.11: Assessment of the functionalisation effect on the PLA structure. SEM analysis on PLA to assess the morphology before (**A,B**) and after the functionalisation with DOPA (**C,D**), with DOPA and GEL (1%w/v) via poly-dopamine coating (**E,F**) and with GEL (1% w/v) and nHA (5% w/w) via poly-dopamine coating (arrows pointing at the nHA deposits) (**G,H**). Bar= 100 µm (**A,C,E,G**) and 500 µm (**B,D,F,H**). Magnification: 35x (**A,C,E,G**) and 100 x (**B,D,F,H**). Representative microCT images of all the 3D printed scaffolds pre-functionalisation (**I**) and post-functionalisation with DOPA (**J**), DOPA/GEL (**K**) and DOPA/GEL/nHA (**L**). All the scaffolds are 13 x 13 x 1 mm. Table reporting the total porosity (%) in the four conditions (**M**).

6.3.6 Subchondral bone: biological evaluation

PLA/DOPA, PLA/GEL and PLA/GEL/nHA scaffolds cytocompatibility was evaluated by Live/Dead after 3 days of Y201s culture. All the scaffold showed a high amount of live cells (green). PLA/DOPA scaffold showed slightly more dead cells (stained in red) (**Figure6.12A**), compared to the scaffold with the presence of GEL (PLA/GEL (**Figure 6.12B**) and PLA/GEL/nHA (**Figure 6.12C**)). No significant variation of cell density was observed in the three scaffolds and a homogenous adherence on the whole structure was seen on the scaffolds in all three circumstances (**Figure6.12A-C**). Y201s viability on the PLA/GEL/nHA scaffold was evaluated up to 7 days: cells were viable at day 7, with just a few dead cells seen (**Figure 6.12D**). At days 3 and 7, cells were evenly dispersed and disseminated over PLA/GEL/nHA scaffold filaments completely covering the scaffold.

Proliferation tendency of Y201s was tested using the MTT assay on the scaffold with (PLA/GEL/nHA) and without nHA (PLA/GEL), up to 21 days of culture (**Figure6.12E**): the number of metabolically active cells increased throughout 21 days of culture ($p<0.0001$) and even doubled from day 7 to day 21 ($p<0.0001$) on both PLA/GEL and PLA/GEL/nHA. No statistical differences were observed at each time point.

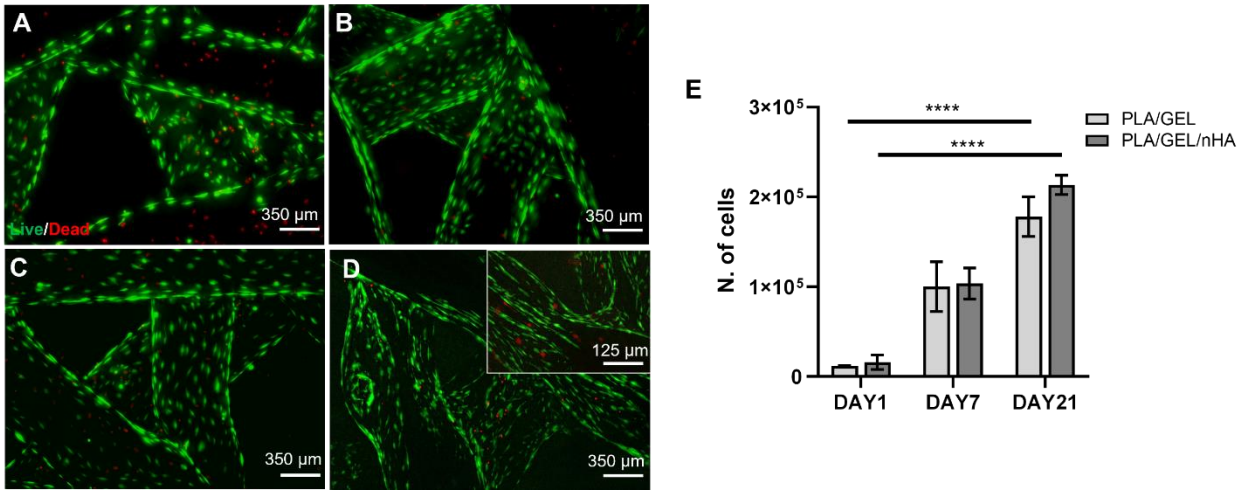

Figure 6.12: Y201s viability on PLA 3D printed scaffolds. Live/Dead viability assessment (calcein staining live cells in green and Ethidium Bromide staining dead cells in red) at day 3 on PLA/DOPA (**A**) and PLA/GEL (**B**); and at day 3 (**C**) and day 7 (**D**) on PLA/GEL/nHA. Number of metabolically active cells at day 1, day 7 and day 21 on PLA/GEL and PLA/GEL/nHA, evaluated with MTT assay (**E**). Statistics: ****$p<0.0001$.

Then, the morphology and organisation of Y201s were determined using DAPI and phalloidin staining on days 3 (**Figure 6.13A**) and 7 (**Figure 6.13B**). Starting from day 3, cells seemed well-spread, elongated and uniformly dispersed over the scaffold surface. F-actin (Phalloidin rhodamine staining) showed the development of podosomes, which let cells adhere to the material's surface.

At day 7, SEM pictures revealed that Y201s were spread, not only on the surface of the PLA/GEL/nHA scaffolds, but within the holes as well (**Figure 6.13C,D**).

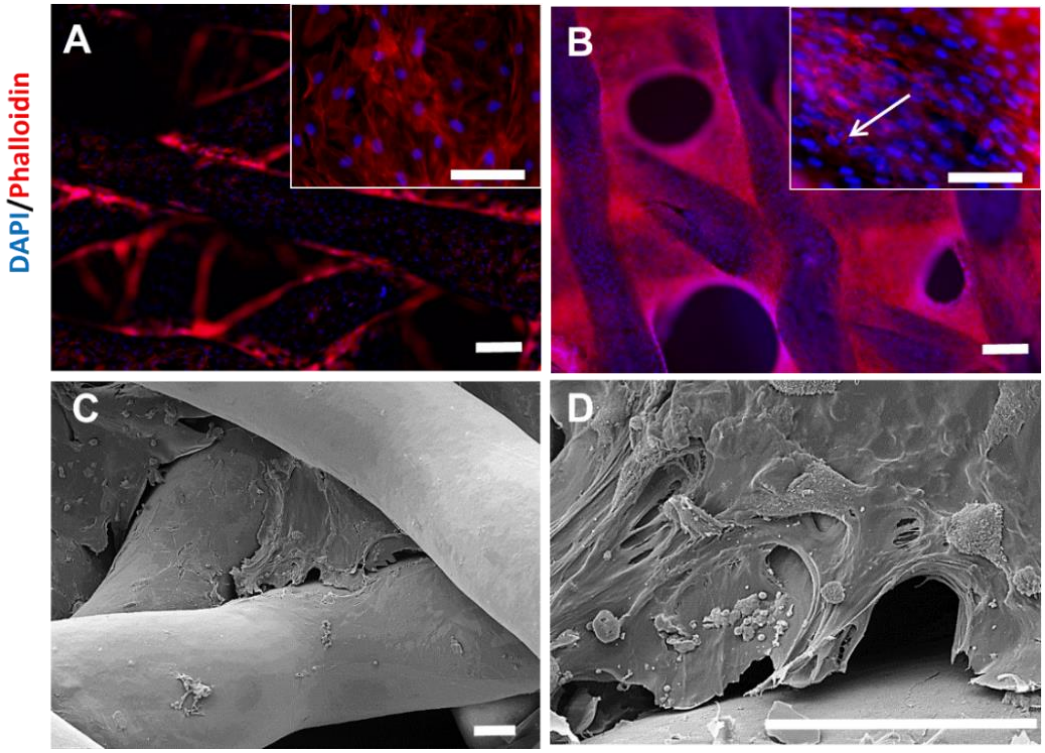

Figure 6.13: Cells distribution and morphology on PLA/GEL/nHA scaffold. Immunostaining of cells cytoskeleton (PhalloidinRhodamine) and Nuclei (DAPI) on PLA/GEL/nHA at day 3 (**A**) and day 7 (**B**): arrows indicate mitosis. Bars= 100 µm. SEM images after 1 day of cells seeding at 250 x (**C**) and 1500 x (**D**).

Y201s osteogenic commitment was evaluated onto PLA/GEL and PLA/GEL/nHA scaffold over 21 days of culture. First, gene expression and protein expression of *runx2*, *alpl* and *sparc/ON* were analysed. Relative expression of *runx2* gene did not show statistical differences between the two conditions at day 1 and day 21, while a statistically significant increase in its gene expression was observed in PLA/GEL/nHA samples, between day 1 to day 21 ($p<0.05$) (**Figure 6.14A**). On the other side, the protein expression level of RUNX2 increased in a time-dependent manner and a statistical difference was observed at day 21 between PLA/GEL and PLA/GEL/nHA samples ($p>0.0001$) (**Figure 6.14D**). Regarding *alpl*, Y201s displayed the highest relative gene expression at day 1, which was then down-regulated at day 21 in both samples ($p<0.001$ for PLA/GEL/nHA and $p<0.0001$ for PLA/GEL) (**Figure 6.14B**). The maturation of the active form of ALP enzyme (200 kDa peptide) instead, showed its maximum representation on day 7 for both samples, however ALP expression was sustained for up to 14 days, only in PLA/GEL/nHA scaffolds ($p<0.0001$ compared to PLA/GEL) (**Figure 6.14E**). ON mRNA (*sparc*) expression was observed at day 1 and decreased over 21 days of culture for both samples ($p<0.0001$ for PLA/GEL and $p<0.05$ for PLA/GEL/nHA) (**Figure 6.14C**). ON protein expression

were discovered on day 1 and showed a peak at day 7. After that, the expression gradually decreased for both samples, with increased expression for PLA/GEL/nHA at each time point ($p<0.0001$) (**Figure 6.14F**).

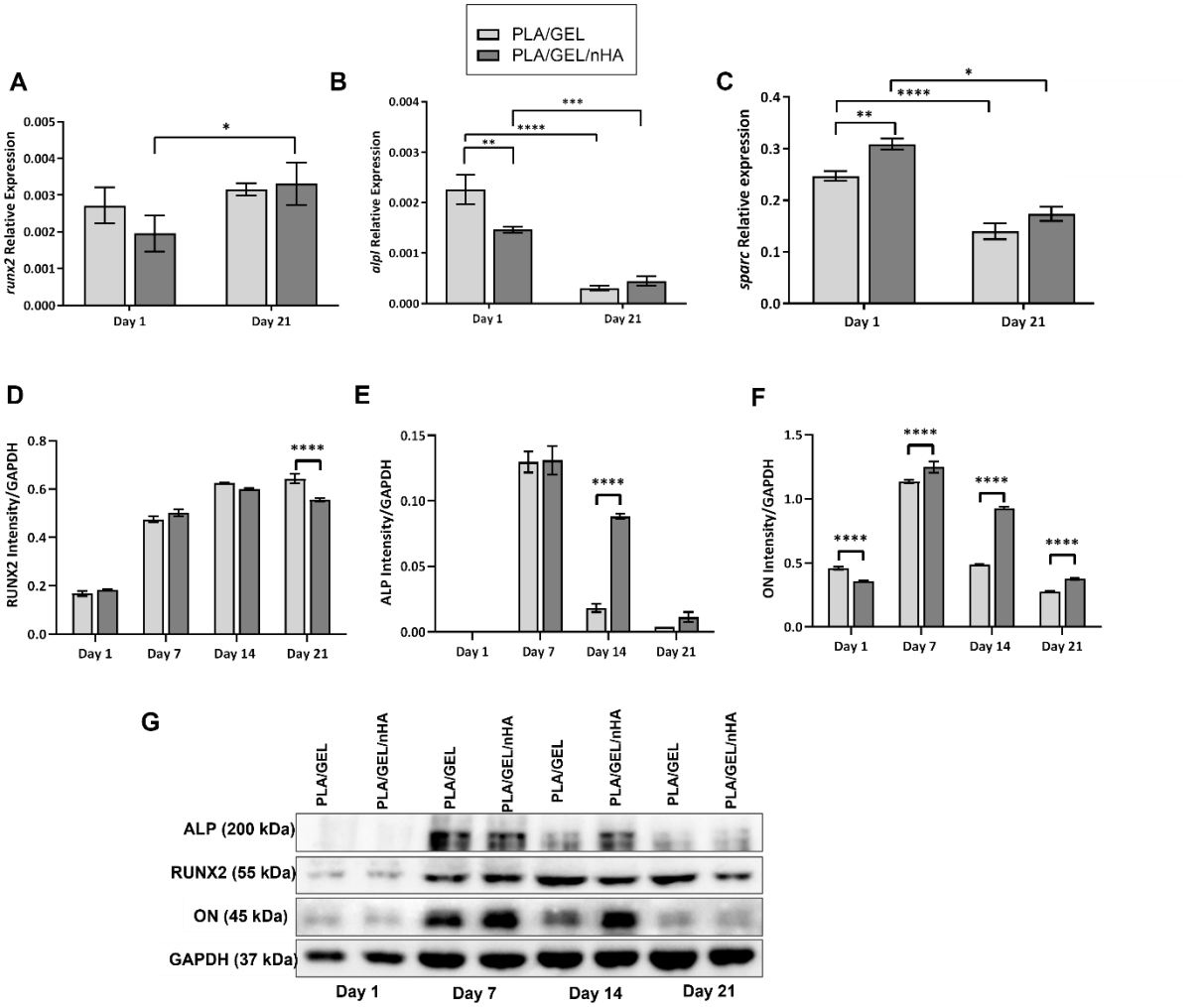

Figure 6.14: Gene RT-qPCR and Western Blot analyses to evaluated respectively genes and proteins expression for assessing the ability of nHA functionalization to promote Y201s osteogenic differentiation onto PLA/GEL/nHA scaffolds, compared to bare PLA/GEL. Relative expression of *runx2* (**A**), *alpl* (**B**) and *sparc* (**C**) by Y201s via RT-qPCR at day 1 and day 21 of culture. Proteins densitometric quantification expressed as intensity normalised to GAPDH at day 1, 7, 14 and 21, for RUNX2 (**D**), ALP active peptide 200KDa (**E**) and ON (**F**). Western blotting membrane of Y201s at days 1, 7, 14 and 21 incubated with ALP, RUNX2, ON and GAPDH antibodies (**G**). Statistics: *$p<0.05$, **$p<0.01$, ***$p<0.001$, ***$p<0.0001$.

ON expression was also evaluated on fixed samples after 21 days of culture via immunofluorescence analysis. Clear evidence of higher ON expression was observed in the PLA/Gel/nHA samples. A very weak staining was observed in PLA/GEL samples instead (**Figure 6.15**).

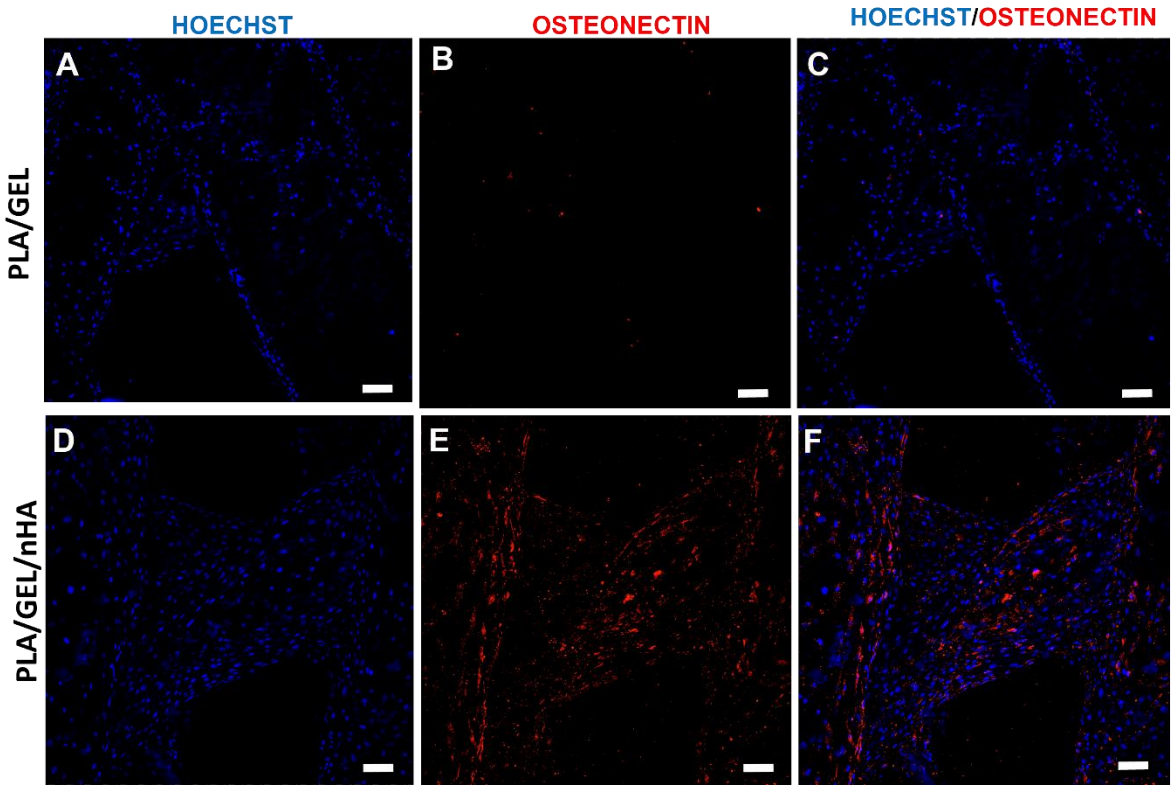

Figure 6.15: Immunofluorescence images of Osteonectin staining (red) and cells nuclei (blue) on PLA/GEL (**A-C**) and PLA/GEL/nHA (**D-F**) scaffolds at day 21 of culture. Bars= 100 µm.

Alizarin Red qualitative and quantitative assessment showed similar results to the ones found with gene and protein expression analyses. From the images in **Figure 6.16**, a more intense red staining (alizarin red) can be observed, especially at day 21, for PLA/GEL/nHA samples (**Figure 6.16 B,D,F**). Indeed, the quantitative investigation revealed a significant rise in Alizarin Red content at days 1, 7 and 21 in PLA/GEL/nHA samples, compared to PLA/GEL ($p<0.0001$). Also, PLA/GEL/nHA showed a higher concentration of Alizarin Red at day 21 compared to days 1 and 7 ($p<0.0001$) (**Figure 6.16G**).

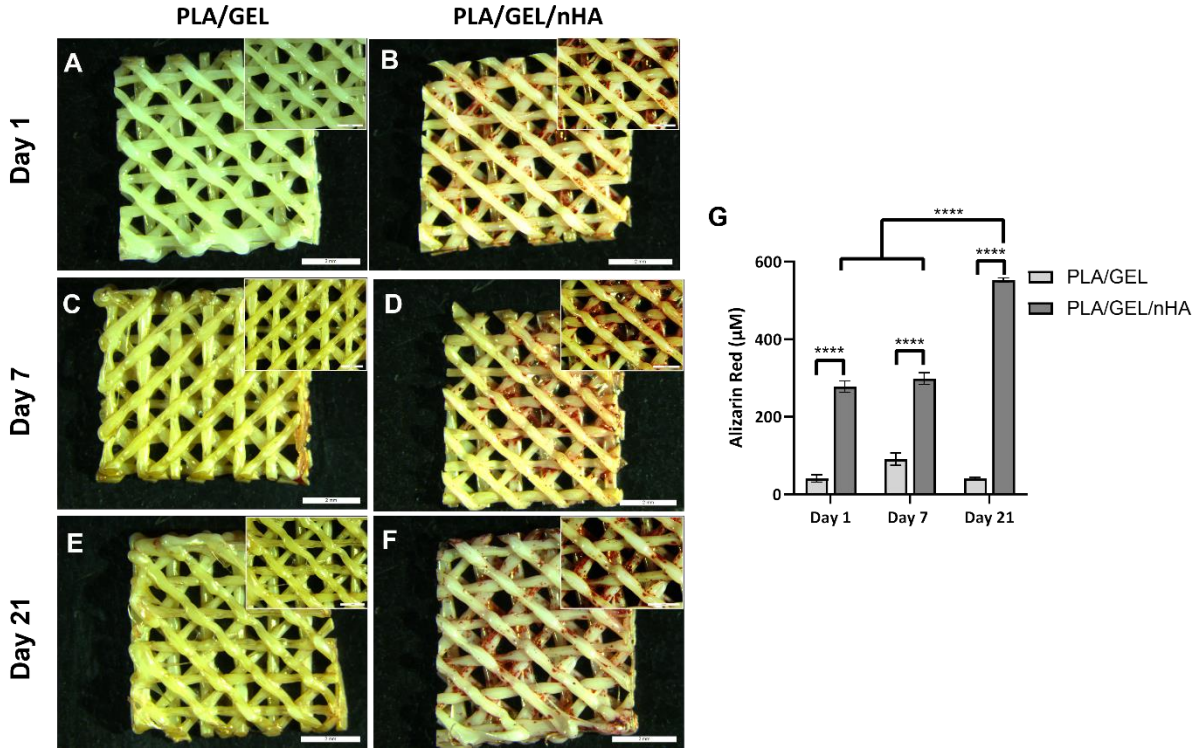

Figure 6.16: Analysis of mineralisation on PLA scaffolds with (PLA/GEL/nHA) and without (PLA/GEL) the presence of nHA: Images at day 1 (**A,B**), day 7 (**C,D**) and day 21 (**E,F**). Higher magnification in the inserts. Bars= 2 mm. Quantification of Alizarin Red at days 1, 7 and 21 (**G**).

6.3.7 Evaluation of pathological features within Subchondral Bone

PLA/GEL/nHA scaffolds were selected for evaluating the Y201s pathological features during the progression of OA (SB-P), compared to the healthy control (SB-H).

First, gene expression analysis was performed for *runx2, collIa2, spp1* and *vegf*. In OA conditions (SB-P), Y201s downregulated *runx2* (**Figure 6.17A**) and *spp1* (**Figure 6.17C**) at each time point ($p<0.0001$). The downregulation of *collIa2* in SB-P model, instead, was only significant after 21 days of culture ($p<0.0001$) (**Figure 6.17B**). On the other side, *vegf* expression was elevated in SB-H models compared to SB-P ($p<0.05$) at day 7, while it showed the opposite behaviour at day 21: it displayed downregulation in SB-H samples at day 21 compared to day 7 ($p<0.001$) and compared to SB-P at day 21 ($p<0.05$) (**Figure 6.17D**).

Protein expression analysis was performed for RANKL and OPG. Y201s showed an increased RANKL expression in both conditions at each time point, with substantial overexpression in pathological circumstances ($p<0.0001$) (**Figure 6.17E**). For each time-point, OPG protein levels in SB-P remained low, while its expression in SB-H models showed a substantial upregulation at day 14, with respect to SB-H at day 7 ($p<0.001$) and to SB-P at day 14 ($p<0.0001$). After then,

OPG was down-regulated, and the SB-H and SB-P models showed low expression at day 21. (**Figure 6.17F**).

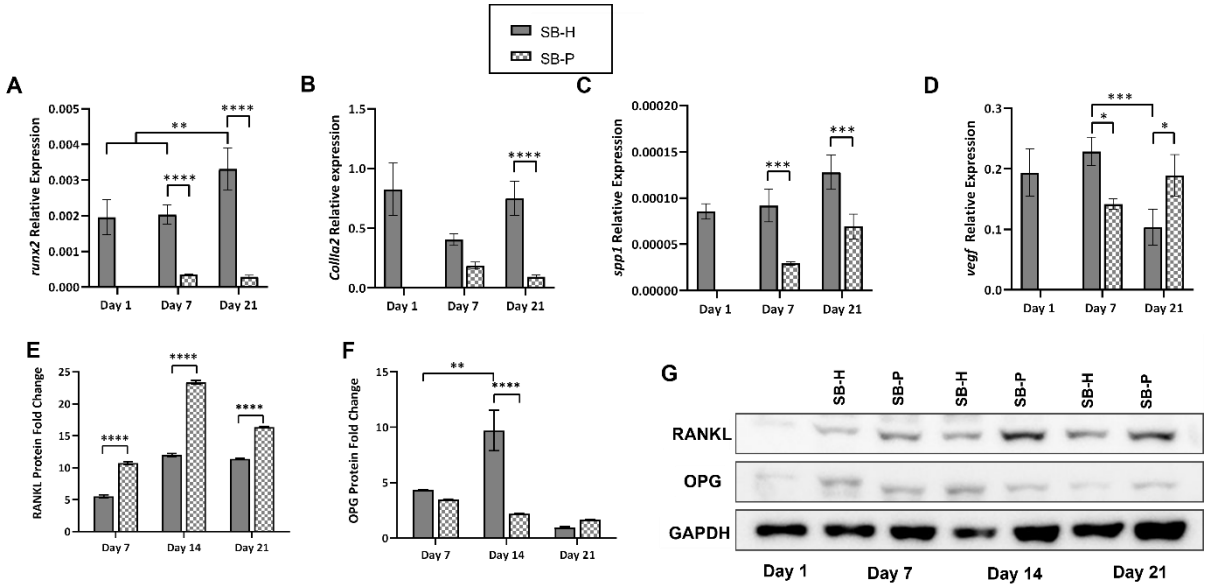

Figure 6.17: Gene RT-qPCR and Western Blot analyses to evaluated respectively genes and proteins expression for assessing the pathological features of PLA/GEL/nHA scaffold with (SB-P) and without (SB-H) the presence of cytokines. Relative gene expression of *runx2* (**A**), *collIa2* (**B**), *spp1* (**C**) and *vegf* (**D**) at day 1, day 14 and 21 in SB-H and SB-P conditions. Proteins densitometric quantification expressed as fold-change at days 7, 14 and 21 with respect of day 1 for RANKL (**E**) and OPG (**F**). Western blotting membrane incubated for RANKL, OPG and GAPDH at days 1, 7, 14 and 21 in SB-H and SB-P samples (**G**). Statistics: *p<0.05, **p<0.01, *** p<0.001 and **** p<0.0001.

After 21 days of culture, Alizarin red staining revealed a significant rise in calcium deposits, mostly in zones of PLA fibres intersection, compared to day 1 (**Figure 6.16B**), day7 (**Figure 6.18A,B**) and day 14 (**Figure 6.18C,D**), in both SB-H and SB-P samples. Indeed, Alizarin Red quantification showed at day 21 an increased concentration in both SB-H and SB-P cultures, compared to days 1,7 and 14 (p<0.0001), with the SB-P models having a much higher value compared to SH-H (~700 µM vs. ~580 µM) (p<0.0001) (**Figure 6.18G**).

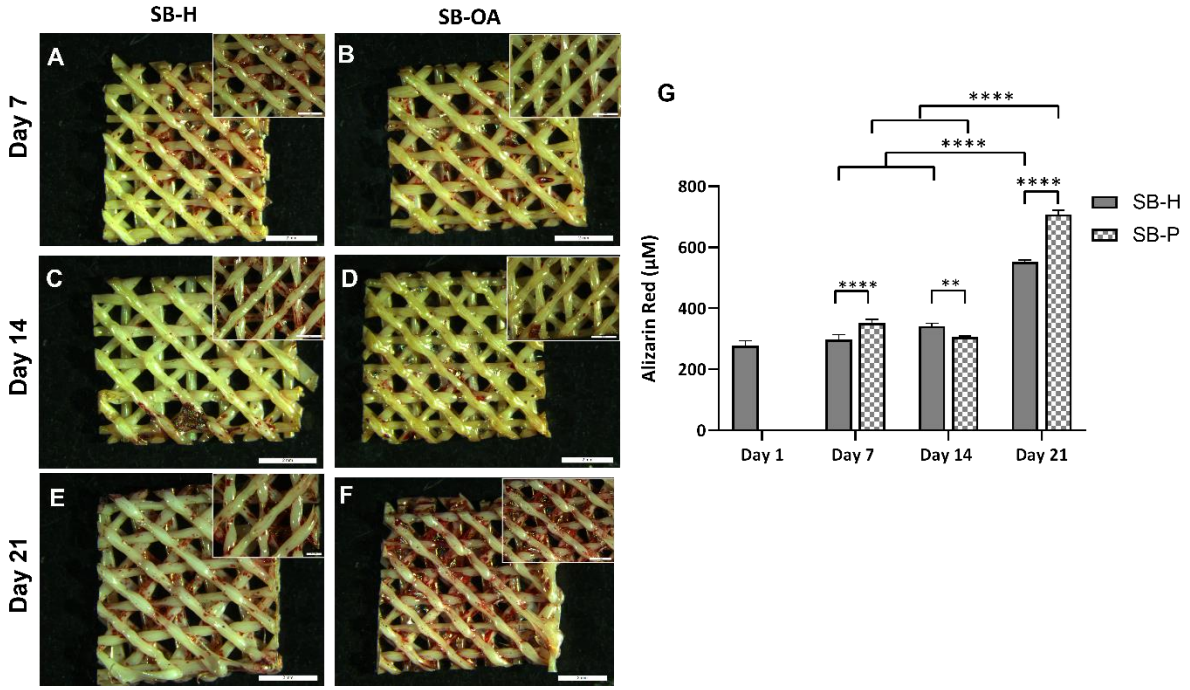

Figure 6.18: Alizarin red analysis at days 1, 7, 14 and 21 in SB-H and SB-P samples, both qualitative (**A-F**) and quantitative (**G**). Higher magnification in the inserts. Bars= 2 mm.

6.3.8 Deep layer: manufacturing and characterisation

For the manufacturing of the deep layer, soft-lithography via PDMS moulding was used (**Figure 6.19**). The obtained PLA master showed a dimension in the concave part (where the PDMS was poured) of 12 mm x 12 mm x 1 mm; the channels had a diameter of 1 mm and a depth of 1 mm. After the PDMS pouring, an image was taken to show the small bubbles of elastomer in the holes of the PLA, which were removed with a needle, to obtain the final PDMS mould (12 x 12 x 2 mm). The mould was cut in 4 squares (4 pillars each) to manufacture the DL construct of 6 x 6 x 2 mm. The obtained GG3 hydrogel showed an optimal shape fidelity without the loss of structure. Y201s-C encapsulated in CSDP15 hydrogel precursor were added within the holes of the multi-channelled construct.

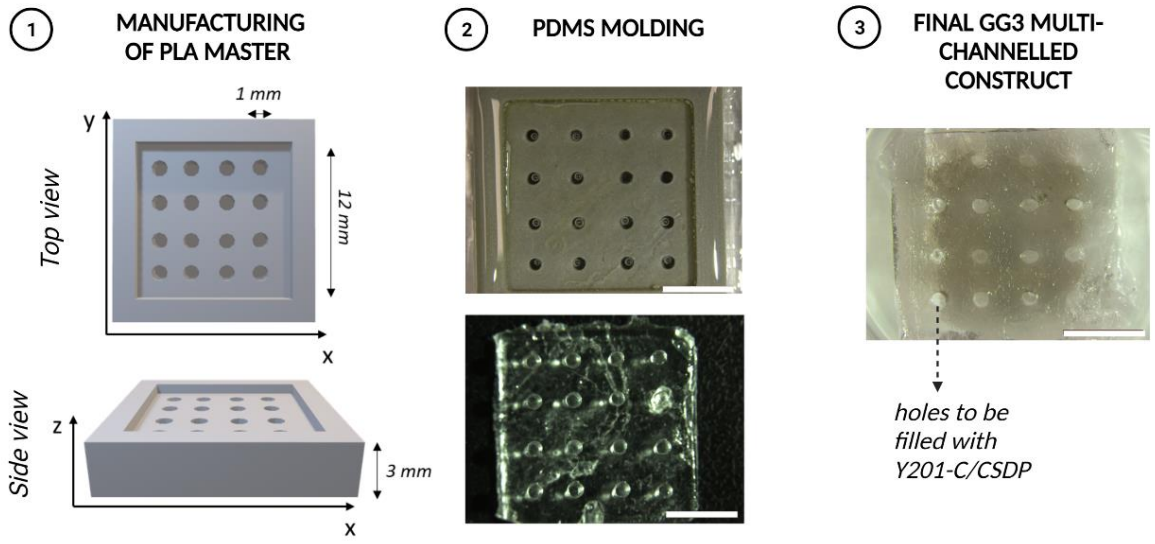

Figure 6.19: Manufacturing process of DL: PLA master fabrication via FDM (1), PDMS molding (2) and the obtained finale GG3 construct, to be filled with CSDP and Y201-C in the holes (3).

6.3.9 Deep layer: biological evaluation

Y201-C viability, when embedded in the DL-mimicking construct was determined on days 1 and 7: a large number of live cells, all of them agglomerated within the GG channels, were observed (**Figure 6.20A,C**); only a few dead cells were identified at day 7 (**Figure 6.20D**). Y201s-C metabolic activity was analysed via MTS assay and showed a decrease in the number of cells metabolically active at day 3 and day 7 with respect to day 1 ($p<0.0001$) (**Figure 6.20E**).

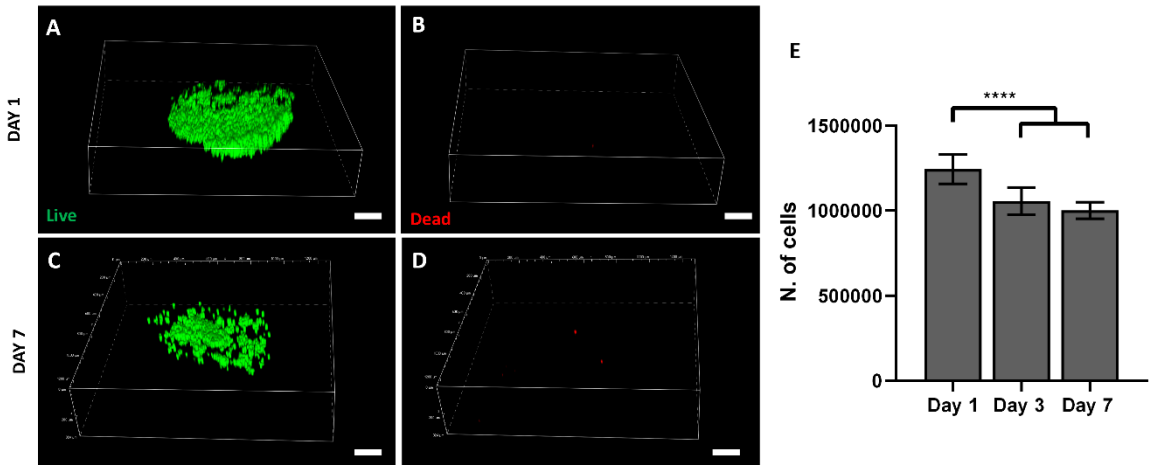

Figure 6.20: Viability of Y201s-C embedded within DL-emulating hydrogel. Live/Dead viability assessment at day 1 and day 7: live cells are stained in green (**A,C**) and dead cells are stained in red (**B,D**). Histogram of cell viability obtained by MTS assay at days 1, 3 and 7 (**E**). Statistics: $p<0.001$.

DAPI and phalloidin staining were used to further assess cells organisation within the construct: most of the cells were distributed inside the CSDP15 hydrogel within the GG3 channels at day 1 (**Figure 6.21A**). On day 7, Y201s-C lost some of the initial assembly supplied by seeding (**Figure 6.21B**): most of the cells were piled one on top of the other inside the channels, while others were scattered in the GG3 hydrogel. However, cells dispersion within the GG3 was observed mainly on the surface of the construct and not in the channel alongside the depth, as observed in **Figure 6.21C**, where the piled-up organisation of the cells can be observed in the x,z plane**.** SEM scans showed at day 1 the rounded morphology of Y201-C (**Figure 6.21F**), together with their organisation within the channels of GG3 (**Figure 6.21E**) Also the different morphology of CSDP15 and GG3 can be observed: smoother for CSDP and rougher for GG3 (**Figure 6.21D**).

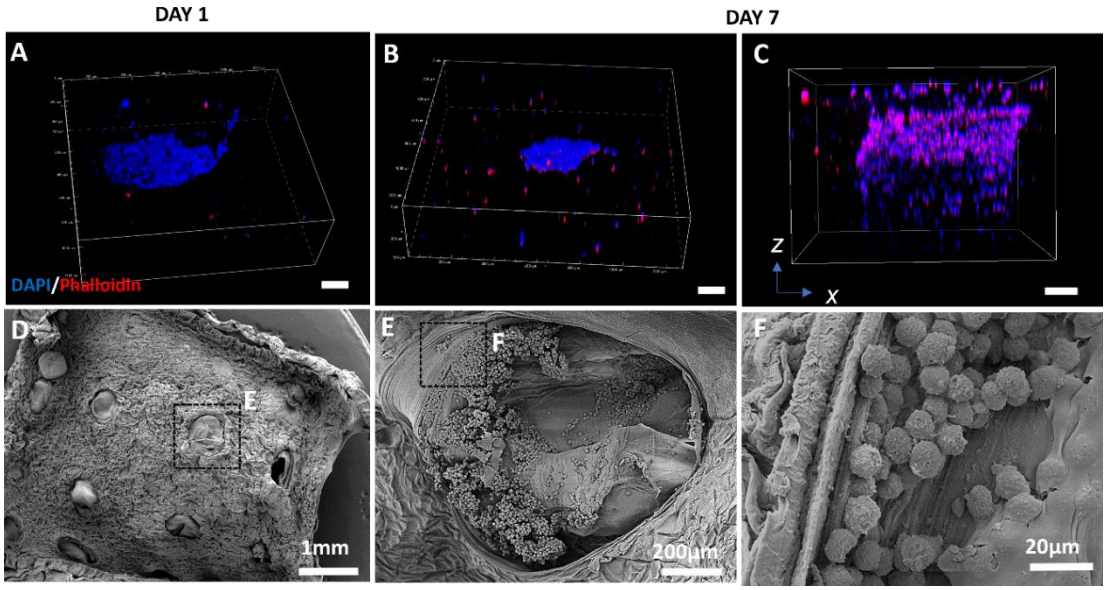

Figure 6.21: DAPI/Phalloidin staining at day 1 (**A**) and day 7 (**B**), with a focus on the x,z axys, to observe the cells organisation through the channels of GG3 (**C**). SEM images at day 1: 50 x (**D**), 250 x (**E**) and 2500 x (**F**).

6.3.10 Evaluation of pathological features within AC Deep Layer

To evaluate the pathological features in the DL, immunofluorescence of COLL X and ACAN was performed and quantified, together with a GAGs quantification and evaluation of the construct's viscoelastic properties.

In **Figure 6.22** are reported the qualitative and quantitative relative intensities of Aggrecan (ACAN) and Collagen X (COLLX) expression by Y201-C chondrocytes. ACAN expression was extremely low on day 1 and abundantly elevated after 21 days of culture in DL-H constructs

(from 18 ± 9 % at day 1 to 90 ± 10 % at day 21), whereas it did not increase up to that level for the DL-P samples at day 21 (from 18 ± 9 % at day 1 to 45 ± 3 % at day 21). COLLX, on the other hand, was undetectable in both samples on day 1 (n.d.), but was found in a small number of cells in the DL-H model on day 21 (12 ± 2 %) and in a large number of cells in the DL-P model on day 21 (49 ± 10 %) (**Figure 6.22A,B**).

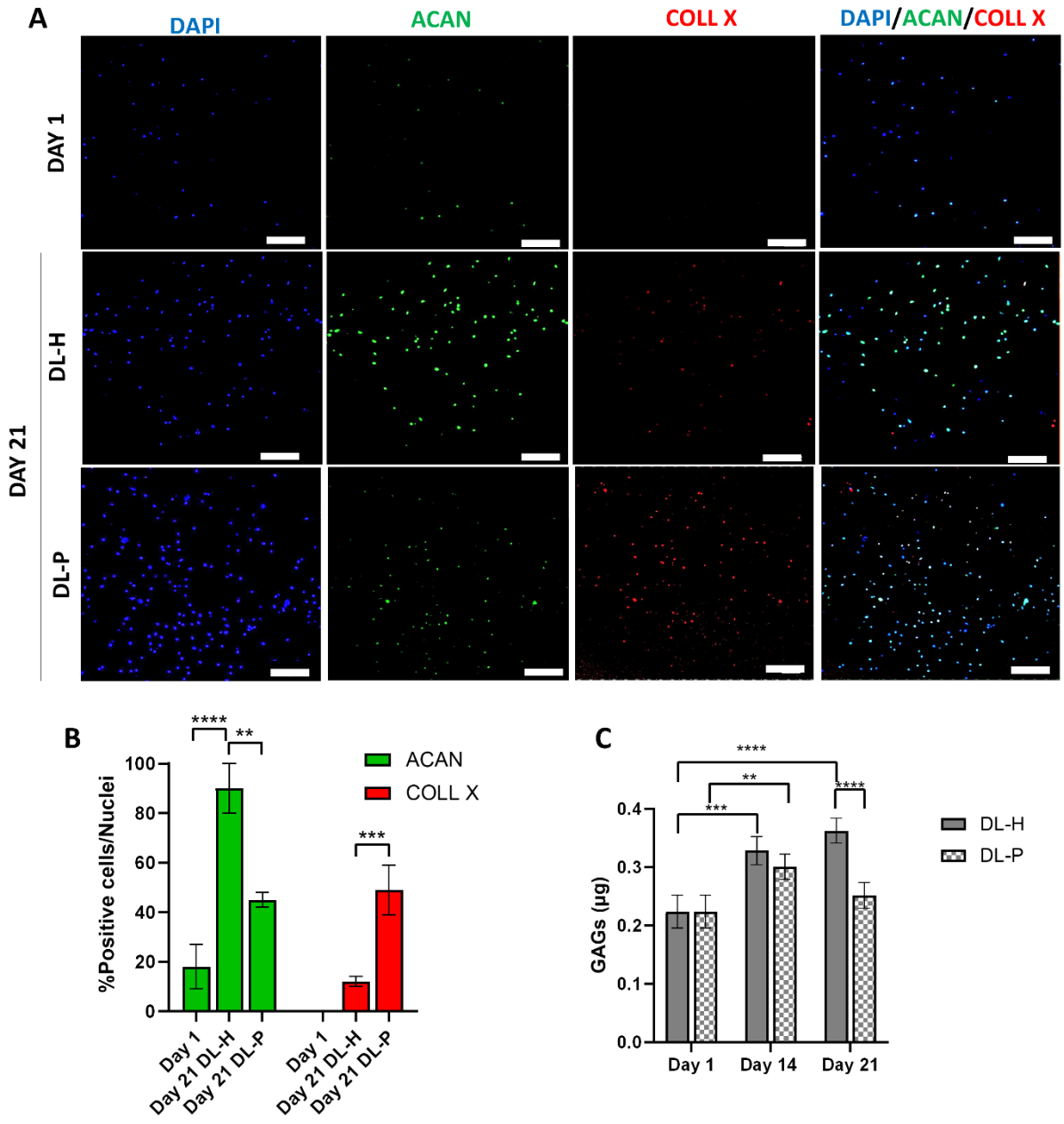

Figure 6.22: Assessment of DL in OA (DL-P) and healthy (DL-H) conditions. Immunofluorescence staining for ACAN (green) and COLLX (red) at days 1 and 21 for DL-H and DL-P: cell nuclei were counterstained with DAPI (**A**). Scale bar: 100 µm. Graph showing the percentage of ACAN and COLLX positive cells with respect to the nuclei (**B**). GAGs quantification at day 1, 14 and 21 in DL-H and DL-P samples: acellular GG-CSDP15 background was subtracted, and data were extrapolated from a standard curve.

GAGs production by Y201-C, showed a similar trend: while no significative differences were observed up to 14 days in DL-H and DL-P samples, a significant difference was observed at day 21 ($p<0.0001$). At day 14, an increase in GAGs production by Y201-C was observed in DL-P, compared to day 1 ($p<0.001$), this was followed by a decrease at day 21. Conversely, in healthy conditions, GAGs production was, not only superior compared to pathological conditions ($p<0.0001$), but even significantly higher compared to day 1 ($p<0.0001$).

To evaluate the change in DL viscoelastic properties in OA conditions, stress-relaxation analysis was performed over the course of 14 days of culture. Indeed, already from the Stress-relaxation curves (stress vs. time) it is possible to notice a difference in the DL-H and DL-P behaviour (**Figure 6.23**): in Healthy condition at day 14 (**Figure 6.23B**), as well as at day 1 (**Figure 6.23A**), a typical graph of a viscoelastic material can be observed, with the samples reaching the equilibrium and stabilising at that stress value (E_Y); on the other side, in OA conditions at day 14, an atypical stress vs. time curve can be observed, where samples never reached the equilibrium and the curve suddenly fell after 400 s. The Peak Young's Modulus (E_P) recorded on day 1 was 9.8 ± 0.1 kPa and it decrease to 1.1 ± 0.2 kPa at equilibrium (E_Y): the relaxation times obtained were viscoelastic relaxation time (τ_1) of 12.8 ± 1.3 s and the poroelastic relaxation time (τ_3) of 2698.8 ± 727.6 s. The E_P modulus did not change significantly from day 1 to day 14 in the DL-H model, where it was 10.7 ± 0.0 kPa, while the E_Y raised up to 4.1 ± 0.2 kPa; the values of τ_1 and τ_3 respectively fell to 7.7 ± 2.0 s and 1471.0 ± 191.6 s. On the other side, the DL-P model showed an E_P modulus of 12.1 ± 0.1 kPa, but it did not reach the E_Y value, due to the breakage: the recorded τ_1 and τ_3 were respectively 8.8 ± 2.4 s, and 1693.5 ± 634.3 s (**Figure 6.23D)**.

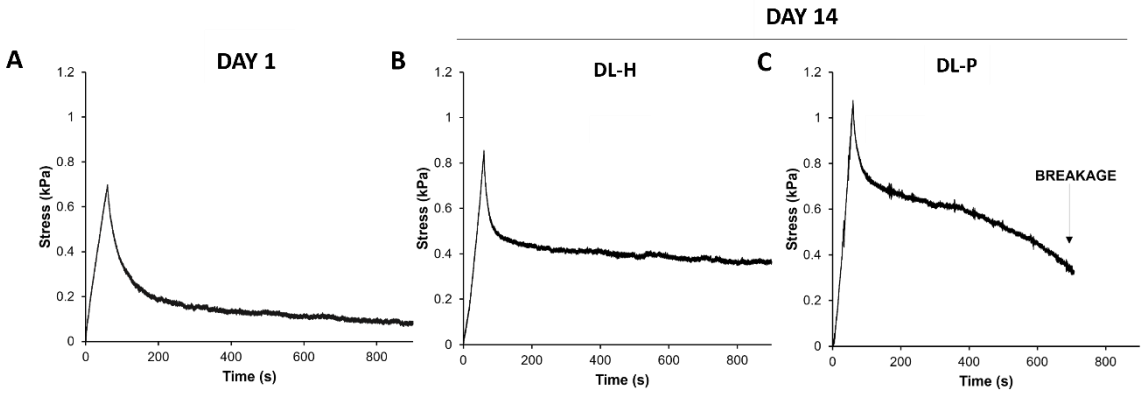

D

Day1			DL-H			DL-P		
E_p (kPa)	τ_1 (s)	τ_3(s)	E_p(kPa)	τ_1(s)	τ_3(s)	E_p(kPa)	τ_1(s)	τ_3(s)
9.8±0.1 kPa	12.8±1.3s	2698.5±727.6 s	10.7±0.0 kPa	7.73±2.0 s	1471.0±191.6 s	12.1±0.1 kPa	8.8±2.4 s	1693.5±634.3 s

Figure 6.23: Stress relaxation curves obtained for DL construct at day 1 (**A**) and at day 14 in healthy (**B**) and pathological (arrow pointing at the breakage point) (**C**) conditions. Table reporting for each sample the Peak Young's modulus, the viscoelastic relaxation time (τ_1) and the poroelastic relaxation time (τ_3).

Finally, the morphology of cells in the DL-H and DL-P constructs were evaluated after 21 days of culture. A lower amount of cells, together with a rougher surface, was observed in OA conditions (**Figure 6.24C,D**).

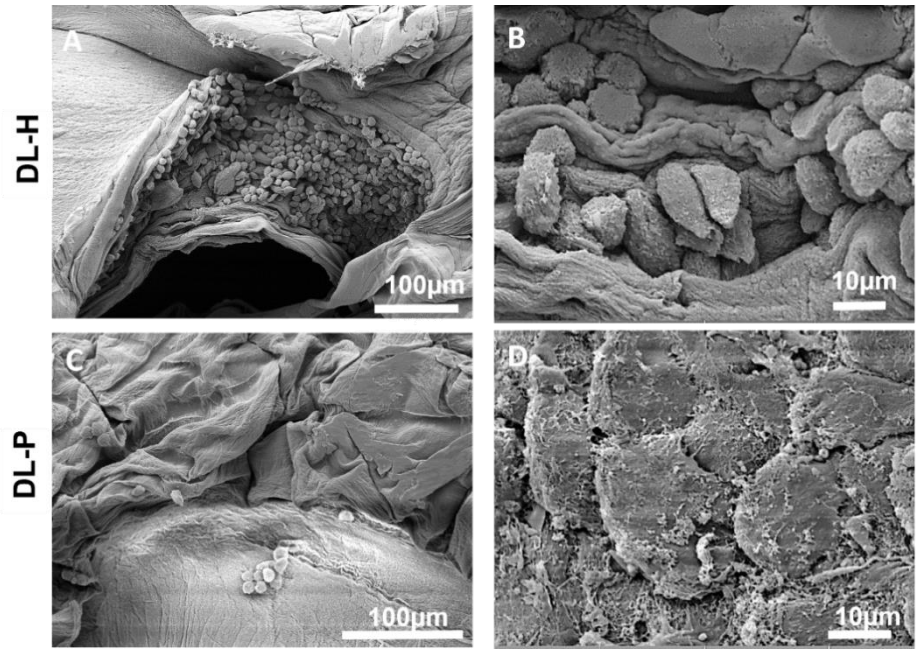

Figure 6.24: Morphological analysis of cells within the DL-H and DL-P constructs, after 21 days of culture.

6.3.11 Middle layer: manufacturing and characterisation

For the manufacturing of the middle layer, GG2 and GG2-MH formulations were selected and analysed in terms of printability and biological commitment for encapsulated Y201-C. The ML was manufactured using bioprinting technology, via extrusion-based bioprinting (**Figure 6.25**). The resulting constructs were crosslinked by UV (MA groups bonds) and DMEM/F12 (ionic bonds), during the bioprinting process for Y201-C-loaded GG2 and GG2-MH bioinks,onto a DMEM/F12-covered printing bed. In **Figure 6.25B** are reported the bioprinted GG2 and GG2-MH constructs made of 4 layers, together with a 10-layer GG2-MH grid, at low and high magnification, to show the ability of bioprinting a bigger size construct without the collapse of the structure. GG2-MH was selected because it led to the obtainment of a more stable and viscous filament extruded and therefore a better resolution.

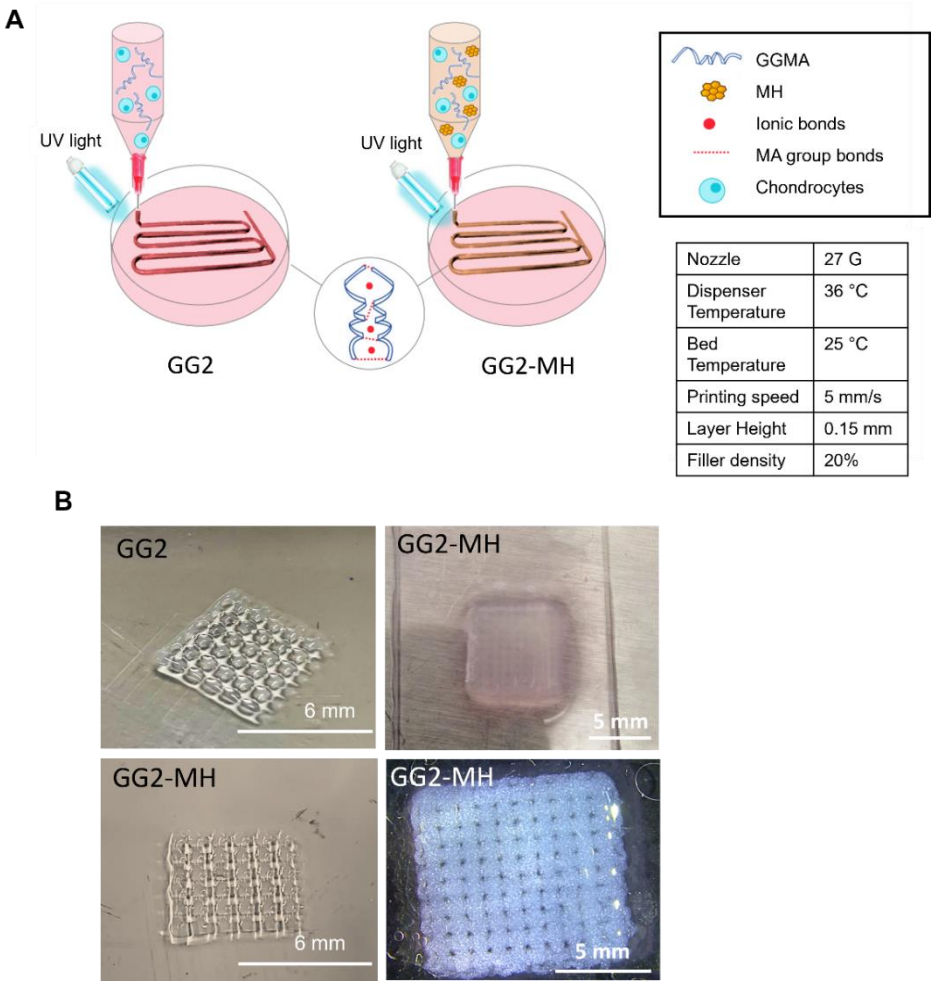

Figure 6.25: Bioprinting procedure for GG2 and GG2-MH for manufacturing AC ML: scheme of the bioprinting process with encapsulated Y201-C and the optimised printing parameters for the Rokit INVIVO bioprinter (**A**). Images of the obtained GG2 and GG2-MH constructs: a four layers grid (left) and a 10-layers construct obtained with GG2-MH selected bioink at different magnifications (right).

Indeed, the printability test showed a spreading ratio of 5.3 ± 0.8 for the GG2 and 3.5 ± 0.1 for the GG2-MH bioink. Also, GG2-MH filament had a more consistent diameter distribution along its length, from 0.5 mm when exiting the nozzle to 1.0 mm at the bottom (**Figure 6.26B,D**), compared to GG2 filament (**Figure 6.26A,C**), whose diameter increased from 0.7 mm to 1.5 mm, from the top to the bottom. In addition, the presence of MH helped to extrude a longer length fibre (~ 13 mm) compared to the GG2, which showed a total length of 7 mm and resembled a drop, more than a filament (**Figure 6.26C**). The filament diameter measured after the fibre deposition and the photocuring (from pictures in **Figure 6.26E,F**) was 7 mm for the GG2 and 3 mm for the GG2-MH. Also, the filament's images in the GFP channel are reported to highlight the presence of the fluorescent MH (**Figure 6.26G,H**).

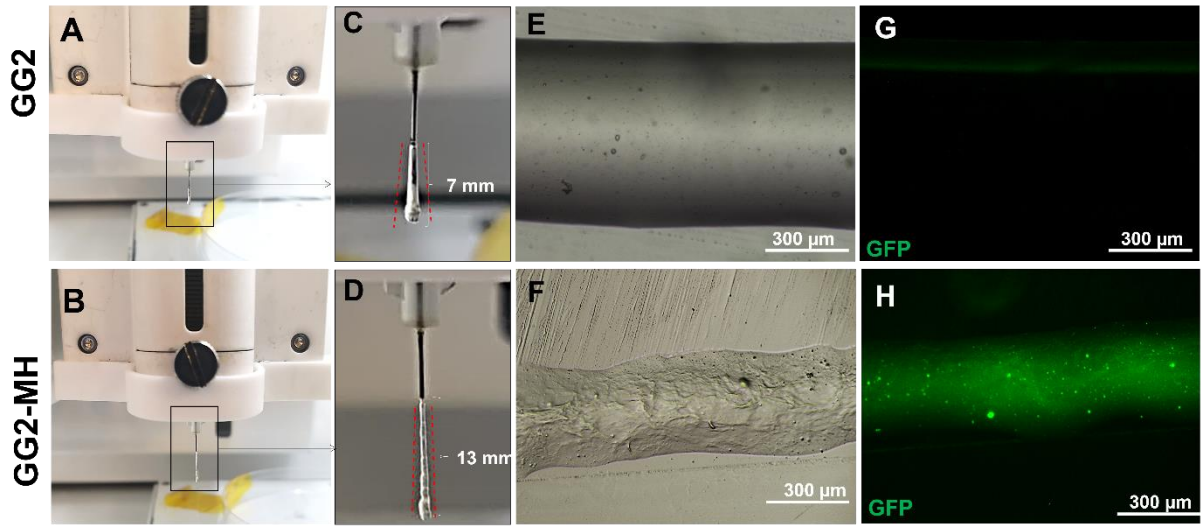

Figure 6.26: Zoom in on the filament extruded before being deposited on the printing bed for GG2 (**A**) and GG2-MH (**B**): the red lines are indicating the change in the diameter alongside the length of the filament; (F,J) Phase contrast pictures of GGMA and GGMA-MH extruded filaments; (G,K) GFP images of GGMA and GGMA-MH extruded filaments.

6.3.12 Middle layer: biological evaluation

The cytocompatibility of GG2 and GG2-MH bioprinted constructs was tested at days 1 and 3 of culture. In both samples cells were alive at both time points (**Figure 6.27A-D**), with a small percentage of dead cells: 2.0 ± 0.5 % at day 1 and 1.8 ± 0.4 % at day 3 for GG2 samples and 9.5 ± 3.5 % at day 1 and 18.0 ± 6.0 % at day 3 for GG2-MH (**Figure 6.27E**).

Also, Y201-C showed a constant number of metabolically active cells up to 7 days of culture, as measured by MTS, with no significant statistical changes between GG2 and GG2-MH or between single samples during the culture time (**Figure 6.27F**).

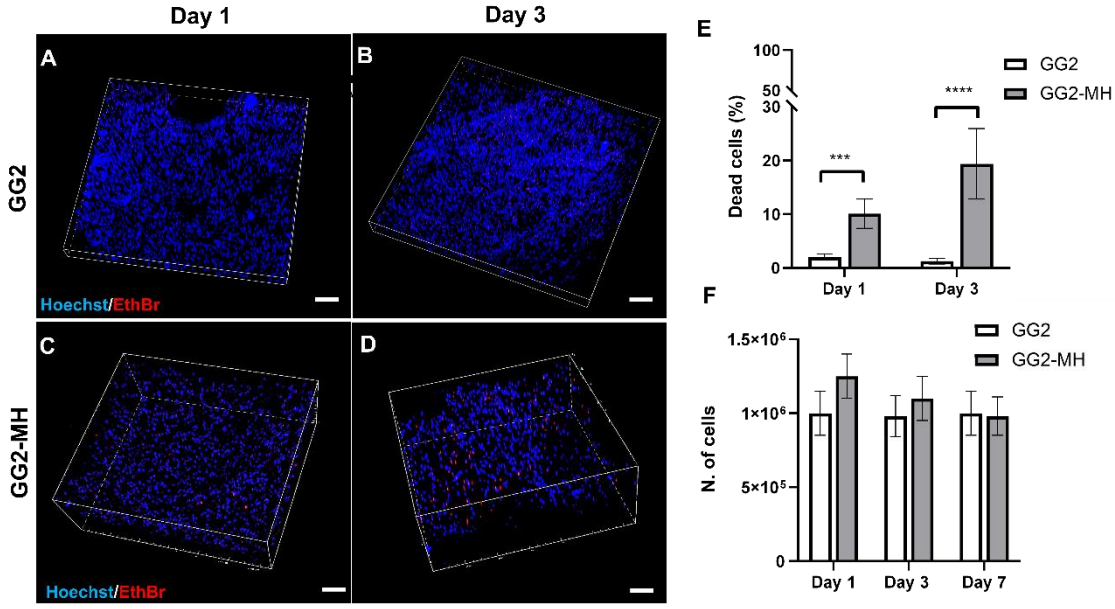

Figure 6.27: Assessment of cells viability within the bioprinted GG2 (**A,B**) and GG2-MH (**C,D**) at day 1 and day 3, via confocal microscopy: 3D view. All cells nuclei are stained in blue (Hoechst) and dead cells are stained in red (Ethidium Bromide). The amount of dead cells are quantified with Image J software, from the obtained images (**E**). Evaluation of the number of metabolically active cells, via MTS assay (**F**). Statistics: ****p<0.0001, ***p<0.001.

Fluorescent labelling was used for GG2 and GG2-MH, to indicate cells distribution within the bioprinted hydrogels on days 1, 3 and 7 of culture (**Figure 6.28A-F**). During the 7 days of culture, cell distribution inside the construct changed: Y201-C were homogenously dispersed in GG2 at days 1, 3 and 7, while Y201-C were homogenously dispersed at days 1 and 3 in GG2-MH constructs and heterogeneously dispersed at day 7. A great difference can be observed at day 7 in 2D (**Figure 6.28E,F)** and 3D images (**Figure 6.28G,H**) between GG2 and GG2-MH samples: GG2-MH samples showed cells migration and the appearance of cell aggregates.

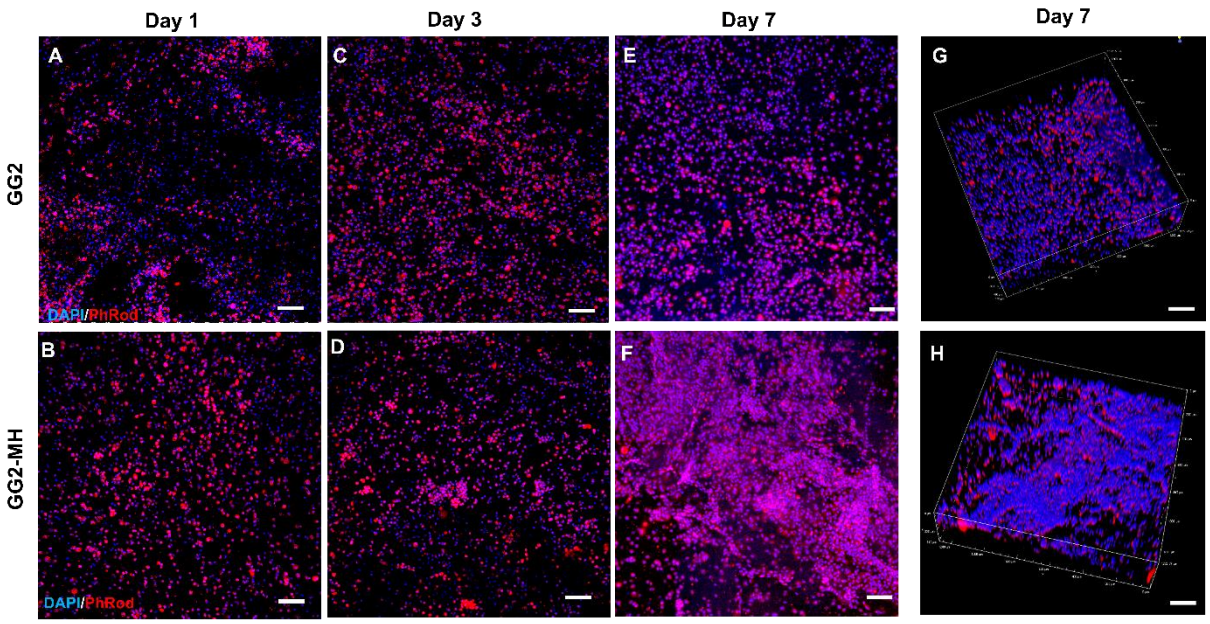

Figure 6.28: Immunostaining of cells nuclei (blue, DAPI) and cytoskeleton (red, PhRhod): 2D images at days 1, 3 and 7 for GG2 (A,C,E) and GG2-MH (B,D,F); 3D view at day 7 for GG2 (G) and GG2-MH (H). Bars= 100 µm.

Y201-C cells morphology was evaluated in GG2 and GG2-MH samples at day 21 of culture: both samples showed numerous cells dispersed within the matrix, possessing a round-shaped morphology with a diameter <20 µm (**Figure 6.29**).

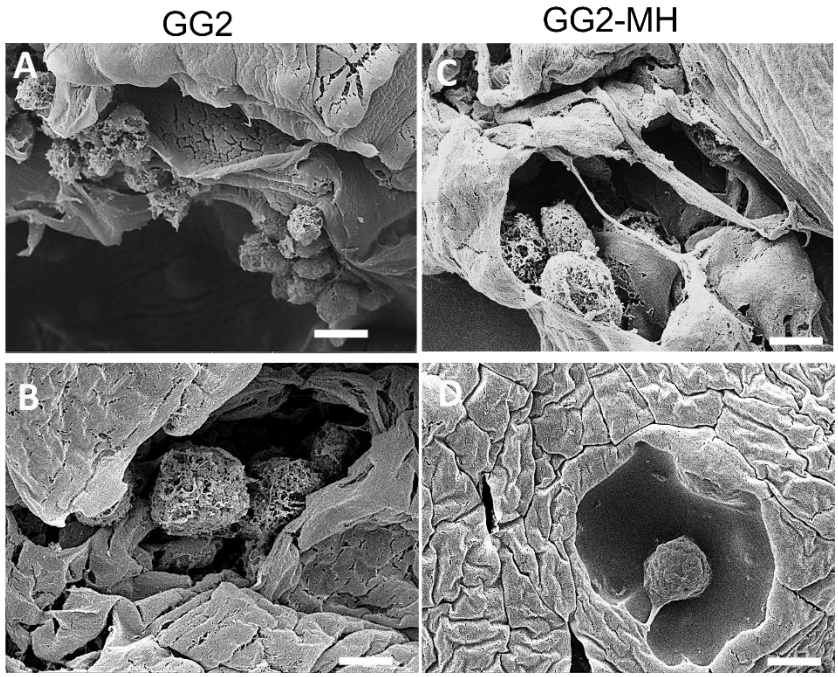

Figure 6.29: SEM analysis of GG2 (**A,B**) and GG2-MH (**C,D**) hydrogels after 21 days of culture at 2000 x (**A,C**) and 4000 x (**B,D**).

6.3.13 Evaluation of pathological features within AC Middle layer

The pathological features were assessed for the ML, for both GG2 and GG2-MH hydrogels, via histology (**Figure 6.30**), GAGs quantification, gene expression analysis and HIC.

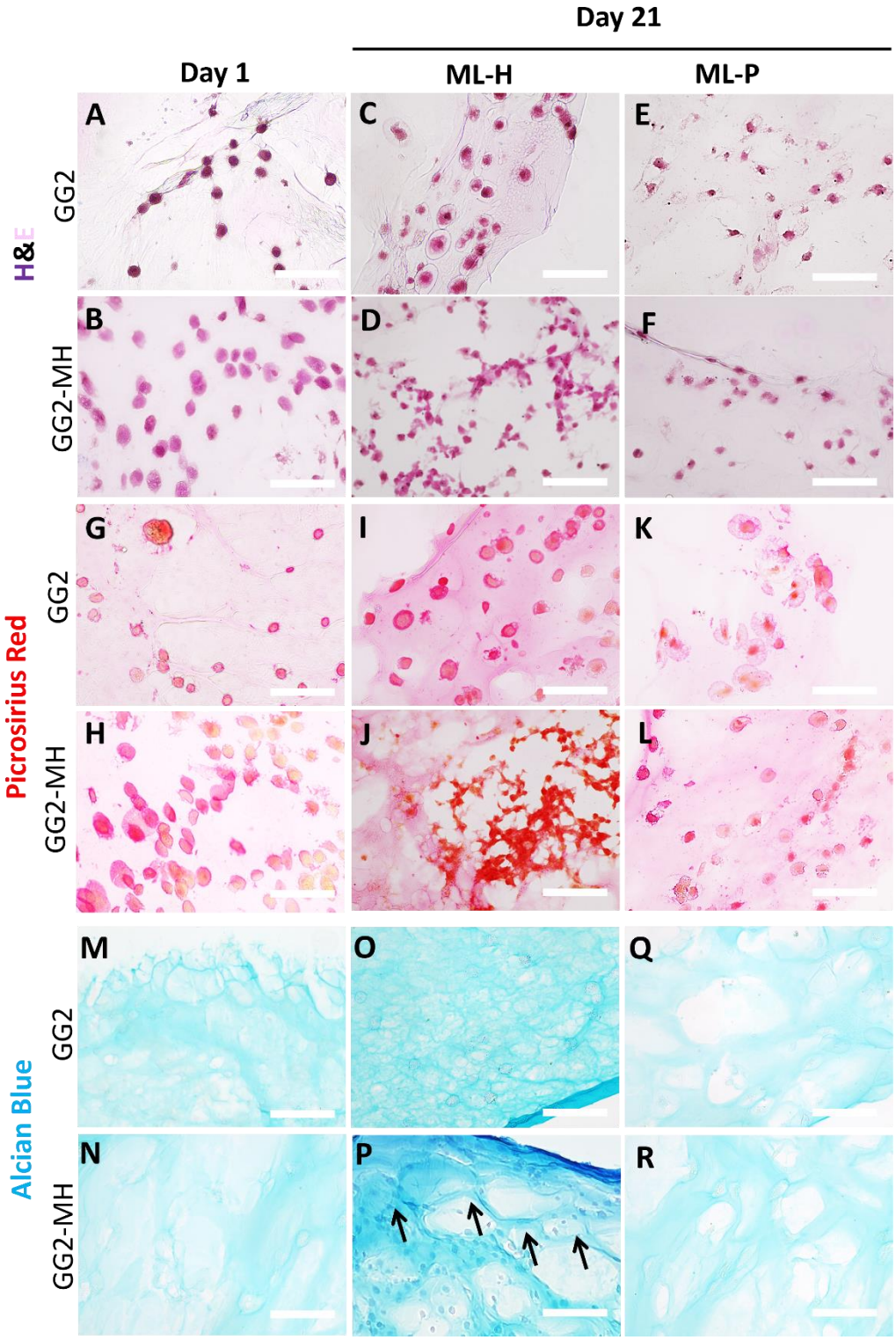

Figure 6.30: Histological analysis of cryosections of GG2 and GG2-MH at day 1 and at day 21 in healthy (GG2-H and GG2-P) and OA conditions (GG2-MH-H and GG2-MH-P). H&E staining of cells nuclei and cytoplasm (**A-F**), Picrosirius red staining of collagen (**G-L**), Alcian blue staining of GAGs (**M-R**). Bars= 150 µm.

H&E staining revealed many chondrocytes within the obtained constructs after 21 days, especially in ML-H samples, mostly localised as typical isogenous groups and with a relatively regular arrangement in the GG2 samples (**Figure 6.30C**), in comparison to the GG2-MH (**Figure 6.30D**) samples, where cells appeared more agglomerated. In OA conditions (ML-P), instead, both GG2 and GG2-MH showed a lower amount of cells (**Figure 6.30E,F**). Both in the presence and absence of honey, histological staining of healthy samples (ML-H) at day 21 revealed an intense staining of GAGs with Alcian Blue and collagen with Picrosirius Red (**Figure 6.30I,J,O,P**), compared to ML-P (**Figure 6.30K,L,Q,R**) and compared to the respective samples at day 1. GG2-MH-H samples at 21 days showed the most intense staining of Picrosirius Red (**Figure 6.30J**) and Alcian Blue (**Figure 6.30P**).

According to the GAGs quantitative analysis (**Figure 6.31**), GG2 samples produced significantly more GAGs on days 7 and 21 of culture ($p<0.0001$) in healthy conditions (GG2-H), compared to OA conditions (GG2-P). Furthermore, from day 1 to day 21, GG2-H samples showed a significant increase of GAGs production over time ($p<0.0001$) (**Figure 6.31A**). Similarly, GG2-MH samples produced significantly more GAGs on days 21 of culture ($p<0.0001$) in healthy conditions (GG2-MH-H), compared to OA conditions (GG2-MH-P), while no statistical differences were observed at day 7. Furthermore, at day 21 GG2-MH-H samples showed a significant increase of GAGs production, compared to day 1 ($p<0.0001$) (**Figure 6.31B**). Also, GG2-MH-H constructs showed higher number of produced GAGs, compared to GG2 on days 7 (~0.22 µg vs. ~0.18 µg respectively) and 21 (~0.26 µg vs. ~0.30 µg), indicating a more progressive ECM development.

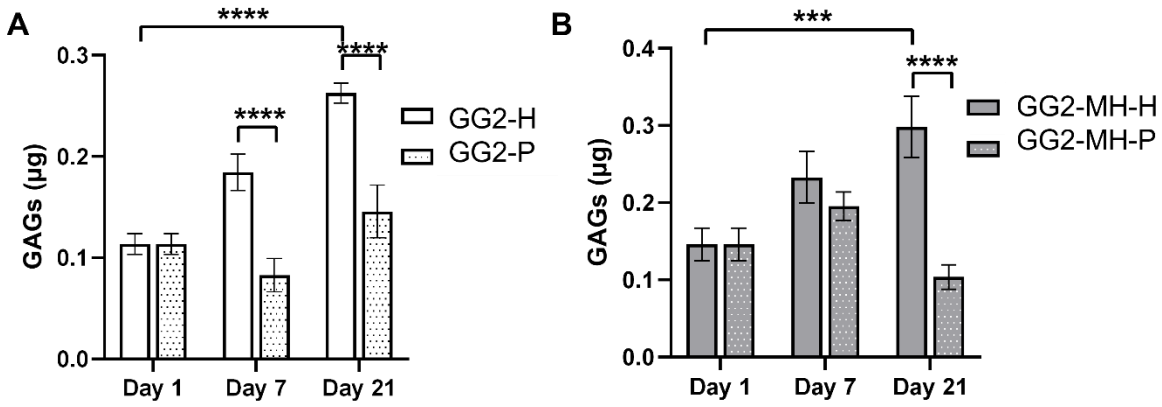

Figure 6.31: GAGs quantification for GG2 (**A**) and GG2-MH (B) at days 1, 7 and 21 in healthy and OA conditions.

Anabolic and catabolic genes fold change was evaluated in GG2 and GG2-MH, in healthy and pathological conditions at day 21, with respect to day 1 (**Figure 6.32**).

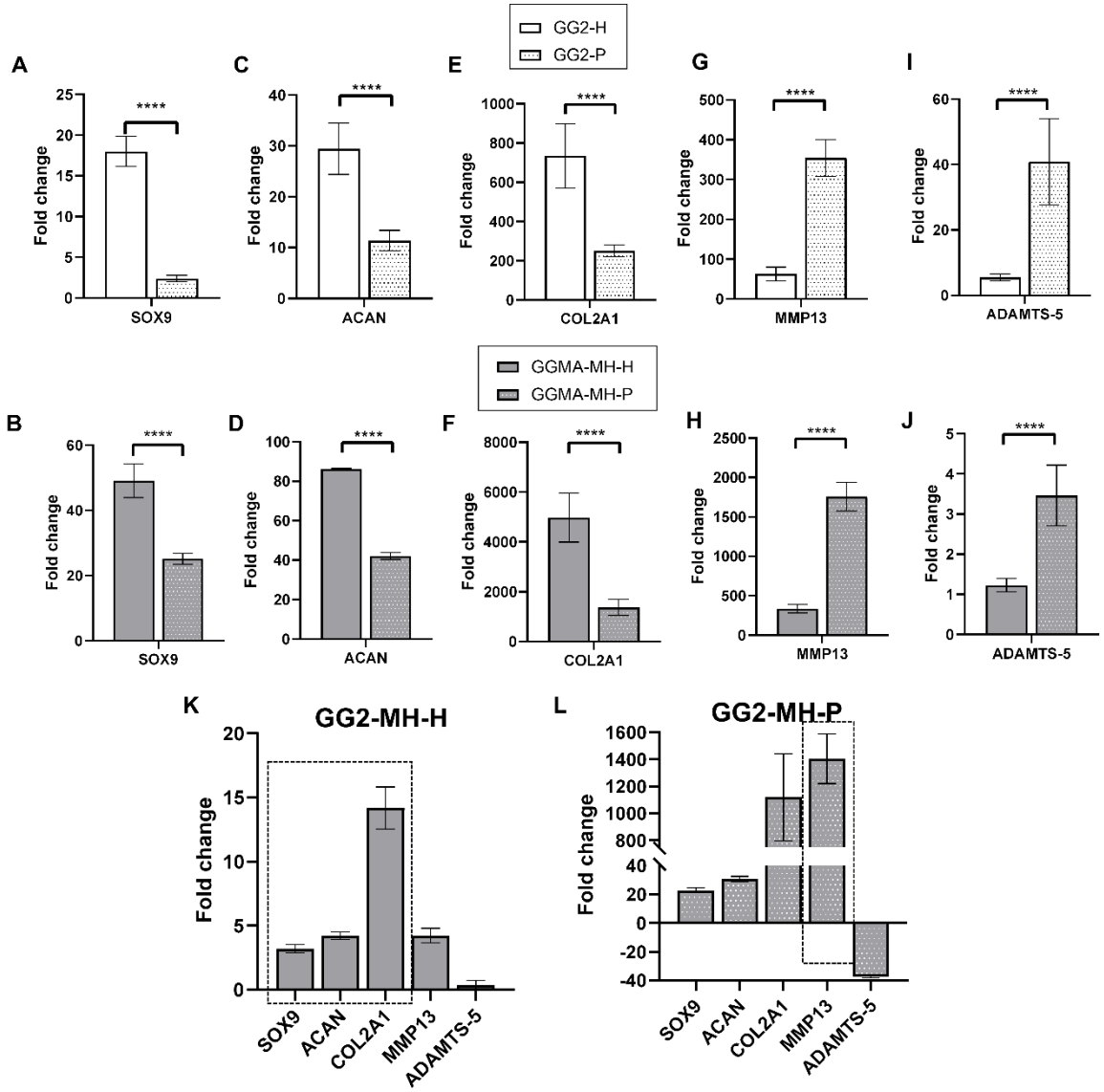

Figure 6.32: Gene RT-qPCR analysis to evaluated the expression of *sox9* (**A,B**)*, acan* (**C,D**)*, col2a1* (**E,F**)*, mmp13* (**G,H**) and *adamts-5* (**I,J**)*,* for assessing the pathological features of GG2 and GG2-MH construct in presence (GG2-P and GG2-MH-P) and absence of cytokines (GG2-H and GG2-MH-H). The fold change at day 21 with respect to day 1 is reported in the graphs. Fold change of *sox9, acan, col2a1, mmp13* and *adamts-5* for GG2-MH-H and GG2-MH-P after 21 days of culture with respect to GG2-H (**J**) and GG2-P (**K**). In the dotted rectangles are put the results which led to the selection of GG2-MH instead of GG2 for the zonal model manufacturing. Statistics: ****p<0.0001.

Y201-C showed a higher *sox9* fold change in GG2-H compared to GG2-P (**Figure 6.32A**) and GG2-MH-H compared to GG2-MH-P (**Figure 6.32B**) (p<0.0001). The same tendency was observed for *acan* (**Figure 6.32C,D**) and *col2a1* (**Figure 6.32E,F**)(p<0.0001). On the contrary,

mmp13 and *adamts-5* displayed their highest expression in pathological conditions for both GG2 and GG2-MH (**Figure 6.32G-J**). Also, the fold change of anabolic and catabolic markers showed that *sox9, acan* and *col2a1* were upregulated of ~3-fold, ~4-fold and ~14-fold, respectively, in GG2-MH-H samples compared to GG2-H (**Figure 6.32K**). Similarly, *mmp13* was up-regulated of ~1500-fold, in GG2-MH-P samples, compared to GG2-P; while *adamts-5* showed a down-regulation in GG2-MH-P of ~37-fold, compared to GG2-P. (**Figure 6.32L**).

IHC results confirmed gene expression analysis. Compared to day 1 (**Figure 6.33A,B**) and to day 21 in OA conditions (**Figure 6.33E,F**), at day 21 in healthy conditions (**Figure 6.33C,D**) samples showed a higher presence of aggrecan, as noticed by the more intense green staining.

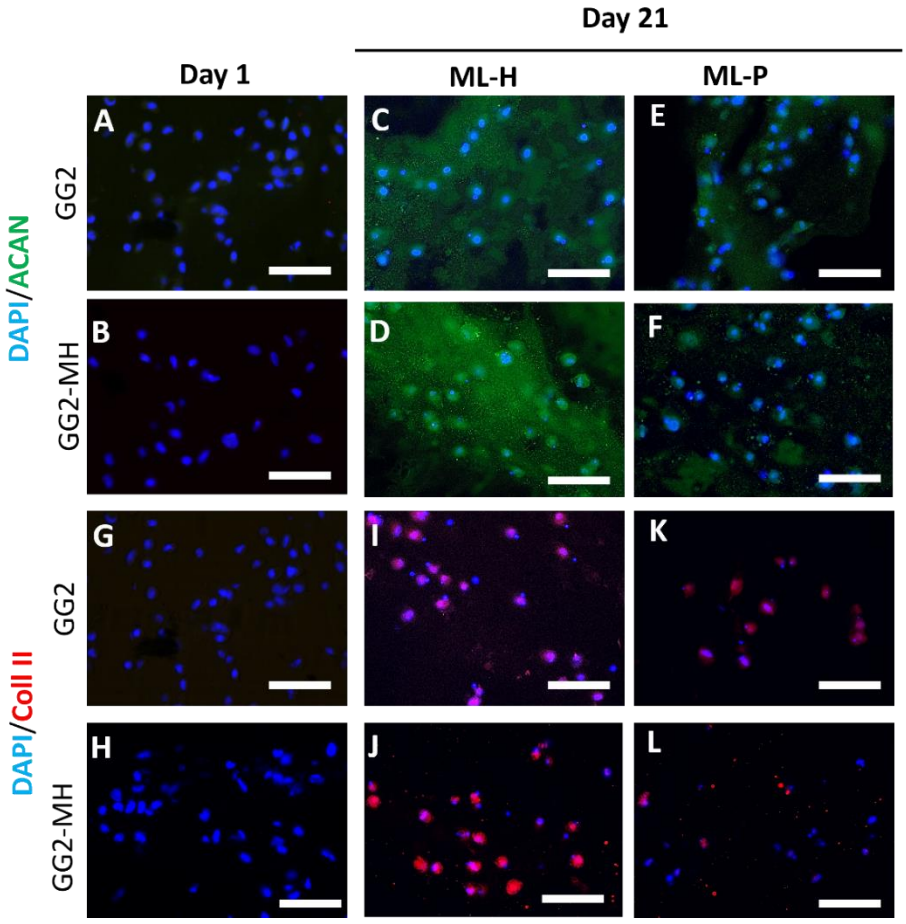

Figure 6.33: Immunohistochemistry analysis of fixed tissue sections: of ACAN (**A-F**) and Coll II (**G-L**), for GG2 and GG2-MH at day 1 and day 21 in healthy (ML-H) and pathological conditions (ML-P). Nuclei were counterstained with DAPI. Bar= 150 µm.

However, in OA samples, some aggrecan staining can be observed. On the other side, Coll II staining was much less intense compared to ACAN, even at day 21 in healthy conditions (**Figure 6.33I,J**). However, even in this case, the intensity of the staining was higher in ML-H at day 21, compared to GG2 and GG2-MH at day 1 (**Figure 6.33G,H**) and to OA conditions at day

21 (**Figure 6.33K,L**). Also, no big differences were observed at day 21 in ML-H and ML-P conditions between the two hydrogels formulations, except from a slight increase in ACAN staining in GG2-MH-H (**Figure 6.33D**), compared to GG2-H (**Figure 6.33C**).

6.3.14 Superficial layer: manufacturing and characterisation

FTIR-ATR spectra of PCL and PCL/GEL showed the typical peaks of PCL (**Figure 6.34**): the asymmetric and symmetric $–CH_2$ stretching at 2949 cm^{-1} and 2868 cm^{-1}; the carbonyl stretching at 1726 cm^{-1}; the stretching of C–O and C–C at 1294 cm^{-1}; the asymmetric and symmetric C–O–C stretching at 1239 cm^{-1} and 1169 cm^{-1}. The addition of GEL in the formulation, led to the addition of two peaks: Amide I at 1638 cm^{-1} and Amide II at 1532 cm^{-1} (Azizi et al., 2018).

A

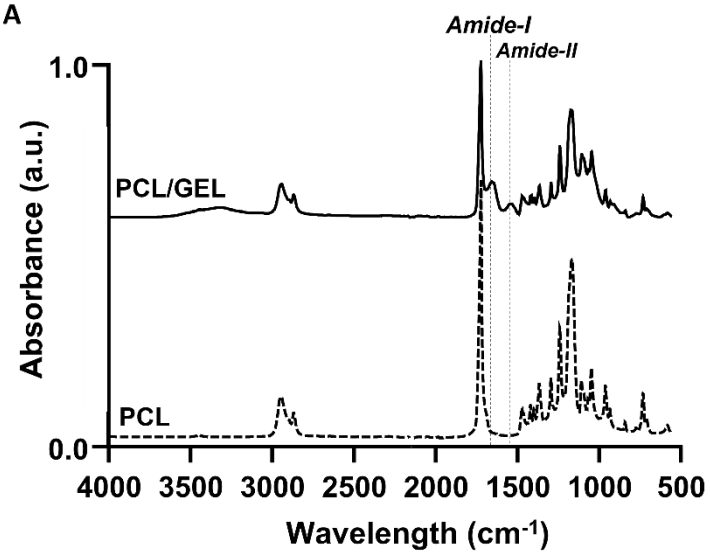

B

PCL	
Wavelength	Peaks
2949 cm^{-1}	*Asymmetric $–CH_2$ stretching*
2868 cm^{-1}	*Symmetric $–CH_2$ stretching*
1726 cm^{-1}	*C=O stretching*
1294 cm^{-1}	*C-O, C-C stretching*
1239 cm^{-1}	*Asymmetric C-O-C stretching*
1169 cm^{-1}	*Symmetric C-O-C*

Figure 6.34: FTIR-ATR spectra of electrospun PCL and PCL/GEL membrane (**A**) and table of the typical PCL peaks and corresponding wavelength (**B**).

Electrospun fibres of varying fiber alignment were produced, as reported in **Figure 6.35.** Compared to PCL/GEL-Random (**Figure 6.35A-C**), PCL/GEL-Aligned membranes showed some degree of fibres orientation (**Figure 6.35D-F**).

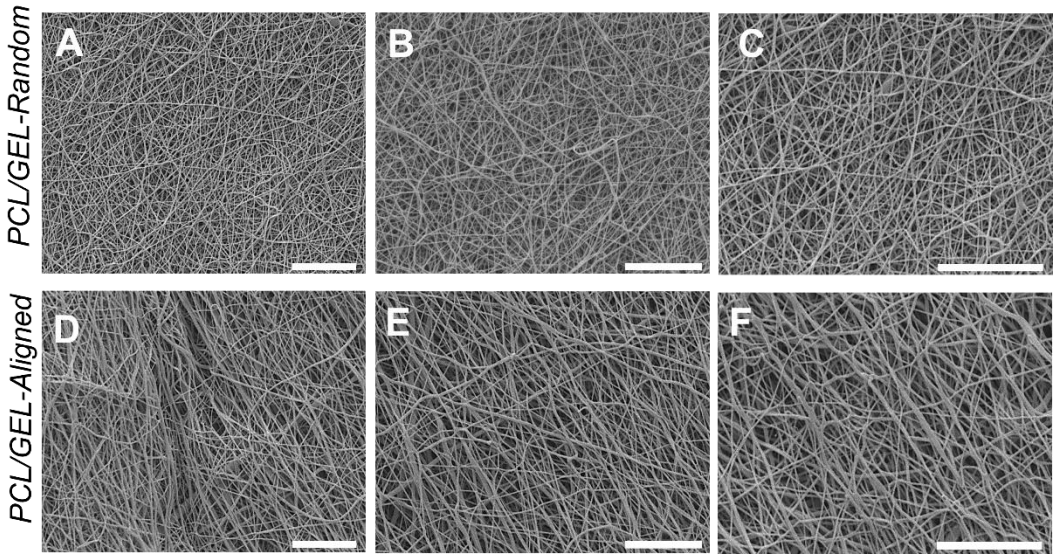

Figure 6.35: Electrospun membranes random (**A-C**) and aligned (**D-F**). Magnifications: 5000 x (**A,D**), 6000 x (**B,E**) and 9000 x (**G,F**). Bars = 10 µm.

6.3.15 Superficial layer: biological evaluation

The viability of Y201-C seeded onto both PCL/GEL-Random and PCL/GEL-Aligned membranes was evaluated via Live/Dead assay (**Figure 6.36**). Both structures led to high cells viability at day 1 and day 3 (live cells stained in green) and just few dead (in red) could be observed at day 1 in both samples. Regarding cells organisation, no differences were observed onto the scaffold at day 1, while a difference in Y201-C organisation onto the membranes could be observed at day 3. Indeed, Y201-C seeded on electrospun PCL/GEL membranes adopted varying morphologies based on the membrane's type. For cells grown on PCL/GEL-Aligned scaffolds, the microstructure orientation of the underlying matrix directed Y201-C into an elongated morphology and organised distribution alongside fibres direction, as shown in both **Figure 6.36** and in **Figure 6.37 D,H,** from the morphology and orientation of cells cytoskeleton, stained with Phalloidin Rhodamine.

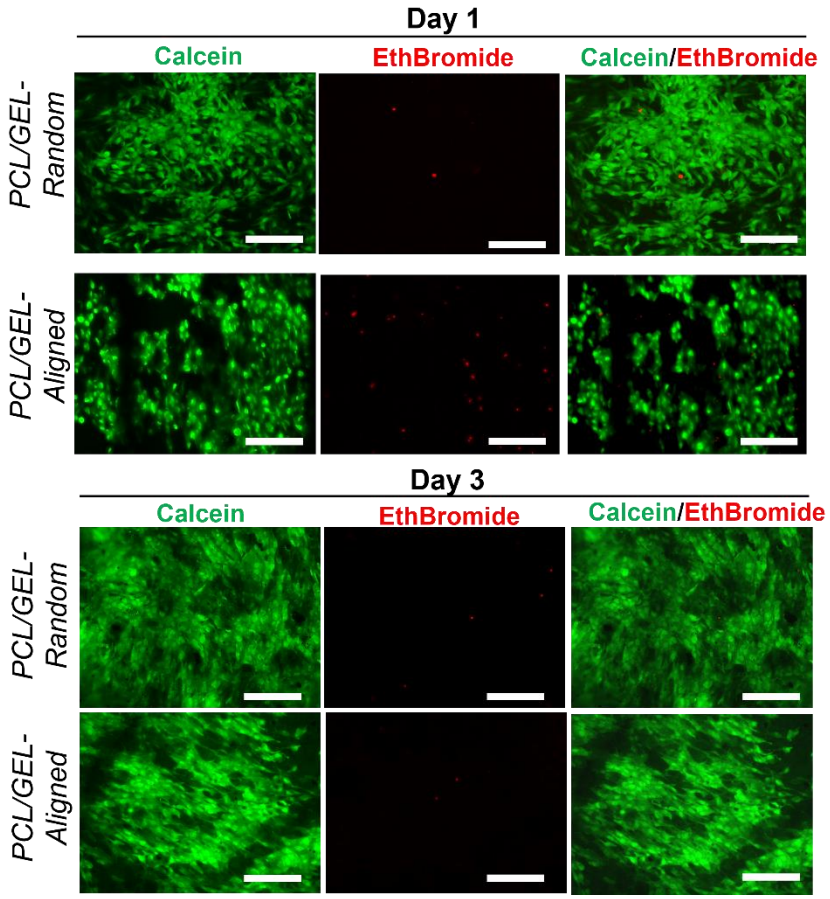

Figure 6.35: Cells viability onto PCL/GEL-Random and PCL/GEL-Aligned membranes at days 1 and 3 of Y201-C culture, evaluated via Live/Dead assay. Live cells are stained in green (calcein) and dead cells in Red (EthBromide).

On the other side, for Y201-C grown onto PCL/GEL-Random scaffolds, the microstructure orientation of the underlying matrix directed cells into a rounder, polygonal morphology and a random organisation onto the membrane, as showed in **Figure 6.36** and in **Figure 6.37 C,G**.

Cells proliferation onto the two structures was analysed via Ki-67 staining and MTT quantitative analysis. From Ki-67 staining, it is visible that Y201-C, at day 7, showed high proliferation, given by the intense staining (green) in both conditions (**Figure 6.37E,G,F,H**).

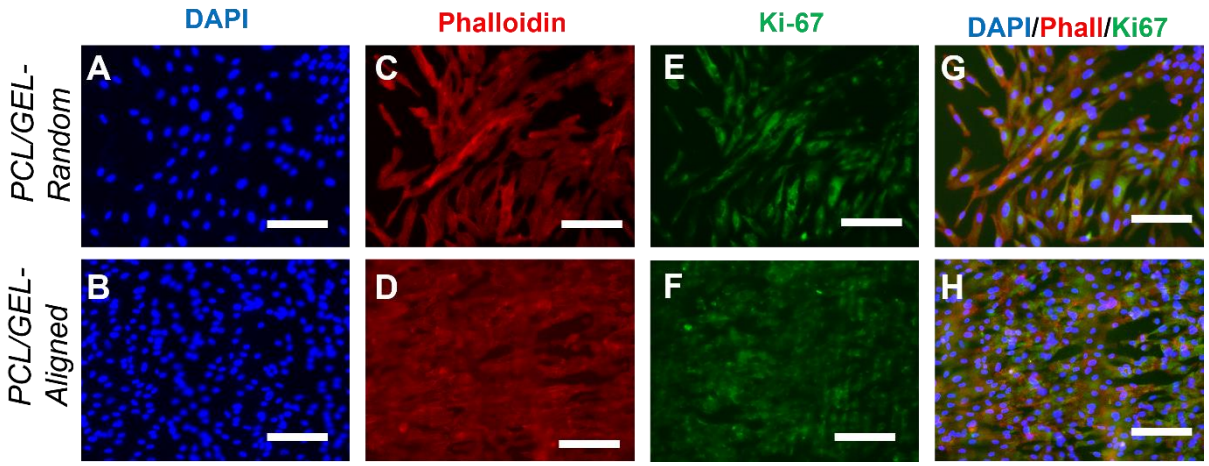

Figure 6.37: Cells distribution and morphology onto PCL/GEL-Random (**A,C,E,G**) and PCL/GEL-Aligned (**B,D,F,H**) membranes at day 7. Immunostaining of cells nuclei (DAPI) (**A,B**) cytoskeleton (PhalloidinRhodamine) (**C,D**), Ki-67 (**E,F**) and merged stainings (**G,H**). Bars= 150 µm.

Also, the number of Y201-C cells with active metabolism activity, was analysed with MTT assay (**Figure 6.38**). Both PCL/GEL-Random and PCL/GEL-Aligned showed a statistically significant increase in the number of cells over the 7 days of culture ($p<0.0001$), reaching the number of ~3.8 x 10^6 cells onto aligned membranes and ~3.5 x 10^6 onto random membranes.

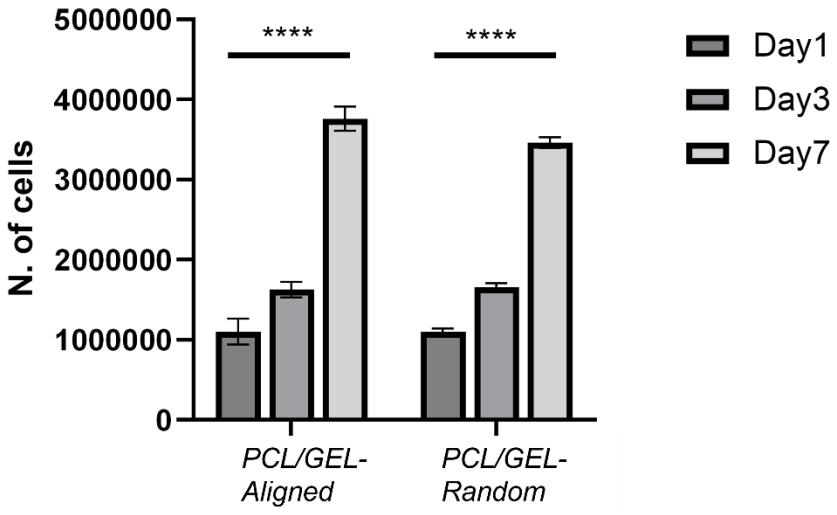

Figure 6.38: Number of metabolically active cells at days 1, 3 and 7 onto PCL/GEL-Random and PCL/GEL-Aligned, evaluated with MTT assay. Statistics: ****$p<0.0001$.

6.3.16 Evaluation of pathological features within AC Superficial layer

PCL/GEL-Aligned were selected for evaluating the pathological feature during the on-set of OA in SL-P, compared to healthy conditions (SL-H). After 3 weeks of culture, histology staining on membrane cryosections showed an intense H&E staining in both SL-H (**Figure 6.39B**) and SL-P (**Figure 6.39C**). However, cells appeared more elongated onto the membrane in healthy conditions, compared to pathological condition, were these appeared more rounded and clustered. This feature was observed in Picrosirius staining, as well. Also, while an intense and uniform red coloration was present in SL-H sections (**Figure 6.39E**), a less intense staining can be observed in SL-P, together with a more fragmented membrane and cells layer: cells appeared to be detaching from the membrane after 21 days of culture (**Figure 6.39F**). Alcian blue staining, instead, showed a very low intensity of staining at days 1 and 21 in SL-H and SL-P (**Figure 6.39 G,H**).

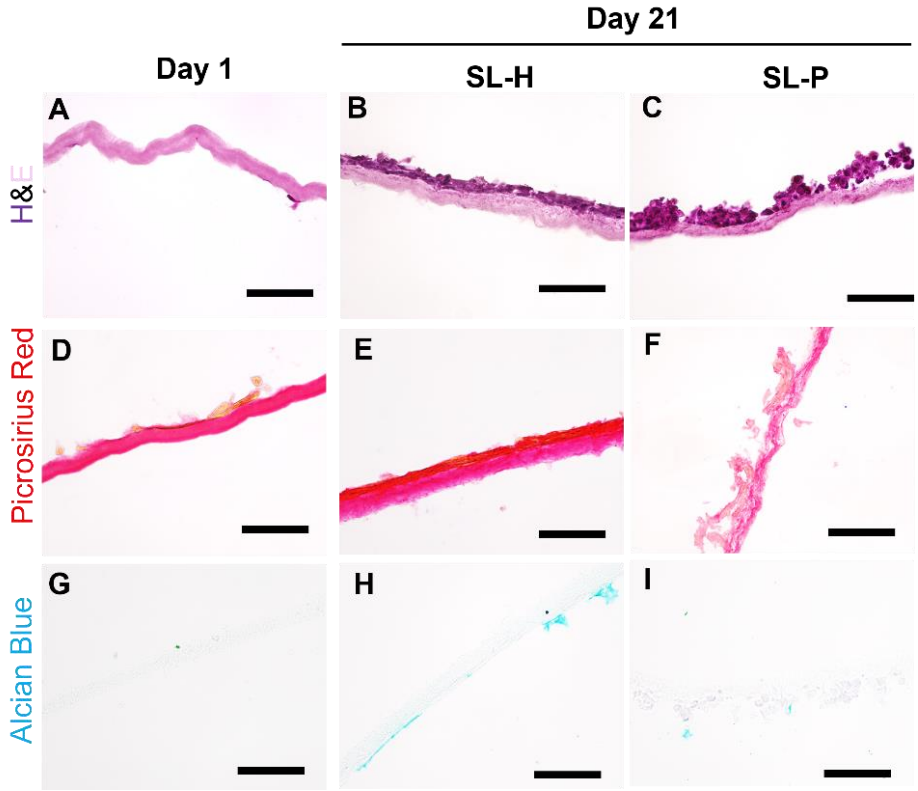

Figure 6.39: Histological analysis of cryosections of SL at day 1, SL-H and SL-P at day 21. H&E staining of cells nuclei and cytoplasm (**A-C**), Picrosirius red staining of collagen (**D-F**), Alcian blue staining of GAGs (**G-I**).

Gene expression analysis was assessed to understand the difference in anabolic and catabolic activity of Y201-C in healthy and OA conditions. In SL-H samples, cells exhibited a significant higher fold-change of *sox9* (0.63 ± 0.05 fold) (**Figure 6.40A**), *acan* (550 ± 80 fold) (**Figure 6.40B**) and *col2a1* (14 ± 3 fold) (**Figure 6.40C**), compared to SL-P (0.19 ± 0.06 fold for *sox9*, 280 ± 30

fold for *acan* and 1-fold for *col2a1*) (p<0.0001). Particularly, *col2a1* was not expressed by cells at day 21 of culture onto the membranes in OA conditions. Conversely, *mmp13* expression was much higher in presence of cytokines in SL-P condition (32 ± 10 fold), compared to SL-H condition (2 ±-1 fold). *Col1a2* and *adamts-5* expression, instead, did not show statistical differences between the two conditions. The ratio of COL2A1/COL1A2 resulted to be ~28 for SL-H and ~2 for SL-P.

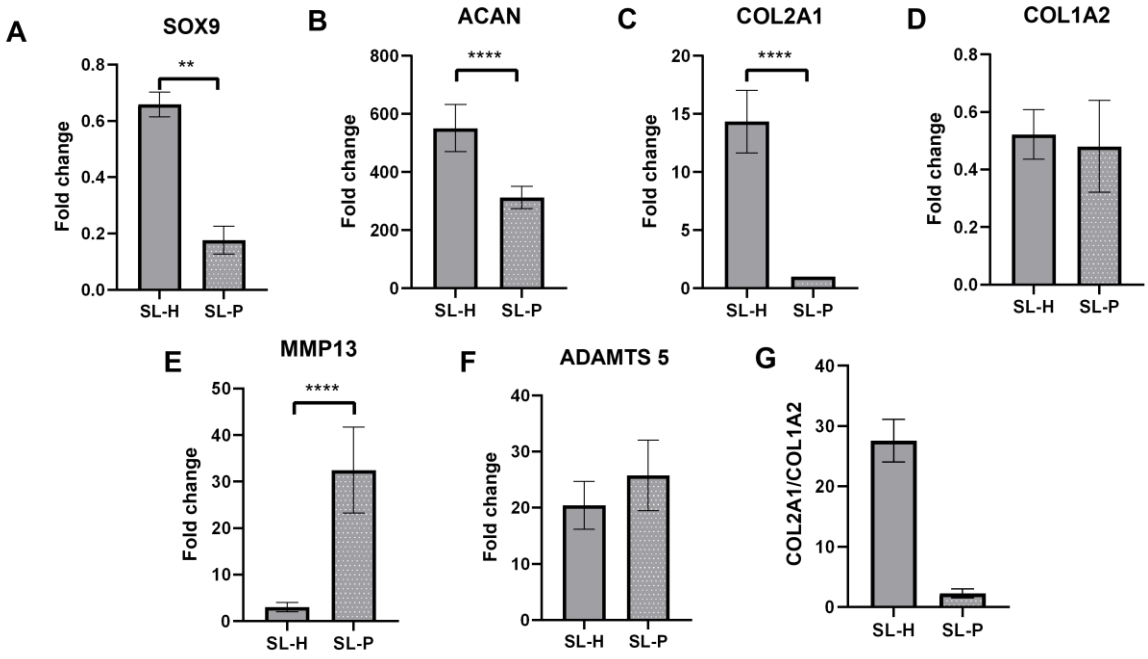

Figure 6.40: Gene RT-qPCR analysis to evaluate the expression of *sox9* (**A**)*, acan* (**B**)*, col2a1* (**C**)*, col1a2* (**D**), *mmp13* (**E**) and *adamts-5* (**F**)*,* for assessing the pathological features of SL in absence (SL-H) or presence (SL-P) of cytokines. The fold change at day 21 with respect to day 1 is reported in the graphs. Ratio of COL2A1 and COL1A2 at day 21 is reported for SL-H and SL-P (**G**). Statistics: ****p<0.0001, **p<0.01.

The results obtained from gene expression analysis were confirmed by Immunohistochemistry on cryosections and by Immunofluorescence on membranes.

IHC staining on cryosections revealed an intense Coll II (**Figure 3.41E,F**) and ACAN (**Figure 3.41N,O**) staining in SL-H samples, compared to SL-P (**Figure 3.41H,I,P,Q**) and compared to SL at day 1 (**Figure 3.41B,C,K,L**). However, in SL-P samples a weak staining can be noticed.

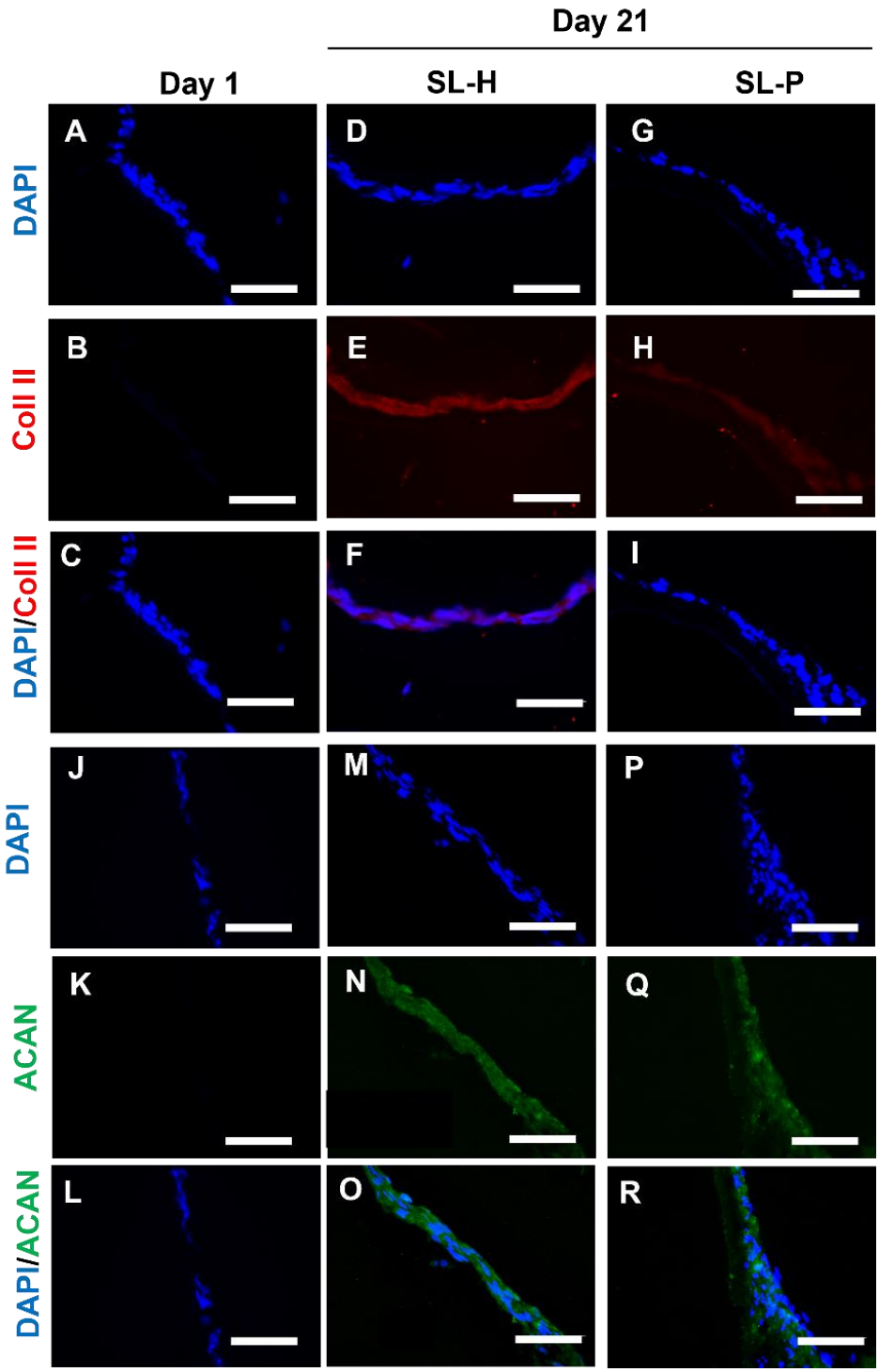

Figure 6.41: Immunohistochemistry analysis of fixed tissue sections: of Coll II (**A-I**) and ACAN (**J-R**) for SL at day 1 and SL-H and SL-P at day 21. Nuclei were counterstained with DAPI. Bar= 125 µm.

Immunofluorescence staining of Coll II on full fixed membranes, showed similar results to the ones obtained by IHC. In fact, in SL-H condition at day 21 (**Figure 6.42E,F**) it was visible a much intense red staining, compared to SL-P at day 21 (**Figure 6.42 H,I**). Also, no Coll II staining was detected at day 1 for SL (**Figure 6.42B,C**).

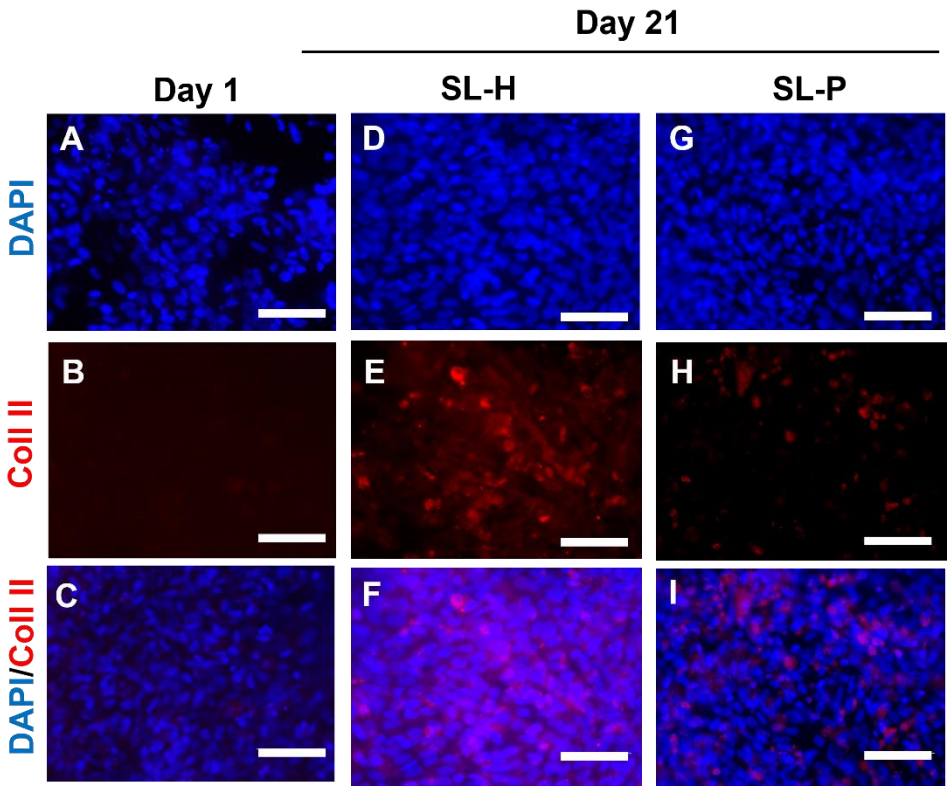

Figure 6.42: Immunofluorescence analysis of Coll II and DAPI on fixed membranes for SL at day 1 (**A-C**) and SL-H (**D-F**) and SL-P (**G-I**) at day 21. Bar= 150 µm.

Morphological analysis by SEM, are showing a different organisation and morphology of cells in healthy and OA conditions. At day 21, Y201-C in SL-H condition (**Figure 6.43C,D**), showed a similar morphology to the one observed at day 1 (**Figure 6.43A,B**). However, the membrane appeared totally covered by cells, organised in a cell-sheet. Also, a fibrous matrix can be observed in this condition (**Figure 6.43D**). In SL-P condition, instead, cells appeared more rounded and less spread alongside the electrospun membrane, as already observed by histological staining. Also, a lot of acellular spaces can be observed on the membrane (**Figure 6.43E,F**)

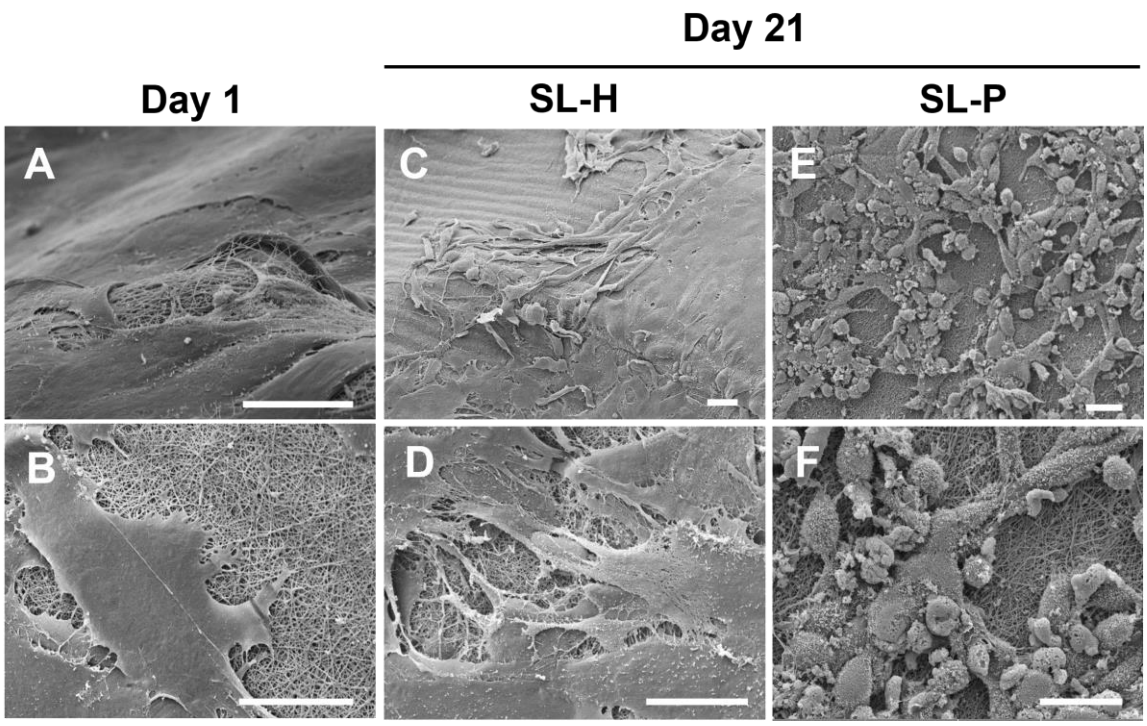

Figure 6.43: Morphological analysis of Y201-C onto the PCL/GEL membranes at day 1 (**A,B**) and at day 21, in SL-H (**C,D**) and SL-P (**E,F**). Magnifications: 400 x (**A,B,D,F**), 750 x (**C**) and 1000 x (**D**). Bars= 20 µm.

6.3.17 Zonal model: manufacturing and characterisation

The final construct obtained was 6 x 6 x 6 mm (W x L x H) (**Figure 6.44C**). The final ratio of cells within the construct was 3:2:1:0.25. Specifically, 14 x 10^6 cells/mL in the SL, 7 x 10^6 cells/mL in the ML, 3.5 x 10^6 cells/mL for the DL and 8.75 x 10^6 cells/mL in the SB.

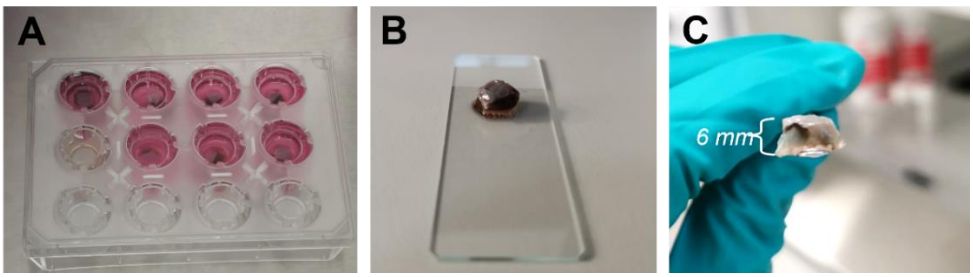

Figure 6.44: Obtained zonal construct, cultured in the 12 well plate with inserts (**A**). Image of the model on a glass slide (**B**) and a zoom (**C**).

6.3.18 Zonal model of AC and SB: biological evaluation

Cells viability, metabolic activity, and their organisation within the different layers of the manufactured zonal model were evaluated.

In **Figure 6.45A**, it can be observed cells viability in the layers of the zonal construct. In all the layers few dead cells can be observed (stained in red). The layer with the a higher amount of dead cells was the SB; . Cells metabolic activity was evaluated in the zonal construct, showing an increase from day 1 (0.2 ± 0.01) and day 3 (0.24 ± 0.02) to day 7 (0.48 ± 0.05) of culture ($p<0.0001$).

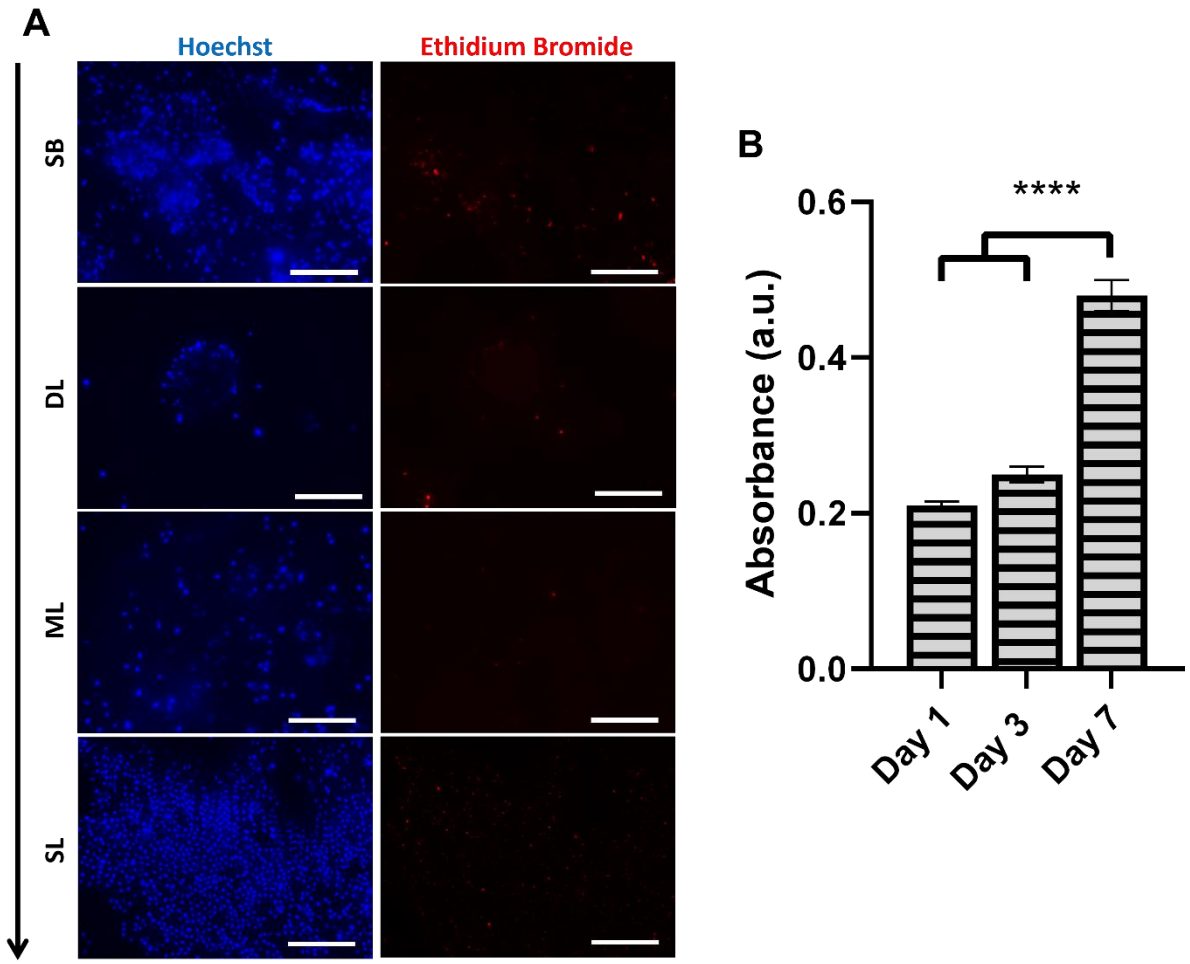

Figure 6.45: Assessment of cells viability within the zonal construct after 24 h of manufacturing: all cells nuclei are stained in blue (Hoechst) and dead cells are stained in red (Ethidium Bromide) (**A**). Evaluation of cells viability via MTS (**B**). Bar= 150 µm. Statistics: ****$p<0.0001$.

The organisation of Y201-C within the AC side of the zonal model was assessed via DAPI and Phalloidin staining. At day 1, rounded cells were dispersed within the channels of GG3 in the DL (**Figure 6.46A,B**) and homogenously dispersed in the ML construct (**Figure 6.46C,D**) and SL

(**Figure 6.46E,F**). At day 7, some cell clusters can be observed in the DL (**Figure 6.46G,H**) and in the ML (**Figure 6.46I,J**), while elongated cells, organised alongside the fibres of the membranes, can be observed in the SL (**Figure 6.46K,L**).

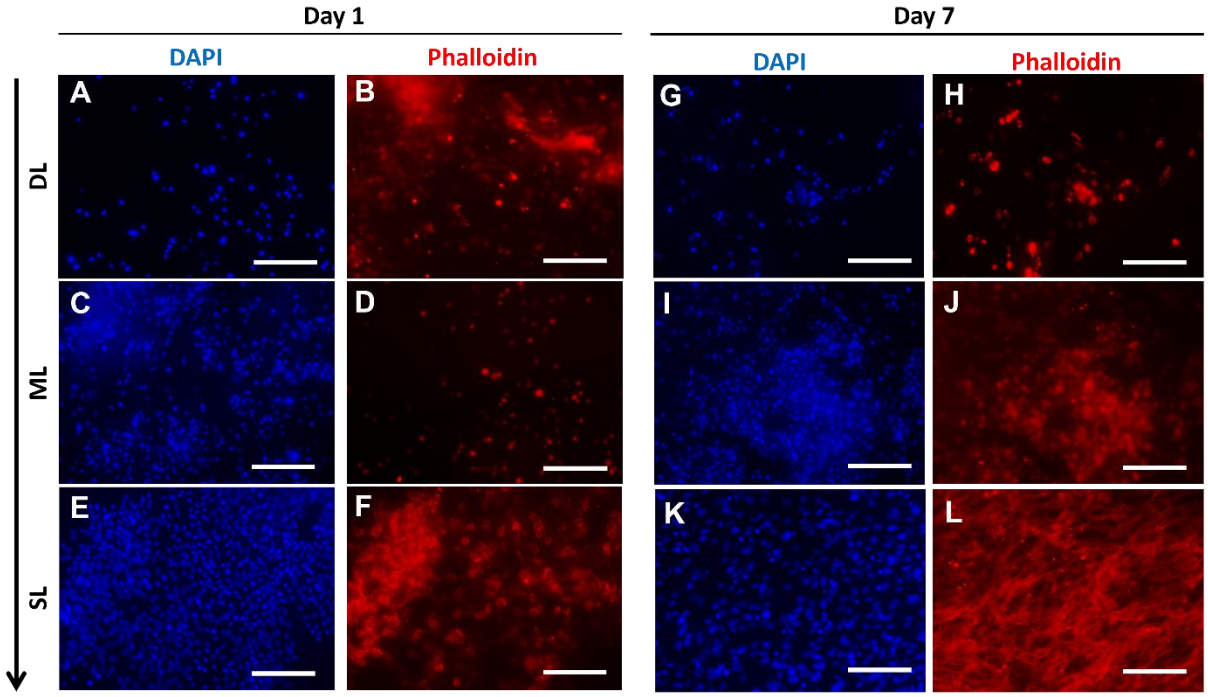

Figure 6.46: Cells distribution and morphology within the zonal model at day 1 (**A-F**) and day 7 (**G-L**). Staining of cells nuclei with DAPI and cytoskeleton with Phalloidin Rhodamine. Bars= 150 µm.

6.3.19 Evaluation of pathological features within the Zonal model of AC and SB

From the histological analysis, in **Figure 6.47**, it can be observed a great difference between the H&E stainings in Healthy condition, where cells nuclei appeared rounded (stained in purple) and homogenously dispersed within the construct (**Figure 6.47A**), while in OA conditions, cells nuclei appeared less rounded, smaller, and fragmented (**Figure 6.47B**). The same feature was observed for the tissue around the cells, which appeared more fragmented in OA conditions, as evidenced from H&E staining and Picrosirius Red staining. Especially, the fragmentation of the SL membrane can be noticed in H&E staining (**Figure 6.47B**). On the other side, in Healthy conditions, the tissue appeared more intact (from H&E staining and from Picrosirius Red staining) and the staining more intense (**Figure 6.47A**), compared to OA conditions (**Figure 6.47B**). Finally, Alcian Blue staining was more intense in the Healthy model (**Figure 6.47A**), especially around the cells and in the SL, compared to the Pathological model (**Figure 6.47B**).

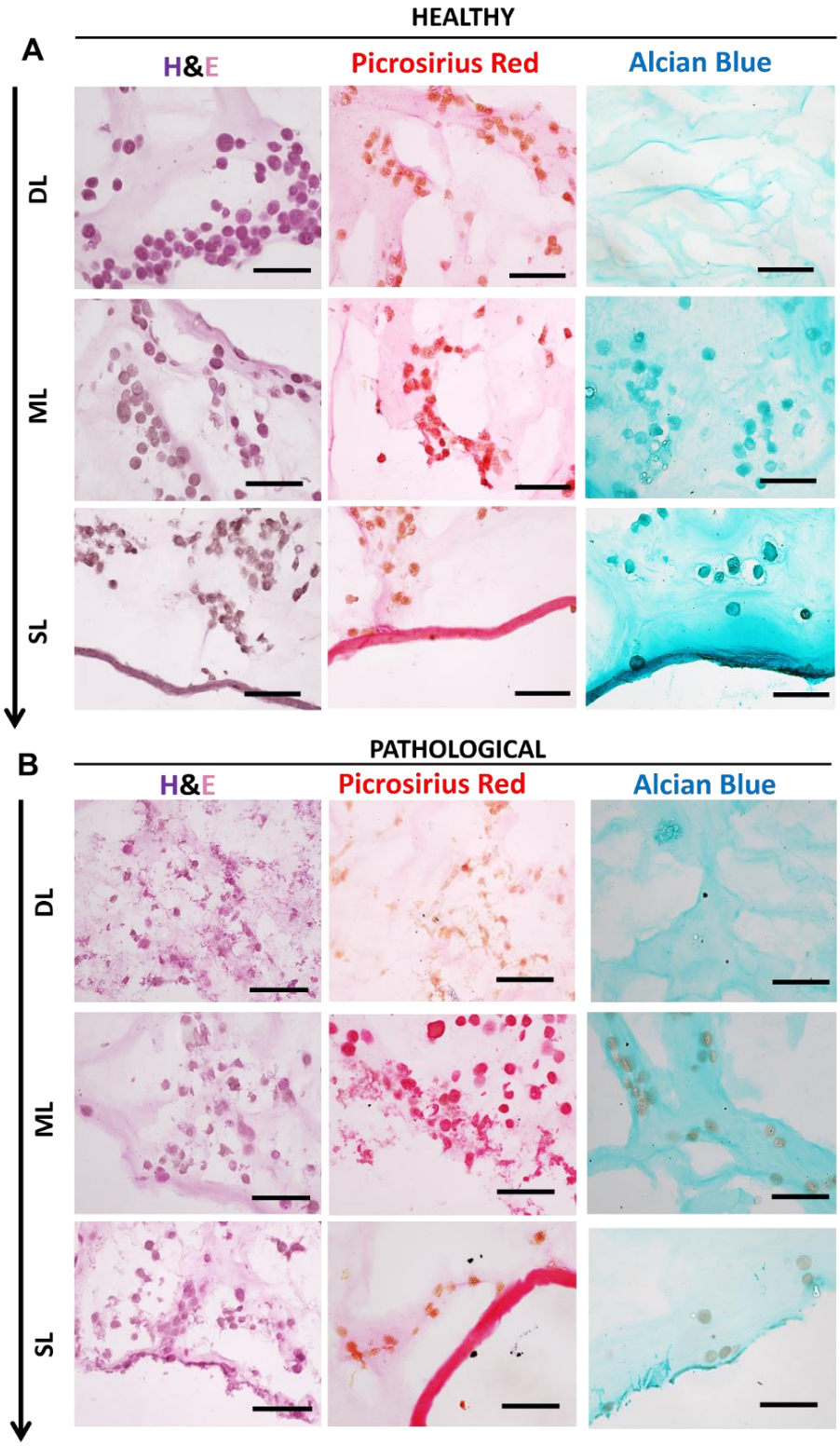

Figure 6.47: Histological analysis of zonal construct cryosections at day 21 in healthy (**A**) and pathological (**B**) conditions. H&E staining of cells nuclei and cytoplasm, Picrosirius red staining of collagen and Alcian blue staining of GAGs. Bars= 150 µm.

In **Figure 6.48** SEM analysis shows the morphology of the construct at day 1. After the dehydration process the height of the construct decreased from 6 mm to 1.5 mm; also, the length and the width of the hydrogel part of the construct (ML and DL) almost halved,

comparing to the SB and SL, which maintained their dimensions. This feature was observed at day 21 as well (**Figure 6.49-6.50**). At day 1 cells appeared homogenously dispersed on the SL (**Figure 6.48E**), as well as within the ML and DL (**Figure 6.48C**).

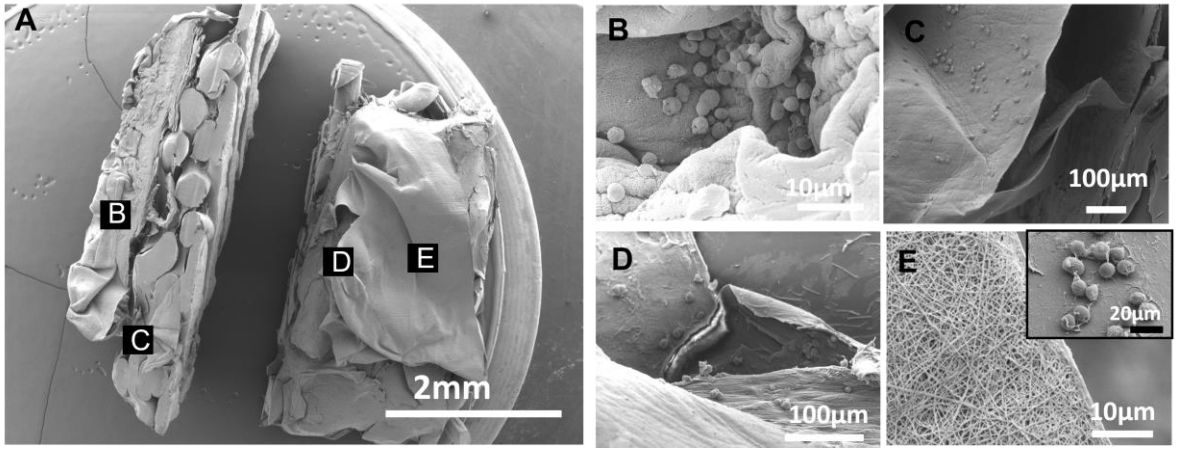

Figure 6.48: Morphological analysis of the obtained construct at day 1: total construct (**A**); zoom on different part of the construct: SL-ML interface (**B**), ML-DL interface (**C**), SL (**D**), morphology of the membrane and Y201-C on it (insert) (**E**).

After 21 days of culture in healthy conditions, the overall construct dimensions didn't change a lot; however, it can be observed the matrix formation within the different layers, in particular in the ML, DL (**Figure 6.49C**) and SB, where cells were stretching between the fibres of matrix produced (**Figure 6.49D**).

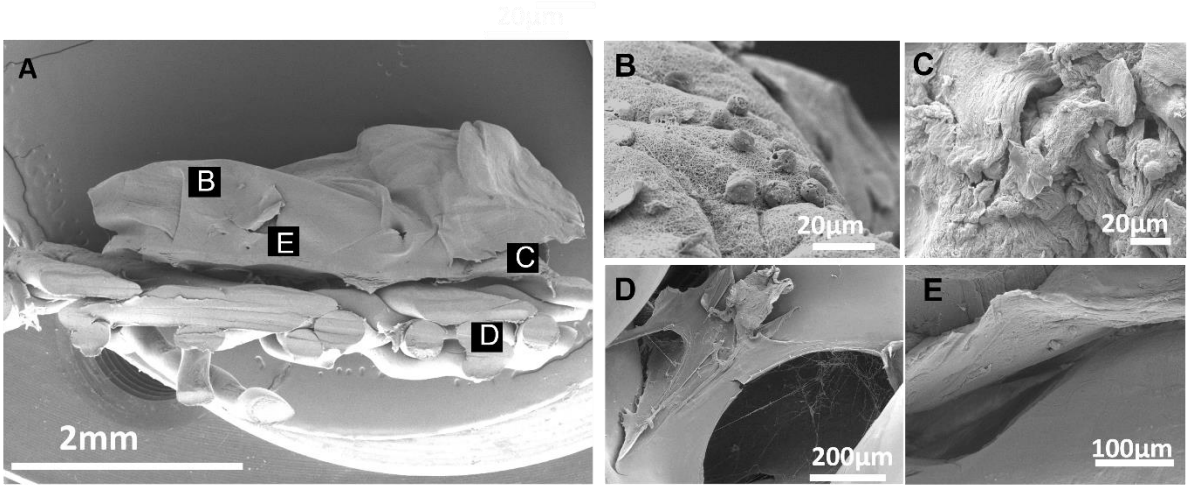

Figure 6.49: Morphological analysis of the obtained construct at day 21 in healthy conditions: total construct (**A**); zoom on different part of the construct: SL (**B**), ML-DL interface (**C**), SB (**D**), SL-ML interface (**E**).

Compared to healthy conditions (**Figure 6.49**), in OA conditions differences were observed in cells morphology: especially on the SL, where cells appeared not adhering to the membrane, but, as well, with a peculiar shape, not perfectly rounded. Also, the presence of apoptotic bodies can be observed (red arrows) (**Figure 6.49C**).

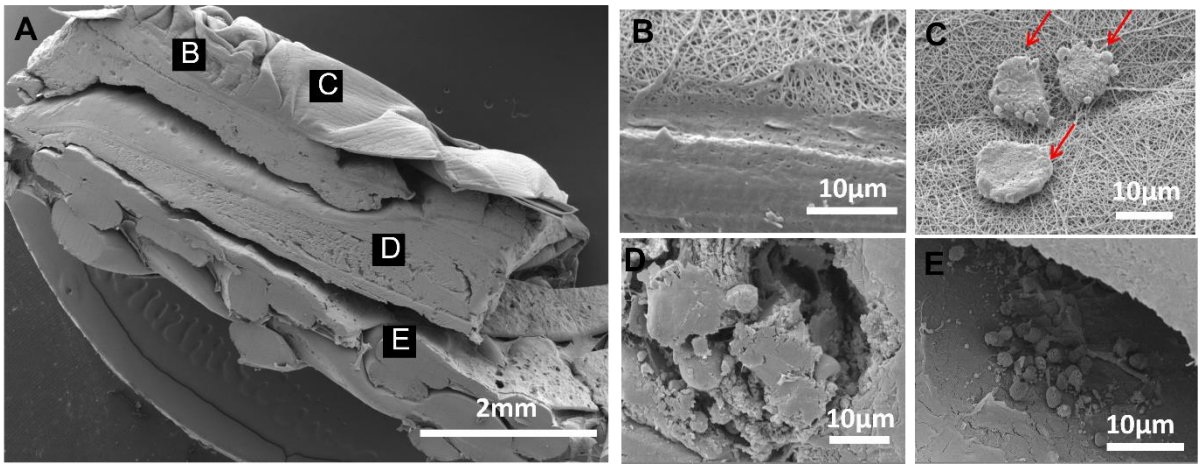

Figure 6.50: Morphological analysis of the obtained construct at day 21 in OA conditions: total construct (**A**); zoom on different part of the construct: SL-ML interface (**B**), SL – red arrows pointing at the apoptotic bodies (**C**), DL (**D**) and SB(**E**).

6.4 Discussion

The main goal of this chapter was to design and manufacture a zonal *in vitro* model of AC, that could mimic not only the ECM composition, but also gradient distribution of cells, their morphology and fate across the four distinct zone of the native tissue, from the superficial layer to the subchondral bone. The biological and functional evaluations were performed in healthy and pathological conditions, mimicking OA pathogenesis, by using the LC-OA *in vitro* model optimised in *Chapter 4*.

6.4.1 Manufacturing and characterisation of AC zones

According to the objectives of this chapter, firstly biomaterials, cells and manufacturing techniques were selected for each layer.

The SB was included in this model due to its influence on AC bio-mechanical properties and biological factors in healthy conditions and during OA pathogenesis; it was manufactured by FDM of PLA, considering the typical organisation of the trabecular bone (**Figure 6.10**) (Guangyi. et al., 2013; Frisbie et al., 2003; Steadman et al., 2010). Since PLA, which has already been widely exploited for bone repair, lacks bioactivity and functional groups, it was functionalised with GEL, to promote cell adhesion (thanks to the presence of RGD motifs,

making it highly effective for cell adhesion) and with nHA, to improve its bioactivity (Wu et al., 2011; Kim et al., 2015; Rodrigues et al., 2016; Gregor et al., 2017; Grémare et al., 2018; Donate et al., 2020). This functionalisation did not influence the overall structure and morphology of the scaffold in terms of fibres diameter and total porosity. However, a slight difference was observed in the morphology of the fibres, with the appearance of nanostructures homogenously spread onto the scaffold, which is desirable for cells adhesion and to stimulate their proliferation (Gregor et al., 2017). Also, the pores diameter was in the range 100-250 µm, which made it ideal as a biomimetic scaffold for bone TE, where the recommended pore size is in the range 100-350 µm (Whang et al., 1999) (**Figure 6.11**). Cytocompatibility studies confirmed the biomaterials' ability to sustain and promote Y201s cells viability and proliferation within 21 days of culture, onto PLA/GEL and PLA/GEL/nHA scaffolds (**Figure 6.12**). Particularly, cells showed a great adhesion onto the PLA/GEL/nHA scaffolds, as highlighted from the SEM and immunostaining images (**Figure 6.13**). Furthermore, PLA/GEL/nHA showed higher biomimicry capability to promote Y201s osteogenic commitment, compared to PLA/GEL without nHA. This was highlighted by the increased expression of RUNX2 protein, which has a central role in controlling the expression of osteogenesis-related genes such as ALP, OPN, COL1A2, OC, and ON (Xu et al., 2015; Stein et al., 2004). Also, compared to PLA/GEL, where ALP expression decreased after 7 days, PLA/GEL/nHA scaffolds sustained ALP expression for up to 14 days boosting the cells mineralisation potential, which was consistent with previous research (Hab et al., 2015; Matsumoto et al., 2011; Pierantozzi et al., 2020). Indeed, PLA/GEL/nHA showed an increased Y201 mineralisation over culture, compared to PLA/GEL, at each time point, by Alizarin Red analysis, in line with previous works (Kim et al., 2013) (**Figure 6.16**). Similarly, cells on PLA/GEL/nHA had increased ON expression in terms of gene (*sparc*) and protein levels (by western blot and immunofluorescence), indicating the ability of the functionalised scaffold to aid bone formation (**Figure 6.14** & **Figure 6.15**). Given the ability of PLA/GEL/nHA samples to show higher levels of osteoblast-related markers than PLA/GEL, the nHA functionalised scaffold was chosen for further investigations.

Regarding the DL, which is characterised by the highest amount of PGs and mechanical performances, two different hydrogels formulations were selected and combined for its manufacturing: CSDP and GG3 (Sharma et al., 2007). CSDP hydrogel was selected for its biomimetic ability, being CS a GAG naturally found in AC (Shin et al., 2021b). and catechol motifs of DP exhibit adhesive capabilities in acidic conditions, resulting in surface coating,

whereas basic pH enhances its cohesive properties, resulting in the production of hydrogels (Saiz-Poseu et al., 2019). Two CSDP concentration were studied prior to the DL manufacturing: CSDP10 and CSDP20. Upon the addition of the $NaIO_4$, the crosslinking salt, the sol/gel transition lasted less than a minute: CSDP10 in 50-60 seconds and CSDP20 in less than 30 seconds. This was the result of the selected $NaIO_4$/Catechol stoichiometric ratio, which was 1.5, compared to a ratio of 1, which led to a complete gelation happens in 10 minutes, which is quite slow for cells encapsulation, and compared to a ratio of 2, which led to an immediate gelation, which was too fast for the hydrogels handling (Scalzone et al., 2019b). Both compositions showed a good porosity and interconnected structure, essential for the nutrient transport, and a hydrophilic nature, with the ability to hold water molecules, remaining stable up to 48 hours (Karoyo & Wilson, 2021). Both the CSDP formulations exhibit a Young's modulus value < 10 kPa, which while being a good value for promoting MSC chondrogenesis *in vitro* (usually in the range 0.5 – 4.0 kPa), but lower than the native AC tissue compressive Young's modulus, which is in the range 100–1000 kPa (**Figure 6.9**) (Kelly et al., 2013; Scalzone et al., 2019b). On the other side, according to several literature works, constructs with a compressive modulus with values ranging from 10 to 40 kPa would be ideal for AC *in vitro* mimicking (Zand-Rajabi & Madadlou, 2016b). Given these considerations, to associate the biomimicry of CS-based hydrogel with enhanced mechanical properties and structure integrity, fundamental for AC DL, CSDP was combined with GG. GG was chemically modified by adding methacrylic groups within the GG polymer chains, as demonstrated from FTIR, hNMR and XPS analysis (**Figure 6.2** & **Tables 6.5-6.6**), to obtain a photo-curable hydrogel, able to be chemically cross-linkable exposing it to UV light and ionically cross-linkable with the addition of divalent cations (present in DMEM/F12 media: $CaCl_2$, $MgSO_4$, Na_2HPO_4, KCl) in physiological conditions (Daniela F Coutinho et al., 2010). GG3 was selected as hydrogel for manufacturing the DL, since it was the one, amongst the three formulations analysed (GG2, GG2-MH and GG3), showing the highest mechanical performances, with a Young's modulus of 31.4 ± 4.2 kPa, which was three-fold higher compared to the ones obtained for CSDP20 and 6-fold higher compared to CSDP10, falling within the range of AC tissue constructs (Kerin et al., 1998). Also, when exposed to unconfined compressed load, GG3 hydrogels-maintained stability up to ~60% strain, showing a good elasticity (**Figure 6.6**). This characteristic was confirmed by rheological analysis, where GG3 showed high stretchability, with a strain value at the yield point of ~25 % (**Figure 6.7**). GG3 was able to gellify in 5 minutes, when only exposed to UV, while its gelation sped up to 3 minutes by combining ionic and photo- crosslinking, which allowed to boost double helix

formation and the creation of junction zones, resulting in the construction of larger crosslinked networks (Wang et al., 2009; Oliveira et al., 2011). GG3 showed high hydrophilicity by water uptake analysis (**Figure 6.4**) and good and interconnected porosity, with a pore size mainly in the range 100-300 µm, optimal for nutrient exchange and cells migration (**Figure 6.5**) (Annabi et al., 2010). GG3 and CSDP were combined to form a multi-channelled structure, like the native DL, via soft lithography technique (Bader & Lee, 2000): the structural integrity and mechanical support was given by the GG3, while the biomimicry was provided by the CSDP, which was seeded together with Y201-C, within the GG3 channels (**Figure 6.19**). However, since the time for seeding all the channels of GG3, CSDP was chosen at a concentration of 15 % (CSDP15) because it was offering the ideal timing for injecting the CSDP15 without having the spreading of the CSDP solution within the whole structure. Y201-C showed good viability, up to 7 days, but they also maintained their typical rounded shape (**Figure 6.21**), and their organisation within the channels of the GG3 (**Figure 6.20**). Indeed Y201-C were distributed alongside the channel's depth, and few of them appeared to be migrating towards the GG3 construct, probably due to the porosity of the GG3. However, it is worth noticing that, after the injection of CSDP15 with Y201-C within the GG3 channels, due to its swelling properties of the CSDP, it slightly overflowed from the channel and that could be the reason why few cells can be observed on the surface of the construct.

For the ML, which is characterised by rounded cells dispersed in a homogenous matrix mainly composed of Coll II and ACAN, it was selected the bioprinting technology, via extrusion-based bioprinting, which allows to obtain cell-laden stable and complex constructs, in an easy, economic, and fast way, with a wide range of materials (Scalzone et al., 2021b). GG2 and GG2-MH were selected for this zone of AC, since these were the formulation able to be extruded (**Figure 6.25**). MH-enrichment showed a favourable influence on the GG2 hydrogel viscoelastic qualities, printability, and Y201-C's chondrogenic potential. Apart from being widely exploited in literature for its antibacterial properties, due to the presence of methylglyoxal (MGO, or Unique Manuka Factor), MH was also found to increase the mechanical properties of hydrogels (Bonifacio et al., 2018). Indeed, the selected concentration of 5% w/v, which was the one offering modest inhibition against several pathogenic bacteria, was the lowest concentration capable of affecting the formulation viscosity for the printability, due to the intrinsic viscosity of the MH itself (Lusby et al., 2005). Indeed, GG2-MH bioink demonstrated a greater printability compared to GG2, by displaying: *(i)* a spreading ratio (SR) of 3.5,

compared to 6.3 of GG2, more proximal to the ideal SR of 1, ideal for having high precision (Schwab et al., 2020); *(ii)* the extrusion of a fibre-like filament two times longer than the drop-like filament produced in the absence of MH. This behaviour might be explained by the inclusion of MH to the GG2 formulation, which improves shear-thinning performance and helps to preserve the filament shape during the bioink extrusion (**Figure 6.26**) (Highley et al., 2015). Furthermore, after one day in cell culture media, no delamination was noticed, indicating that the printed layers adhered well and that the 3D bioprinted constructs were stable in physiological conditions, for GG2 and GG2-MH. Both formulations displayed good hydrophilicity, but, due to the presence of hydrophobic component in MH, GG2-MH formulation absorbed three times less water (1800 ± 20% GG2 vs 500 ± 60% GG2-MH) (**Figure 6.4**) (Maddocks et al., 2013). Regarding the mechanical properties, it was measured a Young's Modulus of ~ 25 kPa for both formulations, ideal for simulating the AC ML (Zhu et al., 2018), but GG2-MH showed increased flexibility and elasticity, by exhibiting stability up to 50 % strain compared to bare GG2 samples, which broke at 30 % strain (**Figure 6.6**) (Abd El-Malek et al., 2017). Rheology supported this trend, by obtaining a strain value at the yield point of 10.5 ± 0.21 % for GG2-MH, compared to 8.0 ± 0.3 % for GG2. In addition, the apparent viscosity, which is a measurement of the fluid's internal resistance to flow, and the G* values of GG2-MH were greater than that of GG2 (**Figure 6.7**). These findings supported Manuka Honey's favourable influence on the GG2-MH hydrogel composition's viscoelastic qualities. GG2 and GG2-MH showed porous interconnected structure, with a pore size in the range 50-250 µm, slightly smaller compared to GG3. However, GG2-MH hydrogel had a more heterogeneous pores size, with a diameter range 78 - 200 µm (**Figure 6.5**). Indeed, while Y201-C viability and metabolic activity, in both bioprinted constructs, was high over 7 days of culture, cells distribution was different (**Figure 6.27**). After 7 days, GG2 hydrogel showed a homogenous distribution of Y201-C, while GG2-MH showed an heterogenous cells distribution, with a tendency to agglomerate and form clusters (**Figure 6.28**). This phenomenon could be related to the heterogeneity of pore sizes and, therefore, the migration of cells could be enhanced where pore sizes in between 50 – 200 µm and limited where the pores are smaller (Nava et al., 2016). Cells tendency to agglomerate was observed, as well, over an extended period of culture: H&E and Picrosirius Red histological analysis on cryosections at day 21 showed the same feature. In addition, Y201-C appeared to produce a higher amount of collagen and GAGs and to have an increased expression of chondrogenic markers (*sox9, col2a1, acan*) in GG2-MH samples, compared to GG2 (**Figure 6.30-6.32**). This behaviour could be associated with the

cells attitude to enhance their chondrogenesis when in close contact, as demonstrated in *Chapter 4* (Zuliani et al., 2018; de Moor et al., 2020; Scalzone, Wang, et al., 2022).

The SL, which is fundamental for the overall functional integrity and protection of the osteochondral tissue (Saarakkala et al., 2004; Wise et al., 2009; Brehm et al., 2006) was manufactured via electrospinning of PCL/GEL aligned nanofibers membrane, since cells in this layer are organised alongside the Coll II fibres, which are in a densely packed in a fashion parallel to the AC surface (Bader & Lee, 2000). Even if PCL was found to be promoting MSCs chondrogenesis in previous studies, herein it was used a blend of PCL and GEL to obtained higher biological performance, stimulating cells adhesion (Owida et al., 2018). Compared to PCL/GEL-Random, PCL/GEL-Aligned showed the orientation of the electrospun fiber in a unique direction (**Figure 6.35**), which was fundamental for inducing cells orientation in a preferential direction, already after 3 days of culture (**Figure 6.36**). After 7 days of culture, cells appeared elongated and packed alongside the fibres (**Figure 6.37**). On the contrary, cells appeared randomly organised onto PCL/GEL-Random membranes (**Figure 6.37**). Both membranes showed good cytocompatibility and supported cells proliferation, as highlighted by the intense staining of Ki-67 proliferation marker (**Figure 6.37**) and metabolic activity after 7 days (Garrigues et al., 2014) (**Figure 6.38**).

6.4.2 Assessment of OA features within the zonal model

The pathological features of cells were analysed within each layer since cells in different zones of AC behave differently during OA pathogenesis. Particularly cells anabolic and catabolic activity was evaluated in terms of gene expression and ECM production.

During OA on-set, joint inflammation results in the progress of osteoclastogenesis in the bone-side. Indeed, by the action of the cytokines, Y201s increased the protein expression of RANKL in SB, involved in osteoclast recruitment and function, by promoting resorption activity and, therefore, mimicking the remodelling rate that depicts osteoarthritic SB, especially in the early stages of the disease (Xu & Teitelbaum, 2013; Findlay & Atkins, 2014). Also, gene expression of *vegfa* was downregulated at day 7 in SB-P condition, compared to SB-H, while it shows the opposite tendency at 21 days. In this regard, the developed SB appears to mimic the stages of OA, with an initial phase of rebuild capacity (day 7) and a late phase of vascularisation (day 21), which is a typical event of OA progression and spreading towards the AC (Yuan et al., 2014; Hamilton et al., 2016). Furthermore, the role of pro-inflammatory cytokines to inhibit

Y201s osteogenesis was confirmed by the repression of *Runx2* expression, and the downstream osteogenic marker *CollIa2* and *spp1*, in SB-P, compared to SB-H (**Figure 6.17**) (Gilbert et al., 2002; Kaneki et al., 2006). On the contrary, Alizarin Red staining and quantification showed a considerable increase in calcium accumulation in the diseased environment at day 21, compared to healthy one. This inconsistency with the *Runx2* downregulation was related to the double actions of cytokines, which can prolong mineralisation by inhibiting PPAR activity and so operating independently of the *Runx2* pathway (Lencel et al., 2011). Mineralization, on the other hand, requires more exploration since it might be linked to both the thickening of the AC-SB interface and the absence of remodelling activity (**Figure 6.18**).

Moving towards the AC side, the different zones of AC showed different behaviour during the 21 of exposure to cytokines. The main element of the DL ECM is ACAN, which is responsible for compressive load resistance because of the osmotic property of its GAGs (Sandy et al., 1992; Kiani et al., 2002). In the manufactured DL-P, ACAN production and GAGs synthesis were altered by the inflamed environment, compared to DL-H conditions, because of the influence of released aggrecanases (ADAMTS and MMPs) (**Figure 6.22**). Consequently, the mechanical properties of the DL changed during OA on-set, as demonstrated by stress-relaxation analyses: DL-P stress-relaxation curve exhibited a collapse, without reaching the equilibrium, demonstrating the loss of the construct viscoelastic properties over 14 days of culture. This behaviour is related to the degradation of the matrix following the increase in the catabolic activity of the cells (Stannus et al., 2010). Indeed, viscoelastic properties of the obtained DL are highly affected by the OA-induced environment, due to the breakage of the internal network which, in turn, deteriorates the mechanical properties of the tissue (**Figure 6.23**) (Mieloch et al., n.d.). On the contrary in healthy conditions at 14 days, samples showed a decreased relaxation time compared to day 1, probably due to an increased permeability, which allows fluid to flow in-out of the cartilage matrix more easily and rapidly, resulting in a lower-stress relaxation time, as well as a 4-fold increase in the equilibrium modulus, defined as the stiffness of the gel as all the fluids flows out, compared to day 1 (Kumar et al., 2018). Another key process in OA development in the DL, which disturbs AC homeostasis, is the hypertrophy of chondrocyte together with their tendency to apoptosis, at a more advanced stage of the disease. Coll X, which is required for AC replacement by mineralisation, was found in the DL-P, while it was absent in the DL-H (Dreier, 2010; Bian, Zhai, Mauck, et al., 2011)

(**Figure 6.22**). Also, Y201-C morphology appeared different in DL-H and DL-P: cells appeared slightly elongated and oriented in a specific direction, which theoretically is the direction of the collagen fibers in the native tissue, in the DL-H, while these appeared more polygonal in OA conditions (**Figure 6.24**) (Camarero-Espinosa et al., 2016a; Camarero-Espinosa et al., 2016b).

From the analysis of ML, with both with GG2 and GG2-MH, a great difference was observed in ECM production, gene expression and cells integrity in healthy (ML-H) and pathological (ML-P) conditions. Regarding the matrix production, ML-H presented much more intense histological staining of Picro Sirius Red, Alcian blue, as well as HIC staining of ACAN and Coll II on tissue sections, compared to ML-P. In fact, the loss of the staining of ECM component can be attributed to ECM degradation by collagenases and aggrecanases during OA (**Figure 6.30** & **Figure 6.33**) (Huang & Wu, 2008; Nagase & Kashiwagi, 2003). Also, the concentration of GAGs was lower in ML-P tissue (**Figure 6.31**). Regarding cells behaviour, the lower number of chondrocytes or their presence with a cell membrane "ghost" and with nucleus lacking basophilic staining, is associated with their death. Indeed, a typical feature of apoptosis is the fragmentation of chondrocyte nuclei, which can also be observed, especially from Picrosirius Red staining and H&E staining (Pritzker et al., 2006). A greater cells nuclei integrity and higher number of cells was observed in ML-H conditions (**Figure 6.30**). Also, gene expression analysis revealed that Y201-C present a higher fold change of anabolic genes (*sox9, acan, col2a1*) in ML-H, compared to ML-P, at day 21. This tendency was reversed for the catabolic genes (*mmp13* and *adamts-5*), as expected. Also, GG2-MH showed an increased *col2a1* and a*can* expression, compared to GG2, proving that the GG2-MH composition favoured ECM protein synthesis and therefore was selected for the manufacturing of the *in vitro* zonal model (**Figure 6.32**).

The SL is the first layer undergoing degeneration during OA. From histological analysis (**Figure 6.39**) and SEM (**Figure 6.43**), it can be observed a difference in cells organisation at day 21: while in SL-H samples chondrocytes appear flattened and forming a cell-sheet onto the membrane, in SL-P cells appeared agglomerated, rounded, and partially detached from the membrane. Integrin dysfunction has been linked to OA pathogenesis, as highlighted in previous research, and the activation or increase of integrin expression is linked to the control of chondrocyte adhesion, since integrins play a key role in cell-to-cell/cell-to-ECM attachment (Jin et al., 2021; Loeser, 2014). It is interesting to note in SL-P, compared to SL-H, how, not

only the cells sheet appeared fragmented, but even the electrospun membrane underneath was broken (**Figure 6.39**). This result could be explained considering that the membrane is made of GEL, which derives from collagen, and the release of collagenases during OA could be the responsible of its degradation (Billinghurst et al., 1997). In fact, gene expression analysis shows a ~30-fold increase of MMP13 at day 21 in SL-P, compared to ~2-fold in SL-H. Coll II is the main element of this layer and the main one undergoing degeneration during OA on-set. As a result of ECM degradation, the level of Coll II drastically decreased in SL-P, as highlighted in the lower intensity of the staining in IHC and Immunofluorescence, compared to SL-H (**Figure 6.41-6.42**). Also, *col2a1* expression followed the same trend (**Figure 6.40**). As expected, the concentration of GAGs (stained with Alcian blue) was low in the superficial layer of AC, in fact its permeability in this layer is higher than that in the other parts of the AC cartilage (Yang et al., 2017) (**Figure 6.39**). However, not only *acan* expression was quite elevated in SL-H and in SL-P (**Figure 6.40**), but ACAN IHC staining showed high intensity at 21 days for SL-H, and slightly lower for SL-P (**Figure 6.41**). This result is in line with other studies which showed that PCL-based fibrous scaffolds supported MSCs chondrogenic differentiation and the production of a proteoglycan-rich ECM, due to the increase in cells proliferation over the 21 days of culture (Feng et al., 2020; Fu et al., 2016). Another element of AC superficial layer is Coll I, which is only present in this layer and, therefore, analysed in here. Coll I is also secreted by de-differentiated chondrocytes in monolayer culture. The ratio of Coll II/Coll I is an excellent indication of chondrocyte differentiation, as well as an excellent indicator of OA progression (Owida et al., 2018; Marlovits et al., 2004). In both SL-H and SL-P there was a very low expression of *col1a2* (< 1-fold with respect to day 1), thus the higher COL2A1/COL1A2 ratio present in SL-H, compared to SL-P, was dictated by the higher expression of *col2a1* rather than *col1a2.* This result is in contrast with the study of Owida et al., who found in their manufactured model of AC high expression of *col1a2* in the superficial layer of AC, due to cells loss of phenotype; however, it should be considered the high number of cells used to emulate the SL and great Y201-C propensity towards the chondrocytes phenotype.

6.4.3 Evaluation of the whole zonal construct

In line with the third objective of this thesis, the zonal model was manufactured by combining the fabrication methods to obtain a hybrid zonal AC construct of 6 x 6 x 6 mm size, which appeared to provide the appropriate zone-specific features, mimicking the microstructural organization of AC ECM and cells, and inducing ECM production. This was the first study in

which it was possible to faithfully respect cells organisation and morphology within the construct, and this was possible thanks to the appropriate selection of fabrication techniques.

The optimised manufacturing process did not affect cells viability, which showed good viability at 24 h and stable metabolic activity over 7 days of culture (**Figure 6.45**). Immunostaining analysis of cells nuclei and cytoskeleton, indeed, showed the presence of elongated Y201-C in the SL, alongside Coll II fibres, rounded and random Y201-C in the ML and Y201-C packed in GG3 columns within the DL, as in the native tissue (**Figure 6.46**) (Buckwalter & Mankin, 1997). However, from the histological analysis at 21 days of culture (**Figure 6.47**), it was noticed cells re-distribution inside the structure, and it was hard to distinguish between the different zones. SL maintained its integrity and cells appeared to be migrating from the DL to the SL. A similar result was obtained by Gegg et al, who found an increase in the cell density in the aligned superficial layer of *in vitro* AC (Gegg & Yang, 2020). Collagen content was the highest in the SL and decreases with depth, while the proteoglycan content, which should be lower in the SL and higher in the DL, appeared higher in the SL/ML, compared to DL (Helen, 1978). However, this could be explained by the cell's migration phenomena towards the SL and, therefore, the deposition of matrix in that zone as a result of cellular condensation (Raghothaman et al., 2014).

In pathological condition, a completely different scenario was found and the typical features of OA were observed:

- fragmented cell nuclei from the H&E staining, sign of dead cells, whereas living cells are characterized by ellipsoidal to round shape (Elmore, 2007b): lots of cells appeared with fragmented nuclei, especially in the DL, which could be associated to the contribution of SB in the on-set of OA disease, and in the SL, which was expected since apoptotic cells are typically located near the articular surface at early stage OA (as noticed in **Figure 6.50**) (McIlwraith et al., 2010);
- cells clusters (complex chondron), especially in the SL and ML;
- fibrillation, which was restricted at the superficial layer (Hauselmann et al., 1996);
- focal cells loss: increasing areas that are devoid of chondrocytes to a point where few cells remain;
- loss of histological staining, especially for GAGs, due to the matrix destruction, which is expected to be the first element of AC to be destroyed, as reported in *section 2.3.4*.

In conclusion, by regulating the spatial environment through the depth of the engineered tissue, it was possible to engineer AC constructs with zonal compositions mimicking the main features of AC in healthy condition and during the progression of AC. Future in-depth studies could be performed to study the mechanical properties of each layer (compressive and tensile) and the way these change when the single layers are combined in the zonal model. Also, the mechanical properties of the whole construct in healthy condition and in pathological condition should be analysed, to evaluate the effect of matrix degradation on the tissue biomechanics. The obtained zonal model closely resembled the main early OA characteristics: cells hyperproliferation, clusterization and detachment from the SL, cells tendency to hypertrophy in the DL and cells propensity to osteoclastogenesis in the SB. Also, in all the layers there was a decrease in the expression of gene or protein usually present in healthy AC, such as aggrecan and Coll II, in parallel to an increase in the expression of catabolic markers, such as *mmp13* and *adamts-5*. The production and release of proteins or molecules from each zone could be studied via proteomic analysis. Hence the optimised *in vitro* zonal model represents a potential useful testing platform for analysing regenerative therapeutic treatments. Additional studies on the possibility of implementing this model within a dynamic system, such as a mechanical stimulation bioreactor system would give more biomimeticity and functionality to the obtained platform.

Chapter 7. Overall discussion and conclusions

In the last decade the clinical and socioeconomic demand of reliable, reproducible, and predictive models of OA has increased, both for studying the main features characterising the disease pathophysiology from early stage, and to identify novel and effective therapeutic treatments (Bartolotti et al., 2021; Craig I. Johnson et al., 2016). Therefore, the rationale behind this PhD research was to develop AC models in the healthy and pathological states, based on the hypothesis that the more the manufactured model is similar to the native tissue in terms of cells organisation, behaviour and matrix composition and structure, the more the model acquires validity. As a first goal it was developed a scaffold-free model of AC, which showed to be a reliable *in vitro* model to study the AC tissue in healthy and OA conditions. Also, this platform was used to validate the use of a bankable cell type, the Y201-C, as an alternative to primary chondrocytes and to successfully test the effectiveness of novel miRNA 140-based therapeutic treatments. Having identified the Y201-C as a promising cell source for AC *in vitro* studies and the cytokines cocktail-induced OA model, as reliable modality to assess the main features of OA, a zonal model of AC in healthy and pathological state was manufactured as second aim of this PhD work.

7.1 Main findings and novelties of this PhD Thesis

Considering the main objectives of this thesis, herein are reported the main findings and novelties obtained from the experimental work performed, which could be source of inspiration for future in-depth studies.

- The obtained scaffold-free *in vitro* optimised spheroids-based model technology, inspired from the clinically approved Chondrosphere®, demonstrated its suitability for the obtainment of a reliable and predictive validation model to be used for clinical translation of *in vitro* models, by using both primary chondrocytes and Y201-C, a bankable cell type. Both cells allowed to the obtainment of a standardizable production of spheroids with predictable size and geometry, which is a fundamental point for the translational potential of this technique (Korneva et al., 2017). Indeed, even if spheroids and micro masses culture were widely explored for AC tissue engineering, the novelty of this work was the combination of several spheroids in the so-called “chondrospheres” to obtain a few mm thick construct, to overcome the limitation of actual spheroids-based model of AC which led to the obtainment of tissues less than 500 µm in size (Kim et al., 2020; Foty

& Steinberg, 2005). When cultured in spheroids, both cells showed high viability as well as high expression of chondrogenic markers (*sox9, col2a1, acan*) and AC ECM production (GAGs). This was due to the cells exposure to physical interactions that more closely reflect behaviour in 3D native tissue and spheroids retain their endogenous ECM, which has instructive potential to promote physiologically accurate connections with their environment, prolong cell survival, and avoids cells de-differentiation (Anderer & Libera, 2002) (*Chapter 4*).

- The optimised *in vitro* cytokine-based OA induction model, tested within the scaffold-free construct, was suitable to observe and study the key events of OA, named cells hyper-proliferation, tendence to hypertrophy and apoptosis, catabolic activity increase over the anabolic one and ECM degradation. For the first time, it was used a cocktail of cytokines, IL-1ß, IL-6 and TNF-α, which showed a synergic effect in altering the environment in which the cells were cultured. Compared to other techniques examined in literature for the obtainment of an OA *in* vitro model, the use of cytokines allowed for the induction of OA-like cell and tissue responses that more closely resemble the native disease at early stage, particularly taking in consideration the importance of synovium-related inflammation effects in the model design, which results in the release of pro-inflammatory mediators (Craig I. Johnson et al., 2016). Even using a low concentration of cytokines (in accordance with values present in human synovium during OA progression), it was possible to observe the main features of OA and, therefore, the concentrations used in LC-OA, were the exploited in the following part of this PhD research (*Chapter 4*).
- Y201-C bankable cell type, demonstrate to be a suitable candidate to produce an engineered reliable AC-like construct, for studying the progression of OA with future insight into treatment strategies. The results obtained for Y201-C and HC were comparable in terms of spheroids formation, cells viability, gene expression and AC ECM production. However, the use of Y201-C allows to obtain reliable models of AC in healthy and OA conditions at lower-cost, higher reproducibility, with higher number of cells available, faster time for producing it, compared to HC, which present the issue of limited availability of donor sites and low yield of isolated cells from autologous tissue (1–5% of the total tissue volume) (Somoza et al., 2014). Therefore Y201-C were selected for the manufacturing and analysis of the *in* vitro zonal model (*Chapter 4*).

- The use of magnetic field-bioreactor exerted an effect on Y201-C, resulting in increased expression of *col2a1* and *mmp13* after 21 days, suggested that the mechanical stimulation with magnetic particles, via shear stress, is influencing cell fate. The inclusion of *in vitro* mechanical stimulation provided by bioreactors in *in vitro* models is a growing modality, since cells can sense and transform external mechanical stimuli into biochemical signalling pathways, that can impact cellular events such as ECM production and cell differentiation. However, this was the first study combining magnetic particles with OA *in vitro* model. Since Coll II is known to resist shear and tensile forces, it was hypothesized that imparting a shear stress to an engineered construct would result in the increased deposition of this protein (Gemmiti & Guldberg, 2009b). However, on the contrary, the typical behaviour of chondrocytes in damaged cartilage at early stage was observed: initial proliferation and increased metabolic activity, enhancing the synthesis of matrix molecules but also contributing to their own destruction by synthesising proinflammatory cytokines, including interleukin, and tissue-destructive enzymes such as matrix MMPs and ADAMTS. This result could be due to, for example, to an inadequate activation of mechanoreceptors such as stretch-activated ion channels or integrins (*Chapter 5*).
- MiRNA-loaded chitosan polyplexes showed to efficiently carry nucleic acids into primary chondrocytes and promote expression of anabolic markers *in vitro,* after only 10 days of culture. At the optimised concentration of chitosan, not only it was possible to obtain an optimal cellular uptake, compared to naked miRNA-140 or to lower concentration, even if exhibiting a positive charge, but even a therapeutic effect on chondrocytes. This result could be associated with the ability of miRNA-140 to inhibit the effect of interleukins, as well as, to rescue the IL-1β repression of *acan* and *col2a1* expression (Ghafouri-Fard et al., 2021). Therefore chitosan-based polyplexes demonstrated to be optimal therapeutic carriers (*Chapter 5*).
- The zonal model obtained by designing, manufacturing, and optimising a four-zone *in vitro* osteochondral zonal model, faithfully reproduced the hierarchical structure of the native tissue, by combining multiple strategies: different manufacturing techniques, selection of multiple materials and two cell types, variation of the cells number. The multi-layered scaffold was comprised of four different compartments with dissimilar architectures, based on the anatomical microstructure of AC. The obtained design achieved the purpose of mimicking the zonal structure of AC and, from the analysis of the single zone of AC, the organization of cells and the biomaterials selected for each single layer, appeared to

regulate cells phenotype and their ECM production, when the layers were singularly studied. For example, within the SL, it was observed that the aligned nanofibres of the electrospun membrane resulted in elongated chondrocyte morphology and increased proliferation over 7 days of culture; the resulting chondrocytes produced Coll I, in addition to Coll II, main element of this layer, which, indeed, is associated with a fibroblast-like phenotype, typical of AC SL (Wise et al., 2009). By contrast, the use of hydrogels in the ML and DL led to a different cell organisation and behaviour. Bioprinting technique allowed to obtain a homogenous cells distribution within the ML; however, over culture, within the MH-loaded GG2 hydrogel, chondrocytes exhibited a rounded morphology and migrated and clustered in small groups, which allowed higher Coll II and Aggrecan production, main elements of this layer, when compared to GG2 hydrogel without MH. For the DL, instead, the use of soft-lithography and the combination of GG3 and CSDP allowed to obtain chondrocytes rounded organised in channelled structure in a GAGs-rich highly hydrated hydrogel, which is the main feature of the deep zone of AC. Also, the selection of decreasing cells number (from 14 million cells/mL in the SL to 3.5 million cells/mL in the DL) and the increase in mechanical properties (from ~24 kPa in ML and ~34 in the DL) over the depth of the biomimetic AC, aided the production of AC-specific protein (Coll II and Aggrecan) in healthy state, within each layer. On the other side, the functionalisation of SB with GEL and nHA, allowed not only cells adhesion, but even induced higher production of bone-like tissue and expression of bone markers, compared to bare the absence of nHA (*Chapter 6*).

- In this thesis it was presented for the first time a study of the zonal features of OA. Indeed, the manufactured model allowed to see the changes in each single zone of the osteochondral tissue during OA pathogenesis. In this regard, chondrocytes cultured in the DL showed the typical tendency to produce more Coll X and less Aggrecan, compared to healthy condition, since they undergo hypertrophic pathway during OA progression (Dreier, 2010). On the other side, chondrocytes in the superficial layer showed the typical features of clusterisation and detachment from the matrix, accompanied by a decreased synthesis of anabolic markers (especially *col2a1*). In the ML, cells mainly showed a decreased synthesis of matrix and an anomalous shape of nuclei and pericellular matrix, characterised by fragmentation. Also, in the obtained whole zonal model, the main early-stage OA characteristics were observed as well. Hence, the model was suitable for inducing the typical cells behaviour during OA on-set (*Chapter 6*).

- The combination of the layers in a zonal construct led to cells migration and their re-arrangement within the whole construct. The zonal model demonstrated to induce distinguished chondrocyte organisation and phenotype and matrix production within AC zones, compared to the layers singularly studied. One of the challenges of the previous studied multilayered scaffold was the discontinuity at the interface between layers, while the gradient of AC should be continuous, otherwise the interface could be subject to delamination under mechanical stress (Fu et al., 2020). Cells migration demonstrated that there was continuity between the different zones of the manufactured zonal model (*Chapter 6*).

7.2 Scaffold-free and zonal model: which one should be chosen?

The results obtained from this PhD work showed that, while both models demonstrated to be useful to study the disease progression, each model can have advantages or disadvantages, based on what is the purpose of their use.

Compared to the zonal model, which was manufactured by combining multiple fabrication techniques and two different cell types, the scaffold-free model was easier to manufacture, since it just required the presence of a membrane support in the second phase of spheroids culture, to aid the chondrospheres formation. Indeed, the zonal model required optimisation of each fabrication technique and, therefore, a change in a single material or manufacturing process, would require further optimisation. Consequently, the scaffold-free model was a more practical model for studying the effect of cytokines to induce OA or the effect of possible therapeutic compounds, as demonstrated in *Chapter 4* and *5*. In addition, taking inspiration from the Spherox™ clinically approved technique, the scaffold-free model was used as a validation model for the zonal model and then, it could be very useful for further validate other models, in a reliable way.

On the other side, the zonal model was more useful to comprehend at the microscale how cells behave in the different layers during OA, considering that the disease is affecting each layer (in terms of matrix degradation and cells fate) differently. For example, the SL is recognised to be the first layer affected by the disease and, in fact, it was observed a strong effect of cytokines on that zone of AC, even if at a low concentration. Also, it was observed that the DL is the one in which cells tend to become hypertrophic and undergo apoptosis during OA on-set, which feature is not present in other parts of the tissue. These zonal-specific characteristics couldn't be observed in the scaffold-free model, where it was difficult to

distinguish between the different zones of the tissue and consequently between different behaviour of cells. Therefore, the zonal model could be of greater interest to future studies on specific zonal targets, such as Coll X in the DL or PRG4 receptors in the SL. In addition, the zonal model with the presence of SB is a more reliable model of OA disease, compared to the scaffold-free model, in which only the cartilage layer features are studied. Indeed, the presence of cytokines inhibited the osteogenesis of Y201s seeded on the underlying bone. Thus, the SB-AC model would be useful to study the interference of SB to the AC pathogenesis during OA, which was already observed to play a crucial role in the initiation and progression of disease, due to vascularisation and inflammation.

In conclusion, I believe that the zonal model could be a great model to study the features of cells in the different layers of AC and SB during OA progression, as observed in the histological analysis of the zonal construct (*Chapter 6*), since the severity of disease is discriminate by evaluating the properties of each layer of the tissue. Also, the zonal model could be used to discover specific zonal target which could interrupt the disease pathogenesis and subsequently design novel pharmaceutical compound or functionalised targeted nanoparticles. On the other side, the scaffold-free model is a more suitable and practical model for testing OA treatments without a zonal specific target, in a reliable and predictive way, as observed for miRNA-based polyplexes. Also, it would be very useful for validating the efficacy of *in vitro* OA models.

7.3 Limitations and future perspectives

This thesis explored most of the literature uncertainties and open questions, especially about the manufacturing and optimisation of a reliable zonal model of OA. However, there are some limitations to address, which I would like to highlight to shed the light on, for possible future studies to be performed to improve the quality of this work.

Even if the mechanical properties of the obtained construct were similar or superior to other literature studies analysed, these were inferior to the native counterparts (Owida et al., 2018; Girão et al., 2018). However, as highlighted by Gegg et al., the analysis of mechanical properties after culturing the constructs for 21 days will accelerate the ECM production, as possible approaches to improve the mechanical properties of the constructs, before they become clinically useful products (Gegg & Yang, 2020). Therefore, a mechanical analysis of the obtained constructs after 21 days of culture could be useful to understand how the

biomechanical properties change as the new ECM is produced and re-arranged. Also, it could be interesting to explore the generation of the stiffness gradient which occurs in the zones of the construct over culture, to assess if the obtained model allows the recapitulation of the gradient observed over depth in the native AC (Dimaraki et al., 2021a).

Further research is also needed to evaluate more appropriate biomarkers and analysis techniques to study tissue models at a superior throughput. Some issues were experienced during this project, for example the difficulty to extract RNA and protein, as well as in the staining process, for the DL of AC, due to the negative influence of the CSDP crosslinking salt in the processing. Also, a deeper insight should be put on the behaviour of the SB in terms of mineralisation during the OA on-set.

In addition, more studies should be performed on the whole zonal model, to understand what happens in terms of cells behaviour within the single zones, after the culture as a zonal construct, such as immunohistochemistry, which would be appropriate to have a clearer idea on the matrix distribution in the zones.

The results obtained for the use of magnetically-stimulated microspheres as a vehicle to exert mechanical load within the zonal model of AC, indicated that follow-up studies are needed for optimising the amounts of particles added to the culture conditions, or the magnetic field gradient magnitudes, before observing beneficial effects. Also, it would be of great interest to evaluate the effect of the magnetic field on cells fate, without the addition of MS to the spheroids, since magnetic field has been successfully used for joint pathologies due to its beneficial effect on improving function in early OA and in limiting the inflammation spreading. Also, this technique was found to be the exploitation of co-cultures with macrophages was discovered to closely mimic the early stage of OA (Dikina et al., 2017). However, this work was performed during 3 months of placement at the end of the PhD, and therefore, it was not possible to repeat and optimise the study.

Furthermore, miRNA-140-based polyplexes showed great potential with primary chondrocytes, in terms of modulating gene expression analysis and reverse le effect of cytokines, the combination of a cocktail of miRNA, such as miRNA-27 or miRNA-146 able to target MMP13 and ADAMTS-5, or the combination of miRNA with other therapeutic compounds (anti-inflammatory molecules) in synergic manner could be beneficial for obtain higher efficacy.

Finally, since OA is a whole joint disease, the addition of macrophages would be a great value to obtain a more reliable *in vitro* model of the disease. Indeed, the exploitation of co-cultures with macrophages was discovered to closely mimic the early stage of OA.

Overall, the scaffold-free model, allowed to study and observe the main features of OA in a reliable and predictive model, and to validate the use of the bankable Y201-C. Consequently, it demonstrated to be valid for testing potential novel treatment modalities for proof-of-concept studies. However, the manufacturing and study of the zonal model of OA, not only allowed the obtainment of a construct which is more similar to the native environment, but it was possible to observe how the cells singularly behave in each layer and how important it is for having a reliable model, to reproduce all the environment which surround cells *in vivo*. This is of great importance to understand the utility of the models and of this study, in comparison to the literature up to now, in which a focus on just cells or just on the matrix was exploited.

Appendix: List of publication and congresses participation

- Peer reviewed publications

[1] **A Scalzone**, G Cerqueni, M A Bonifacio, M Pistillo, S cometa, M Mattioli-Belmonte, X N Wang, K Dalgarno, A M Ferreira, E De Giglio & P Gentile "Valuable effect of Manuka Honey in increasing the printability and chondrogenic potential of a naturally derived bioink", 2022, Materials Today Bio, 100287.

This publication is part of the work in Chapter 6, and regards the optimisation of the MH-loaded GGMA bioink, which was then used to manufacture the ML of the zonal model of AC.

[2] G Cerqueni, **A Scalzone**, C Licini, P Gentile & M Mattioli-Belmonte, "Insights into oxidative stress in bone tissue and novel challenges for biomaterials", 2021, Materials Science and Engineering: C, 112433

This review was written in collaboration with Universita' Politecnica delle Marche. It focuses on the mechanisms of oxidative stress generated by an implant and suitable ways for its modulation. The contribution of author of this Thesis is on the biomaterials part.

[3] **A Scalzone**, X N Wang, K Dalgarno, A M Ferreira, P Gentile, "A chondrosphere-based scaffold free approach to manufacture an in-vitro articular cartilage model", 2022, Tissue Engineering Part A

This publication is part of the work in Chapter 4 and regards the optimisation of the scaffold-free model in healthy conditions.

[4] **A Scalzone**, M A Bonifacio, S Cometa, F Cucinotta, E De Giglio, A M Ferreira, P Gentile, "pH-triggered adhesiveness and cohesiveness of chondroitin sulphate-catechol biopolymer for soft tissue regeneration", 2020, Frontiers in Bioengineering and Biotechnology, 8, 712

This publication is part of the work in Chapter 6 and regards the exploiting of CSDP hydrogel for its adhesive and cohesive properties, for soft tissue engineering. This hydrogel was used in this work for the DL of the zonal model of AC.

[5] R M Dewhurst, **A Scalzone**, J Buckley, C Mattu, K Rankin, P Gentile, A M Ferreira-Duarte "Biodegradable bone cement loaded with doxorubicin-based nanoparticles: In Vitro behavior of co-cultured osteosarcoma and mesenchymal stem cells", 2020, Frontiers in Bioengineering and Biotechnology, 8:754

This publication was performed together with a MRes student. The contribution of author of this Thesis is on the cellular tests.

[6] M A Bonifacio, A Cochis, S Cometa, P Gentile, **A Scalzone**, A C Scalia, L Rimondini, E De Giglio, "From the Sea to the Bee: Gellan gum-Honey-Diatom composite to deliver resveratrol for cartilage regeneration under oxidative stress conditions", 2020, Carbohydrate polymers, 245:116410.

This work was performed in collaboration with Politecnico di Bari. It focuses on the analysis of GG-MH hydrogels for AC regeneration. The contribution of author of this Thesis is on the characterisation of the gellan gum hydrogels physico-chemical properties.

[7] D Pierantozzi, **A Scalzone**, S Jindal, L Stīpniece, K Š Ancāne, K Dalgarno, P Gentile, E Mancuso, "Effect of structural design and material formulation on mechanical and biological performance of 3D printed composite scaffolds for bone tissue engineering", 2020, Composites Science and Technologies 191:108069.

This work was performed in collaboration with Ulster University. The contribution of author of this Thesis is on all the cellular study.

[8] M A Bonifacio, A Cochis, S Cometa, **A Scalzone**, P Gentile, G Procino, S Milano, A C Scalia, L Rimondini, E De Giglio, "Data on the influence of inorganic clays to improve mechanical and healing properties of antibacterial Gellan gum-Manuka honey hydrogels", 2020, Data in brief 28:105096

[9] M A Bonifacio, A Cochis, S Cometa, **A Scalzone**, P Gentile, G Procino, S Milano, A C Scalia, L Rimondini, E De Giglio, "Advances in cartilage repair: the influence of inorganic clays to improve mechanical and healing properties of antibacterial Gellan gum-Manuka honey hydrogels", 2019, Materials Science and Engineering C 28:105096.

The two above works were performed in collaboration with Politecnico di Bari. They focus on the analysis of clays-loaded GG-MH hydrogels for AC regeneration. The contribution of author of this Thesis is on the characterisation of the gellan gum hydrogels physico-chemical properties.

[10] **A Scalzone**, AM Ferreira, C Tonda-Turo, G Ciardelli, K Dalgarno, P Gentile "The interplay between chondrocyte spheroids and mesenchymal stem cells boosts cartilage regeneration within a 3D natural-based hydrogel", 2019, Scientific Reports 9(1):1-12.

This publication is related to the Master Thesis project of the author of this Thesis, in collaboration with Politecnico di Torino. This was based on the manufacturing of a thermosensitive chitosan hydrogel as a cell co-culture platform for AC regeneration.

- Book Chapters

[1] **A Scalzone**, C Tonda-Turo, AM Ferreira, P Gentile. "24- 3D-printed Soft Hydrogels Cell Encapsulation", 2021, Soft Matter for Biomedical Applications, The Royal Society of Chemistry. Edited by: H. Azevedo, J.F. Mano and J. Borges, pp 594-625.

This book chapter was written by the author of this Thesis and regards the bioprinting of hydrogel-based bioinks. Part of the information included in this book chapter can be found in Chapter 2.

- Further publications

M A Bonifacio, A Cochis, S Cometa, P Gentile, **A Scalzone**, A C Scalia, L Rimondini, P Mastrolilli, E De Giglio, "A bioprintable Gellan Gum/Lignin hydrogel: a smart and sustainable route for cartilage regeneration", in submission phase.

This work was performed in collaboration with Politecnico di Bari. It focuses on the bioprinting of GG-lignin hydrogels for AC regeneration. The contribution of author of this Thesis is on the bioprinting part and assessment of cells viability post-printing.

A Scalzone & G Cerqueni, X N Wang, K Dalgarno, A M Ferreira, M Mattioli-Belmonte & P Gentile "An in vitro engineered osteochondral tissues as tool to study OA environment", in preparation

This publication is part of the work in Chapter 6, and it is in collaboration with Universita' Politecnica delle Marche. It regards the optimisation of the DL and SB and their study in healthy and OA conditions.

A Scalzone, G Cerqueni, X N Wang, K Dalgarno, A M Ferreira, M Mattioli-Belmonte & P Gentile "Osteoarthritis pathogenesis: a cytokine-induced in vitro spheroid-based study model", in preparation

This publication is part of the work in Chapter 4. It regards the optimisation of the cytokines cocktail in the scaffold-free model.

- <u>Communication at Conferences/Seminars</u>

[1] Galvanus International pharmaceutical conference (27 – 28 Apr. 2022 –Valencia)

PODIUM PRESENTATION: "In vitro modelling of osteoarthritis as platform for testing miRNA-based therapeutic polyplexes"

[2] European Society for Biomaterials congress (5 – 9 Sep. 2021 - online)

PODIUM PRESENTATIONS: "Osteoarthritis pathogenesis: a cytokine-induced in vitro spheroid-based study model" & "Photocurable Manuka Honey-enriched gellan gum-based bioink for engineered articular cartilage constructs"

[3] Italian Society for Biomaterials (11 – 14 Jul. 2021 Lecce)

PODIUM PRESENTATION: "A cytokine-induced in vitro model of osteoarthritis pathogenesis"

[4] 3D Bioprinting workshop (17 – 18 Jun. 2021 Università Federico II di Napoli - online)

ORGANISER AND SPEAKER: "3D printing and Bioprinting: when engineering meets biology"

[5] World Biomaterial congress (11 – 15 Dec. 2020 - online)

PODIUM PRESENTATION: "An in vitro human cartilage repair model of the Chondrosphere™ technique"

[6] INSIGHT Public Lecture (26 Nov. 2020 Newcastle University – online)

LECTURE: "Engineered in vitro models of osteochondral tissue in healthy and pathological conditions"

[7] ROKIT Invivo Webinair: Current advances in tissue engineering in regenerative medicine: application of tissue-specific stem cells (24 Jul. 2020 - online)

SPEAKER: "Current osteochondral tissue engineering status and application"

[8] Versus Arthritis Research UK meeting (27 Sep. 2019 Newcastle University)

POSTER PRESENTATION: "An in vitro model of the Chondrosphere™ technique"

[9] European Society for Biomaterials congress (9 – 13 Sep. 2019 Dresden)

PODIUM PRESENTATION: "Chondrocytes-embedded 3D hydrogel as environment for cartilage production"

[10] Italian Society for Biomaterials (5-7 Jun. 2019 Caserta)

PODIUM PRESENTATION & BEST ORAL PRESENTATION AWARD: "MSCs-Chondrocytes spheroids crosstalk in co-culture speeds up GAGs and collagen production through a natural-based hydrogel"

[11] TERMIS 2019-Tissue Engineering & Regenerative Medicine EU conference (27-31 May 2019 Rhodes)

PODIUM PRESENTATION: "Engineered co-culture strategies using chitosan-based hydrogels for facilitated articular cartilage regeneration"

References

Abd El-Malek, F.F., Yousef, A.S. & El-Assar, S.A. (2017) 'Hydrogel film loaded with new formula from manuka honey for treatment of chronic wound infections', *Journal of Global Antimicrobial Resistance*, 11pp. 171–176.

Akhtar, N., Rasheed, Z., Ramamurthy, S., Anbazhagan, A.N., Voss, F.R. & Haqqi, T.M. (2010) 'MicroRNA-27b regulates the expression of matrix metalloproteinase 13 in human osteoarthritis chondrocytes', *Arthritis and Rheumatism*, 62(5), pp. 1361–1371.

Akkiraju, H. & Nohe, A. (2015) 'Role of chondrocytes in cartilage formation, progression of osteoarthritis and cartilage regeneration', *Journal of Developmental Biology*, 3(4), pp. 177–192.

Alexopoulos, L.G., Williams, G.M., Upton, M.L., Setton, L.A. & Guilak, F. (2005) 'Osteoarthritic changes in the biphasic mechanical properties of the chondrocyte pericellular matrix in articular cartilage', *Journal of Biomechanics*, 38(3), pp. 509–517.

Alford, J.W. & Cole, B.J. (2005) 'Cartilage Restoration, Part 1: Basic Science, Historical Perspective, Patient Evaluation, and Treatment Options', *The American Journal of Sports Medicine*, 33(2), pp. 295–306.

Amiable, N., Martel-Pelletier, J., Lussier, B., Tat, S.K., Pelletier, J.P. & Boileau, C. (2011) 'Proteinase-activated receptor-2 gene disruption limits the effect of osteoarthritis on cartilage in mice: A novel target in joint degradation', *Journal of Rheumatology*, 38(5), pp. 911–920.

Anderer, U. & Libera, J. (2002) 'In vitro engineering of human autogenous cartilage', *Journal of Bone and Mineral Research*, 17(8), pp. 1420–1429.

Andersen, M., Howard, K.A., Paludan, S.R., Besenbacher, F. & Kjems, J. (2008) 'Delivery of siRNA from lyophilized polymeric surfaces', *Biomaterials*, 29(4), pp. 506–512.

Andrew, C.D., Susan, E.C., Emily, M.R. & Daniel, J.K. (2016) 'A comparison of different bioinks for 3D bioprinting of fibrocartilage and hyaline cartilage', *Biofabrication*, 8(4), p. 45002.

Annabi, N., Nichol, J.W., Zhong, X., Ji, C., Koshy, S., Khademhosseini, A. & Dehghani, F. (2010) 'Controlling the porosity and microarchitecture of hydrogels for tissue engineering', *Tissue Engineering - Part B: Reviews*, 16(4), pp. 371–383.

Armiento, A.R., Stoddart, M.J., Alini, M. & Eglin, D. (2018) 'Biomaterials for articular cartilage tissue engineering: Learning from biology', *Acta Biomaterialia*, 65pp. 1–20.

Armoiry, X., Cummins, E., Connock, M., Metcalfe, A., Royle, P., Johnston, R., Rodrigues, J., Waugh, N. & Mistry, H. (2019) 'Autologous Chondrocyte Implantation with Chondrosphere for Treating Articular Cartilage Defects in the Knee: An Evidence Review Group Perspective of a NICE Single Technology Appraisal', *PharmacoEconomics*, 37(7), pp. 879–886.

Arno, M.C., Inam, M., Weems, A.C., Li, Z., Binch, A.L.A., Platt, C.I., Richardson, S.M., Hoyland, J.A., Dove, A.P. & O'Reilly, R.K. (2020) 'Exploiting the role of nanoparticle shape in enhancing hydrogel adhesive and mechanical properties', *Nature Communications*, 11(1), .

Arthritis Research UK (2011) *Osteoarthritis in numbers*, (207711), .

Ashammakhi, N., Ahadian, S., Xu, C., Montazerian, H., Ko, H. & Nasiri, R. (2019) *Materials Today Bio Bioinks and bioprinting technologies to make heterogeneous and biomimetic tissue constructs*, 1(May), .

Autologous, F.T., Scaffold, C., Approved, P., Conference, F.D.A., Today, C., Standard, E., Cambridge, T., Newswire, G., Corporation, V., Recker, D., Treatment, M. & Colangelo, N. (2017) *FDA Approves MACI for the Treatment of Symptomatic Cartilage Defects of the Knee in Adults*, pp. 1–3.

Azizi, M., Azimzadeh, M., Afzali, M. & Alafzadeh, M. (2018) *Characterization and optimization of using calendula officinalis extract in fabrication of polycaprolactone-gelatin electrospun nanofibers for wound dressing applications Modeling and Optimization of DNA Biosensors View project Microfluidic sperm selectio*, 6(2), pp. 34–46.

Bader, D. & Lee, D. (2000) 'Chapter 4 Structure - Properties of soft tissues articular cartilage', *Pergamon Materials Series*, 4(C), pp. 75–103.

Bae, H.C., Park, H.J., Wang, S.Y., Yang, H.R., Lee, M.C. & Han, H.S. (2018) 'Hypoxic condition enhances chondrogenesis in synovium-derived mesenchymal stem cells', *Biomaterials Research*, 22(1), pp. 1–8.

Baek, J.S., Carlomagno, C., Muthukumar, T., Kim, D., Park, J.H., Song, J.E., Migliaresi, C., Motta, A., Reis, R.L. & Khang, G. (2019) 'Evaluation of Cartilage Regeneration in Gellan Gum/agar Blended Hydrogel with Improved Injectability', *Macromolecular Research*, 27(6), pp. 558–564.

Bakhshandeh, B., Soleimani, M., Paylakhi, S.H. & Ghaemi, N. (2012) 'A microRNA signature associated with chondrogenic lineage commitment', *Journal of Genetics*, 91(2), pp. 171–182.

Bartolotti, I., Roseti, L., Petretta, M., Grigolo, B. & Desando, G. (2021) 'A roadmap of in vitro models in osteoarthritis: A focus on their biological relevance in regenerative medicine', *Journal of Clinical Medicine*, 10(9), .

Basad, E., Wissing, F.R., Fehrenbach, P., Rickert, M., Steinmeyer, J. & Ishaque, B. (2015) 'Matrix-induced autologous chondrocyte implantation (MACI) in the knee: clinical outcomes and challenges', *Knee Surgery, Sports Traumatology, Arthroscopy*, 23(12), pp. 3729–3735.

Bastos, A.R., Raquel Maia, F., Miguel Oliveira, J., Reis, R.L. & Correlo, V.M. (2021) 'Influence of gellan gum-hydroxyapatite spongy-like hydrogels on human osteoblasts under long-term osteogenic differentiation conditions', *Materials Science and Engineering C*, 129(September), p. 112413.

Bautista, C.A., Park, H.J., Mazur, C.M., Aaron, R.K. & Bilgen, B. (2016) 'Effects of chondroitinase ABC-Mediated proteoglycan digestion on decellularization and recellularization of articular cartilage', *PLoS ONE*, 11(7), pp. 1–15.

Bellini, D., Cencetti, C., Meraner, J., Stoppoloni, D., D'Abusco, A.S. & Matricardi, P. (2015) 'An in situ gelling system for bone regeneration of osteochondral defects', *European Polymer Journal*, 72pp. 642–650.

Bellotti, C., Duchi, S., Bevilacqua, A., Lucarelli, E. & Piccinini, F. (2016) 'Long term morphological characterization of mesenchymal stromal cells 3D spheroids built with a rapid method based on entry-level equipment', *Cytotechnology*, 68(6), pp. 2479–2490.

Benam, K.H., Dauth, S., Hassell, B., Herland, A., Jain, A., Jang, K.-J., Karalis, K., Kim, H.J., MacQueen, L., Mahmoodian, R., Musah, S., Torisawa, Y., van der Meer, A.D., Villenave, R., Yadid, M., Parker, K.K. & Ingber, D.E. (2015) 'Engineered in vitro disease models.', *Annual review of pathology*, 10(January), pp. 195–262.

Bennett, J.M., Reeves, G., Billman, G.E. & Sturmberg, J.P. (2018) 'Inflammation-nature's way to efficiently respond to all types of challenges: Implications for understanding and managing "the epidemic" of chronic diseases', *Frontiers in Medicine*, 5(NOV), pp. 1–30.

Bhosale, A.M. & Richardson, J.B. (2008) 'Articular cartilage: Structure, injuries and review of management', *British Medical Bulletin*, 87(1), pp. 77–95.

Bian, L., Zhai, D.Y., Mauck, R.L. & Burdick, J.A. (2011) 'Coculture of Human Mesenchymal Stem Cells and Articular Chondrocytes Reduces Hypertrophy and Enhances Functional Properties of Engineered Cartilage', *Tissue Engineering Part A*, 17(7–8), pp. 1137–1145.

Bian, L., Zhai, D.Y., Tous, E., Rai, R., Mauck, R.L. & Burdick, J.A. (2011) 'Enhanced MSC chondrogenesis following delivery of TGF-β3 from alginate microspheres within hyaluronic acid hydrogels in vitro and in vivo', *Biomaterials*, 32(27), pp. 6425–6434.

Billinghurst, R.C., Dahlberg, L., Ionescu, M., Reiner, A., Bourne, R., Rorabeck, C., Mitchell, P., Hambor, J., Diekmann, O., Tschesche, H., Chen, J., van Wart, H. & Poole, A.R. (1997) 'Enhanced cleavage of type II collagen by collagenases in osteoarthritic articular cartilage', *Journal of Clinical Investigation*, 99(7), pp. 1534–1545.

Blanco, F.J., Guitian, R., Vázquez-Martul, E., de Toro, F.J. & Galdo, F. (1998) 'Osteoarthritis chondrocytes die by apoptosis: A possible pathway for osteoarthritis pathology', *Arthritis and Rheumatism*, 41(2), pp. 284–289.

Blom, A., van der Kraan, P. & van den Berg, W. (2007) 'Cytokine Targeting in Osteoarthritis', *Current Drug Targets*, 8(2), pp. 283–292.

Boehme, K.A. & Rolauffs, B. (2018) 'Onset and progression of human osteoarthritis—Can growth factors, inflammatory cytokines, or differential miRNA expression concomitantly induce proliferation, ECM degradation, and inflammation in articular cartilage?', *International Journal of Molecular Sciences*, 19(8), .

Bonifacio, M.A., Cochis, A., Cometa, S., Scalzone, A., Gentile, P., Procino, G., Milano, S., Scalia, A.C., Rimondini, L. & de Giglio, E. (2020) 'Advances in cartilage repair: The influence of inorganic clays to improve mechanical and healing properties of antibacterial Gellan gum-Manuka honey hydrogels', *Materials Science and Engineering C*, 108(August 2019), p. 110444.

Bonifacio, M.A., Cometa, S., Cochis, A., Gentile, P., Ferreira, A.M., Azzimonti, B., Procino, G., Ceci, E., Rimondini, L. & de Giglio, E. (2018) 'Antibacterial effectiveness meets improved mechanical properties: Manuka honey/gellan gum composite hydrogels for cartilage repair', *Carbohydrate Polymers*, 198(April), pp. 462–472.

Bonifacio, M.A., Gentile, P., Ferreira, A.M., Cometa, S. & De Giglio, E. (2017) 'Insight into halloysite nanotubes-loaded gellan gum hydrogels for soft tissue engineering applications', *Carbohydrate Polymers*, 163pp. 280–291.

van den Bosch, M.H.J. (2019) 'Inflammation in osteoarthritis: is it time to dampen the alarm(in) in this debilitating disease?', *Clinical and Experimental Immunology*, 195(2), pp. 153–166.

Bosman, F.T., Visser, B.C. & van Oeveren, J. (1996) 'Apoptosis: Pathophysiology of programmed cell death', *Pathology Research and Practice*, 192(7), pp. 676–683.

Boussif, O., LezoualC'H, F., Zanta, M.A., Mergny, M.D., Scherman, D., Demeneix, B. & Behr, J.P. (1995) 'A versatile vector for gene and oligonucleotide transfer into cells in culture and in vivo: Polyethylenimine', *Proceedings of the National Academy of Sciences of the United States of America*, 92(16), pp. 7297–7301.

Brehm, W., Aklin, B., Yamashita, T., Rieser, F., Trüb, T., Jakob, R.P. & Mainil-Varlet, P. (2006) 'Repair of superficial osteochondral defects with an autologous scaffold-free cartilage construct in a caprine model: implantation method and short-term results', *Osteoarthritis and Cartilage*, 14(12), pp. 1214–1226.

Brittberg, M., Lindahl, A., Nilsson, A., Ohlsson, C., Isaksson, O. & Peterson, L. (1994) 'Treatment of Deep Cartilage Defects in the Knee with Autologous Chondrocyte Transplantation', *New England Journal of Medicine*, 331(14), pp. 889–895.

Brown, E.T.T., Damen, A.H.A. & Thambyah, A. (2020a) 'The mechanical significance of the zonally differentiated collagen network of articular cartilage in relation to tissue swelling', *Clinical Biomechanics*, (December), .

Brown, E.T.T., Damen, A.H.A. & Thambyah, A. (2020b) 'The mechanical significance of the zonally differentiated collagen network of articular cartilage in relation to tissue swelling', *Clinical Biomechanics*, 79(September), .

Brown, W.E., DuRaine, G.D., Hu, J.C. & Athanasiou, K.A. (2019) 'Structure-function relationships of fetal ovine articular cartilage', *Acta Biomaterialia*, 87pp. 235–244.

Buckley, M.R., Gleghorn, J.P., Bonassar, L.J. & Cohen, I. (2008) 'Mapping the depth dependence of shear properties in articular cartilage', *Journal of Biomechanics*, 41(11), pp. 2430–2437.

Buckwalter, J.A. (1998) 'Articular Cartilage: Injuries and Potential for Healing', *Journal of Orthopaedic & Sports Physical Therapy*, 28(4), pp. 192–202.

Buckwalter, J.A. & Mankin, H.J. (1997) 'Articular cartilage. Part I: Tissue design and chondrocyte-matrix interactions', *Journal of Bone and Joint Surgery - Series A*, 79(4), pp. 600–611.

Buckwalter, J.A. & Mankin, H.J. (1998) 'Articular cartilage: tissue design and chondrocyte-matrix interactions.', *Instructional course lectures*, 47pp. 477–486.

Cai, G., Liu, W., He, Y., Huang, J., Duan, L., Xiong, J., Liu, L. & Wang, D. (2019) 'Recent advances in kartogenin for cartilage regeneration', *Journal of Drug Targeting*, 27(1), pp. 28–32.

Camarero-Espinosa, S., Rothen-Rutishauser, B., Foster, E.J. & Weder, C. (2016) 'Articular cartilage: From formation to tissue engineering', *Biomaterials Science*, 4(5), pp. 734–767.

Camarero-Espinosa, S., Rothen-Rutishauser, B., Weder, C. & Foster, E.J. (2016) 'Directed cell growth in multi-zonal scaffolds for cartilage tissue engineering', *Biomaterials*, 74pp. 42–52.

Carmagnola, I., Chiono, V., Ruocco, G., Scalzone, A., Gentile, P., Taddei, P. & Ciardelli, G. (2020) 'Plga membranes functionalized with gelatin through biomimetic mussel-inspired strategy', *Nanomaterials*, 10(11), pp. 1–17.

Caron, M.M., Derks, K.W., Sanderink, L., van Rhijn, L.W., Peffers, M.J. & Welting, T.J. (2018) 'The gate to controlling chondrogenic differentiation: transcriptional regulation by SOX9 in ATDC5 cells', *Osteoarthritis and Cartilage*, 26(2018), p. S109.

Cencetti, C., Bellini, D., Longinotti, C., Martinelli, A. & Matricardi, P. (2011) 'Preparation and characterization of a new gellan gum and sulphated hyaluronic acid hydrogel designed for epidural scar prevention', *Journal of Materials Science: Materials in Medicine*, 22(2), pp. 263–271.

Cerqueira, M.T., Da Silva, L.P., Santos, T.C., Pirraco, R.P., Correlo, V.M., Reis, R.L. & Marques, A.P. (2014) 'Gellan gum-hyaluronic acid spongy-like hydrogels and cells from adipose tissue synergize promoting neoskin vascularization', *ACS Applied Materials and Interfaces*, 6(22), pp. 19668–19679.

Chaunier, L., Guessasma, S., Belhabib, S., Della Valle, G., Lourdin, D. & Leroy, E. (2018) 'Material extrusion of plant biopolymers: Opportunities & challenges for 3D printing', *Additive Manufacturing*, 21(January 2017), pp. 220–233.

Chen, C.H., Kuo, C.Y. & Chen, J.P. (2018) 'Effect of cyclic dynamic compressive loading on chondrocytes and adipose-derived stem cells co-cultured in highly elastic cryogel scaffolds', *International Journal of Molecular Sciences*, 19(2), pp. 1–20.

Chen, F.H., Rousche, K.T. & Tuan, R.S. (2006) 'Technology insight: Adult stem cells in cartilage regeneration and tissue engineering', *Nature Clinical Practice Rheumatology*, 2(7), pp. 373–382.

Chen, S., Qin, L., Wu, X., Fu, X., Lin, S., Chen, D., Xiao, G., Shao, Z. & Cao, H. (2020) 'Moderate Fluid Shear Stress Regulates Heme Oxygenase-1 Expression to Promote Autophagy and ECM Homeostasis in the Nucleus Pulposus Cells', *Frontiers in Cell and Developmental Biology*, 8(March), pp. 1–14.

Chen, Y., Song, J., Wang, S. & Liu, W. (2021) 'PVA-Based Hydrogels: Promising Candidates for Articular Cartilage Repair', *Macromolecular Bioscience*, 21(10), pp. 1–12.

Cosenza, S., Ruiz, M., Toupet, K., Jorgensen, C. & Noël, D. (2017) 'Mesenchymal stem cells derived exosomes and microparticles protect cartilage and bone from degradation in osteoarthritis', *Scientific Reports*, 7(1), pp. 1–12.

Costantini, M., Idaszek, J., Szöke, K., Jaroszewicz, J., Dentini, M., Barbetta, A., Brinchmann, J.E. & Święszkowski, W. (2016) '3D bioprinting of BM-MSCs-loaded ECM biomimetic hydrogels for in vitro neocartilage formation', *Biofabrication*, 8(3), .

Cotter, E.J., Wang, K.C., Yanke, A.B. & Chubinskaya, S. (2018) 'Bone Marrow Aspirate Concentrate for Cartilage Defects of the Knee: From Bench to Bedside Evidence', *Cartilage*, 9(2), pp. 161–170.

Coutinho, Daniela F, Sant, S., Shin, H., Oliveira, J.T., Gomes, E., Neves, N.M., Khademhosseini, A. & Reis, R.L. (2010) 'Modified Gellan Gum hydrogels with tunable physical and mechanical properties', *Biomaterials*, 31(29), pp. 7494–7502.

Coutinho, Daniela F., Sant, S. v., Shin, H., Oliveira, J.T., Gomes, M.E., Neves, N.M., Khademhosseini, A. & Reis, R.L. (2010) 'Modified Gellan Gum hydrogels with tunable physical and mechanical properties', *Biomaterials*, 31(29), pp. 7494–7502.

Cubo, N., Garcia, M., Del Cañizo, J.F., Velasco, D. & Jorcano, J.L. (2017) '3D bioprinting of functional human skin: Production and in vivo analysis', *Biofabrication*, 9(1), .

Cummins, E., Armoiry, X., Metcalfe, A., Royle, P., Mistry, H., Johnston, R., Rodrigues, J. & Waugh, N. (2017) 'Autologous chondrocyte implantation with Spherox for treating articular cartilage defects in the knee . (NICE ID 851)', *Warwick Evidence ERG report*, pp. 1–104.

Darling, E.M., Pritchett, P.E., Evans, B.A., Superfine, R., Zauscher, S. & Guilak, F. (2009) 'Mechanical properties and gene expression of chondrocytes on micropatterned substrates following dedifferentiation in monolayer', *Cellular and Molecular Bioengineering*, 2(3), pp. 395–404.

D'arrigo, D., Roffi, A., Cucchiarini, M., Moretti, M., Candrian, C. & Filardo, G. (2019) 'Secretome and extracellular vesicles as new biological therapies for knee osteoarthritis: A systematic review', *Journal of Clinical Medicine*, 8(11), .

Datta, S., Barua, R. & Das, J. (2020) 'Importance of Alginate Bioink for 3D Bioprinting in Tissue Engineering and Regenerative Medicine', in Leonel Pereira (ed.) *Alginates*. [Online]. Rijeka: IntechOpen.

Davies, R. & Kuiper, N. (2019) 'Regenerative Medicine: A Review of the Evolution of Autologous Chondrocyte Implantation (ACI) Therapy', *Bioengineering*, 6(1), p. 22.

Davisson, T., Kunig, S., Chen, A., Sah, R. & Ratcliffe, A. (2002) 'Static and dynamic compression modulate matrix metabolism in tissue engineered cartilage', *Journal of Orthopaedic Research*, 20(4), pp. 842–848.

Denayer, T., Stöhrn, T. & Van Roy, M. (2014) 'Animal models in translational medicine: Validation and prediction', *New Horizons in Translational Medicine*, 2(1), pp. 5–11.

Dikina, A.D., Lai, B.P., Cao, M., Zborowski, M. & Alsberg, E. (2017) 'Magnetic field application or mechanical stimulation: Via magnetic microparticles does not enhance chondrogenesis in mesenchymal stem cell sheets', *Biomaterials Science*, 5(7), pp. 1241–1245.

Dimaraki, A., Díaz-payno, P.J., Minneboo, M., Nouri-goushki, M., Hosseini, M., Kops, N., Narcisi, R., Mirzaali, M.J., van Osch, G.J.V.M., Fratila-apachitei, L.E. & Zadpoor, A.A. (2021a) 'Bioprinting of a zonal-specific cell density scaffold: A biomimetic approach for cartilage tissue engineering', *Applied Sciences (Switzerland)*, 11(17), .

Dimaraki, A., Díaz-payno, P.J., Minneboo, M., Nouri-goushki, M., Hosseini, M., Kops, N., Narcisi, R., Mirzaali, M.J., van Osch, G.J.V.M., Fratila-apachitei, L.E. & Zadpoor, A.A. (2021b) 'Bioprinting of a zonal-specific cell density scaffold: A biomimetic approach for cartilage tissue engineering', *Applied Sciences (Switzerland)*, 11(17), .

Dissanayaka, W.L. & Zhang, C. (2020) 'Scaffold-based and Scaffold-free Strategies in Dental Pulp Regeneration', *Journal of Endodontics*, 46(9), pp. S81–S89.

D'Lima, D.D., Fregly, B.J., Patil, S., Steklov, N. & Colwell, C.W. (2012) 'Knee joint forces: Prediction, measurement, and significance', *Proceedings of the Institution of Mechanical Engineers, Part H: Journal of Engineering in Medicine*, 226(2), pp. 95–102.

Donate, R., Monzón, M. & Alemán-Domínguez, M.E. (2020) 'Additive manufacturing of PLA-based scaffolds intended for bone regeneration and strategies to improve their biological properties', *E-Polymers*, 20(1), pp. 571–599.

Dong, J., Li, L., Fang, X. & Zang, M. (2021) 'Exosome-encapsulated microrna-127-3p released from bone marrow-derived mesenchymal stem cells alleviates osteoarthritis through regulating cdh11-mediated wnt/β-catenin pathway', *Journal of Pain Research*, 14pp. 297–310.

Douglas, T., Wlodarczyk, M., Pamula, E., Declercq, H., de Mulder, E., Bucko, M., Balcaen, L., Vanhaecke, F., Cornelissen, R., Dubruel, P., Jansen, J. & Leeuwenburgh, S. (2014) 'Enzymatic mineralization of gellan gum hydrogel for bone tissue-engineering applications and its enhancement by polydopamine', *Journal of Tissue Engineering and Regenerative Medicine*, 8(11), pp. 906–918.

Douglas, T.E.L., Pilarz, M., Lopez-Heredia, M., Brackman, G., Schaubroeck, D., Balcaen, L., Bliznuk, V., Dubruel, P., Knabe-Ducheyne, C., Vanhaecke, F., Coenye, T. & Pamula, E. (2017) 'Composites of gellan gum hydrogel enzymatically mineralized with calcium–zinc phosphate for bone regeneration with antibacterial activity', *Journal of Tissue Engineering and Regenerative Medicine*, 11(5), pp. 1610–1618.

Dreier, R. (2010) 'Hypertrophic differentiation of chondrocytes in osteoarthritis: The developmental aspect of degenerative joint disorders', *Arthritis Research and Therapy*, 12(5), .

Duarte Campos, D.F., Blaeser, A., Weber, M., Jäkel, J., Neuss, S., Jahnen-Dechent, W. & Fischer, H. (2013) 'Three-dimensional printing of stem cell-laden hydrogels submerged in a hydrophobic high-density fluid', *Biofabrication*, 5(1), .

DuRaine, G.D., Brown, W.E., Hu, J.C. & Athanasiou, K.A. (2015) 'Emergence of Scaffold-Free Approaches for Tissue Engineering Musculoskeletal Cartilages', *Annals of Biomedical Engineering*, 43(3), pp. 543–554.

Echtermeyer, F., Bertrand, J., Dreier, R., Meinecke, I., Neugebauer, K., Fuerst, M., Lee, Y.J., Song, Y.W., Herzog, C., Theilmeier, G. & Pap, T. (2009) 'Syndecan-4 regulates ADAMTS-5 activation and cartilage breakdown in osteoarthritis', *Nature Medicine*, 15(9), pp. 1072–1076.

Elmore, S. (2007a) 'Apoptosis: A Review of Programmed Cell Death', *Toxicologic Pathology*, 35(4), pp. 495–516.

Elmore, S. (2007b) 'Apoptosis: A Review of Programmed Cell Death', *Toxicologic Pathology*, 35(4), pp. 495–516.

EMA (2017) 'Spherox, CHMP Assessment report', *Ema*, 44(May), .

Eschen, C., Kaps, C., Widuchowski, W., Fickert, S., Zinser, W., Niemeyer, P. & Roël, G. (2020) 'Clinical outcome is significantly better with spheroid-based autologous chondrocyte implantation manufactured with more stringent cell culture criteria', *Osteoarthritis and Cartilage Open*, 2(1), p. 100033.

European Parliament (2010) 'Directive 2010/63/EU - On the protection of animals used for scientific purposes', *Official Journal of the European Union*, pp. 33–79.

Fan, Z., Söder, S., Oehler, S., Fundel, K. & Aigner, T. (2007) 'Activation of Interleukin-1 Signaling Cascades in Normal and Osteoarthritic Articular Cartilage', *The American Journal of Pathology*, 171(3), pp. 938–946.

Fath, D.M., Kong, X., Liang, D., Lin, Z., Chou, A., Jiang, Y., Fang, J., Caro, J. & Sang, N. (2006) 'Histone deacetylase inhibitors repress the transactivation potential of hypoxia-inducible factors independently of direct acetylation of HIF-α', *Journal of Biological Chemistry*, 281(19), pp. 13612–13619.

Federico, S. & Herzog, W. (2008) 'On the permeability of fibre-reinforced porous materials', *International Journal of Solids and Structures*, 45(7–8), pp. 2160–2172.

Feng, B., Ji, T., Wang, X., Fu, W., Ye, L., Zhang, H. & Li, F. (2020) 'Engineering cartilage tissue based on cartilage-derived extracellular matrix cECM/PCL hybrid nanofibrous scaffold', *Materials and Design*, 193p. 108773.

Findlay, D.M. & Atkins, G.J. (2014) 'Osteoblast-chondrocyte interactions in osteoarthritis', *Current Osteoporosis Reports*, 12(1), pp. 127–134.

Foty, R.A. & Steinberg, M.S. (2005) 'The differential adhesion hypothesis: A direct evaluation', *Developmental Biology*, 278(1), pp. 255–263.

Freeman, E.C., Weiland, L.M. & Meng, W.S. (2013) 'Modeling the proton sponge hypothesis: Examining proton sponge effectiveness for enhancing intracellular gene delivery through multiscale modeling', *Journal of Biomaterials Science, Polymer Edition*, 24(4), pp. 398–416.

Fu, L., Yang, Z., Gao, C., Li, H., Yuan, Z., Wang, F., Sui, X., Liu, S. & Guo, Q. (2020) 'Advances and prospects in biomimetic multilayered scaffolds for articular cartilage regeneration', *Regenerative Biomaterials*, 7(6), pp. 527–542.

Fu, N., Liao, J., Lin, S., Sun, K., Tian, T., Zhu, B. & Lin, Y. (2016) 'PCL-PEG-PCL film promotes cartilage regeneration in vivo', *Cell Proliferation*, 49(6), pp. 729–739.

Gao, L., Orth, P., Cucchiarini, M. & Madry, H. (2017) 'Effects of solid acellular type-I/III collagen biomaterials on in vitro and in vivo chondrogenesis of mesenchymal stem cells', *Expert Review of Medical Devices*, 14(9), pp. 717–732.

Gao, Y., Liu, S., Huang, J., Guo, W., Chen, J., Zhang, L., Zhao, B., Peng, J., Wang, A., Wang, Y., Xu, W., Lu, S., Yuan, M. & Guo, Q. (2014) 'The ECM-cell interaction of cartilage extracellular matrix on chondrocytes', *BioMed Research International*, 2014.

Garrigues, N.W., Little, D., Sanchez-Adams, J., Ruch, D.S. & Guilak, F. (2014) 'Electrospun cartilage-derived matrix scaffolds for cartilage tissue engineering', *Journal of Biomedical Materials Research - Part A*, 102(11), pp. 3998–4008.

Gegg, C. & Yang, F. (2020) 'Spatially patterned microribbon-based hydrogels induce zonally-organized cartilage regeneration by stem cells in 3D', *Acta Biomaterialia*, 101pp. 196–205.

Gemmiti, C. v. & Guldberg, R.E. (2009a) 'Shear stress magnitude and duration modulates matrix composition and tensile mechanical properties in engineered cartilaginous tissue', *Biotechnology and Bioengineering*, 104(4), pp. 809–820.

Gemmiti, C. v. & Guldberg, R.E. (2009b) 'Shear Stress Magnitude and Duration Modulates Matrix Composition and Tensile Mechanical Properties in Engineered Cartilaginous Tissue', *Biotechnol Bioeng.*, 104(4), pp. 809–820.

Ghafouri-Fard, S., Bahroudi, Z., Shoorei, H., Abak, A., Ahin, M. & Taheri, M. (2021) 'microRNA-140: A miRNA with diverse roles in human diseases', *Biomedicine and Pharmacotherapy*, 135p. 111256.

Giannasi, C., Niada, S., Magagnotti, C., Ragni, E., Andolfo, A. & Brini, A.T. (2020) 'Comparison of two ASC-derived therapeutics in an in vitro OA model: secretome versus extracellular vesicles', *Stem Cell Research and Therapy*, 11(1), pp. 1–15.

Gilbert, L., He, X., Farmer, P., Rubin, J., Drissi, H., van Wijnen, A.J., Lian, J.B., Stein, G.S. & Nanes, M.S. (2002) 'Expression of the osteoblast differentiation factor RUNX2 (Cbfa1/AML3/Pebp2αA) is inhibited by tumor necrosis factor-α', *Journal of Biological Chemistry*, 277(4), pp. 2695–2701.

Gilbert, S.J., Bonnet, C.S. & Blain, E.J. (2021) 'Mechanical cues: Bidirectional reciprocity in the extracellular matrix drives mechano-signalling in articular cartilage', *International Journal of Molecular Sciences*, 22(24), .

Gioffredi, E., Boffito, M., Calzone, S., Giannitelli, S.M., Rainer, A., Trombetta, M., Mozetic, P. & Chiono, V. (2016) 'Pluronic F127 Hydrogel Characterization and Biofabrication in Cellularized Constructs for Tissue Engineering Applications', *Procedia CIRP*, 49(iii), pp. 125–132.

Gionet-Gonzales, M.A. & Leach, J.K. (2018) 'Engineering principles for guiding spheroid function in the regeneration of bone, cartilage, and skin', *Biomedical Materials (Bristol)*, 13(3), pp. 1–27.

Girão, A.F., Semitela, Â., Ramalho, G., Completo, A. & Marques, P.A.A.P. (2018) 'Mimicking nature: Fabrication of 3D anisotropic electrospun polycaprolactone scaffolds for cartilage tissue engineering applications', *Composites Part B: Engineering*, 154(April), pp. 99–107.

Glyn-Jones, S., Palmer, A.J.R., Agricola, R., Price, A.J., Vincent, T.L., Weinans, H. & Carr, A.J. (2015) 'Osteoarthritis', *The Lancet*, 386(9991), pp. 376–387.

Gobbi, A., Lane, J.G., Longo, U.G. & Dallo, I. (2021) *Joint Function Preservation: A Focus on the Osteochondral Unit*. Springer Nature.

Godbey, W.T., Wu, K.K. & Mikos, A.G. (1999) 'Poly(ethylenimine) and its role in gene delivery', *Journal of Controlled Release*, 60(2–3), pp. 149–160.

Goldring, M.B. (2012) 'Chondrogenesis, chondrocyte differentiation, and articular cartilage metabolism in health and osteoarthritis', *Therapeutic Advances in Musculoskeletal Disease*, 4(4), pp. 269–285.

Goldring, M.B. (2000a) 'The role of the chondrocyte in osteoarthritis', *Arthritis and Rheumatism*, 43(9), pp. 1916–1926.

Goldring, M.B. (2000b) 'The role of the chondrocyte in osteoarthritis', *Arthritis and Rheumatism*, 43(9), pp. 1916–1926.

Goldring, M.B. & Marcu, K.B. (2009) 'Cartilage homeostasis in health and rheumatic diseases', *Arthritis Research and Therapy*, 11(3), .

Goldring, M.B., Otero, M., Tsuchimochi, K., Ijiri, K. & Li, Y. (2008) 'Defining the roles of inflammatory and anabolic cytokines in cartilage metabolism', *Annals of the Rheumatic Diseases*, 67(Suppl 3), pp. iii75--iii82.

Grad, S., Lee, C.R., Gorna, K., Gogolewski, S., Wimmer, M.A. & Alini, M. (2005) 'Surface motion upregulates superficial zone protein and hyaluronan production in chondrocyte-seeded three-dimensional scaffolds', *Tissue Engineering*, 11(1–2), pp. 249–256.

Gregor, A., Filová, E., Novák, M., Kronek, J., Chlup, H., Buzgo, M., Blahnová, V., Lukášová, V., Bartoš, M., Nečas, A. & Hošek, J. (2017) 'Designing of PLA scaffolds for bone tissue replacement fabricated by ordinary commercial 3D printer', *Journal of Biological Engineering*, 11(1), pp. 1–21.

Grémare, A., Guduric, V., Bareille, R., Heroguez, V., Latour, S., L'heureux, N., Fricain, J.C., Catros, S. & le Nihouannen, D. (2018) 'Characterization of printed PLA scaffolds for bone tissue engineering', *Journal of Biomedical Materials Research - Part A*, 106(4), pp. 887–894.

Grenier, S., Bhargava, M.M. & Torzilli, P.A. (2014) 'An in vitro model for the pathological degradation of articular cartilage in osteoarthritis', *Journal of biomechanics*, 47(3), pp. 645–652.

Guangyi., L., J., Y., J., G., T.S., C., N.J., P., C., Z. & M.H., Z. (2013) 'Subchondral bone in osteoarthritis: Insight into risk factors and microstructural changes', *Arthritis Research and Therapy*, 15(6), .

Guilak, F. (2000) 'The deformation behavior and viscoelastic properties of chondrocytes in articular cartilage', *Biorheology*, 37(1–2), pp. 27–44.

Guilak, F., Alexopoulos, L.G., Upton, M.L., Youn, I., Choi, J.B., Cao, L., Setton, L.A. & Haider, M.A. (2006) 'The pericellular matrix as a transducer of biomechanical and biochemical signals in articular cartilage', *Annals of the New York Academy of Sciences*, 1068(1), pp. 498–512.

Hab, S.-W., Jangc, H.L., Namc, K.T. & Jr, G.R.B. (2015) 'Nano-hydroxyapatite modulates osteoblast lineage commitment by stimulation of DNA methylation and regulation of gene expression', *Biomaterials*, 176(3), pp. 139–148.

Haider, A., Haider, S. & Kang, I.K. (2018) 'A comprehensive review summarizing the effect of electrospinning parameters and potential applications of nanofibers in biomedical and biotechnology', *Arabian Journal of Chemistry*, 11(8), pp. 1165–1188.

Hamilton, J.L., Nagao, M., Levine, B.R., Chen, D., Olsen, B.R. & Im, H.J. (2016) 'Targeting VEGF and Its Receptors for the Treatment of Osteoarthritis and Associated Pain', *Journal of Bone and Mineral Research*, 31(5), pp. 911–924.

Han, L., Wang, M., Li, P., Gan, D., Yan, L., Xu, J., Wang, K., Fang, L., Chan, C.W., Zhang, H., Yuan, H. & Lu, X. (2018) 'Mussel-Inspired Tissue-Adhesive Hydrogel Based on the Polydopamine-

Chondroitin Sulfate Complex for Growth-Factor-Free Cartilage Regeneration', *ACS Applied Materials and Interfaces*, 10(33), pp. 28015–28026.

Harris, J.D., Siston, R.A., Pan, X. & Flanigan, D.C. (2010) 'Autologous chondrocyte implantation: A systematic review', *Journal of Bone and Joint Surgery - Series A*, 92(12), pp. 2220–2233.

Hashimoto, S., Setareh, M., Ochs, R.L. & Lotz, M. (1997) 'Fas/Fas ligand expression and induction of apoptosis in chondrocytes', *Arthritis and Rheumatism*, 40(10), pp. 1749–1755.

Hauselmann, H.J., Flechtenmacher, J., Michal, L., Thonar, J.-M A, Shinmei, M., Kueltner, K.E., Aydelotte, M.B., Michal, ; L, Thonar, J-M A, Kuettner, K.E. & Rush, : (1996) 'The superficial layer of human articular cartilage is more susceptible to interleukin-1 damage than the deeper layers'. ARTHRITIS & RHEUMATISM 39 (3).

He, X. & Deng, L. (2021) 'Potential of mir-25-3p in protection of chondrocytes: Emphasis on osteoarthritis', *Folia Histochemica et Cytobiologica*, 59(1), pp. 30–39.

He, X., Feng, B., Huang, C., Wang, H., Ge, Y., Hu, R., Yin, M., Xu, Z., Wang, W., Fu, W. & Zheng, J. (2015) 'Electrospun gelatin/polycaprolactone nanofibrous membranes combined with a coculture of bone marrow stromal cells and chondrocytes for cartilage engineering', *International Journal of Nanomedicine*, 10pp. 2089–2099.

Helen, M. (1978) 'Proteoglycans of cartilage', *J. clin. Path.*, 12pp. 67–81.

Heraud, F., Heraud, A. & Harmand, M.F. (2000) 'Apoptosis in normal and osteoarthritic human articular cartilage', *Annals of the Rheumatic Diseases*, 59(12), pp. 959–965.

Highley, C.B., Rodell, C.B. & Burdick, J.A. (2015) *Direct 3D Printing of Shear-Thinning Hydrogels into Self- Healing Hydrogels*, pp. 5075–5079.

Hollander, A.P., Pidoux, I., Reiner, A., Rorabeck, C., Bourne, R. & Poole, A.R. (1995) 'Damage to type II collagen in aging and osteoarthritis starts at the articular surface, originates around chondrocytes, and extends into the cartilage with progressive degeneration', *Journal of Clinical Investigation*, 96(6), pp. 2859–2869.

Hospodiuk, M., Dey, M., Sosnoski, D. & Ozbolat, I.T. (2017) 'The bioink: A comprehensive review on bioprintable materials', *Biotechnology Advances*, 35(2), pp. 217–239.

Hu, B., el Haj, A.J. & Dobson, J. (2013) 'Receptor-targeted, magneto-mechanical stimulation of osteogenic differentiation of human bone marrow-derived mesenchymal stem cells', *International Journal of Molecular Sciences*, 14(9), pp. 19276–19293.

Hu, H., Yang, W., Zeng, Q., Chen, W., Zhu, Y. Bin, Liu, W., Wang, S., Wang, B., Shao, Z. & Zhang, Y. (2020) 'Promising application of Pulsed Electromagnetic Fields (PEMFs) in musculoskeletal disorders', *Biomedicine and Pharmacotherapy*, 131p. 110767.

Huang, C.C., Hagar, K.L., Frost, L.E., Sun, Y. & Cheung, H.S. (2004) 'Effects of Cyclic Compressive Loading on Chondrogenesis of Rabbit Bone-Marrow Derived Mesenchymal Stem Cells', *Stem Cells*, 22(3), pp. 313–323.

Huang, K. & Wu, L.D. (2008) 'Aggrecanase and Aggrecan degradation in osteoarthritis: A review', *Journal of International Medical Research*, 36(6), pp. 1149–1160.

Hunziker, E.B., Quinn, T.M. & Häuselmann, H.J. (2002) 'Quantitative structural organization of normal adult human articular cartilage', *Osteoarthritis and Cartilage*, 10(7), pp. 564–572.

Hutmacher, D.W. (2006) 'Scaffolds in tissue engineering bone and cartilage', *The Biomaterials: Silver Jubilee Compendium*, 21pp. 175–189.

Iulian, A., Dan, L., Camelia, T., Claudia, M. & Sebastian, G. (2018) 'Synthetic Materials for Osteochondral Tissue Engineering', in J Miguel Oliveira, Sandra Pina, Rui L Reis, & Julio San Roman (eds.) *Osteochondral Tissue Engineering: Nanotechnology, Scaffolding-Related Developments and Translation*. [Online]. Cham: Springer International Publishing. pp. 31–52.

James, S., Fox, J., Afsari, F., Lee, J., Clough, S., Knight, C., Ashmore, J., Ashton, P., Preham, O., Hoogduijn, M., Ponzoni, R.D.A.R., Hancock, Y., Coles, M. & Genever, P. (2015) 'Multiparameter Analysis of Human Bone Marrow Stromal Cells Identifies Distinct Immunomodulatory and Differentiation-Competent Subtypes', *Stem Cell Reports*, 4(6), pp. 1004–1015.

Jamshidi, P., Chouhan, G., Williams, R.L., Cox, S.C. & Grover, L.M. (2016) 'Modification of gellan gum with nanocrystalline hydroxyapatite facilitates cell expansion and spontaneous osteogenesis', *Biotechnology and Bioengineering*, 113(7), pp. 1568–1576.

Jana, S., Levengood, S.K.L. & Zhang, M. (2016) 'Anisotropic Materials for Skeletal-Muscle-Tissue Engineering', *Advanced Materials*, 28(48), pp. 10588–10612.

Jeuken, R.M., Roth, A.K., Peters, R.J.R.W., van Donkelaar, C.C., Thies, J.C., van Rhijn, L.W. & Emans, P.J. (2016) 'Polymers in cartilage defect repair of the knee: Current status and future prospects', *Polymers*, 8(6), pp. 1–30.

Jia, S., Wang, J., Zhang, T., Pan, W., Li, Z., He, X., Yang, C., Wu, Q., Sun, W., Xiong, Z. & Hao, D. (2018) 'Multilayered Scaffold with a Compact Interfacial Layer Enhances Osteochondral Defect Repair', *ACS Applied Materials and Interfaces*, 10(24), pp. 20296–20305.

Jiang, L., Lin, J., Zhao, S., Wu, J., Jin, Y., Yu, L., Wu, N., Wu, Z., Wang, Y. & Lin, M. (2021) 'ADAMTS5 in Osteoarthritis: Biological Functions, Regulatory Network, and Potential Targeting Therapies', *Frontiers in Molecular Biosciences*, 8p. 692.

Jiang, X., Liu, J., Liu, Q., Lu, Z., Zheng, L., Zhao, J. & Zhang, X. (2018) 'Therapy for cartilage defects: Functional ectopic cartilage constructed by cartilage-simulating collagen, chondroitin sulfate and hyaluronic acid (CCH) hybrid hydrogel with allogeneic chondrocytes', *Biomaterials Science*, 6(6), pp. 1616–1626.

Jin, H., Jiang, S., Wang, R., Zhang, Y., Dong, J. & Li, Y. (2021) 'Mechanistic Insight Into the Roles of Integrins in Osteoarthritis', *Frontiers in Cell and Developmental Biology*, 9(June), .

Johnson, Craig I., Argyle, D.J. & Clements, D.N. (2016) 'In vitro models for the study of osteoarthritis', *Veterinary Journal*, 209pp. 40–49.

Johnson, Craig I, Argyle, D.J. & Clements, D.N. (2016) 'In vitro models for the study of osteoarthritis', *The Veterinary Journal*, 209pp. 40–49.

Kalamegam, G., Memic, A., Budd, E., Abbas, M. & Mobasheri, A. (2018) 'A Comprehensive Review of Stem Cells for Cartilage Regeneration in Osteoarthritis.', *Advances in experimental medicine and biology*,

Kaneki, H., Guo, R., Chen, D., Yao, Z., Schwarz, E.M., Zhang, Y.E., Boyce, B.F. & Xing, L. (2006) 'Tumor necrosis factor promotes Runx2 degradation through up-regulation of Smurf1 and Smurf2 in osteoblasts', *Journal of Biological Chemistry*, 281(7), pp. 4326–4333.

Kang, D., Zhang, H.-B., Nitta, Y., Fang, Y.-P. & Nishinari, K. (2015) 'Gellan', in Kishan Gopal Ramawat & Jean-Michel Mérillon (eds.) *Polysaccharides: Bioactivity and Biotechnology*. [Online]. Cham: Springer International Publishing. pp. 1627–1682.

Kapoor, M., Martel-Pelletier, J., Lajeunesse, D., Pelletier, J.P. & Fahmi, H. (2011) 'Role of proinflammatory cytokines in the pathophysiology of osteoarthritis', *Nature Reviews Rheumatology*, 7(1), pp. 33–42.

Karoyo, A.H. & Wilson, L.D. (2021) 'A review on the design and hydration properties of natural polymer-based hydrogels', *Materials*, 14(5), pp. 1–36.

Karsdal, M.A., Madsen, S.H., Christiansen, C., Henriksen, K., Fosang, A.J. & Sondergaard, B.C. (2008) 'Cartilage degradation is fully reversible in the presence of aggrecanase but not matrix metalloproteinase activity', *Arthritis Research and Therapy*, 10(3), pp. 1–12.

Katz, J.N. (2006) 'Total joint replacement in osteoarthritis', *Best Practice and Research: Clinical Rheumatology*, 20(1), pp. 145–153.

Kellgren, J.H. & Lawrence, J.S. (1956) 'RADIOLOGICAL ASSESSMENT OF OSTEO-ARTHROSIS', *Ann. rheum. Dis.*, 16(4), pp. 494–502.

Kelly, T.A.N., Roach, B.L., Weidner, Z.D., Mackenzie-Smith, C.R., O'Connell, G.D., Lima, E.G., Stoker, A.M., Cook, J.L., Ateshian, G.A. & Hung, C.T. (2013) 'Tissue-engineered articular cartilage exhibits tension-compression nonlinearity reminiscent of the native cartilage', *Journal of Biomechanics*, 46(11), pp. 1784–1791.

Kerin, A.J., Wisnom, M.R. & Adams, M.A. (1998) 'The compressive strength of articular cartilage', *Proceedings of the Institution of Mechanical Engineers, Part H: Journal of Engineering in Medicine*, 212(4), pp. 273–280.

Khrishnan, R., Park, S., Eckstein, F. & Ateshian, G.A. (2003) 'Inhomogeneous Cartilage Properties Enhance Superficial Interstitial Fluid Support and Frictional Properties, But Do not Provide a Homogeneous State of Stress Ramaswamyess', *J Biomech Eng*, 125(5), pp. 569–577.

Kiani, C., Chen, L., Wu, Y.J., Yee, A.J. & Yang, B.B. (2002) 'Structure and function of aggrecan', *Cell Research*, 12(1), pp. 19–32.

Kilmer, C.E., Battistoni, C.M., Cox, A., Breur, G.J., Panitch, A. & Liu, J.C. (2020) 'Collagen Type i and II Blend Hydrogel with Autologous Mesenchymal Stem Cells as a Scaffold for Articular Cartilage Defect Repair', *ACS Biomaterials Science and Engineering*, 6(6), pp. 3464–3476.

Kim, H., Kim, H.M., Jang, J.E., Kim, C.M., Kim, E.Y., Lee, D. & Khang, G. (2013) 'Osteogenic differentiation of bone marrow stem cell in poly(lactic-co-glycolic acid) scaffold loaded various ratio of hydroxyapatite', *International Journal of Stem Cells*, 6(1), pp. 67–74.

Kim, S. jeong, Kim, E.M., Yamamoto, M., Park, H. & Shin, H. (2020) 'Engineering Multi-Cellular Spheroids for Tissue Engineering and Regenerative Medicine', *Advanced Healthcare Materials*, 9(23), pp. 1–18.

Kim, T.K., Sharma, B., Williams, C.G., Ruffner, M.A., Malik, A., McFarland, E.G. & Elisseeff, J.H. (2003) 'Experimental model for cartilage tissue engineering to regenerate the zonal organization of articular cartilage', *Osteoarthritis and Cartilage*, 11(9), pp. 653–664.

Kirchmajer, D.M. & Panhuis, M. In Het (2014) 'Robust biopolymer based ionic-covalent entanglement hydrogels with reversible mechanical behaviour', *Journal of Materials Chemistry B*, 2(29), pp. 4694–4702.

Klein, T.J., Chaudhry, M., Bae, W.C. & Sah, R.L. (2007) 'Depth-dependent biomechanical and biochemical properties of fetal, newborn, and tissue-engineered articular cartilage', *Journal of Biomechanics*, 40(1), pp. 182–190.

Klein, T.J., Malda, J., Sah, R.L. & Hutmacher, D.W. (2009) 'Tissue Engineering of Articular Cartilage with Biomimetic Zones', *Tissue Engineering Part B: Reviews*, 15(2), pp. 143–157.

Klein, T.J., Schumacher, B.L., Schmidt, T.A., Li, K.W., Voegtline, M.S., Masuda, K., Thonar, E.J.M.A. & Sah, R.L. (2003) 'Tissue engineering of stratified articular cartilage from chondrocyte subpopulations', *Osteoarthritis and Cartilage*, 11(8), pp. 595–602.

Kloppenburg, M. & Berenbaum, F. (2020) 'Osteoarthritis year in review 2019: epidemiology and therapy', *Osteoarthritis and Cartilage*, 28(3), pp. 242–248.

Kock, L., van Donkelaar, C.C. & Ito, K. (2012) 'Tissue engineering of functional articular cartilage: The current status', *Cell and Tissue Research*, 347(3), pp. 613–627.

Koivisto, J.T., Gering, C., Karvinen, J., Maria Cherian, R., Belay, B., Hyttinen, J., Aalto-Setälä, K., Kellomäki, M. & Parraga, J. (2019) 'Mechanically Biomimetic Gelatin-Gellan Gum Hydrogels for 3D Culture of Beating Human Cardiomyocytes', *ACS Applied Materials and Interfaces*, 11(23), pp. 20589–20602.

Korneva, J. v, Karalkin, P.A., Gladkaya, I.S. & Gryadunova, A.A. (2017) *The Scalable Standardized Biofabrication of Tissue Spheroids from Different Cell Types Using Nonadhesive Technology*, 4(1), pp. 53–60.

Korpayev, S., Kaygusuz, G., Şen, M., Orhan, K., Oto, Ç. & Karakeçili, A. (2020) 'Chitosan/collagen based biomimetic osteochondral tissue constructs: A growth factor-free approach', *International Journal of Biological Macromolecules*, 156pp. 681–690.

Koudan, E. V., Gryadunova, A.A., Karalkin, P.A., Korneva, J. V., Meteleva, N.Y., Babichenko, I.I., Volkov, A. V., Rodionov, S.A., Parfenov, V.A., Pereira, F.D.A.S., Khesuani, Y.D., Mironov, V.A. & Bulanova, E.A. (2020) 'Multiparametric Analysis of Tissue Spheroids Fabricated from Different Types of Cells', *Biotechnology Journal*, 1900217pp. 1–12.

Kreuz, P.C., Müller, S., Ossendorf, C., Kaps, C. & Erggelet, C. (2009) 'Treatment of focal degenerative cartilage defects with polymer-based autologous chondrocyte grafts: Four-year clinical results', *Arthritis Research and Therapy*, 11(2), .

Kumar, R., Pierce, D.M., Isaksen, V., Davies, C.D.L., Drogset, J.O. & Lilledahl, M.B. (2018) 'Comparison of compressive stress-relaxation behavior in osteoarthritic (ICRS graded) human articular cartilage', *International Journal of Molecular Sciences*, 19(2), .

Kwon, H., Brown, W.E., Lee, C.A., Wang, D., Paschos, N., Hu, J.C. & Athanasiou, K.A. (2019) 'Surgical and tissue engineering strategies for articular cartilage and meniscus repair', *Nature Reviews Rheumatology*, 15(9), pp. 550–570.

Lafont, J.E. (2010) 'Lack of oxygen in articular cartilage: Consequences for chondrocyte biology', *International Journal of Experimental Pathology*, 91(2), pp. 99–106.

Lakshminarayanan, S. (2018) 'Micro/Nano Patterning on Polymers Using Soft Lithography Technique', *Micro/Nanolithography - A Heuristic Aspect on the Enduring Technology*, (May), .

Lattermann, C. (2022) *Early Osteoarthritis*.

Le, L.T.T., Swingler, T.E., Crowe, N., Vincent, T.L., Barter, M.J., Donell, S.T., Delany, A.M., Dalmay, T., Young, D.A. & Clark, I.M. (2016) 'The microRNA-29 family in cartilage homeostasis and osteoarthritis', *Journal of Molecular Medicine*, 94(5), pp. 583–596.

Lee, D.A. & Bader, D.L. (1997) 'Compressive strains at physiological frequencies influence the metabolism of chondrocytes seeded in agarose', *Journal of Orthopaedic Research*, 15(2), pp. 181–188.

Lee, J.H., Badar, F., Matyas, J., Qu, X. & Xia, Y. (2016) 'Topographical variations in zonal properties of canine tibial articular cartilage due to early osteoarthritis: a study using 7-T magnetic resonance imaging at microscopic resolution', *MAGMA*, 29(4), pp. 681–690.

Lee, J.K., Link, J.M., Hu, J.C.Y. & Athanasiou, K.A. (2017) 'The self-assembling process and applications in tissue engineering', *Cold Spring Harbor Perspectives in Medicine*, 7(11), pp. 1–18.

Lee, S., Choi, J., Youn, J., Lee, Y., Kim, W., Choe, S., Song, J., Reis, R.L. & Khang, G. (2021) 'Development and evaluation of gellan gum/silk fibroin/chondroitin sulfate ternary injectable hydrogel for cartilage tissue engineering', *Biomolecules*, 11(8), pp. 1–17.

Lencel, P., Delplace, S., Hardouin, P. & Magne, D. (2011) 'TNF-α stimulates alkaline phosphatase and mineralization through PPARγ inhibition in human osteoblasts', *Bone*, 48(2), pp. 242–249.

Lepage, S.I.M., Robson, N., Gilmore, H., Davis, O., Hooper, A., St John, S., Kamesan, V., Gelis, P., Carvajal, D., Hurtig, M. & Koch, T.G. (2019) 'Beyond Cartilage Repair: The Role of the Osteochondral Unit in Joint Health and Disease', *Tissue Engineering - Part B: Reviews*, 25(2), pp. 114–125.

Leung, B.M., Lesher-Perez, S.C., Matsuoka, T., Moraes, C. & Takayama, S. (2015) 'Media additives to promote spheroid circularity and compactness in hanging drop platform', *Biomaterials Science*, 3(2), pp. 336–344.

Levorson, E.J., Sreerekha, P.R., Chennazhi, K.P., Kasper, F.K., Nair, S. V & Mikos, A. (2014) *Fabrication and characterization of multiscale electrospun scaffolds for cartilage regeneration*, 8(1), pp. 1–22.

Li, H., Davison, N., Moroni, L., Feng, F., Crist, J., Salter, E., Bingham, C.O. & Elisseeff, J. (2012) *Evaluating Osteoarthritic Chondrocytes through a Novel 3-Dimensional In Vitro System for Cartilage Tissue Engineering and Regeneration*,

Li, L., Newton, P.T., Bouderlique, T., Sejnohova, M., Zikmund, T., Kozhemyakina, E., Xie, M., Krivanek, J., Kaiser, J., Qian, H., Dyachuk, V., Lassar, A.B., Warman, M.L., Barenius, B., Adameyko, I. & Chagin, A.S. (2017) 'Superficial cells are self-renewing chondrocyte progenitors, which form the articular cartilage in juvenile mice', *FASEB Journal*, 31(3), pp. 1067–1084.

Li, L.P., Buschmann, M.D. & Shirazi-Adl, A. (2003) 'Strain-rate Dependent Stiffness of Articular Cartilage in Unconfined Compression', *Journal of Biomechanical Engineering*, 125(2), pp. 161–168.

Li, Q., Xu, S., Feng, Q., Dai, Q., Yao, L., Zhang, Y., Gao, H., Dong, H., Chen, D. & Cao, X. (2021) '3D printed silk-gelatin hydrogel scaffold with different porous structure and cell seeding strategy for cartilage regeneration', *Bioactive Materials*, 6(10), pp. 3396–3410.

Li, X., Liu, B., Pei, B., Chen, J., Zhou, D., Peng, J., Zhang, X., Jia, W. & Xu, T. (2020) 'Inkjet Bioprinting of Biomaterials', *Chemical Reviews*, 120(19), pp. 10793–10833.

Li, X., Xu, Q., Johnson, M., Wang, X., Lyu, J., Li, Y., McMahon, S., Greiser, U., Sigen, A. & Wang, W. (2021) 'A chondroitin sulfate based injectable hydrogel for delivery of stem cells in cartilage regeneration', *Biomaterials Science*, 9(11), pp. 4139–4148.

Li, Y., Wei, X., Li, P., Chen, C., Wang, X., Jiao, Q., Wang, D., Wei, F., Zhang, J. & Wei, L. (2015) 'The Role of miRNAs in Cartilage Homeostasis', *Current Genomics*, 16(6), pp. 393–404.

Li, Y., Yuan, F., Song, Y. & Guan, X. (2020) 'miR-17-5p and miR-19b-3p prevent osteoarthritis progression by targeting EZH2', *Experimental and Therapeutic Medicine*, 20(2), pp. 1653–1663.

Libera, J., Anderer, U., Fritsch, K.-G. & Josimovic-Alasevic Olivera; (2012) 'METHOD FOR IN VITRO PRODUCTION OF THREE-DIMIENSIONAL VITAL CARTILAGE TSSUE AND USE THEREOF AS TRANSPLANT MATERAL', *United states patent*, 2(12), .

Licini, C., Montalbano, G., Ciapetti, G., Cerqueni, G., Vitale-Brovarone, C. & Mattioli-Belmonte, M. (2020) 'Analysis of multiple protein detection methods in human osteoporotic bone extracellular matrix: From literature to practice', *Bone*, 137(January), p. 115363.

Lima, J., Gonçalves, A.I., Rodrigues, M.T., Reis, R.L. & Gomes, M.E. (2015) 'The effect of magnetic stimulation on the osteogenic and chondrogenic differentiation of human stem cells derived from the adipose tissue (hASCs)', *Journal of Magnetism and Magnetic Materials*, 393pp. 526–536.

Lin, P.M., Chen, C.T.C. & Torzilli, P.A. (2004) 'Increased stromelysin-1 (MMP-3), proteoglycan degradation (3B3- and 7D4) and collagen damage in cyclically load-injured articular cartilage', *Osteoarthritis and Cartilage*, 12(6), pp. 485–496.

Liu, C.F. & Lefebvre, V. (2015) 'The transcription factors SOX9 and SOX5/SOX6 cooperate genome-wide through super-enhancers to drive chondrogenesis', *Nucleic Acids Research*, 43(17), pp. 8183–8203.

Liu, J., Li, L., Suo, H., Yan, M., Yin, J. & Fu, J. (2019) '3D printing of biomimetic multi-layered GelMA/nHA scaffold for osteochondral defect repair', *Materials and Design*, 171p. 107708.

Liu, J., Yang, B., Li, M., Li, J. & Wan, Y. (2020) 'Enhanced dual network hydrogels consisting of thiolated chitosan and silk fibroin for cartilage tissue engineering', *Carbohydrate Polymers*, 227(August 2019), p. 115335.

Liu, X., Howard, K.A., Dong, M., Andersen, M., Rahbek, U.L., Johnsen, M.G., Hansen, O.C., Besenbacher, F. & Kjems, J. (2007) 'The influence of polymeric properties on chitosan/siRNA nanoparticle formulation and gene silencing', *Biomaterials*, 28(6), pp. 1280–1288.

Livak, K.J. & Schmittgen, T.D. (2001a) 'Analysis of relative gene expression data using real-time quantitative PCR and the 2-ΔΔCT method', *Methods*, 25(4), pp. 402–408.

Livak, K.J. & Schmittgen, T.D. (2001b) 'Analysis of relative gene expression data using real-time quantitative PCR and the 2-ΔΔCT method', *Methods*, 25(4), pp. 402–408.

Loeser, R.F. (2014) 'Integrins and chondrocyte-matrix interactions in articular cartilage', *Matrix Biology*, 39pp. 11–16.

Löfgren, M., Svala, E., Lindahl, A., Skiöldebrand, E. & Ekman, S. (2018) 'Time-dependent changes in gene expression induced in vitro by interleukin-1β in equine articular cartilage', *Research in Veterinary Science*, 118(April), pp. 466–476.

Luo, Y. & Amromanoh, O. (2021) 'Bone Organic-Inorganic Phase Ratio Is a Fundamental Determinant of Bone Material Quality', *Applied Bionics and Biomechanics*, 2021.

Luo, Y. & Wu, X. (2020) 'Bone Quality is Dependent on the Quantity and Quality of Organic–Inorganic Phases', *Journal of Medical and Biological Engineering*, 40(2), pp. 273–281.

Lusby, P.E., Coombes, A.L. & Wilkinson, J.M. (2005) *Bactericidal Activity of Different Honeys against Pathogenic Bacteria*, 36pp. 464–467.

Lutz, W., Sanderson, W. & Scherbov, S. (2008) 'The coming acceleration of global population ageing', *Nature*, 451p. 716.

Ma, P.X. & Zhang, R. (1999) 'Synthetic nano-scale fibrous extracellular matrix', *Journal of Biomedical Materials Research*, 46(1), pp. 60–72.

Maddocks, S.E., Jenkins, R.E., Samuel, R., Purdy, K.J. & Cooper, R.A. (2013) *Manuka honey inhibits adhesion and invasion of medically important wound bacteria*, pp. 1523–1536.

Madry, H., Gao, L., Eichler, H., Orth, P. & Cucchiarini, M. (2017) 'Bone Marrow Aspirate Concentrate-Enhanced Marrow Stimulation of Chondral Defects', *Stem Cells International*, 2017.

Mallet, J., Lembo, D. & Cagno, V. (2016) *Galus et al ., 2016 Carbohydrate Polymers-Supporting data Supporting data - Hexagonal-shaped chondroitin sulfate self-assemblies have exalted anti-HSV-2 activity*, (September 2015), .

March L, Cross M, Arden N, Hawker G. (2016) 'Osteoarthritis: A Serious Disease, Submitted to the U. S. Food and Drug Administration', *Oarsi*, pp. 1–103.

Marlovits, S., Hombauer, M., Truppe, M., Vècsei, V. & Schlegel, W. (2004) 'Changes in the ratio of type-I and type-II collagen expression during monolayer culture of human chondrocytes', *Journal of Bone and Joint Surgery - Series B*, 86(2), pp. 286–295.

Martel-Pelletier, J., Barr, A.J., Cicuttini, F.M., Conaghan, P.G., Cooper, C., Goldring, M.B., Goldring, S.R., Jones, G., Teichtahl, A.J. & Pelletier, J.P. (2016) 'Osteoarthritis', *Nature Reviews Disease Primers*, 2.

Maruotti, N., Corrado, A. & Cantatore, F.P. (2017) 'Osteoblast role in osteoarthritis pathogenesis', *Journal of Cellular Physiology*, 232(11), pp. 2957–2963.

Marycz, K., Smieszek, A., Targonska, S., Walsh, S.A., Szustakiewicz, K. & Wiglusz, R.J. (2020) 'Three dimensional (3D) printed polylactic acid with nano-hydroxyapatite doped with europium(III) ions (nHAp/PLLA@Eu3+) composite for osteochondral defect regeneration and theranostics', *Materials Science and Engineering C*, 110(April 2019), p. 110634.

Massari, L., Benazzo, F., Falez, F., Perugia, D., Pietrogrande, L., Setti, S., Osti, R., Vaienti, E., Ruosi, C. & Cadossi, R. (2019) 'Biophysical stimulation of bone and cartilage: state of the art and future perspectives', *International Orthopaedics*, 43(3), pp. 539–551.

Mathy-Hartert, M., Hogge, L., Sanchez, C., Deby-Dupont, G., Crielaard, J.M. & Henrotin, Y. (2008) 'Interleukin-1β and interleukin-6 disturb the antioxidant enzyme system in bovine chondrocytes: a possible explanation for oxidative stress generation', *Osteoarthritis and Cartilage*, 16(7), pp. 756–763.

Matsumoto, T., Tadokoro, M., Hattori, K., Ougushi, H. & Satou, J. (2011) 'Osteogenic Differentiation of Mesenchymal Stem Cells/Polymer Composites with HA In Vitro', *Bioceramics Development and Applications*, 1pp. 1–4.

Matsusue, Y., Yamamuro, T. & Hama, H. (1993) 'Arthroscopic multiple osteochondral transplantation to the chondral defect in the knee associated with anterior cruciate ligament disruption', *Arthroscopy: The Journal of Arthroscopic & Related Surgery*, 9(3), pp. 318–321.

Matyas, J.R., Huang, D., Chung, M. & Adams, M.E. (2002) 'Regional quantification of cartilage type II collagen and aggrecan messenger RNA in joints with early experimental osteoarthritis', *Arthritis and Rheumatism*, 46(6), pp. 1536–1543.

Mauck, R.L., Yuan, X. & Tuan, R.S. (2006) 'Chondrogenic differentiation and functional maturation of bovine mesenchymal stem cells in long-term agarose culture', *Osteoarthritis and Cartilage*, 14(2), pp. 179–189.

McCarthy, H.S. & Roberts, S. (2013) 'A histological comparison of the repair tissue formed when using either Chondrogide® or periosteum during autologous chondrocyte implantation', *Osteoarthritis and Cartilage*, 21(12), pp. 2048–2057.

McClurg, O., Tinson, R. & Troeberg, L. (2021) 'Targeting cartilage degradation in osteoarthritis', *Pharmaceuticals*, 14(2), pp. 1–19.

McCormick, F., Cole, B.J., Nwachukwu, B., Harris, J.D., Adkisson, H.D. & Farr, J. (2013) 'Treatment of focal cartilage defects with a juvenile allogeneic 3-dimensional articular cartilage graft', *Operative Techniques in Sports Medicine*, 21(2), pp. 95–99.

McIlwraith, C.W., Frisbie, D.D., Kawcak, C.E., Fuller, C.J., Hurtig, M. & Cruz, A. (2010) 'The OARSI histopathology initiative - recommendations for histological assessments of osteoarthritis in the horse', *Osteoarthritis and Cartilage*, 18(SUPPL. 3), pp. S93–S105.

Meliconi, R., Pulsatelli, L., Addimanda, O., Brusi, V. & Pavloska, B. (2013) 'New findings in osteoarthritis pathogenesis: Therapeutic implications', *Therapeutic Advances in Chronic Disease*, 4(1), pp. 23–43.

Mente, P.L. & Lewis, J.L. (1989) 'Experimental method for the measurement of the elastic modulus of trabecular bone tissue', *Journal of Orthopaedic Research*, 7(3), pp. 456–461.

Mescher, A. (2016) *Junqueira's Basic Histology Text & Atlas (14th ed.)*.

Middendorf, J.M., Dugopolski, C., Kennedy, S., Blahut, E., Cohen, I. & Bonassar, L.J. (2020) 'Heterogeneous matrix deposition in human tissue engineered cartilage changes the local shear modulus and resistance to local construct buckling', *Journal of Biomechanics*, (xxxx), .

Mieloch, A.A., Richter, M., Trzeciak, T., Giersig, M. & Dalibor Rybka, J. (n.d.) *Clinical Medicine Osteoarthritis Severely Decreases the Elasticity and Hardness of Knee Joint Cartilage: A Nanoindentation Study*,

Miller, I., Min, M., Yang, C., Tian, C., Gookin, S., Carter, D. & Spencer, S.L. (2018) 'Ki67 is a Graded Rather than a Binary Marker of Proliferation versus Quiescence', *Cell Reports*, 24(5), pp. 1105-1112.e5.

Miyaki, S., Sato, T., Inoue, A., Otsuki, S., Ito, Y., Yokoyama, S., Kato, Y., Takemoto, F., Nakasa, T., Yamashita, S., Takada, S., Lotz, M.K., Ueno-Kudo, H. & Asahara, H. (2010) 'MicroRNA-140 plays dual roles in both cartilage development and homeostasis', *Genes and Development*, 24(11), pp. 1173–1185.

Miyoshi, E., Takaya, T. & Nishinari, K. (1996) 'Rheological and thermal studies of gel-sol transition in gellan gum aqueous solutions', *Carbohydrate Polymers*, 30(2–3), pp. 109–119.

Mobasheri, A., Kalamegam, G., Musumeci, G. & Batt, M.E. (2014) 'Chondrocyte and mesenchymal stem cell-based therapies for cartilage repair in osteoarthritis and related orthopaedic conditions', *Maturitas*, 78(3), pp. 188–198.

Mohan, N., Mohanan, P. V., Sabareeswaran, A. & Nair, P. (2017) 'Chitosan-hyaluronic acid hydrogel for cartilage repair', *International Journal of Biological Macromolecules*, 104pp. 1936–1945.

De Moor, L., Beyls, E. & Declercq, H. (2020) 'Scaffold Free Microtissue Formation for Enhanced Cartilage Repair', *Annals of Biomedical Engineering*, 48(1), pp. 298–311.

de Moor, L., Fernandez, S., Vercruysse, C., Tytgat, L., Asadian, M., de Geyter, N., van Vlierberghe, S., Dubruel, P. & Declercq, H. (2020) 'Hybrid Bioprinting of Chondrogenically Induced Human Mesenchymal Stem Cell Spheroids', *Frontiers in Bioengineering and Biotechnology*, 8(May), pp. 1–20.

Moorhouse, R., Colegrove, G.T., Sandford, P.A., Baird, J.K. & Kang, K.S. (1981) 'Solution Properties of Polysaccharides', in *ACS Symposium series*. [Online]. 1981 p. 111.

Moreira Teixeira, L.S., Leijten, J.C.H., Sobral, J., Jin, R., van Apeldoorn, A.A., Feijen, J., van Blitterswijk, C., Dijkstra, P.J. & Karperien, M. (2012) 'High throughput generated micro-aggregates of chondrocytes stimulate cartilage formation in vitro and in vivo', *European Cells and Materials*, 23(June), pp. 387–399.

Mori, M., Nakajima, M., Mikami, Y., Seki, S., Takigawa, M., Kubo, T. & Ikegawa, S. (2006) 'Transcriptional regulation of the cartilage intermediate layer protein (CILP) gene', *Biochemical and Biophysical Research Communications*, 341(1), pp. 121–127.

Mouser, V.H.M., Levato, R., Mensinga, A., Dhert, W.J.A., Gawlitta, D. & Malda, J. (2020) 'Bio-ink development for three-dimensional bioprinting of hetero-cellular cartilage constructs', *Connective Tissue Research*, 61(2), pp. 137–151.

Mouser, V.H.M., Melchels, F.P.W., Visser, J., Dhert, W.J.A., Gawlitta, D. & Malda, J. (2016) 'Yield stress determines bioprintability of hydrogels based on gelatin-methacryloyl and gellan gum for cartilage bioprinting', *Biofabrication*, 8(3), .

Mow, V.C., Kuei, S.C., Lai, W.M. & Armstrong, C.G. (1980) 'Biphasic creep and stress relaxation of articular cartilage in compression: Theory and experiments', *Journal of Biomechanical Engineering*, 102(1), pp. 73–84.

Muldrew, K., Chung, M., Novak, K., Schachar, N.S., Zernicke, R.F., Mcgann, L.E., Rattner, J.B. & Matyas, J.R. (2001) *Evidence of chondrocyte repopulation in adult ovine articular cartilage following cryoinjury and long-term transplantation*, pp. 432–439.

Munir, N., McDonald, A. & Callanan, A. (2020) 'Integrational Technologies for the Development of Three-Dimensional Scaffolds as Platforms in Cartilage Tissue Engineering', *ACS Omega*, 5(22), pp. 12623–12636.

Murphy, C.L., Thoms, B.L., Vaghjiani, R.J. & Lafont, J.E. (2009) 'Hypoxia. HIF-mediated articular chondrocyte function: prospects for cartilage repair.', *Arthritis research & therapy*, 11(1), p. 213.

Murphy, S. V. & Atala, A. (2014) '3D bioprinting of tissues and organs', *Nature Biotechnology*, 32(8), pp. 773–785.

Murray, I.R., Benke, M.T. & Mandelbaum, B.R. (2016) 'Management of knee articular cartilage injuries in athletes: chondroprotection, chondrofacilitation, and resurfacing', *Knee Surgery, Sports Traumatology, Arthroscopy*, 24(5), pp. 1617–1626.

Muzzarelli, R.A.A., Greco, F., Busilacchi, A., Sollazzo, V. & Gigante, A. (2012) 'Chitosan, hyaluronan and chondroitin sulfate in tissue engineering for cartilage regeneration: A review', *Carbohydrate Polymers*, 89(3), pp. 723–739.

Nagase, H. & Kashiwagi, M. (2003) 'Aggrecanases and cartilage matrix degradation', *Arthritis Research and Therapy*, 5(2), pp. 94–103.

Narkhede, A.A. & Rao, S.S. (2017) *Electrospun Biomaterials for Cancer Research BT - Electrospun Biomaterials and Related Technologies*, in Jorge Almodovar (ed.) [Online]. Cham: Springer International Publishing. pp. 169–205.

National Institute For Health and Care Excellence (2017a) *Autologous chondrocyte implantation for treating symptomatic articular cartilage defects of the knee*, pp. 1–25.

National Institute For Health and Care Excellence (2017b) *Final appraisal determination-Autologous chondrocyte implantation using chondrosphere for treating symptomatic articular cartilage defects of the knee*, (December), p. 16.

Nava, M.M., Draghi, L., Giordano, C. & Pietrabissa, R. (2016) 'The effect of scaffold pore size in cartilage tissue engineering', *Journal of Applied Biomaterials and Functional Materials*, 14(3), pp. e223–e229.

Nefla, M., Holzinger, D., Berenbaum, F. & Jacques, C. (2016) 'The danger from within: Alarmins in arthritis', *Nature Reviews Rheumatology*, 12(11), pp. 669–683.

Neogi, T. (2013) 'The epidemiology and impact of pain in osteoarthritis', *Osteoarthritis and Cartilage*, 21(9), pp. 1145–1153.

Ng, H.Y., Lee, K.A. & Shen, Y. (2017) 'Articular Cartilage : Structure , Composition , Injuries and Repair', *JSM Bone and Joint Diseases*, 1(2), pp. 1–6.

Ngadimin, K.D., Stokes, A., Gentile, P. & Ferreira, A.M. (2021) 'Biomimetic hydrogels designed for cartilage tissue engineering', *Biomaterials Science*, 9(12), pp. 4246–4259.

O'Brien, J., Hayder, H., Zayed, Y. & Peng, C. (2018) 'Overview of microRNA biogenesis, mechanisms of actions, and circulation', *Frontiers in Endocrinology*, 9(AUG), pp. 1–12.

Ogura, T., Mosier, B.A., Bryant, T. & Minas, T. (2017) 'A 20-Year Follow-up after First-Generation Autologous Chondrocyte Implantation', *American Journal of Sports Medicine*, 45(12), pp. 2751–2761.

Okamura, Y., Aoki, Y., Obayashi, T., Tadaka, S., Ito, S., Narise, T. & Kinoshita, K. (2015) 'COXPRESdb in 2015: Coexpression database for animal species by DNA-microarray and RNAseq-based expression data with multiple quality assessment systems', *Nucleic Acids Research*, 43(D1), pp. D82–D86.

Oliveira, J.M., Caridade, S.G., Oliveira, J.T., Sousa, R.A. & Mano, J.F. (2011) *Gellan gum-based hydrogels for intervertebral disc tissue-engineering applications*, (December 2010), pp. 97–107.

Oliveira, J.T., Martins, L., Picciochi, R., Malafaya, P.B., Sousa, R.A., Neves, N.M., Mano, J.F. & Reis, R.L. (2009) *Gellan gum : A new biomaterial for cartilage tissue engineering applications*,

Omelyanenko, N.P., Karalkin, P.A., Bulanova, E.A., Koudan, E. V., Parfenov, V.A., Rodionov, S.A., Knyazeva, A.D., Kasyanov, V.A., Babichenko, I.I., Chkadua, T.Z., Khesuani, Y.D., Gryadunova, A.A. & Mironov, V.A. (2018) 'Extracellular Matrix Determines Biomechanical Properties of Chondrospheres during Their Maturation In Vitro', *Cartilage*,

Osidak, E.O., Kozhukhov, V.I., Osidak, M.S. & Domogatsky, S.P. (2020) *Collagen as Bioink for Bioprinting : A Comprehensive Review*, pp. 1–10.

Owida, H.A., Yang, R., Cen, L., Kuiper, N.J. & Yang, Y. (2018) 'Induction of zonal-specific cellular morphology and matrix synthesis for biomimetic cartilage regeneration using hybrid scaffolds', *Journal of the Royal Society Interface*, 15(143), .

Pacelli, S., Paolicelli, P., Moretti, G., Petralito, S., Di Giacomo, S., Vitalone, A. & Casadei, M.A. (2016) 'Gellan gum methacrylate and laponite as an innovative nanocomposite hydrogel for biomedical applications', *European Polymer Journal*, 77pp. 114–123.

Palumbo, F.S., Federico, S., Pitarresi, G., Fiorica, C. & Giammona, G. (2020) 'Gellan gum-based delivery systems of therapeutic agents and cells', *Carbohydrate Polymers*, 229(June 2019), p. 115430.

Papadaki, M., Rinotas, V., Violitzi, F., Thireou, T., Panayotou, G., Samiotaki, M. & Douni, E. (2019) 'New insights for RANKL as a proinflammatory modulator in modeled inflammatory arthritis', *Frontiers in Immunology*, 10(FEB), pp. 1–19.

Park, S.H., Seo, J.Y., Park, J.Y., Ji, Y.B., Kim, K., Choi, H.S., Choi, S., Kim, J.H., Min, B.H. & Kim, M.S. (2019) 'An injectable, click-crosslinked, cytomodulin-modified hyaluronic acid hydrogel for cartilage tissue engineering', *NPG Asia Materials*, 11(1), pp. 1–16.

Park, S.J., Cheon, E.J., Lee, M.H. & Kim, H.A. (2013) 'MicroRNA-127-5p regulates matrix metalloproteinase 13 expression and interleukin-1β-induced catabolic effects in human chondrocytes', *Arthritis and Rheumatism*, 65(12), pp. 3141–3152.

Peric, M., Dumic-Cule, I., Grcevic, D., Matijasic, M., Verbanac, D., Paul, R., Grgurevic, L., Trkulja, V., Bagi, C.M. & Vukicevic, S. (2015) 'The rational use of animal models in the evaluation of novel bone regenerative therapies', *Bone*, 70pp. 73–86.

Pierantozzi, D., Scalzone, A., Jindal, S., Stīpniece, L., Šalma-Ancāne, K., Dalgarno, K., Gentile, P. & Mancuso, E. (2020) '3D printed Sr-containing composite scaffolds: Effect of structural design and material formulation towards new strategies for bone tissue engineering', *Composites Science and Technology*, 191.

De Pieri, A., Rochev, Y. & Zeugolis, D.I. (2021) 'Scaffold-free cell-based tissue engineering therapies: advances, shortfalls and forecast', *npj Regenerative Medicine*, 6(1), .

Piluso, S., Li, Y., Abinzano, F., Levato, R., Teixeira, L.M., Karperien, M., Leijten, J., Weeren, R. van & Malda, J. (2019) 'Mimicking the Articular Joint with In Vitro Models', *Trends in Biotechnology*, xxpp. 1–15.

Porter, S.;, Clark, I.M.;, Kevorkian, L. & Edwards, D. (2005) 'The ADAMTS metalloproteinases Sarah', *Biochemical Journal*, 386pp. 15–27.

Prabu, P., Rome, S., Sathishkumar, C., Aravind, S., Mahalingam, B., Shanthirani, C.S., Gastebois, C., Villard, A., Mohan, V. & Balasubramanyam, M. (2015) 'Circulating miRNAs of "Asian Indian phenotype" identified in subjects with impaired glucose tolerance and patients with type 2 diabetes', *PLoS ONE*, 10(5), pp. 1–14.

Pritzker, K.P.H., Gay, S., Jimenez, S.A., Ostergaard, K., Pelletier, J.P., Revell, K., Salter, D. & van den Berg, W.B. (2006) 'Osteoarthritis cartilage histopathology: Grading and staging', *Osteoarthritis and Cartilage*, 14(1), pp. 13–29.

Puelacher, W.C., Kim, S.W., Vacanti, J.P., Schloo, B., Mooney, D. & Vacanti, C.A. (1994) 'Tissue-engineered growth of cartilage: the effect of varying the concentration of chondrocytes seeded onto synthetic polymer matrices', *International Journal of Oral and Maxillofacial Surgery*, 23(1), pp. 49–53.

Qin, D., Xia, Y. & Whitesides, G.M. (2010) 'Soft lithography for micro- and nanoscale patterning', *Nature Protocols*, 5(3), pp. 491–502.

Quinn, F.X., Hatakeyama, T., Yoshida, H., Takahashi, M. & Hatakeyama, H. (1993) 'The conformational properties of gellan gum hydrogels', *Polymer Gels and Networks*, 1(2), pp. 93–114.

Quinn, T.M., Hunziker, E.B. & Häuselmann, H.J. (2005) 'Variation of cell and matrix morphologies in articular cartilage among locations in the adult human knee', *Osteoarthritis and Cartilage*, 13(8), pp. 672–678.

Raghothaman, D., Leong, M.F., Lim, T.C., Toh, J.K.C., Wan, A.C.A., Yang, Z. & Lee, E.H. (2014) 'Engineering cell matrix interactions in assembled polyelectrolyte fiber hydrogels for mesenchymal stem cell chondrogenesis', *Biomaterials*, 35(9), pp. 2607–2616.

Ravalli, S., Szychlinska, M.A., Lauretta, G. & Musumeci, G. (2020) 'New insights on mechanical stimulation of mesenchymal stem cells for cartilage regeneration', *Applied Sciences (Switzerland)*, 10(8), .

Ren, X., Li, Jinxiu, Li, Jiayi, Jiang, Y., Li, L., Yao, Q., Ke, Q. & Xu, H. (2019) 'Aligned porous fibrous membrane with a biomimetic surface to accelerate cartilage regeneration', *Chemical Engineering Journal*, 370(March), pp. 1027–1038.

Ren, X., Wang, F., Chen, C., Gong, X., Yin, L. & Yang, L. (2016a) 'Engineering zonal cartilage through bioprinting collagen type II hydrogel constructs with biomimetic chondrocyte density gradient', *BMC Musculoskeletal Disorders*, 17(1), pp. 1–10.

Ren, X., Wang, F., Chen, C., Gong, X., Yin, L. & Yang, L. (2016b) 'Engineering zonal cartilage through bioprinting collagen type II hydrogel constructs with biomimetic chondrocyte density gradient', *BMC Musculoskeletal Disorders*, 17(1), pp. 1–10.

Richards Grayson, A.C., Doody, A.M. & Putnam, D. (2006) 'Biophysical and structural characterization of polyethylenimine-mediated siRNA delivery in vitro', *Pharmaceutical Research*, 23(8), pp. 1868–1876.

Rikkers, M., Korpershoek, J. V., Levato, R., Malda, J. & Vonk, L.A. (2022) 'The clinical potential of articular cartilage-derived progenitor cells: a systematic review', *npj Regenerative Medicine*, 7(1), pp. 1–20.

Rodrigues, N., Benning, M., Ferreira, A.M., Dixon, L. & Dalgarno, K. (2016) 'Manufacture and Characterisation of Porous PLA Scaffolds', *Procedia CIRP*, 49pp. 33–38.

Roughley, P.J. (2001) 'Articular cartilage and changes in arthritis noncollagenous proteins and proteoglycans in the extracellular matrix of cartilage', *Arthritis Research*, 3(6), pp. 342–347.

Roughley, P.J. (2006) 'The structure and function of cartilage proteoglycans', *European Cells and Materials*, 12pp. 92–101.

Roughley, P.J. & Mort, J.S. (2014) 'The role of aggrecan in normal and osteoarthritic cartilage', *Journal of Experimental Orthopaedics*, 1(1), pp. 1–11.

Ruan, M.Z.C., Erez, A., Guse, K., Dawson, B., Bertin, T., Chen, Y., Jiang, M.-M., Yustein, J., Gannon, F. & Lee, B.H.L. (2013) 'PROTEOGLYCAN 4 EXPRESSION PROTECTS AGAINST THE DEVELOPMENT OF OSTEOARTHRITIS', *Sci Transl Med.*, 13(5), .

Saarakkala, S., Töyräs, J., Hirvonen, J., Laasanen, M.S., Lappalainen, R. & Jurvelin, J.S. (2004) 'Ultrasonic quantitation of superficial degradation of articular cartilage', *Ultrasound in Medicine and Biology*, 30(6), pp. 783–792.

Saiz-Poseu, J., Mancebo-Aracil, J., Nador, F., Busqué, F. & Ruiz-Molina, D. (2019) 'The Chemistry behind Catechol-Based Adhesion', *Angewandte Chemie - International Edition*, 58(3), pp. 696–714.

Salgado, C., Jordan, O. & Allémann, E. (2021) 'Osteoarthritis in vitro models: Applications and implications in development of intra-articular drug delivery systems', *Pharmaceutics*, 13(1), pp. 1–23.

Samvelyan, H.J., Hughes, D., Stevens, C. & Staines, K.A. (2020) 'Models of Osteoarthritis: Relevance and New Insights', *Calcified Tissue International*, (0123456789), .

Sanchez, C., Deberg, M.A., Piccardi, N., Msika, P., Reginster, J.Y.L. & Henrotin, Y.E. (2005) 'Subchondral bone osteoblasts induce phenotypic changes in human osteoarthritic chondrocytes', *Osteoarthritis and Cartilage*, 13(11), pp. 988–997.

Sandell, L.J. & Aigner, T. (2001) *Articular cartilage and changes in Arthritis Cell biology of osteoarthritis*,

Sandy, J.D., Flannery, C.R., Neame, P.J. & Stefan Lohmander, L. (1992) 'The structure of aggrecan fragments in human synovial fluid: Evidence for the involvement in osteoarthritis of a novel proteinase which cleaves the Glu 373-Ala 374 bond of the interglobular domain', *Journal of Clinical Investigation*, 89(5), pp. 1512–1516.

Santamaria, S., Cuffaro, D., Nuti, E., Ciccone, L., Tuccinardi, T., Liva, F., D'Andrea, F., de Groot, R., Rossello, A. & Ahnström, J. (2021) 'Exosite inhibition of ADAMTS-5 by a glycoconjugated arylsulfonamide', *Scientific Reports*, 11(1), pp. 1–13.

Scaffaro, R., Lopresti, F., Botta, L. & Maio, A. (2016) 'Mechanical behavior of polylactic acid/polycaprolactone porous layered functional composites', *Composites Part B: Engineering*, 98pp. 70–77.

Scalzone, A., Bonifacio, M.A., Cometa, S., Cucinotta, F., de Giglio, E., Ferreira, A.M. & Gentile, P. (2020) 'pH-Triggered Adhesiveness and Cohesiveness of Chondroitin Sulfate-Catechol Biopolymer for Biomedical Applications', *Frontiers in Bioengineering and Biotechnology*, 8(June), pp. 1–14.

Scalzone, A., Cerqueni, G., Bonifacio, M.A., Pistillo, M., Cometa, S., Mattioli, M., Wang, X.N., Dalgarno, K., Ferreira, A.M., Giglio, E. de & Gentile, P. (2022) 'Valuable effect of Manuka Honey in increasing the printability and chondrogenic potential of a naturally derived bioink', *Materials Today Bio*, 14(May), p. 100287.

Scalzone, A., Ferreira, A.M., Tonda-Turo, C., Ciardelli, G., Dalgarno, K. & Gentile, P. (2019a) 'The interplay between chondrocyte spheroids and mesenchymal stem cells boosts cartilage regeneration within a 3D natural-based hydrogel', *Scientific Reports*, 9(1), pp. 1–12.

Scalzone, A., Ferreira, A.M., Tonda-Turo, C., Ciardelli, G., Dalgarno, K. & Gentile, P. (2019b) 'The interplay between chondrocyte spheroids and mesenchymal stem cells boosts cartilage regeneration within a 3D natural-based hydrogel', *Scientific Reports*, 9(1), pp. 1–12.

Scalzone, A., Tonda-Turo, C., Ferreira, A.M. & Gentile, P. (2021a) '3D-printed Soft Hydrogels for Cell Encapsulation', in *Soft Matter for Biomedical Applications*. [Online]. pp. 594–625.

Scalzone, A., Tonda-Turo, C., Ferreira, A.M. & Gentile, P. (2021b) '3D-printed Soft Hydrogels for Cell Encapsulation', in *Soft Matter for Biomedical Applications*. [Online]. pp. 594–625.

Scalzone, A., Wang, X.N., Dalgarno, K., Ferreira, A.M. & Gentile, P. (2022) 'A chondrosphere-based scaffold free approach to manufacture an in vitro articular cartilage model', *Tissue Engineering Part A*, 28(1–2), pp. 84–93.

Schade, A., Delyagina, E., Scharfenberg, D., Skorska, A., Lux, C., David, R. & Steinhoff, G. (2013) 'Innovative strategy for microRNA delivery in human mesenchymal stem cells via magnetic nanoparticles', *International Journal of Molecular Sciences*, 14(6), pp. 10710–10726.

Schiavi, J., Reppel, L., Charif, N., de Isla, N., Mainard, D., Benkirane-Jessel, N., Stoltz, J.F., Rahouadj, R. & Huselstein, C. (2018) 'Mechanical stimulations on human bone marrow mesenchymal stem cells enhance cells differentiation in a three-dimensional layered scaffold', *Journal of Tissue Engineering and Regenerative Medicine*, 12(2), pp. 360–369.

Schmidt, T.A., Gastelum, N.S., Han, E.H., Nugent-Derfus, G.E., Schumacher, B.L. & Sah, R.L. (2008) 'Differential regulation of proteoglycan 4 metabolism in cartilage by IL-1α, IGF-I, and TGF-β1', *Osteoarthritis and Cartilage*, 16(1), pp. 90–97.

Schubert, T., Anders, S., Neumann, E., Schölmerich, J., Hofstädter, F., Grifka, J., Libera, J. & Schedel, J. (2009) *Long-term effects of chondrospheres on cartilage lesions in an autologous chondrocyte implantation model as investigated in the SCID mouse model*, pp. 455–460.

Schwab, A., Levato, R., D'Este, M., Piluso, S., Eglin, D. & Malda, J. (2020) 'Printability and Shape Fidelity of Bioinks in 3D Bioprinting', *Chemical Reviews*, 120(19), pp. 11028–11055.

Schwartz, R., Malpica, M., Thompson, G.L. & Miri, A.K. (2020) 'Cell encapsulation in gelatin bioink impairs 3D bioprinting resolution', *Journal of the Mechanical Behavior of Biomedical Materials*, 103(November 2019), p. 103524.

Shah, S., Otsuka, T., Bhattacharjee, M. & Laurencin, C.T. (2021) 'Minimally Invasive Cellular Therapies for Osteoarthritis Treatment', *Regenerative Engineering and Translational Medicine*, 7(1), pp. 76–90.

Sharifi, N. & Gharravi, A.M. (2019) 'Shear bioreactors stimulating chondrocyte regeneration, a systematic review', *Inflammation and Regeneration*, 39(1), pp. 1–8.

Sharma, B., Williams, C.G., Kim, T.K., Sun, D., Malik, A., Khan, M., Leong, K. & Elisseeff, J.H. (2007) 'Designing zonal organization into tissue-engineered cartilage', *Tissue Engineering*, 13(2), pp. 405–414.

Shen, P.C., Lu, C.C., Chou, S.H., Liu, Z.M., Su, S.J. & Tien, Y.C. (2021) 'Zonal-layered chondrocyte sheets for repairment of full-thickness articular cartilage defect: A mini-pig model', *Biomedicines*, 9(12), .

Shenoy, S.L., Bates, W.D., Frisch, H.L. & Wnek, G.E. (2005) 'Role of chain entanglements on fiber formation during electrospinning of polymer solutions: Good solvent, non-specific polymer-polymer interaction limit', *Polymer*, 46(10), pp. 3372–3384.

Shin, H., Olsen, B.D. & Khademhosseini, A. (2014) 'Gellan gum microgel-reinforced cell-laden gelatin hydrogels', *Journal of Materials Chemistry B*, 2(17), pp. 2508–2516.

Shin, J., Kang, E.H., Choi, S., Jeon, E.J., Cho, J.H., Kang, D., Lee, H., Yun, I.S. & Cho, S.W. (2021a) 'Tissue-Adhesive Chondroitin Sulfate Hydrogel for Cartilage Reconstruction', *ACS Biomaterials Science and Engineering*, 7(9), pp. 4230–4243.

Shin, J., Kang, E.H., Choi, S., Jeon, E.J., Cho, J.H., Kang, D., Lee, H., Yun, I.S. & Cho, S.W. (2021b) 'Tissue-Adhesive Chondroitin Sulfate Hydrogel for Cartilage Reconstruction', *ACS Biomaterials Science and Engineering*, 7(9), pp. 4230–4243.

Shoulders, M.D. & Raines, R.T. (2009) 'Collagen structure and stability', *Annual Review of Biochemistry*, 78pp. 929–958.

Si, H.B., Zeng, Y., Liu, S.Y., Zhou, Z.K., Chen, Y.N., Cheng, J.Q., Lu, Y.R. & Shen, B. (2017) 'Intra-articular injection of microRNA-140 (miRNA-140) alleviates osteoarthritis (OA) progression by modulating extracellular matrix (ECM) homeostasis in rats', *Osteoarthritis and Cartilage*, 25(10), pp. 1698–1707.

Siebuhr, A.S., Werkmann, D., Bay-Jensen, A.C., Thudium, C.S., Karsdal, M.A., Serruys, B., Ladel, C., Michaelis, M. & Lindemann, S. (2020) 'The anti-ADAMTS-5 nanobody® M6495 protects cartilage degradation ex vivo', *International Journal of Molecular Sciences*, 21(17), pp. 1–14.

Sill, T.J. & von Recum, H.A. (2008) 'Electrospinning: Applications in drug delivery and tissue engineering', *Biomaterials*, 29(13), pp. 1989–2006.

Silva, A.K.A., Richard, C., Bessodes, M., Scherman, D. & Merten, O.W. (2009) 'Growth factor delivery approaches in hydrogels', *Biomacromolecules*, 10(1), pp. 9–18.

Da Silva, L.P., Cerqueira, M.T., Sousa, R.A., Reis, R.L., Correlo, V.M. & Marques, A.P. (2014) 'Engineering cell-adhesive gellan gum spongy-like hydrogels for regenerative medicine purposes', *Acta Biomaterialia*, 10(11), pp. 4787–4797.

Silva-Correia, J., Zavan, B., Vindigni, V., Silva, T.H., Oliveira, J.M., Abatangelo, G. & Reis, R.L. (2013) 'Biocompatibility evaluation of ionic- and photo-crosslinked methacrylated gellan gum hydrogels: In vitro and in vivo study', *Advanced Healthcare Materials*, 2(4), pp. 568–575.

Smith, L.R., Kok, H.J., Zhang, B., Chung, D., Spradlin, R.A., Rakoczy, K.D., Lei, H., Boesze-Battaglia, K. & Barton, E.R. (2020) 'Matrix metalloproteinase 13 from satellite cells is required for efficient muscle growth and regeneration', *Cellular Physiology and Biochemistry*, 54(3), pp. 333–353.

Somoza, R.A., Welter, J.F., Correa, D. & Caplan, A.I. (2014) 'Chondrogenic Differentiation of Mesenchymal Stem Cells: Challenges and Unfulfilled Expectations', *Tissue Engineering Part B: Reviews*, 20(6), pp. 596–608.

Sophia Fox, A.J., Bedi, A. & Rodeo, S.A. (2009a) 'The basic science of articular cartilage: Structure, composition, and function', *Sports Health*, 1(6), pp. 461–468.

Sophia Fox, A.J., Bedi, A. & Rodeo, S.A. (2009b) 'The basic science of articular cartilage: Structure, composition, and function', *Sports Health*, 1(6), pp. 461–468.

Stannus, O., Jones, G., Cicuttini, F., Parameswaran, V., Quinn, S., Burgess, J. & Ding, C. (2010) 'Circulating levels of IL-6 and TNF-α are associated with knee radiographic osteoarthritis and knee cartilage loss in older adults', *Osteoarthritis and Cartilage*, 18(11), pp. 1441–1447.

Stein, G.S., Lian, J.B., van Wijnen, A.J., Stein, J.L., Montecino, M., Javed, A., Zaidi, S.K., Young, D.W., Choi, J.Y. & Pockwinse, S.M. (2004) 'Runx2 control of organization, assembly and activity of the regulatory machinery for skeletal gene expression', *Oncogene*, 23(24), pp. 4315–4329.

Steinberg, M.S. (1996) 'Adhesion in Development: An Historical Overview', *Developmental Biology*, 180(0312), pp. 377–388.

Stevens, L.R., Gilmore, K.J., Wallace, G.G. & In het Panhuis, M. (2016) 'Tissue engineering with gellan gum', *Biomaterials Science*, 4(9), pp. 1276–1290.

Strunov, A., Boldyreva, L. V, Pavlova, G.A., Pindyurin, A. V, Gatti, M. & Kiseleva, E. (2016) 'MethodsX A simple and effective method for ultrastructural analysis of mitosis in Drosophila S2 cells', *MethodsX*, 3pp. 551–559.

Sun, A.X., Numpaisal, P. on, Gottardi, R., Shen, H., Yang, G. & Tuan, R.S. (2016) 'Cell and Biomimetic Scaffold-Based Approaches for Cartilage Regeneration', *Operative Techniques in Orthopaedics*, 26(3), pp. 135–146.

Sun, K., Tao, C. & Wang, D.A. (2022) 'Scaffold-free approaches for the fabrication of engineered articular cartilage tissue', *Biomedical materials (Bristol, England)*, 17(2), .

T., T., T., S., M., N.N., H., Y., D., Y., M., O., N., M., T., K., Y., K., Y., N., H., F., M., N.N., M., I., K., T., M., W., I., H., Tahara, T., Shibata, T., Nakamura, M., et al. (2009) 'Hsa-miR-34c suppresses growth and invasion of human laryngeal carcinoma cells via targeting c-Met', *International Journal of Molecular Medicine*, 23(4), pp. 521–527.

Tat, S.K., Pelletier, J.P., Velasco, C.R., Padrines, M. & Martel-Pelletier, J. (2009) 'New perspective in osteoarthritis: The OPG and RANKL system as a potential therapeutic target?', *Keio Journal of Medicine*, 58(1), pp. 29–40.

Thakur, A., Ranote, S., Kumar, D., Bhardwaj, K.K., Gupta, R. & Chauhan, G.S. (2018) 'Synthesis of a PEGylated Dopamine Ester with Enhanced Antibacterial and Antifungal Activity', *ACS Omega*, 3(7), pp. 7925–7933.

Thibault, M., Poole, A.R. & Buschmann, M.D. (2002) 'Cyclic compression of cartilage/bone explants in vitro leads to physical weakening, mechanical breakdown of collagen and release of matrix fragments', *Journal of Orthopaedic Research*, 20(6), pp. 1265–1273.

Thorvaldsson, A., Silva-Correia, J., Oliveira, J.M., Reis, R.L., Gatenholm, P. & Walkenström, P. (2013) 'Development of nanofiber-reinforced hydrogel scaffolds for nucleus pulposus regeneration by a combination of electrospinning and spraying technique', *Journal of Applied Polymer Science*, 128(2), pp. 1158–1163.

Tío, L., Triginer, L., Ribes, A., Camps, P., Torres-Claramunt, R., Monllau, J.C. & Monfort, J. (2022) 'CARTILAGE DEGRADATION STATUS OF KNEE OSTEOARTHIRTIC PATIENTS CAN BE PREDICTED BY CHONDROCYTE GENE EXPRESSION ANALYSIS', *Annals of the Rheumatic Diseases*, 81(Suppl 1), pp. 1158.2-1159.

Tofiño-Vian, M., Guillén, M.I., Pérez Del Caz, M.D., Silvestre, A. & Alcaraz, M.J. (2018) 'Microvesicles from Human Adipose Tissue-Derived Mesenchymal Stem Cells as a New Protective Strategy in Osteoarthritic Chondrocytes', *Cellular Physiology and Biochemistry*, 47(1), pp. 11–25.

Tonda-turo, C., Carmagnola, I., Chiappone, A. & Feng, Z. (2020) 'Bioprinting Photocurable chitosan as bioink for cellularized therapies towards personalized scaffold architecture', *Bioprinting*, 18(December 2019), p. e00082.

Torzilli, P.A., Dethmers, D.A., Rose, D.E. & Schryuer, H.F. (1983) 'Movement of interstitial water through loaded articular cartilage', *Journal of Biomechanics*, 16(3), pp. 169–179.

Tsai, C.C., Kuo, S.H., Lu, T.Y., Cheng, N.C., Shie, M.Y. & Yu, J. (2020) 'Enzyme-Cross-linked Gelatin Hydrogel Enriched with an Articular Cartilage Extracellular Matrix and Human Adipose-Derived Stem Cells for Hyaline Cartilage Regeneration of Rabbits', *ACS Biomaterials Science and Engineering*, 6(9), pp. 5110–5119.

Urlic, I. & Ivkovic, A. (2021) 'Cell Sources for Cartilage Repair—Biological and Clinical Perspective Inga', *Cells*, 10(2496), .

Ventura, R.D. (2021) 'An Overview of Laser-assisted Bioprinting (LAB) in Tissue Engineering Applications', *Medical Lasers*, 10(2), pp. 76–81.

Verma, P. & Dalal, K. (2011) 'ADAMTS-4 and ADAMTS-5: Key enzymes in osteoarthritis', *Journal of Cellular Biochemistry*, 112(12), pp. 3507–3514.

Versus Arthritis (2021) *The State of Musculoskeletal Health 2021*,

Vieira, S., da Silva Morais, A., Garet, E., Silva-Correia, J., Reis, R.L., González-Fernández, Á. & Miguel Oliveira, J. (2019) 'Self-mineralizing Ca-enriched methacrylated gellan gum beads for bone tissue engineering', *Acta Biomaterialia*, 93(xxxx), pp. 74–85.

Vikingsson, L., Vinals-Guitart, A., Valera-Martínez, A., Riera, J., Vidaurre, A., Gallego Ferrer, G. & Gómez Ribelles, J.L. (2016) 'Local deformation in a hydrogel induced by an external magnetic field', *Journal of Materials Science*, 51(22), pp. 9979–9990.

Vilela, C.A., Correia, C., da Silva Morais, A., Santos, T.C., Gertrudes, A.C., Moreira, E.S., Frias, A.M., Learmonth, D.A., Oliveira, P., Oliveira, J.M., Sousa, R.A., Espregueira-Mendes, J.D. & Reis, R.L. (2018) 'In vitro and in vivo performance of methacrylated gellan gum hydrogel formulations for cartilage repair*', *Journal of Biomedical Materials Research - Part A*, 106(7), pp. 1987–1996.

Vincent, T.L., McLean, C.J., Full, L.E., Peston, D. & Saklatvala, J. (2007) 'FGF-2 is bound to perlecan in the pericellular matrix of articular cartilage, where it acts as a chondrocyte mechanotransducer', *Osteoarthritis and Cartilage*, 15(7), pp. 752–763.

Vizoso, F.J., Eiro, N., Cid, S., Schneider, J. & Perez-Fernandez, R. (2017) 'Mesenchymal stem cell secretome: Toward cell-free therapeutic strategies in regenerative medicine', *International Journal of Molecular Sciences*, 18(9), .

Vogel, W., Gish, G.D., Alves, F. & Pawson, T. (1997) *<1-s2.0-S1097276500800039-main.pdf>*, 1pp. 13–23.

Vonk, L.A., Kragten, A.H.M., Dhert, W.J.A., Saris, D.B.F. & Creemers, L.B. (2014) 'Overexpression of hsa-miR-148a promotes cartilage production and inhibits cartilage degradation by osteoarthritic chondrocytes', *Osteoarthritis and Cartilage*, 22(1), pp. 145–153.

de Vries-van Melle, M.L., Mandl, E.W., Kops, N., Koevoet, W.J.L.M., Verhaar, J.A.N. & van Osch, G.J.V.M. (2011) 'An Osteochondral Culture Model to Study Mechanisms Involved in Articular Cartilage Repair', *Tissue Engineering Part C: Methods*, 18(1), pp. 45–53.

Vyavahare, S., Teraiya, S., Panghal, D. & Kumar, S. (2020) 'Fused deposition modelling: a review', *Rapid Prototyping Journal*, 26(1), pp. 176–201.

Walzer, S.M., Toegel, S., Chiari, C., Farr, S., Rinner, B., Weinberg, A.M., Weinmann, D., Fischer, M.B. & Windhager, R. (2021) 'A 3-Dimensional In Vitro Model of Zonally Organized Extracellular Matrix', *Cartilage*, 13(2_suppl), pp. 336S-345S.

Wang, D., Li, C., Gong, Y., Wang, C., Lai, R.C., Su, K., Zhang, F. & Wang, D. (2009) *An improved injectable polysaccharide hydrogel : modified gellan gum for long-term cartilage regeneration in vitro*, 19(14), .

Wang, J., Zhang, F., Tsang, W.P., Wan, C. & Wu, C. (2017) 'Fabrication of injectable high strength hydrogel based on 4-arm star PEG for cartilage tissue engineering', *Biomaterials*, 120pp. 11–21.

Wang, P., Guan, P.P., Guo, C., Zhu, F., Konstantopoulos, K. & Wang, Z.Y. (2013) 'Fluid shear stress-induced osteoarthritis: Roles of cyclooxygenase-2 and its metabolic products in inducing the expression of proinflammatory cytokines and matrix metalloproteinases', *FASEB Journal*, 27(12), pp. 4664–4677.

Warren, H. & In Het Panhuis, M. (2015) 'Highly conducting composite hydrogels from gellan gum, PEDOT:PSS and carbon nanofibres', *Synthetic Metals*, 206pp. 61–65.

Weber, A.E., Bolia, I.K. & Trasolini, N.A. (2021) 'Biological strategies for osteoarthritis: from early diagnosis to treatment', *International Orthopaedics*, 45(2), pp. 335–344.

Wehland, M., Steinwerth, P., Aleshcheva, G., Sahana, J., Hemmersbach, R., Lützenberg, R., Kopp, S., Infanger, M. & Grimm, D. (2020) 'Tissue engineering of cartilage using a random positioning machine', *International Journal of Molecular Sciences*, 21(24), pp. 1–24.

Wei, W., Ma, Y., Yao, X., Zhou, W., Wang, X., Li, C., Lin, J., He, Q., Leptihn, S. & Ouyang, H. (2021) 'Advanced hydrogels for the repair of cartilage defects and regeneration', *Bioactive Materials*, 6(4), pp. 998–1011.

Weitzmann, M.N. (2013) 'The Role of Inflammatory Cytokines, the RANKL/OPG Axis, and the Immunoskeletal Interface in Physiological Bone Turnover and Osteoporosis', *Scientifica*, 2013pp. 1–29.

Wen, C., Lu, L. & Li, X. (2014) 'An interpenetrating network biohydrogel of gelatin and gellan gum by using a combination of enzymatic and ionic crosslinking approaches', *Polymer International*, 63(9), pp. 1643–1649.

Whang, K., Elenz, D.R., Nam, E.K., Tsai, D.C., Thomas, C.H., Nuber, G.W., Glorieux, F.H., Travers, R., Sprague, S.M. & Healy, K.E. (1999) 'Engineering bone regeneration with bioabsorbable scaffolds with novel microarchitecture', *Tissue Engineering*, 5(1), pp. 35–51.

Williams, C.G., Kim, T.K., Taboas, A., Malik, A., Manson, P. & Elisseeff, J. (2003) 'In Vitro Chondrogenesis of Bone Marrow-Derived', *Tissue engineering*, 9(4), pp. 679–688.

Wise, J.K., Yarin, A.L., Megaridis, C.M. & Cho, M. (2009) 'Chondrogenic differentiation of human mesenchymal stem cells on oriented nanofibrous scaffolds: Engineering the superficial zone of articular cartilage', *Tissue Engineering - Part A*, 15(4), pp. 913–921.

Wojdasiewicz, P., Poniatowski, Ł.A. & Szukiewicz, D. (2014) 'The role of inflammatory and anti-inflammatory cytokines in the pathogenesis of osteoarthritis', *Mediators of Inflammation*, 2014.

Woodfield, T., Lim, K., Morouço, P., Levato, R., Malda, J. & Melchels, F. (2017) *5.14 Biofabrication in tissue engineering*. Vol. 5.

Wu, Q. (1995) 'A recent experience of CABG operation in fifty patients', *Chinese Journal of Cardiology*, 23(4), pp. 256-257+311.

Wu, Y., Kennedy, P., Bonazza, N., Yu, Y., Dhawan, A. & Ozbolat, I. (2021) 'Three-Dimensional Bioprinting of Articular Cartilage: A Systematic Review', *Cartilage*, 12(1), pp. 76–92.

Xiao, P., Zhu, X., Sun, J., Zhang, Y., Qiu, W., Li, J. & Wu, X. (2021) 'LncRNA NEAT1 regulates chondrocyte proliferation and apoptosis via targeting miR-543/PLA2G4A axis', *Human Cell*, 34(1), pp. 60–75.

Xin, S., Chimene, D., Garza, J.E., Gaharwar, A.K. & Alge, D.L. (2019) 'Clickable PEG hydrogel microspheres as building blocks for 3D bioprinting', *Biomaterials Science*, 7(3), pp. 1179–1187.

Xu, F. & Teitelbaum, S.L. (2013) 'Osteoclasts: New Insights', *Bone Research*, 1(1), pp. 11–26.

Xu, J.H., Li, Z.H., Hou, Y.D. & Fang, W.J. (2015) 'Potential mechanisms underlying the Runx2 induced osteogenesis of bone marrow mesenchymal stem cells', *American Journal of Translational Research*, 7(12), pp. 2527–2535.

Xu, Z., Li, Z., Jiang, S. & Bratlie, K.M. (2018) 'Chemically Modified Gellan Gum Hydrogels with Tunable Properties for Use as Tissue Engineering Scaffolds', *ACS Omega*, 3(6), pp. 6998–7007.

Yang, J., Shen, M., Wen, H., Luo, Y., Huang, R., Rong, L. & Xie, J. (2020) 'Recent advance in delivery system and tissue engineering applications of chondroitin sulfate', *Carbohydrate Polymers*, 230(235), p. 115650.

Yang, X., Konstantini I, M., Zhe, C., Christopher, C., David, K. & Farid, B. (2017) *Introduction to Cartilage Yang*.

Yeung, P., Cheng, K., Yan, C. & Chan, B.P. (2019) 'Microencapsulation of human osteoarthritis chondrocytes in collagen microsphere - an in vitro model for osteoarthritis studies', *Osteoarthritis and Cartilage*, 27(2019), p. S426.

Yeung, P., Zhang, W., Wang, X.N., Yan, C.H. & Chan, B.P. (2018) 'A human osteoarthritis osteochondral organ culture model for cartilage tissue engineering', *Biomaterials*, 162pp. 1–21.

Yilmaz, E.N. & Zeugolis, D.I. (2020) 'Electrospun Polymers in Cartilage Engineering—State of Play', *Frontiers in Bioengineering and Biotechnology*, 8(February), pp. 1–17.

Yokota, H., Goldring, M.B. & Sun, H. Bin (2003) 'CITED2-mediated Regulation of MMP-1 and MMP-13 in Human Chondrocytes under Flow Shear', *Journal of Biological Chemistry*, 278(47), pp. 47275–47280.

Yu, F., Cao, X., Li, Y., Zeng, L., Yuan, B. & Chen, X. (2014) 'An injectable hyaluronic acid/PEG hydrogel for cartilage tissue engineering formed by integrating enzymatic crosslinking and Diels-Alder "click chemistry"', *Polymer Chemistry*, 5(3), pp. 1082–1090.

Yu, F., Cao, X., Zeng, L., Zhang, Q. & Chen, X. (2013) 'An interpenetrating HA/G/CS biomimic hydrogel via Diels-Alder click chemistry for cartilage tissue engineering', *Carbohydrate Polymers*, 97(1), pp. 188–195.

Yuan, Q., Sun, L., Li, J.J. & An, C.H. (2014) 'Elevated VEGF levels contribute to the pathogenesis of osteoarthritis', *BMC Musculoskeletal Disorders*, 15(1), pp. 1–8.

Zand-Rajabi, H. & Madadlou, A. (2016a) 'Caffeine-loaded whey protein hydrogels reinforced with gellan and enriched with calcium chloride', *International Dairy Journal*, 56pp. 38–44.

Zand-Rajabi, H. & Madadlou, A. (2016b) 'Caffeine-loaded whey protein hydrogels reinforced with gellan and enriched with calcium chloride', *International Dairy Journal*, 56pp. 38–44.

Zarrintaj, P., Manouchehri, S., Ahmadi, Z., Saeb, M.R., Urbanska, A.M., Kaplan, D.L. & Mozafari, M. (2018) 'Agarose-based biomaterials for tissue engineering', *Carbohydrate Polymers*, 187(December 2017), pp. 66–84.

Zelinka, A.A. & Kandel, R.A. (2019) 'In vitro formed deep zone cartilage tissues: a model to study formation of the zone of calcified cartilage', *Osteoarthritis and Cartilage*, 27(2019), pp. S164–S165.

Zhang, B., Wang, L., Song, P., Pei, X., Sun, H., Wu, L., Zhou, C., Wang, K., Fan, Y. & Zhang, X. (2021) '3D printed bone tissue regenerative PLA/HA scaffolds with comprehensive performance optimizations', *Materials and Design*, 201p. 109490.

Zhang, L., Hu, J. & Athanasiou, K.A. (2009) 'The Role of Tissue Engineering in Articular Cartilage Repair and Regeneration', *Crit Rev Biomed Eng*, 37(1–2), pp. 1–57.

Zhang Y and Jordan M (2010) 'Epidemiology of Osteoarthritis', *Clin Geriatr Med.*, 26(154), pp. 355–369.

Zhao, J., Griffin, M., Cai, J., Li, S., Bulter, P.E.M. & Kalaskar, D.M. (2016) 'Bioreactors for tissue engineering: An update', *Biochemical Engineering Journal*, 109pp. 268–281.

Zhao, R., Wang, S., Jia, L., Li, Q., Qiao, J. & Peng, X. (2019) 'Interleukin-1 receptor antagonist protein (IL-1Ra) and miR-140 overexpression via pNNS-conjugated chitosan-mediated gene transfer enhances the repair of full-Thickness cartilage defects in a rabbit model', *Bone and Joint Research*, 8(3), pp. 165–178.

Zhou, P.H., Qiu, B., Deng, R.H., Li, H.J., Xu, X.F. & Shang, X.F. (2018) 'Chondroprotective effects of hyaluronic acid-chitosan nanoparticles containing plasmid DNA encoding cytokine response modifier A in a rat knee osteoarthritis model', *Cellular Physiology and Biochemistry*, 47(3), pp. 1207–1216.

Zhou, X., Liu, D., You, L. & Wang, L. (2010) 'Quantifying fluid shear stress in a rocking culture dish', *Journal of Biomechanics*, 43(8), pp. 1598–1602.

Zhu, D., Tong, X., Trinh, P. & Yang, F. (2018) 'Mimicking Cartilage Tissue Zonal Organization by Engineering Tissue-Scale Gradient Hydrogels as 3D Cell Niche', *Tissue Engineering - Part A*, 24(1–2), pp. 1–10.

Zhu, H., Gong, H., Liu, Q. & Chen, H.H. (2017) *Three-dimensional Bioprinting for Cartilage Regeneration*, pp. 49–74.

Zhu, H., Gong, H., Lui, Q. & Chen, H.H. (2017) 'Tissue engineering and nanotheranostics', *Tissue Engineering and Nanotheranostics*, (December 2017), pp. 1–294.

Zia, K.M., Tabasum, S., Khan, M.F., Akram, N., Akhter, N., Noreen, A. & Zuber, M. (2018) 'Recent trends on gellan gum blends with natural and synthetic polymers: A review', *International Journal of Biological Macromolecules*, 109pp. 1068–1087.

Zong, H., Wang, B., Li, G., Yan, S., Zhang, K., Shou, Y. & Yin, J. (2020) 'Biodegradable High-Strength Hydrogels with Injectable Performance Based on Poly(l -Glutamic Acid) and Gellan Gum', *ACS Biomaterials Science and Engineering*, 6(8), pp. 4702–4713.

Zuliani, C.C., Bombini, M.F., de Andrade, K.C., Mamoni, R., Pereira, A.H. & Coimbra, I.B. (2018) 'Micromass cultures are effective for differentiation of human amniotic fluid stem cells into chondrocytes', *Clinics*, 73(7), pp. 1–8.